Measurement of the properties of the Standard Model Higgs boson in the H →ZZ∗→4l decay channel with the ATLAS Experiment at CERN

Benhar Noccioli, Eleonora

UNIVERSITÉ DE GENÈVE
Département de physique nucléaire et corpusculaire

FACULTÉ DES SCIENCES
Prof. honoraire Allan Clark
Prof. Giuseppe Iacobucci
Dr. Gabriella Pásztor

Measurement of the properties of the Standard Model Higgs boson in the $H \to ZZ^* \to 4\ell$ decay channel with the ATLAS Experiment at CERN

THÈSE

présentée à la Faculté des sciences de l'Université de Genève
pour obtenir le grade de Docteur ès sciences, mention physique

par

Eleonora Benhar Noccioli

d'Italie

Thèse N° 4814

GENÈVE
Atelier d'impression ReproMail
2015

UNIVERSITÉ DE GENÈVE

FACULTÉ DES SCIENCES

Doctorat ès sciences
Mention physique

Thèse de *Madame Eleonora BENHAR NOCCIOLI*

intitulée :

"Measurement of the Properties of the Standard Model Higgs Boson in the H->ZZ*->4ℓ Decay Channel with the ATLAS Experiment at CERN"

La Faculté des sciences, sur le préavis de Monsieur A. CLARK, professeur honoraire et directeur de thèse (Département de physique nucléaire et corpusculaire), Monsieur G. IACOBUCCI, professeur ordinaire et codirecteur de thèse (Département de physique nucléaire et corpusculaire), Madame G. PASZTOR, docteure et codirectrice de thèse (Department of Physics, Carleton University, Ottawa, Canada), Monsieur T. GOLLING, professeur associé (Département de physique nucléaire et corpusculaire), Monsieur A. NISATI, professeur (Dipartimento di Fisica e Istituto Nazionale di Fisica Nucleare, Università di Roma I 'La Sapienza', Roma, Italia), autorise l'impression de la présente thèse, sans exprimer d'opinion sur les propositions qui y sont énoncées.

Genève, le 19 août 2015

Thèse - 4814 -

Le Doyen

N.B. - La thèse doit porter la déclaration précédente et remplir les conditions énumérées dans les "Informations relatives aux thèses de doctorat à l'Université de Genève".

Acknowledgments

First and foremost, I am indebted to my supervisor, Prof. Allan G. Clark, for giving me the opportunity to join the ATLAS group at the University of Geneva. I am very grateful for the encouragement and support he has shown me during my years as a PhD, and for making sure I would survive the ATLAS jungle with the guidance of two fantastic postdocs.

Thanks José, for all that you've taught me during my first year; it has been a real pleasure working with you.

A special thanks goes to Gabi, for guiding me through the rest of my PhD. Thank you for sharing with me your knowledge on electrons, Higgs, and particle physics in general, and for always being available to talk and answer questions. Most all, I would like to thank you for teaching me that everything in life, even physics, needs to be approached with optimism. I will do my best to always follow your example.

I would like to thank all my colleagues at the University of Geneva, for the interesting, enriching and stimulating years spent together.

Thanks to Tica, for making bureaucracy bearable, and for being so incredibly efficient that now I really miss working for a Swiss institution.

A big thank you goes also to all my friends, near and far, for the good times shared and for all the rest...

I of course need to thank my wonderful family, for always encouraging me all along this path. Thank you dad, for teaching me a great deal of the things I needed to go through this PhD, for patiently reading also this thesis and for the constant feedback. Thank you mom, for somehow always being able to confort me and to give the right advice even if you live one thousand kilometres away. Thank you Bella, for displaying my theses on the shelf to impress your friends even if you hate physics, and for forgiving me for bringing another physicist into the family... Thank you also to Anna and Enea, for the true and continued affection, and for giving me such a special husband.

Finally, my biggest thanks goes to my husband, Giacomo. Thank you for truly sharing with me each day of our lives, for always believing in me, even when I couldn't, for always being by my side, for your encouragement and support, through the good and the most difficult times. None of this would have been possible without you.

Abstract

The research described in this thesis has contributed to the exciting discovery and then to the precise measurement of the properties of the Higgs boson, the long-sought particle that eluded physicists for almost 50 years from its first prediction. The work was done in the context of the $H \to ZZ^* \to 4\ell$ analysis, which has provided a unique opportunity to search for the Higgs boson and to confirm its SM-like nature.

The sensitivity of such analysis critically depends on our ability to efficiently reconstruct and identify leptons, and more generally on our knowledge of the electron and muon response of our detector. An important part of this thesis work was thus devoted to the study and improvement of several aspects of the electron reconstruction, focusing particularly on the challenging low-E_{T} region, which becomes critical when searching for a light Higgs boson.

A careful evaluation of the background sources is another key ingredient of the $H \to ZZ^* \to 4\ell$ analysis, and was the objective of the second part of the work done for this thesis. The main background is given by the irreducible ZZ^* SM production, which leads to good quality and well-isolated final-state leptons, and it is thus reliably estimated from simulation. This is not the case for the reducible backgrounds from Z+jets (including both light and heavy quarks) and top quark pair production, contributing significantly in the mass range below 180 GeV, where one of the Z bosons is produced off-shell. Data-driven techniques were required for the estimation of these backgrounds, with special care needed for electron backgrounds, which can arise from misidentified light-flavour hadrons, heavy-flavour semi-leptonic decays, as well as from photon conversions to an electron-positron pair.

Thanks to the great achievements obtained in the electron reconstruction, identification and energy calibration, as well as in other aspects of the analysis including the background estimation, an improved measurement of the Higgs boson mass in the $H \to ZZ^* \to 4\ell$ decay channel was recently published. The new measurement, based on the full Run 1 integrated luminosity recorded by the ATLAS detector (~ 25 fb^{-1}), features both statistical and systematic uncertainties reduced, compared to the previous publication [1] based on the same dataset. The measured mass, $m_H = 124.51 \pm 0.52$ (stat) ± 0.04 (syst) GeV, was combined with the result obtained in the $H \to \gamma\gamma$ decay channel to provide the best ATLAS measurement of the Higgs boson mass [2]. Furthermore, with an achieved precision of better than 0.2%, the combination of these results with those from the CMS collaboration represent the most precise measurement of the Higgs boson mass yet and among the most precise measurements performed at the LHC to date [3].

An improved measurement of the Higgs boson production and couplings was also recently finalised, again exploiting the entire Run 1 data statistics [4]. This analysis, which performs

an event categorisation according to the ggF, VBF and VH production modes, measured the signal strengths for gluon fusion and for vector-boson fusion to be $1.66^{+0.45}_{-0.41}$ (stat.)$^{+0.25}_{-0.15}$ (syst.) and $0.26^{+1.60}_{-0.91}$ (stat.)$^{+0.36}_{-0.23}$ (syst.), respectively. A fit to the different categories assuming a single overall signal strength was also performed, resulting in $\mu = 1.44^{+0.34}_{-0.31}$ (stat.)$^{+0.21}_{-0.11}$ (syst.).

The categorised analysis was also used to quantify the compatibility with the SM predictions, and no significant deviation was observed.

Finally, the last part of the work done for this thesis has focused on the first measurement of the fiducial and differential cross sections of the Higgs boson production in the $H \to ZZ^* \to 4\ell$ analysis, which is based on 20.3 fb^{-1}of pp collision data produced at $\sqrt{s} = 8$ TeV [5]. Fiducial cross sections are quoted in order to minimise the model dependence of the acceptance corrections related to the extrapolation to phase-space regions not covered by the detector. A fit to the $m_{4\ell}$ distribution is performed in order to extract the fiducial cross section, while a simpler cut-and-count method is used to determine the signal yields for the differential cross section measurements, performed in several observables related to the Higgs boson production and decay. The fiducial cross sections are corrected for detector effects to be directly compared to theoretical calculations. No significant deviations from the SM have been observed. The measured value of the inclusive fiducial cross section is $\sigma^{\text{fid}}_{\text{tot}} = 2.11^{+0.53}_{-0.47}$ (stat.) $\pm\, 0.08$ (syst.) fb^{-1}, to be compared with the theoretical prediction from Ref. [6] for a Higgs boson mass of 125.4 GeV, which is 1.30 ± 0.13 fb^{-1}.

Résumé

Le travail présenté dans cette thèse a contribué à la passionnante découverte et à la mesure précise des propriétés du boson de Higgs, cette particule longtemps recherchée qui a échappé aux physiciens pendant près de 50 ans depuis que son existence fut postulée. Le travail a été fait dans le contexte de l'étude du boson de Higgs dans sa désintégration en quatre leptons (électrons et/ou muons), qui a fourni une opportunité unique de rechercher le boson de Higgs et de confirmer sa compatibilité avec le modèle standard, en utilisant les données enregistrées par l'expérience ATLAS au LHC.

La sensibilité d'une telle analyse dépend essentiellement de notre capacité à reconstruire efficacement les leptons et à les identifier. Elle repose aussi, plus généralement, sur notre connaissance de la réponse des électrons et des muons dans le détecteur. Une partie importante de ce travail de thèse a donc été consacré à l'étude et à l'amélioration de plusieurs aspects de la reconstruction des électrons, en se concentrant en particulier sur la région de basse énergie transverse, qui devient critique lorsqu'on recherche un boson de Higgs léger.

Une évaluation minutieuse des sources de bruit de fond est un autre ingrédient clé de l'analyse $H \to ZZ^* \to 4\ell$, et constitue l'objectif de la deuxième partie du travail effectué pour cette thèse. Le bruit de fond principal est constitué de la production modèle standard irréductible de ZZ^*, qui produit dans l'état final des leptons de bonne qualité et bien isolés, et qui peut donc tre estimé de manière fiable à partir de la simulation. Ce n'est pas le cas pour les bruits de fond réductibles du Z+jets (incluant des quarks légers et lourds) et de la production de paires de quarks top, qui contribuent de manière significative dans la region de masse inférieure à 180 GeV, où l'un des bosons Z est produit virtuellement. Des techniques utilisant les données expérimentales ont été développées pour l'estimation de ces bruits de fond. Une attention particulière a été nécessaire pour les bruits de fond incluant des électrons, qui peuvent provenir de hadrons légers mal identifiés, de désintégrations semi-leptoniques de quarks lourds ainsi que de conversions de photons en paires électron-positon.

Grâce aux améliorations apportées dans la reconstruction, l'identification et la calibration en énergie des électrons, ainsi que dans d'autres aspects de l'analyse incluant l'estimation du bruit de fond, une mesure améliorée de la masse du boson de Higgs dans le canal de désintégration $H \to ZZ^* \to 4\ell$ a été récemment publiée. Le nouveau résultat, basé sur une luminosité intégrée de 25 fb^{-1}, présente des incertitudes statistique et systématique réduites, par rapport à la publication précédente basée sur les mme données [1]. La masse mesurée, $m_H = 124.51 \pm 0.52$ (stat) ± 0.04 (syst) GeV, a été combinée avec le résultat obtenu dans l'analyse du canal de désintégration $H \to \gamma\gamma$ pour obtenir la mesure la plus précise de la masse du boson de Higgs dans l'expérience ATLAS [2]. En outre, avec une précision inférieure à 0.2%,

la combinaison de ces résultats avec ceux de la collaboration CMS représente la mesure la plus précise de la masse du boson de Higgs, et figure parmi les mesures les plus précises réalisées au LHC à ce jour [3].

Une mesure améliorée de la production et des couplages du boson de Higgs a également été finalisée récemment, en utilisant à nouveau la totalité des données enregistrées par ATLAS pendant la période "Run 1" [4]. Cette analyse, effectuée avec une catégorisation des événements en fonction des différents modes de production ggF, VBF et VH, a mesuré une amplitude de signal de $1.66^{+0.45}_{-0.41}$ (stat.)$^{+0.25}_{-0.15}$ (syst.) pour la fusion de gluons et de $0.26^{+1.60}_{-0.91}$ (stat.)$^{+0.36}_{-0.23}$ (syst.) pour la fusion de bosons vecteurs, respectivement. Un ajustement dans les différentes catégories, en prenant l'hypothèse d'une amplitude de signal globale a aussi été effectué, le résultat obtenu est $\mu = 1.44^{+0.34}_{-0.31}$ (stat.)$^{+0.21}_{-0.11}$ (syst.).

L'analyse catégorisée a également été utilisée pour quantifier la compatibilité avec les prédictions du modèle standard. Aucune déviation significative n'a été observée.

Enfin, la dernière partie du travail effectué dans le cadre de cette thèse a porté sur la première mesure des sections efficaces fiducielles et différentielles du boson de Higgs dans le canal de désintégration $H \to ZZ^* \to 4\ell$, qui est basée sur une luminosité intégrée de 20.3 fb^{-1} produite à $\sqrt{s} = 8$ TeV [5]. Les sections efficaces fiducielles sont citées afin de minimiser la dépendance du modèle aux corrections en acceptance liées à l'extrapolation vers des espaces de phase non couverts par le détecteur. Un ajustement à la distribution de $m_{4\ell}$ est effectué afin d'extraire la section efficace fiducielle, tandis qu'une méthode plus simple de type expérience de comptage est utilisée pour determiner le nombre d'événements de signal pour les mesures de section efficace différentielle. Ces mesures sont effectuées sur différents observables liées à la production et la désintégration du boson de Higgs. Les sections efficaces fiducielles sont corrigées pour des effets de détecteur afin d'être directement comparables aux calculs théoriques. Aucune déviation significative par rapport au modèle standard n'a été observée. La valeur mesurée de la section efficace fiducielle inclusive est de $\sigma^{\text{fid}}_{\text{tot}} = 2.11^{+0.53}_{-0.47}$ (stat.) $\pm$ 0.08 (syst.) fb^{-1}, et doit tre comparée avec la prédiction théorique de la Ref. [6] pour une masse du boson de Higgs de 125.4 GeV, qui est de 1.30 ± 0.13 fb^{-1}.

Contents

Introduction

The field of high energy physics investigates the nature of the elementary constituents of matter and the interactions that govern their behaviour. During the past decades, enormous progress was made in the field, and the continuous interplay between theoretical and experimental efforts finally led to the development of an impressively accurate description of the available data - the Standard Model of particle physics. In this context, a fundamental role is played by the Brout-Englert-Higgs (BEH) mechanism, which predicts the existence of a new boson to explain how elementary particles acquire mass. Until the turn-on of the Large Hadron Collider (LHC), this was the only prediction of the SM not yet experimentally verified.

The inability to predict the value of the Higgs mass, and its very low production rates, have indeed made the search for the Higgs boson an extremely difficult task. Over the past 20 years the Large Electron-Positron (LEP) collider at CERN and the Tevatron at Fermilab have been both focusing on the Higgs search, and the LHC was mainly built to finally confirm the existence of this elusive particle, or exclude it, pointing the way to new physics beyond the SM.

At the start of LHC operations in 2010, the presence of a Higgs boson with mass below 115 GeV was ruled out by LEP data, and a fit to precision electro-weak data favoured a rather light Higgs, with masses below approximately 200 GeV. In the remaining mass range, the $H \to ZZ^* \to 4\ell$ decay channel, universally known as the "golden channel", offered a unique opportunity in the search for the Higgs boson. Despite its relatively low cross section, this channel indeed provides a clean signature and a high signal-to-background ratio, as well as the capability of fully reconstructing the final state.

In July 2012 the results of this search, combined with those obtained from the $H \to \gamma\gamma$ and $H \to WW$ channels, finally led to the observation of a new particle consistent with the long-sought Higgs boson, with a mass of about 125 GeV. Since then, having analysed two and a half times more data than was available for the discovery announcement, the $H \to ZZ^* \to 4\ell$ analysis has allowed to precisely measure the properties of the new particle, thus shedding light on its nature.

The sensitivity of the $H \to ZZ^* \to 4\ell$ analysis depends critically on our ability to efficiently reconstruct and identify leptons, and more generally on our knowledge of the electron and muon response of our detector. An important part of this thesis work was thus devoted to the study and improvement of several aspects of the electron reconstruction, focusing particularly on the challenging low-E_{T} region, which becomes critical when searching for a light Higgs boson.

A careful evaluation of the background sources is a key ingredient of the $H \to ZZ^* \to 4\ell$ analysis, and was the objective of the second part of the work done for this thesis. The main background is given by the irreducible ZZ^* SM production, which leads to good quality and

well-isolated final-state leptons, and it is thus reliably estimated from simulation. This is not the case for the reducible backgrounds from Z+jets (including both light and heavy quarks) and top quark pair production, contributing significantly in the mass range below 180 GeV, where one of the Z bosons is produced off-shell. Data-driven techniques were required for the estimation of these backgrounds, with special care needed for electron backgrounds, which can arise from misidentified light-flavour hadrons, heavy-flavour semi-leptonic decays, as well as from photon conversions to an electron-positron pair.

The great improvements in the lepton reconstruction, as well as in other aspects of the analysis including the background estimation, have led to the most precise ATLAS measurement of the Higgs boson mass, obtained from the combination of the $H \to ZZ^* \to 4\ell$ and the $H \to \gamma\gamma$ decay channels results. An improved measurement of the Higgs boson production and couplings was also recently finalised. The full Run 1 integrated luminosity recorded by the ATLAS detector, corresponding to approximately 25 fb^{-1}, was used for these measurements.

Finally, the last part of the work done for this thesis has focused on the first measurement of the fiducial and differential cross sections of the Higgs boson production in the $H \to ZZ^* \to 4\ell$ analysis, which is based on 20.3 fb^{-1}of pp collision data produced at $\sqrt{s} = 8$ TeV.

This thesis is organised as follows. Chapter 1 briefly introduces the theoretical formalism of the Standard Model, and gives a review of the most important experimental results obtained in the searches for the Higgs boson.

Chapter 2 and Chapter 3 illustrate the experimental setup, outlining the main features of the LHC and the ATLAS detector, respectively.

The reconstruction of the main physics objects used in $H \to ZZ^* \to 4\ell$ analysis are presented in Chapter 4, with particular emphasis given to electrons. The validation of an improved electron track reconstruction algorithm, conceived to achieve a high and uniform efficiency for electrons that undergo energy loss due to bremsstrahlung in the detector, is described here. The new multivariate electron energy calibration is also presented here, as well as the studies performed to validate its performance within the context of the $H \to ZZ^* \to 4\ell$ analysis.

Chapter 5 describes the electron identification criteria used in ATLAS, and the measurements performed to determine the efficiency of these selections. This chapter includes the documentation of a new method, developed to extract the identification efficiencies in the low-E_{T} region using isolated electrons arising from promptly produced J/ψ resonances.

The last four chapters discuss the measurement of the properties of the Higgs boson in the decay channel $H \to ZZ^* \to 4\ell$. Chapter 6 and Chapter 7 address those aspects of the analysis which are mostly common to all the measurements.

Chapter 6 outlines the analysis event selection, as well as the data and simulated samples that are used. A comparison study performed on different MC generators, aimed at reducing the uncertainty on the ZZ^* background contribution, is also discussed here.

A detailed description of the reducible background estimation, is given in Chapter 7. This includes the documentation of a newly developed fully data-driven method for the estimation of the background involving electron in the final state.

The final ATLAS Run 1 measurements of the Higgs boson mass, production and couplings in the $H \to ZZ^* \to 4\ell$ decay channel are presented in Chapter 8.

Chapter 9 presents the newly published measurement of the fiducial and differential cross sections of the Higgs boson production based on the 8 TeV data sample.

Finally, the results of this thesis are summarised in the Conclusions.

Chapter 1

The Higgs Boson: Introduction and Theoretical Background

This chapter reviews the theoretical foundations and the motivations of the work presented in this thesis. Section 1.1 presents an introduction to the SM, with particular emphasis on the role of the spontaneous symmetry breaking and the Higgs boson. The searches carried out at several high-energy experiments and culminated with the discovery of a new particle are reviewed in Section 1.2.

1.1 The Standard Model of Particle Physics

The SM describes nature in terms of a set of fundamental particles and their interactions [7–11]. It provides a unified description of three of the four observed forces: electromagnetic, weak and strong, which are the only ones relevant to the physics of elementary particles away from the Planck scale ($\sim 10^{19}$ GeV).

The conceptual framework underlying the development of the SM is based on the formalism of Quantum Field Theory (QFT), which emerged as a solution to the problem of reconciling the principles of quantum mechanics with the theory of special relativity.

In QFT particles are described by quantised field operators

$$\psi(x), A^{\mu}(x), ... \tag{1.1}$$

depending on their position in Minkowski space. Quarks and leptons, the constituents of matter, are associated with fields of half integer spin, referred to as fermions. The dynamics of the system are generated by the Lagrangian density, $\mathcal{L}(x)$, which is a local function of the fields $\psi(x)$ and of their derivatives $\partial_{\mu}\psi(x)$. If the Lagrangian density is invariant under some continuous group of local transformations of the fields, the corresponding theory is said to be a gauge theory, and the set of transformations will form the gauge group, or symmetry group, of the theory.

In order to be invariant, the Lagrangian density must include a vector field associated with each generator of the gauge group. The particles described by these fields, called gauge bosons, are the carriers of the interaction. They have spin one and vanishing masses.

The fundamental dynamical role played by symmetries is spelled out in Noether's theorem, stating that any continuous symmetry of the Lagrangian density implies the existence of a conservation law. The conserved quantities observed in nature are in fact accounted for within the SM, and determine its gauge structure. The SM Lagrangian density, $\mathcal{L}_{SM}$, is written in the form:

$$\mathcal{L}_{\mathrm{SM}} = \mathcal{L}_{\mathrm{QCD}} + \mathcal{L}_{\mathrm{EW}} \ , \tag{1.2}$$

and is invariant under the local transformations belonging to the symmetry group

$$SU(3)_C \otimes SU(2)_L \otimes U(1)_Y \ . \tag{1.3}$$

The $SU(3)_C$ symmetry accounts for colour, the conserved charge of the fundamental theory of strong interactions: Quantum Chromo-Dynamics (QCD). The $SU(2)_L \otimes U(1)_Y$ group is instead related to the electroweak sector, in which the weak hypercharge Y and weak isospin I, both linked to electric charge, are conserved.

1.1.1 Quantum electrodynamics

The development of Quantum Electro-Dynamics (QED), the extraordinarily successful theory describing electromagnetic interactions involving electrons (as well as their antiparticles, the positrons) and photons, was the first great achievement of QFT.

The electrons are electrically charged fermions of mass m, described by the Dirac field $\psi(x)$, while the photon is a massless gauge boson described by the vector field $A^\mu(x)$. As mentioned in the previous section, the presence of the gauge boson is dictated by the symmetry of the system, and makes the Lagrangian density invariant under the joint transformations of the electron and photon fields:

$$\begin{aligned} \psi(x) &\to U(x)\psi(x) = e^{i\alpha(x)}\psi(x), \\ A_\mu(x) &\to U(x)A_\mu(x) = A_\mu(x) + \frac{1}{e}\partial_\mu\alpha(x), \end{aligned} \tag{1.4}$$

where $\alpha(x)$ is an arbitrary function of the space-time coordinates. Hence, QED is a gauge theory, invariant under transformations of the abelian group[1] $U(1)$. The Lagrangian density can be written as

$$\mathcal{L}_{\mathrm{QED}} = -\frac{1}{4}F^{\mu\nu}F_{\mu\nu} + \overline{\psi}(i\gamma^\mu D_\mu - m)\psi, \tag{1.5}$$

where $F^{\mu\nu}$ is the electromagnetic tensor[2], γ^μ are Dirac matrices[3], and $\overline{\psi} = \psi^\dagger\gamma^0$. The covariant

[1] An abelian group, or commutative group, is a group in which the result of applying the group operation to two group elements does not depend on their order.

[2] The electromagnetic tensor is defined such that $F_{\mu\nu} = \partial_\mu A_\nu - \partial_\nu A_\mu$.

[3] The Dirac matrices, or gamma matrices, are defined by the anticommutation relation: $\{\gamma^\mu, \gamma^\nu\} = 2g^{\mu\nu}I_4$, where $g^{\mu\nu}$ is the metric sensor, and I_4 is the 4×4 identity matrix.

derivative D_μ is defined by:

$$D_\mu = \partial_\mu - ieA_\mu,$$

where e is the coupling constant between the electron and photon fields.

The fundamental role played by gauge symmetries is particularly evident in QED. The conserved quantity corresponding to the Noether current associated with gauge invariance of the Lagrangian Eq. (1.5) can be identified with the electric charge, e, which is long known to be conserved in nature.

The Lagrangian density Eq. (1.5) can be easily extended to describe the electromagnetic interactions of all other charged fermions described in the SM.

The theory's predictions have been confirmed with impressive precision by a large number of experimental results, such as the measurement of the electron's anomalous magnetic moment, and the Lamb shift of hydrogen energy levels.

1.1.2 Quantum chromodynamics

QCD is the fundamental theory describing the strong interactions of quarks and gluons [12–15]. As seen from Eq. (1.3), it is a gauge theory invariant under transformations of the $SU(3)$ group. As a consequence of $SU(3)$ being a non-abelian group, the eight[4] associated gauge bosons, the gluons, can have self-interactions, unlike the case of QED. Colour, the conserved charge associated to this gauge symmetry, is thus carried by both quarks and gluons, which can appear in six and eight coloured states (red, green, blue, the corresponding anticolours and their combinations), respectively. A peculiar feature of QCD is that coloured particles are bound within colour-neutral states such as mesons and baryons, and cannot be observed is isolation. This property goes under the name of *colour confinement*.

The QCD Lagrangian density can again be written in terms of the covariant derivative

$$D_\mu = \partial_\mu + ig_s T_a G^a_\mu \ ,$$

as

$$\mathcal{L}_{\text{QCD}} = -\frac{1}{4} F^a_{\mu\nu} F^{a,\mu\nu} + \bar{q}(i\gamma^\mu D_\mu - m)q \ , \tag{1.6}$$

where $g_s = \sqrt{4\pi\alpha_s}$ is the coupling constant of strong interactions, T_a are the eight generators of $SU(3)$, and G^a_μ represent the gluon fields. The field tensors $F^a_{\mu\nu}$ include the gluon self-interaction term and are defined as:

$$F^a_{\mu\nu} = \partial_\mu G^a{}_\nu - \partial_\nu G^a{}_\mu - g_s f_{aik} G^j{}_\mu G^k{}_\nu \qquad [T_a, T_b] = i f_{abc} T_c, \tag{1.7}$$

where f_{abc} are the structure constants of the $SU(3)$ group[5].

[4] $SU(3)$ is the group of 3×3 unitary matrices with determinant 1; the number of independent generators T^a, which is equal to $n^2 - 1$ for all special unitary groups $SU(n)$, is thus eight.

[5] Note that for an abelian theory $f_{abc} = 0$.

Finally, QCD exhibits *asymptotic freedom*. This property is a consequence of the strong energy dependence of the coupling constant, which becomes weaker as the energy increases. This feature plays a fundamental role for the predictive power of the theory, as it allows for the use of perturbation theory in powers of α_s (perturbative QCD), provided that the energy scale of the considered process is much higher that the masses of the participating hadrons.

1.1.3 Fermi theory of the β decay

Weak interactions were first identified by Fermi as the ones responsable for the β decay of radioactive nuclei, which he described, following a first suggestion from Pauli, as the decay of a neutron into a proton with the emission of an electron and an anti-neutrino, a particle still unknown at the time, and presumed to be massless as well as chargeless:

$$n \rightarrow p + e^{-} + \bar{\nu}_e \ . \tag{1.8}$$

Drawing an analogy with QED, Fermi pictured the interaction Lagrangian driving β-decay as the product of two currents accounting for the hadronic and the leptonic components involved in the decay:

$$\mathcal{L}_F = G_F \ (\overline{\psi}_P \gamma^\mu \psi_n) \ (\overline{\psi}_e \gamma_\mu \psi_\nu) \ . \tag{1.9}$$

In the above Lagrangian all particles are represented by Dirac fields, and G_F is the Fermi coupling constant. The theory predicted a contact interaction, with no propagators involved [16]. Following a great number of experimental observations, including the evidence for CP violation in weak interactions, Fermi theory was adapted and generalised over the years, and finally transformed in the theory usually referred to as the $V - A$ theory, whose Lagrangian can be written as:

$$\mathcal{L}_{weak} = \frac{G_F}{\sqrt{2}} \ [\overline{\psi}_P \gamma^\mu \ (1 + \frac{g_A}{g_V} \gamma_5) \ \psi_n] \ [\overline{\psi}_e \gamma_\mu \ (1 - \gamma_5) \ \psi_\nu] \ . \tag{1.10}$$

Despite the excellent agreement with experimental results, this description is however theoretically unsatisfactory, as it violates unitarity and was found to be non renormalisable. These limitations were overcome by hypothesising that, rather than being a contact interaction, the weak force is instead a short range interaction mediated by massive gauge bosons, with masses much higher than the energy scales relevant to experimental data. These gauge bosons emerge naturally in the electroweak unification.

1.1.4 Electroweak unification

The $SU(2)_L \times U(1)$ component of the SM is given by the electroweak theory, the fundamental theory formulated by Weinberg, Glashow and Salam which unifies the description of electromagnetic and weak interactions. The symmetry group is determined as the minimal

algebra containing the electromagnetic and weak currents, seen in the previous sections:

$$J_\mu^W = \overline{\psi}_e \, \gamma_\mu \, (1 - \gamma_5) \, \psi_\nu \tag{1.11}$$

$$J_\mu^{em} = \overline{\psi}_e \, \gamma^\mu \, \psi_e \, . \tag{1.12}$$

The weak hypercharge and the weak isospin corresponding to this symmetry group are linked to the electric charge by the relation

$$Q = I_3 + \frac{Y}{2} \tag{1.13}$$

where I_3 is the third component of the weak isospin. According to their chirality eigenstate, fermions are represented in the theory as left-handed and right-handed fields, defined as:

$$\psi_L = P_L \, \psi = \frac{1}{2}(1 - \gamma^5)\psi, \tag{1.14}$$

$$\psi_R = P_R \, \psi = \frac{1}{2}(1 + \gamma^5)\psi, \tag{1.15}$$

where P_L (P_R) is the left (right)-handed projection operator. The hypercharge gauge symmetry involves both chiralities, i.e. the Lagrangian density is invariant under the $U(1)$ transformations:

$$\psi_{L,R} \rightarrow e^{i\alpha(x)\frac{Y}{2}} \psi_{L,R} \, . \tag{1.16}$$

The weak isospin symmetry, on the other hand, only involves left-handed particles, which transform as doublets under $SU(2)$:

$$\psi_L \rightarrow e^{i\beta_a(x)\frac{\tau^a}{2}} \psi_L, \tag{1.17}$$

where $\frac{\tau^a}{2}$ are $SU(2)$ generators[6]. Leptons and quarks are thus classified in the SM as left-handed doublets with isospin $I = 1/2$, and right-handed singlets with $I = 0$. In the minimal model there are three families of quarks:

$$\begin{pmatrix} u \\ d \end{pmatrix}_L , \quad \begin{pmatrix} c \\ s \end{pmatrix}_L , \quad \begin{pmatrix} t \\ b \end{pmatrix}_L , \quad (u)_R \, , \quad (d)_R \, , \quad (c)_R \, , \quad (s)_R \, , \quad (t)_R \, , \quad (b)_R \, ,$$

and analogously three families of leptons:

$$\begin{pmatrix} \nu_e \\ e \end{pmatrix}_L , \quad \begin{pmatrix} \nu_\mu \\ \mu \end{pmatrix}_L , \quad \begin{pmatrix} \nu_\tau \\ \tau \end{pmatrix}_L , \quad (e)_R \, , \quad (\mu)_R \, , \quad (\tau)_R \, .$$

Right-handed neutrinos are omitted in the electroweak Lagrangian, and more generally in the SM, as they are completely neutral under $SU(2)_L \times U(1)$.

[6] τ^a are the 2×2 Pauli matrices, defined by the commutation relation: $[\tau^i, \tau^j] = \epsilon^{ijk}\tau_k$, where ϵ^{ijk} is the Levi-Civita symbol.

As a consequence of the local gauge symmetry under $SU(2) \times U(1)$ the theory predicts four gauge bosons: a triplet W_i^μ $(i = 1, 2, 3)$ for $SU(2)_L$, coupling only to left handed particles, and a singlet B^μ for $U(1)_Y$. Assuming only one fermionic field for simplicity, the electroweak Lagrangian can be expressed as:

$$\mathcal{L}_{EW} = -\frac{1}{4} W^i_{\mu\nu} W_i^{\mu\nu} - \frac{1}{4} B_{\mu\nu} B^{\mu\nu} + i\bar{\psi}\gamma_\mu D_\mu \psi, \tag{1.18}$$

with

$$W_i^{\mu\nu} = \partial^\nu W_i^\mu - \partial^\mu W_i^\nu - g\epsilon_{ijk} W_j^\mu W_k^\nu, \tag{1.19}$$

$$B^{\mu\nu} = \partial^\nu B^\mu - \partial^\mu B^\nu, \tag{1.20}$$

and

$$D_\mu = \partial_\mu + igW_\mu^i I_i + i\frac{g'}{2} B_\mu Y, \tag{1.21}$$

where g and g' are the $SU(2)$ and $U(1)$ coupling constants, respectively. The physical fields, which unlike the case of QED and QCD do not correspond directly to the gauge bosons appearing in the Lagrangian, are instead obtained from their linear combinations

$$\begin{aligned} A^\mu &= \sin\theta_W W_3^\mu + \cos\theta_W B^\mu, \\ Z^\mu &= \cos\theta_W W_3^\mu - \sin\theta_W B^\mu, \\ W_\pm^\mu &= \frac{W_1^\mu \mp i W_2^\mu}{\sqrt{2}}, \end{aligned} \tag{1.22}$$

where θ_W is the weak mixing angle, related to the coupling constants via the relations:

$$\sin\theta_W = \frac{g'}{\sqrt{g^2 + g'^2}}. \tag{1.23}$$

A part from the photon A^μ, and the $W_\pm^\mu$ bosons of the β decay, the theory thus requires the existence of another neutral gauge boson, called Z^0.

In should be noted that the Lagrangian in Eq. (1.18) does not contain any mass term, as this would violate explicitly its gauge invariance. The theory at this stage thus predicts massless fermions and massless gauge bosons, in clear contradiction with experimental observations. The masses of the fermions had in fact already been measured and found to be non-zero, while the very fact that the $W^\pm$ and Z^0 bosons had not yet been discovered at the time the theory was developed, as well as the experimental validity of Fermi theory, indicated that they had to be very heavy.

1.1.5 How particles acquire mass: spontaneous symmetry breaking and the Higgs–Brout–Englert mechanism

The derivation of a unified and renormalisable theory of electromagnetic and weak interactions is based on the notion of spontaneously broken symmetry and the Higgs-Brout-Englert mechanism [17–19]. Within this conceptual framework, it has been possible to solve the problem of the vanishing masses of both charged leptons and gauge bosons, dictated by the requirement of invariance under transformations of the gauge group $SU(2)_L \times U(1)_Y$. The key new element of the theory is the scalar field ϕ, which drives the spontaneous breaking of the $SU(2)_L \times U(1)_Y$ symmetry, preserving at the same time the $U(1)$ gauge symmetry of electromagnetic interactions, whose gauge boson, the photon, is indeed massless:

$$SU(2)_L \times U(1)_Y \rightarrow U(1)_{em} \ . \tag{1.24}$$

The complex scalar field consists of a isospin doublet with hypercharge $Y = 1$:

$$\phi = \begin{pmatrix} \phi^+ \\ \phi^0 \end{pmatrix} \tag{1.25}$$

and its contribution to the Lagrangian of Eq. (1.18) is:

$$\mathcal{L}_\phi = (D_\mu \phi)^\dagger (D^\mu \phi) - V(\phi) \ , \tag{1.26}$$

where the covariant derivative is defined as

$$D_\mu \phi = \left(\partial_\mu + igW_\mu^i \cdot \frac{\tau^i}{2} + ig' \frac{1}{2} B_\mu \right) \phi \ , \tag{1.27}$$

and

$$V(\phi) = \mu^2 \phi^\dagger \phi + \lambda (\phi^\dagger \phi)^2 \ . \tag{1.28}$$

For the potential V to have a finite lower bound, i.e. for the theory to be stable, it has to be $\lambda > 0$. The value of μ, on the other hand, can have both positive or negative values, and depending on its sign the ground state will be unique ($\mu^2 > 0$, with minimum value at $\phi = 0$), or degenerate ($\mu^2 < 0$), as can be seen from Figure 1.1. Focusing on the latter case, $\mu^2 < 0$, we can now introduce the symmetry breaking choosing a particular direction in the $Re(\phi) - Im(\phi)$ plane, corresponding to the vacuum expectation value of the scalar field

$$\phi_0 = \langle 0 | \ \phi \ | 0 \rangle = \begin{pmatrix} 0 \\ v \end{pmatrix} \ ,$$
$$v = \sqrt{\frac{-\mu^2}{2\lambda}}. \tag{1.29}$$

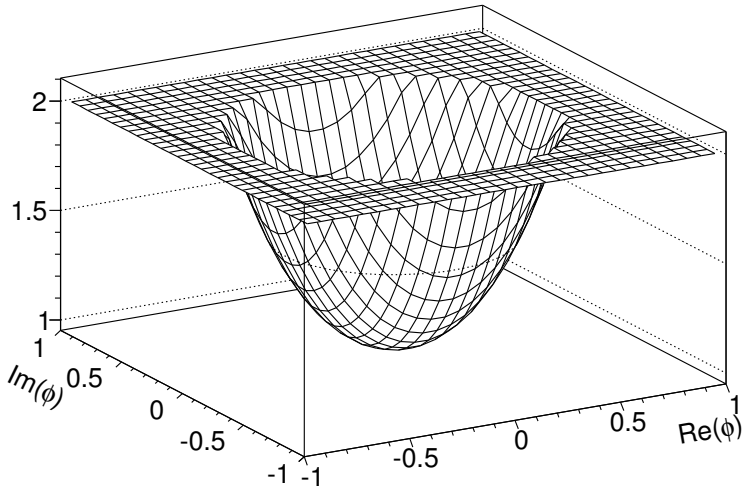

(a)

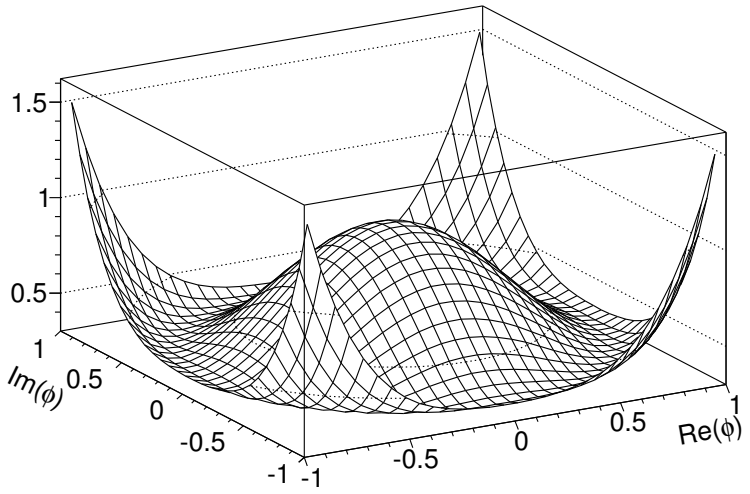

(b)

Figure 1.1 $V(\phi)$ potential defined in Eq. (1.28) for (a) $\mu^2 > 0$, and (b) $\mu^2 < 0$.

In order to correctly identify the physical particles predicted by the theory, we need to express the scalar field in the so called *unitary gauge*:

$$\phi(x) = \begin{pmatrix} 0 \\ v + \frac{h(x)}{\sqrt{2}} \end{pmatrix} . \tag{1.30}$$

In the scalar doublet there is thus only one physical state corresponding to a new neutral scalar particle, called the *Higgs boson*. The remaining three degrees of freedom are "absorbed" by the $SU(2)$ bosons, allowing them to acquire a mass. This can be seen by replacing the field in

Eq. (1.30) in the kinetic part of the Lagrangian density:

$$\mathcal{L} \;=\; \frac{1}{2}\,\partial_\mu h(x)\;\partial^\mu h(x) \;+\; \frac{g^2}{4}v^2 W_\mu^i W_i^\mu \;+\; \frac{g'^2}{4}v^2 B_\mu B^\mu \;-\; \frac{gg'}{2}v^2 W_\mu^3 B^\mu \;. \tag{1.31}$$

The mass terms of the physical fields can be identified using the relations in Eq (1.22), and are found to be:

$$m_W = \frac{v}{2}\,g \;, \tag{1.32}$$

$$\tag{1.33}$$

$$m_Z = \frac{v}{2}\,\sqrt{g^2+g'^2} \;. \tag{1.34}$$

The vacuum expectation v can be related directly to the Fermi constant, which is precisely estimated from muon lifetime measurements, and its value can be thus predicted:

$$v^{-2} = \frac{g^2}{2m_W^2} = 2\sqrt{2}G_F \qquad\qquad v \simeq 247 \text{ GeV} \;. \tag{1.35}$$

The masses of the fermions are instead generated by Yukawa terms describing the interaction between the Higgs field and fermion fields. Considering for simplicity only the first leptonic family, one can write:

$$\mathcal{L}_{e\phi} \;=\; g_e\,\left(\,\bar{\ell}_L\phi e_R \;+\; \bar{e}_R\phi^\dagger\ell_L\,\right) \;. \tag{1.36}$$

After spontaneous symmetry breaking and in the unitary gauge, the term $\bar{\ell}_L\phi$ becomes:

$$\bar{\ell}_L\phi \;=\; \bar{\nu}_L\phi^+ + \bar{e}_L\phi^0 = \bar{e}_L\left(v+\frac{h}{\sqrt{2}}\right) \;, \tag{1.37}$$

from which one has:

$$\mathcal{L}_{e\phi} \;=\; g_e\,v\,\bar{e}e \;+\; g_e\,\frac{h}{\sqrt{2}}\,\bar{e}e \;. \tag{1.38}$$

The first term of the Lagrangian can be identified as the electron's mass, which is thus equal to:

$$m_e = g_e\,v \;. \tag{1.39}$$

The second term describes the interaction between the Higgs boson and the electron, or more generally the fermions, which is found to be proportional to the fermion's mass. Using Eq (1.35), the coupling constants can be written as:

$$g_f = \left(2\sqrt{2}G_F\right)^{1/2} m_f \;. \tag{1.40}$$

and are thus completely determined. This coupling structure provides a distinctive signature for the identification of the Higgs boson. The mass of the Higgs boson, which is equal to $m_H = -\mu^2 = 4\lambda v^2$, remains on the other hand a free parameter of the theory.

1.1.6 Theoretical constraints on the Higgs boson mass

Although the Higgs boson mass is a free parameter of the SM, there exist some theoretical arguments which allow to set limits on its value [20–23]. It must be noted that these constraints are typically not very rigorous, as they can often be evaded by postulating the existence of new physics which enters the theory at an energy scale above that of current experiments.

A first bound can be set on the grounds of *triviality*. The general argument goes as follows: due to the self-interactions of the Higgs scalar fiels, the quartic coupling λ changes with the effective energy scale Q. The running value of λ can be written as:

$$\lambda(Q) \;=\; \frac{\lambda(\eta)}{1 - \frac{3}{4\pi^2}\log\frac{Q^2}{\eta^2}\lambda(\eta)} \;, \tag{1.41}$$

from which one can see how $\lambda(Q)$ increases with the scale, eventually becoming infinite for some value of Q (Landau Pole). To avoid this, $\lambda(\eta)$ has to be set to zero, which essentially removes the interaction term of the Lagrangian, leading to a *trivial* theory. To obtain an upper bound on the Higgs mass we require instead that the quartic coupling be finite up to a certain energy scale Λ_c, above which either the theory becomes non-perturbative, or new physics enters the picture. The bound thus depends on the value of the considered Λ_c.

A bound on the Higgs mass can also be derived by the requirement that spontaneous symmetry breaking actually occurs, that is for $V(\eta) < V(0)$. This condition is equivalent to the requirement that λ remain positive at all scales, and if not fulfilled it would lead to the potential being unbounded from below and having no state of minimum energy. The vacuum stability condition results in a lower bound on the Higgs mass (*stability bound*), which is again dependent on the cut-off Λ_c.

The upper and lower theoretical bounds described above are shown as a function of the new physics energy scale Λ_c in Figure 1.2.

Finally, another limit on the Higgs mass can be set in order to recover unitarity in the high energy scattering of longitudinal W and Z bosons (*unitarity bound*). The amplitude of these processes exhibit indeed a quadratic dependence on energy, which is cancelled by the introduction of diagrams involving the Higgs boson, provided its mass satisfies the condition

$$m_H < \sqrt{\frac{8\pi\sqrt{2}}{3G_F}} \simeq 1 \text{ TeV} \;, \tag{1.42}$$

or that new physics come in at a similar energy scale.

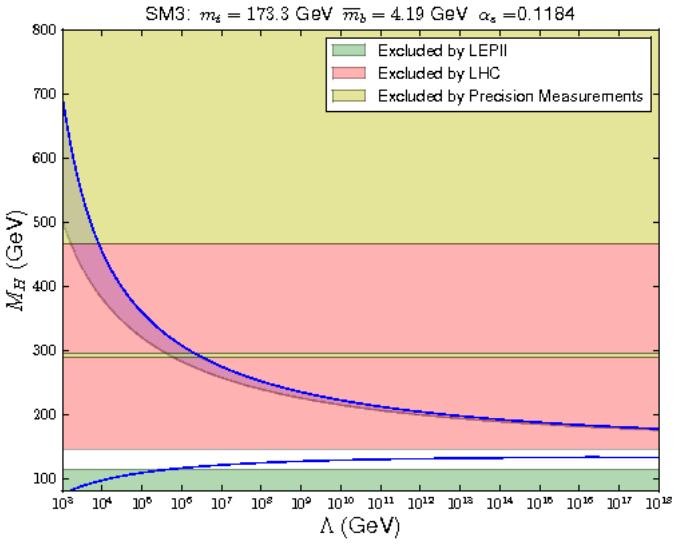

Figure 1.2 The stability and triviality bounds for the Standard Model Higgs boson mass, as a function of the cut-off scale Λ_c. The horizontal bars indicate the Higgs exclusion limits from LEP, LHC, and electroweak precision measurements [24].

1.2 Looking for the Higgs Boson

The inability to predict the value of the Higgs mass, and its very low production rates, have made the search for the Higgs boson an extremely difficult task. Over the past 20 years the Large Electron-Positron (LEP) collider at CERN and the Tevatron at Fermilab have focused on the search for this elusive particle and the LHC was built mainly to finally confirm or exclude its existence.

In the remainder of this chapter we will give a brief description of the most relevant Higgs production mechanism and decay channels at the LHC in Sections 1.2.1 and 1.2.2, respectively. A review of the most important experimental results obtained in the searches for the Higgs boson, finally leading to the discovery of a new particle, are presented in Section 1.2.3. The prospects of the measurements that followed the Higgs discovery, aimed at determining the precise nature of this new particle, are outlined in Section 1.2.4.

1.2.1 Production mechanism

Several mechanisms contribute to the production of SM Higgs bosons in proton-proton collisions. The cross sections of the most relevant production mechanisms at the LHC are shown in Figure 1.3(a) as a function of the Higgs boson mass (at $\sqrt{s} = 8$ TeV), and in Figure 1.3(b) as a function of the center-of-mass energy, assuming $m_H = 125$ GeV. The representative diagrams of these processes are depicted in Figure 1.4.

The production mechanism with the largest cross section is the gluon-fusion (ggF) process, mediated by the exchange of a virtual heavy top quark. As seen in Section 1.1.5, the Higgs coupling to fermions is proportional to their masses, and contributions from lighter quarks propagating in the loop are thus suppressed by m_q^2. The lowest order Feynman diagram of

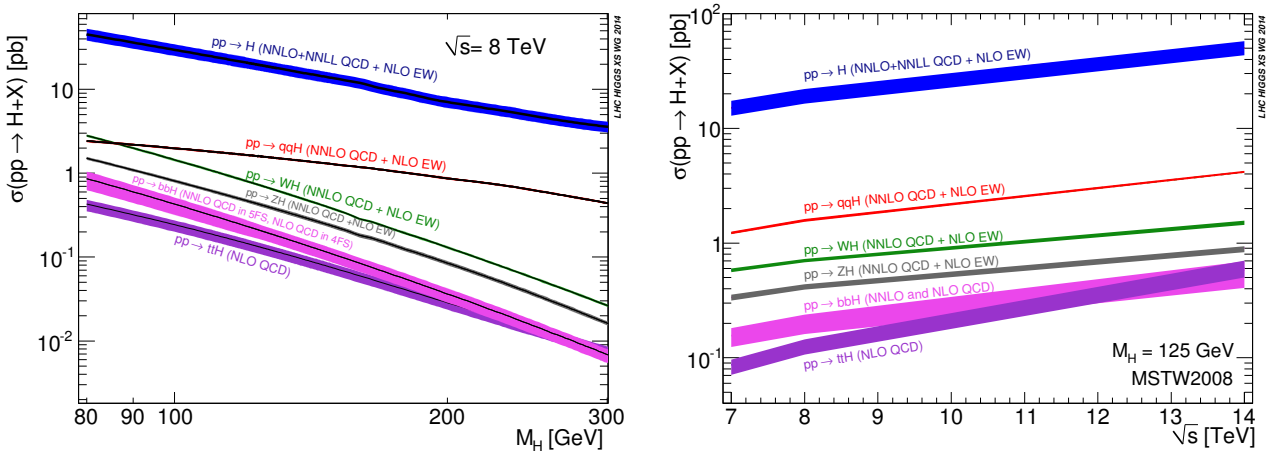

(a) **(b)**

Figure 1.3 Cross sections of the most relevant Higgs production mechanisms at the LHC as a function of (a) the Higgs mass m_H at $\sqrt{s} = 8$ TeV, and (b) the center-of-mass energy, assuming $m_H = 125$ GeV [6]

the gluon fusion mechanism can be seen in Figure 1.4(a). This process provides the largest production rate for the entire Higgs mass range of interest.

The production mode with the second-largest cross section at the LHC is the vector boson fusion (VBF) shown in Fig 1.4(c), which proceeds through the scattering of two (anti-)quarks, mediated by t- or u-channel exchange of a W or Z boson, with the Higgs boson radiated off the weak-boson propagator. The scattered quarks give rise to two hard jets in the forward and backward regions of the detector, which provide a useful handle to identify VBF events, as will be seen in Chapter 6. This mechanism only becomes competitive for very high values of the Higgs mass, while its cross section is about one order of magnitude smaller than that of ggF processes for $m_H < 500$ GeV (see Figure 1.3).

Higgs boson particles can also be produced in association with a vector boson (WH/ZH), and this process constitutes the next most relevant production mechanism after ggF and VBF. In this case, as shown from the diagram in 1.4(b), the Higgs is radiated from an intermediate gauge boson, a Z or a W, and the process is also referred to *Higgsstrahlung*. Thanks to the possibility of reconstructing the decay particles produced by the vector bosons, this mechanism provides a very clean signature.

Finally, one can consider the Higgs radiation off top or bottom quarks, called $t\bar{t}H$ and $b\bar{b}H$ production, respectively. The cross section of such processes, shown in Figure 1.4(d), is however essentially negligible compared to the other production mechanisms described above.

Table 1.1 summarises the Higgs boson production cross sections for the considered mechanism, as well as the total cross section values, for a Higgs mass of 125 GeV. Numbers are presented as a function of the center of mass energy for $\sqrt{s} = 7$, 8 and 14 TeV, which correspond to the values used in the 2011 and 2012 data-taking campaigns, and the LHC design value (see Chapter 2), respectively. The uncertainties associated to the cross sections are also shown.

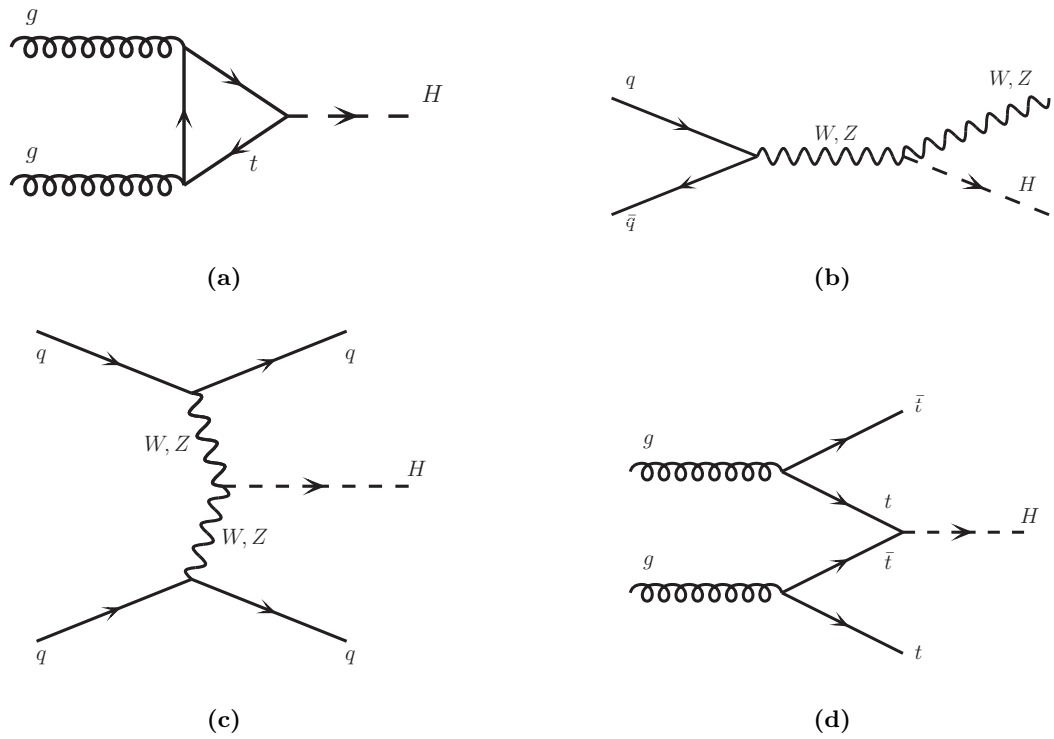

Figure 1.4 Lowest order Feynman diagrams for different production mechanisms of the Higgs boson: (a) gluon-gluon fusion, (b) associated production with a $W^{\pm}$ or Z, (c) vector boson fusion and (d) $t\bar{t}H$associated production (analogous to that of $b\bar{b}H$).

Table 1.1 The SM Higgs boson production cross sections at $m_H = 125$ GeV in pp collisions, for different values of the center of mass energy [6].

$\sqrt{s}$ (TeV)	Production cross section (pb) for $m_H = 125$ GeV						
	ggF	VBF	WH	ZH	$t\bar{t}H$	$b\bar{b}H$	total
7	15.13	1.22	0.58	0.34	0.09	0.16	17.52
8	19.27	1.58	0.71	0.42	0.13	0.20	22.31
13	43.92	3.75	1.38	0.87	0.51	0.52	50.95

1.2.2 Decay channels

The relevance of the various decay modes contributing to the Higgs total decay width in pp collisions greatly depends on the value of the Higgs boson mass, as well as on the experimental challenges they present. The branching ratios of the different decay modes are shown in Figures 1.5(a) and 1.5(b) for $\sqrt{s} = 8$ TeV as a function of m_H, in the mass ranges 80–200 GeV and 80 GeV–1 TeV, respectively. Three different mass regions can be identified, for which the sensitivity of the various channels differs.

In the low mass region, for $m_H < 130$ GeV, the five decay channels that can play a role at the LHC are listed in Table 1.2, which displays their branching ratios and mass resolutions assuming $m_H = 125$ GeV.

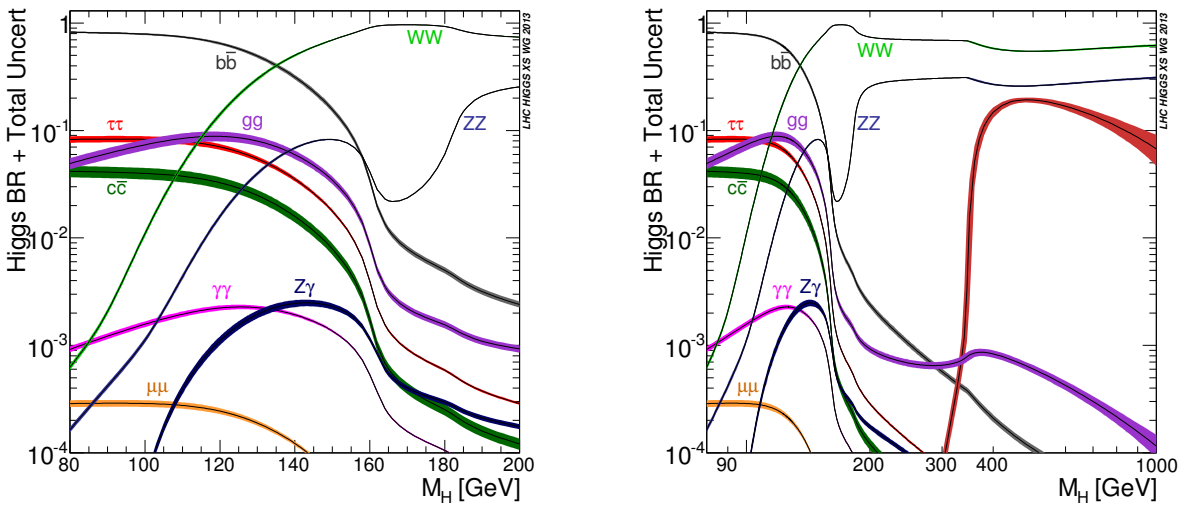

(a) **(b)**

Figure 1.5 Standard Model Higgs boson decay branching ratios as a function of m_H in the mass ranges 80–200 GeV (a) and 80 GeV–1 TeV (b) [6]

The dominant decay channel is represented by $H \to b\bar{b}$ which is however extremely difficult to study due to the very large background contamination and poor mass resolution. The situation is similar for the $H \to \tau^+\tau^-$ channel.

A definitely more promising channel to look at is the $H \to \gamma\gamma$, which has a much lower rate, but a higher signal-to-background (S/B) ratio of approximately 10^{-2}. It has a distinctive signature with two very energetic isolated photons forming a narrow invariant mass peak.

Another important channel at low masses is the $H \to ZZ$, in which one of the two Z bosons is taken to be on-shell, and both Z decay into pairs of leptons (electrons or muons). This channel has an extremely low rate, as can be seen from Figure 1.6, which shows the production cross section times decay branching ratio (BR) for the various Higgs decay final states. However, the $H \to ZZ^* \to 4\ell$ channel offers a clean signature and the highest S/B, which is $\mathcal{O}(1)$. Moreover, as for the $H \to \gamma\gamma$, all final state particles can be very precisely measured and the reconstructed m_H resolution is excellent.

Finally, the last relevant decay channel at such low masses is the $H \to WW$, in which the intermediate bosons decay leptonically. The experimental signature in the $H \to WW^* \to \ell\nu\ell\nu$ searches consists of two energetic charged leptons and high missing transverse momentum. The presence of neutrinos in the final state makes it impossible to reconstruct the final state, and leads to a poor resolution on the Higgs mass. All production modes can be explored via the $H \to \gamma\gamma$, the $H \to ZZ^* \to 4\ell$ and the $H \to WW^* \to \ell\nu\ell\nu$ decay channels, whereas a search via the gluon fusion process is precluded for the fermionic decay channels, due to the overwhelming multijet background. These channels are therefore typically studied in associated VH and VBF production modes.

In the intermediate mass range, for $130 < m_H < 180$ GeV, the Higgs bosons decay primarily into pairs of vector bosons, $H \to WW$ and $H \to ZZ$, in which one of the gauge bosons remains virtual until the kinematic threshold at $2m_V$ is reached.

In the range $2m_W < m_H < 2m_Z$, where the W bosons are both real while the Z is still off-

shell, the WW BR is almost 100%. The most promising final states are once again the $H \to WW^* \to \ell\nu\ell\nu$ and the $H \to ZZ^* \to 4\ell$, with the latter providing the highest S/B and better mass resolution.

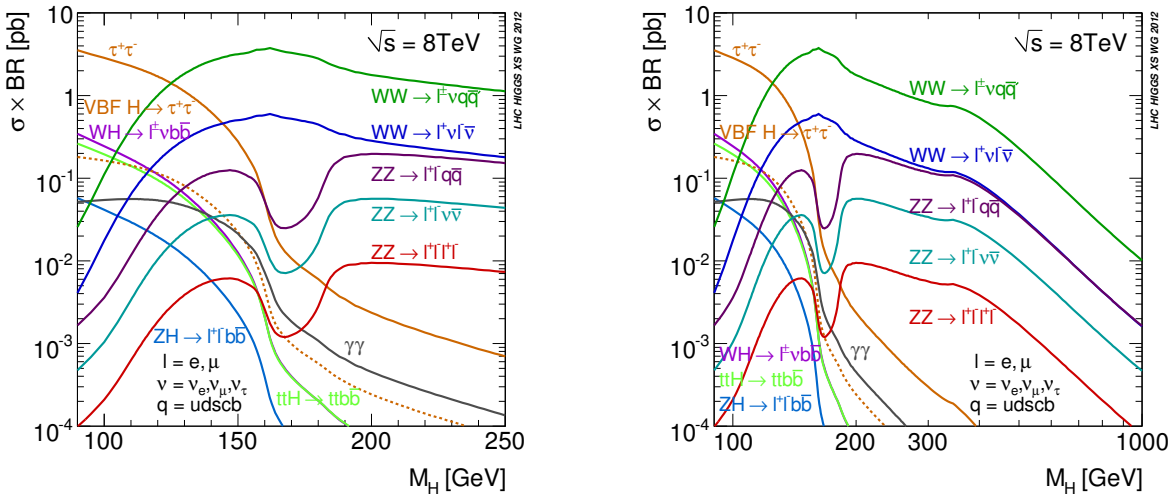

Figure 1.6 Standard Model Higgs boson production cross section times branching ratio at $\sqrt{s} = 8$ TeV as a function of the m_H in the mass ranges 90–250 GeV (a) and 90 GeV–1 TeV (b) [6].

Finally, in the high mass region, for 180 GeV $< m_H <$ 1 TeV, the most sensitive channel for the identification of the Higgs boson is the $H \to ZZ$, with subsequent decay into two quarks and two leptons $H \to ZZ \to \ell\ell qq$, into two neutrinos and two leptons $H \to ZZ \to \ell\ell\nu\nu$, or into four leptons.

Table 1.2 The branching ratio, mass resolution and signal-to-background ratio of the five most sensitive channels in low mass SM Higgs boson searches at the LHC. A mass of 125 GeV is assumed [6].

Decay channel	Branching ratio	Mass resolution
$H \to \gamma\gamma$	2.28×10^{-3}	$1-2\%$
$H \to ZZ^* \to 4\ell$	1.25×10^{-4}	$1-2\%$
$H \to WW^* \to \ell\nu\ell\nu$	1.06×10^{-2}	20%
$H \to \tau^+\tau^-$	6.32×10^{-2}	10%
$H \to b\bar{b}$	5.77×10^{-1}	15%

The total decay width of the Higgs boson, Γ_H, is shown in Figure 1.7 as a function of the Higgs boson mass. For low values of m_H the width is very narrow, with $\Gamma_H <$ 10 MeV up to approximately $m_H = 130$ GeV. It then increases rapidly once the WW kinematic threshold at $2m_W$ is reached, and goes up to ∼1 GeV at the opening of the ZZ on-shell decay. For larger

masses Γ_H continues to increase becoming comparable with the Higgs mass, until – for masses of approximately 1 TeV – the Higgs boson becomes a very broad resonance.

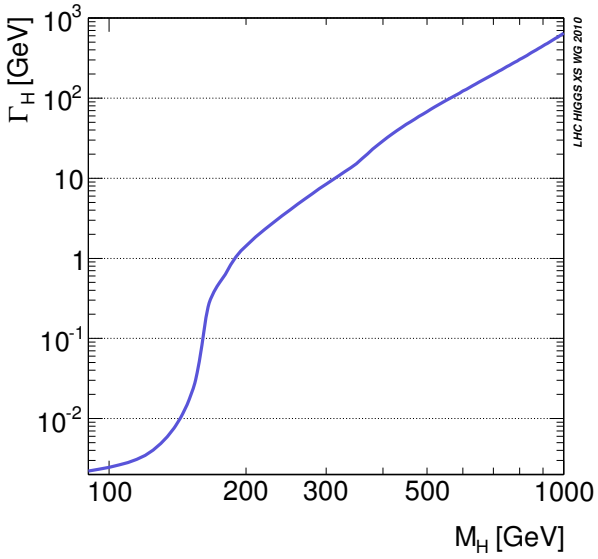

Figure 1.7 Total decay width of the Higgs boson as a function of m_H [6].

1.2.3 Discovery of a new particle

Direct searches for the Higgs boson were conducted by the ALEPH, DELPHI, L3, and OPAL experiments at the LEP e^+e^- collider. The combination of LEP data, corresponding to approximately 2.5 fb^{-1}collected at center-of-mass energies up to 209 GeV, yielded a limit on the Higgs mass. The search relied mainly on the Higgsstrahlung production mechanism ($e^+e^- \to Z^* \to ZH$), and on the decay of the Higgs into a pair of b quarks. The existence of a SM Higgs boson with mass $m_H < 114.4$ GeV was excluded at 95% CL, as shown in Figure 1.8 [25].

Precision measurements in the electroweak sector were also used to set indirect experimental bounds on the Higgs mass, by accounting for Higgs mass contributions to radiative corrections. A global fit of precision electroweak measurements from LEP, SLC (SLAC Large Collider), and the Tevatron, visible in Figure 1.9, suggests $m_H = 91^{+30}_{-23}$ [26].

Following the shutdown of the LEP collider in 2000, the direct search for the Higgs boson continued with the CDF and DØ experiments at the Tevatron $p\bar{p}$ collider. The combined results from approximately 10 fb^{-1} collected at $\sqrt{s} = 1.96$ TeV allowed to exclude two mass ranges: between 90 GeV and 109 GeV, and between 149 GeV and 182 GeV [27]. The most important production mechanisms were in this case the associate production with W or Z bosons and the gluon fusion, while the most sensitive decay channel was $H \to b\bar{b}$.

The start of operations at the LHC pp collider in 2010 opened up a new search landscape for the Higgs boson, with higher center-of mass energies, $\sqrt{s} = 7, 8$ TeV, and higher luminosities. Finally, in July 2012 the ATLAS and CMS collaborations announced the observation of a new particle with a mass of about 125 GeV within the searches for the SM Higgs boson [28,29]. The analysed data corresponded to integrated luminosities of up to 4.8 (5.1) fb^{-1} at $\sqrt{s} = 7$ TeV

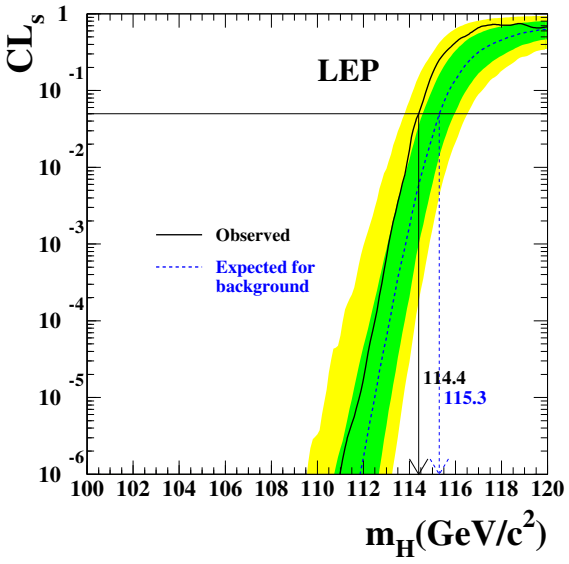

Figure 1.8 The ratio $CL_s = CL_{s+b}/CL_b$ for the signal plus background hypothesis, as a function of the test mass m_H. Solid line: observation; dashed line: median background expectation. The dark and light shaded bands around the median expectation for the background hypothesis correspond to the 68% and 95% probability bands. The intersection of the horizontal line for $CL_s = 0.05$ with the observed curve is used to define the 95% confidence level lower bound on the mass of the Standard Model Higgs boson [25].

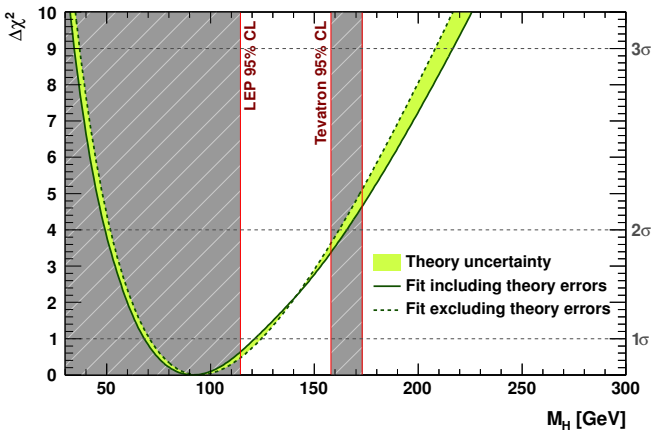

Figure 1.9 $\Delta\chi^2$ of the fit of electroweak data as a function of m_H. The solid (dashed) line gives the results when including (ignoring) theoretical errors. The grey bands represent the 95% CL exclusion range from direct searches at Tevatron and LEP; these results are not included in the fit [26].

and 5.9 (5.3) at $\sqrt{s} = 8$ TeV recorded by the ATLAS and CMS experiments, respectively. Figures 1.10(a) and 1.10(b) show the results from both experiments at the time of the discovery, in terms of local p_0-value, which quantifies the consistency of the observed data with the background-only hypothesis. ATLAS observed the largest excess of events with a significance of 5.9 standard deviations at a mass $m_H = 126.5$ GeV, exceeding the expected value of 4.6σ if a SM Higgs boson were present at such a mass. The excess of events was first observed in the $H \to ZZ^* \to 4\ell$ and the $H \to \gamma\gamma$ channels, and confirmed by the $H \to WW \to \ell\nu\ell\nu$ channel.

Furthermore, the result was confirmed by the CDF and DØ experiments, in which a broad excess was seen in the mass range $115 < m_H < 140$ GeV with a significance of 3 standard deviations at $m_H = 125$ GeV, as seen in Figure 1.11 [27].

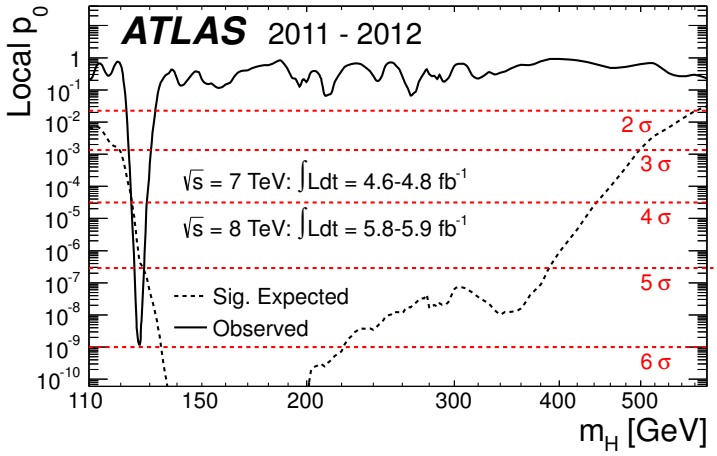

(a)

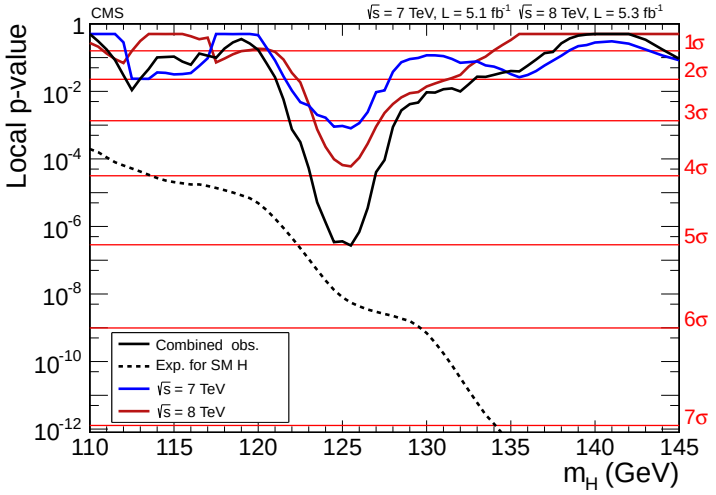

(b)

Figure 1.10 (a) The observed (solid) local p_0 as a function of m_H and the expectation (dashed) for a SM Higgs boson signal hypothesis at the given mass. Results are obtained using ATLAS data [28]. (b) The observed local p_0 for 7 TeV and 8 TeV data, and their combination as a function of the SM Higgs boson mass. The dashed line shows the expected local p_0 for a SM Higgs boson with a mass m_H. Results are obtained using CMS data [29].

1.2.4 What next?

Since July 2012, having analysed two and a half times more data than was available for the discovery announcement, both experiments have engaged in precise measurements of the new particle's properties in order to investigate its nature. As discussed in Section 1.1.5, all the Higgs couplings are fixed unambiguously once its mass is known. The measurement of the new boson

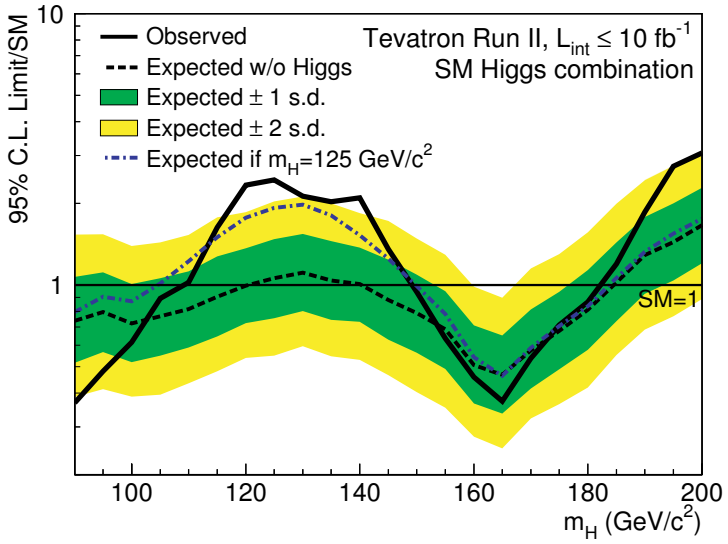

Figure 1.11 Ratios of the 95% C.L. expected and observed limit to the SM cross section as a function of Higgs boson mass for the combined CDF and DØ searches. The dark- and light shaded bands indicate, respectively, the one and two s.d. probability regions in which the limits are expected to fluctuate in the absence of signal. The blue short-dashed line shows median expected limits assuming the SM Higgs boson is present at $m_H = 125$ GeV [27].

mass is thus fundamentally important, and has been carried out in all sensitive decay channels, with the $H \to ZZ^* \to 4\ell$ and the $H \to \gamma\gamma$ providing the most precise results [2,3,30]. The couplings of the new boson have been tested by studying the production rates with events categorised according to the characteristics of the different production modes. No significant deviations from the expected couplings of the SM Higgs boson have been observed up to now [4, 30]. The compatibility with the Standard Model predictions was also confirmed by the measurements of the particle's spin-CP properties [31, 32]. Finally, to further characterise the production and decay properties of the new boson, first measurements of fiducial and differential cross sections have been carried out by the ATLAS collaboration in the $H \to ZZ^* \to 4\ell$ [5] and the $H \to \gamma\gamma$ [33] channels, and show no significant discrepancy with respect to the theoretical SM predictions.

The experimental observations have made by now evident that the new particle is indeed the Higgs boson predicted by the BEH mechanism. It remains an open question, however, whether this is the Higgs boson of the Standard Model of particle physics, or possibly the lightest of several bosons predicted in some theories that go beyond the Standard Model. Searches for additional Higgs states are hence particularly important, and are part of the ATLAS physics program.

Chapter 2

The Large Hadron Collider

The LHC, located at the European Organization for Nuclear Research (CERN), is currently the world's largest and most powerful particle accelerator. Four major experiments are hosted at the LHC: ATLAS [34] and CMS [35], the so called general purpose detectors, ALICE [36] and LHCb [37], targeting the study of quark-gluon plasma and the slight differences between matter and antimatter, respectively. These experiments are designed to exploit the full physics potential of the LHC with an extremely wide and diverse program of measurements and searches. After the stringent tests of the Standard Model of particle physics provided at CERN by the LHC predecessor, the LEP accelerator, the construction of the LHC was mainly motivated by the searches for the last missing piece of the SM, the elusive Higgs particle, and for new physics signals beyond it.

The LHC is a two-ring superconducting hadron accelerator and collider, designed to provide proton-proton collisions. It is installed in the pre-existing 26.7 km tunnel that was constructed for the LEP machine [38], and it is the latest addition to CERN's accelerator complex, as shown in Figure 2.1. Each accelerating structure boosts the energy of the particles along the way, to finally achieve the designed center-of-mass energy of 14 TeV (approximately 7 times higher than the energy achieved at the Tevatron). In addition the LHC can be operated with lead ions at 2.76 TeV per nucleon.

The remarkable potential of the LHC lies not only in the high collision energy, but also in the instantaneous luminosity, that was designed to be as high as $10^{34}\mathrm{cm}^{-2}\mathrm{s}^{-1}$ [40]. The number of events generated for a specific process can be written as $N = L \cdot \sigma$, where σ represents the cross section of the process taken into account, and $L = \int \mathcal{L} dt$ is the luminosity, integrated over time, provided by the machine. The intent of the LHC is to explore physics which has not been seen so far, thus the cross sections of the processes of interest will be very small and the luminosity must be the highest possible.
The instantaneous luminosity at the interaction points along the LHC is determined by the beam parameters and can be written as follows:

$$\mathcal{L} = \frac{N_b^2 n_b f_{\mathrm{rev}} \gamma_r}{4\pi \varepsilon_{\mathrm{n}} \beta^*} \cdot F \tag{2.1}$$

where N_b is the number of particles per bunch, n_b the number of bunches per beam, f_{rev}

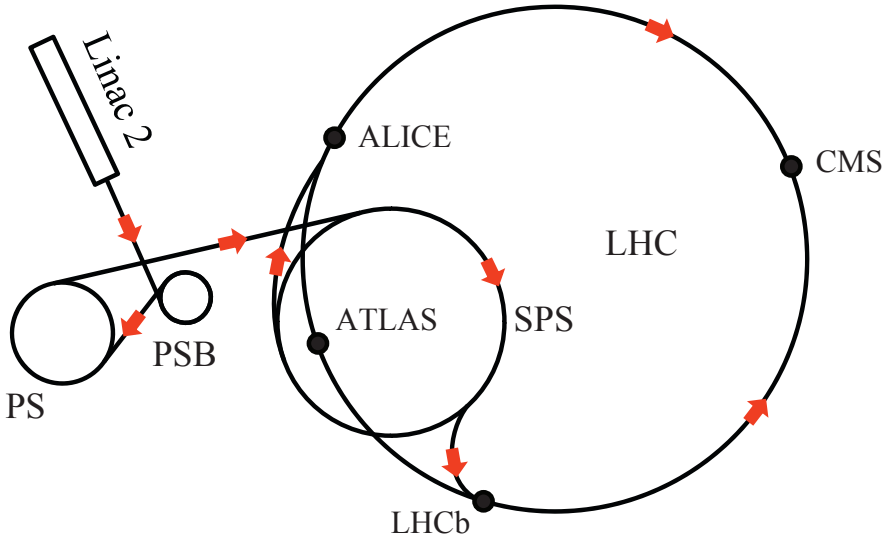

Figure 2.1 Schematic view of the CERN accelerator complex. The protons bunches are passed through the Linac2, the Proton Synchrotron Booster (PSB), the Proton Synchrotron (PS), and the Super Proton Synchrotron (SPS) facilities before being injected into the main LHC ring. The beams are progressively accelerated and eventually brought to collision at the LHC experiments. Figure not to scale. Adapted from reference [39].

the revolution frequency, γ_r the relativistic gamma factor, ε_{n} the normalised transverse beam emittance, and β^* the beta function at the collision point. F is the so-called geometric luminosity reduction factor, which arises from the non-zero crossing angle of the beams at the interaction point. All these parameters have been optimised to ensure maximal luminosity. The decision of colliding protons itself, instead of protons and anti-protons as done at the Tevatron, was driven by the need of reaching such high luminosities [41].

Parameter	2010	2011	2012	Nominal
Center-of-mass energy [TeV]	7	7	8	14
N_b $[10^{11}]$	1.2	1.5	1.6	1.7
n_b^{max}	348	1380	1380	2808
ε_n $[\mu\mathrm{m}]$	2.4-4	1.9-2.4	2.2-2.5	3.75
β^* $[m]$	3.5	$1.5 \rightarrow 1$	0.6	0.55
Crossing angle $[\mu\mathrm{rad}]$	200	240	290	285
Bunch spacing [ns]	150	$75 \rightarrow 50$	50	25
μ	4	19	35	23
$\mathcal{L}_{\mathrm{max}}^{\mathrm{inst}}$ $[10^{34}\,\mathrm{cm}^{-2}\,\mathrm{s}^{-1}]$	0.02	0.4	0.76	1

Table 2.1 Nominal configuration values together with the actual values during the 2010, 2011, and 2012 data taking periods for a numbers of relevant LHC beam parameters.

Table 2.1 shows, for a number of important beam parameters, the nominal configuration values together with the actual values reached during the 2010, 2011, and 2012 data taking periods. All parameters gradually improved during the first Run of the LHC, and some of them even exceed their design specifications. We are currently in the long shutdown phase, and the next round of data taking is scheduled to start in June 2015, at a center-of-mass energy of 13 TeV.

It is important to note the different center-of-mass energy values used in 2011 and 2012, which correspond to 7 TeV and 8 TeV, respectively. Since many theoretical and experimental parameters depend on the center-of-mass energy, the two datasets are treated separately in our analyses, and combined at a later stage.

The peak instantaneous luminosity ($\mathcal{L}_{\text{max}}$) delivered to ATLAS per day versus time in 2010, 2011 and 2012 is shown in Figure 2.2(a). On the other hand, Figure 2.3 shows the cumulative luminosity versus time delivered to and recorded by ATLAS, as well as the amount of data certified to be of good quality, both for 7 TeV and 8 TeV centre-of-mass energy. The total recorded luminosity amounts to 5.08 fb^{-1} and 21.3 fb^{-1} for 2011 and 2012 respectively. The exact integrated luminosities used in the analyses are in general smaller due to detector inefficiencies, which depend on the objects we consider in our final state.

The incredibly high luminosity delivered by the LHC in 2012 is reflected by two additional important parameters, also shown in Table 2.1: the time intervals between neighbouring bunches, Δt, and the number of interactions per bunch crossing at peak luminosity, μ. The first quantity affects the so-called out-of-time pile-up which describes the overlap of interactions from two consecutive bunch crossings in a particle detector due to its finite readout timing resolution. The latter quantity, also shown as a function of time in Figure 2.2(b), specifies instead the amount of in-time pile-up interactions, i.e. the number of pp interactions per bunch-crossing, which is proportional to the instantaneous luminosity and reduces the experimental resolution. The distribution of the mean number of interactions per bunch crossing, $< \mu >$, is shown in Figure 2.4 weighted with the luminosities achieved during 2011 and 2012 data taking. The much harsher pile-up conditions in 2012, clearly visible from the figure, required the detector and object performance to be re-optimised, as will be seen in the following chapters.

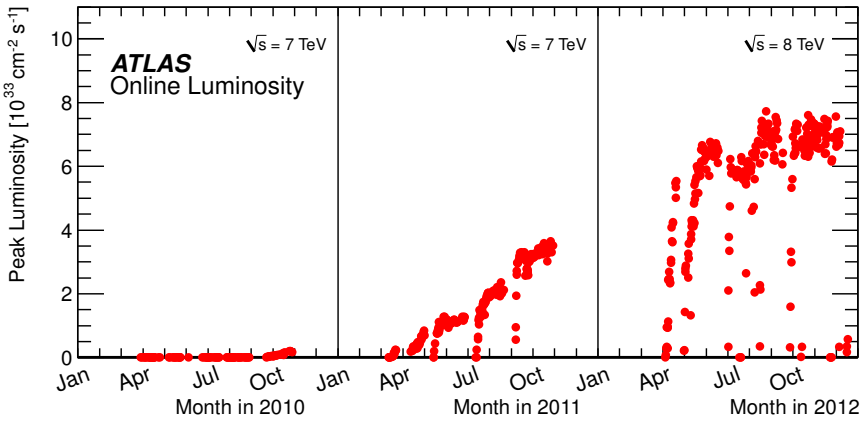

(a)

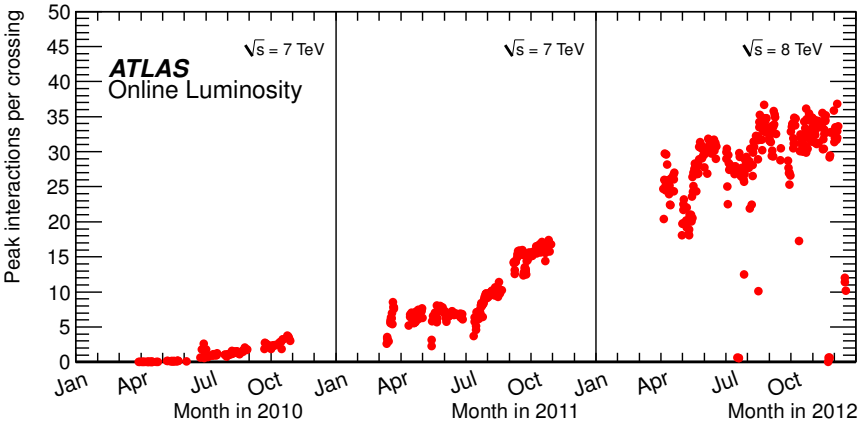

(b)

Figure 2.2 Peak instantaneous luminosity delivered to ATLAS (a), and the corresponding mean number of interactions per bunch crossing (b), as a function of time during the *pp* runs of 2010, 2011 and 2012. The average number of interactions is taken for all bunch crossings in a lumi-block [42].

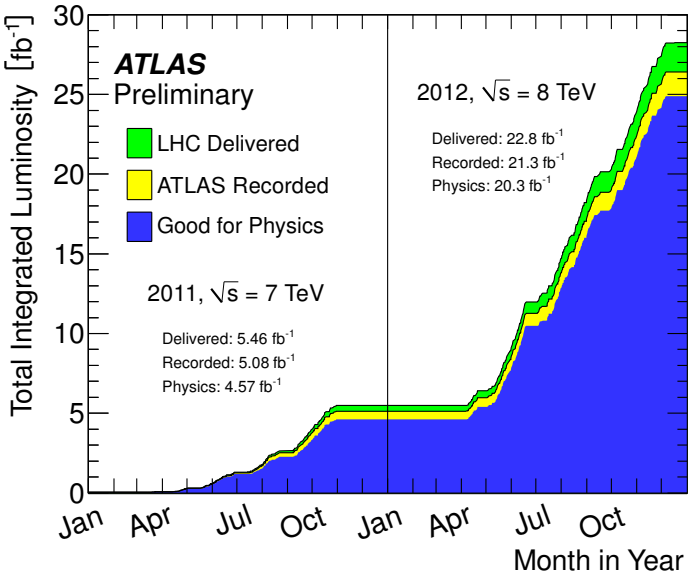

Figure 2.3 Cumulative luminosity versus time delivered to (green), recorded by ATLAS (yellow), and certified to be good quality data (blue) during stable beams conditions and for *pp* collisions at 7 and 8 TeV centre-of-mass energy in 2011 and 2012 [42].

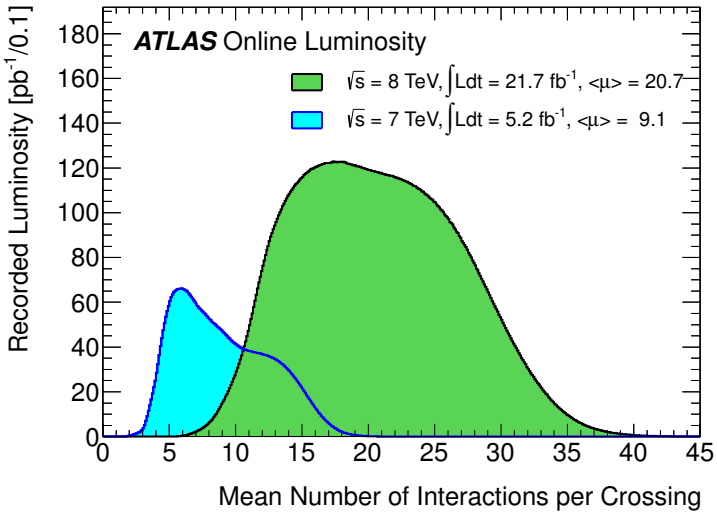

Figure 2.4 Luminosity-weighted distributions of the mean number of interactions per bunch crossing for the 2011 and 2012 data [42].

Chapter 3

The ATLAS Detector

3.1 General overview

The ATLAS (A Toroidal LHC ApparatuS) detector is situated in an underground cavern along the LHC. It was designed to explore the TeV scale, looking for the Higgs boson, as well as for any sign of physics beyond the SM, while keeping the capability of high-accuracy measurements of known objects such as heavy quarks and gauge bosons. The physics processes of interest might correspond to very different experimental signatures, and for this reason ATLAS is usually referred to as a general-purpose experiment.
It has a forward-backward symmetric cylindrical structure, with the axis along the beam direction. The cylinder is composed by a central part, called barrel, and perpendicular endcap disks to cover the forward region. It is the biggest detector of its kind ever built, with a length of 44 m, a diameter of 25 m, and a weight of approximately 7000 tons.

As can be seen from Figure 3.1, ATLAS consists of several specialised sub-detectors which are positioned in layers around the interaction point. A brief description of the various sub-detectors is given in the remainder of this chapter. Section 3.3 presents the innermost layer, i.e. the Inner Detector (ID). Surrounded by a 2 Tesla solenoid magnet, the ID is in charge of measuring the momenta of all charged particles close to the beam pipe and of finding primary and secondary vertices. Moving outwards, the electromagnetic and hadronic calorimeters, illustrated in Section 3.4, allow to measure the energy of electrons and photons, and of jets, respectively. The outermost part of the detector is occupied by the muon spectrometer, which is enclosed by the toroidal magnet system and assures a precise measurement of the muon track parameters. A description of the muon spectrometer is found in Section 3.5.

Finally, the online and offline acquisition and processing of data from the ATLAS detectors are presented in Section 3.6 and 3.7, respectively.

The final section of this Chapter briefly describes the SCT online monitoring, whose maintenance was part of the qualification work required to the author of this thesis to become a member of the ATLAS collaboration.

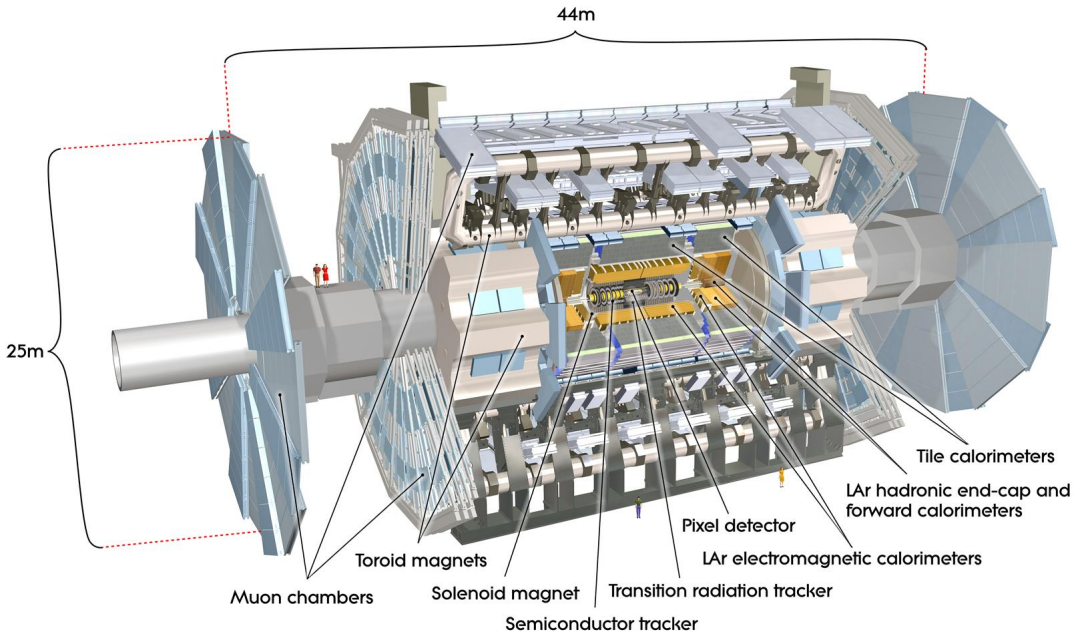

Figure 3.1 Cut-away view of the ATLAS detector [34].

3.2 Coordinate System

ATLAS uses a right-handed coordinate system with the origin located at the nominal interaction point is used. The $x-y$ plane is perpendicular to the beam line and is referred to as the transverse plane. The positive x-axis points to the center of the LHC ring, while the positive y-axis points upwards. The z-axis runs along the direction of the beam, and is used to divide the detector in two regions: the "A-side" (positive z-values) and the "C-side" (negative z-values).
Cylindrical coordinates are defined by the radius r from the origin, the azimuthal angle with respect to the positive x-axis, ϕ, and the polar angle with respect to the positive z-axis, θ. The latter is usually expressed in terms of pseudorapidity:

$$\eta = -\ln\left(\tan\frac{\theta}{2}\right) \tag{3.1}$$

This choice is driven by the fact that, in the case of a massless particle, pseudorapidity is equivalent to the rapidity, defined as

$$y = \frac{1}{2}\ln\frac{E+p_z}{E-p_z} \tag{3.2}$$

for a particle with energy E and longitudinal momentum p_z. Differences in this quantity are indeed Lorentz-invariant under a boost along in the z-axis, and this is a fundamental advantage

in hadron colliders such as the LHC, where the momentum fraction of the interacting partons inside the hadrons along the z-axis is not known.

Energies and momenta are measured in the transverse plane, where conservation laws can be applied.

Finally, the angular distance between two particles in the $\eta - \phi$ coordinate system is in general expressed in terms of:

$$\Delta R = \sqrt{\Delta\eta^2 + \Delta\phi^2} \ . \tag{3.3}$$

3.3 The Inner Detector

The Inner Detector (ID) measures the position of charged particles as they traverse the detector. It is made of three sub-detectors , which are built using two technologies: silicon planar sensors for the Pixel and the SemiConductor Tracker (SCT), and straw drift tubes for the Transition Radiation Tracker (TRT). The ID is capable of providing excellent pattern recognition and momentum resolution of charged-particle tracks, as well as precise reconstruction of primary and secondary interaction vertices. Moreover, the TRT eases the particle identification providing discrimination between electrons and hadrons. The ID is built around the beam pipe with a cylindrical geometry, and has a length and diameter of 6.2 m and 2.1 m, respectively. It consists of central barrel layers, centred on the interaction point, and end-cap wheels or disks at either end of the barrel. Figure 3.2 shows a cut-away of the ID barrel, while Figure 3.3 shows a cut-away of one of the ID endcaps [43, 44].

The track momentum and the sign of the particles' charge can be reconstructed thanks to the superconducting solenoidal magnet surrounding the ID. The generated 2T magnetic field is aligned with the beam pipe, and bends the track in the $x - y$ plane. The solenoid, visible in Figure 3.4, has a length of 5 m and a diameter of 2.5 m, and it was designed to be as thin as possible, to minimise energy losses upstream of the calorimeters. Its thickness amounts to only 45 mm, corresponding to 0.66 radiation lengths[1].

3.3.1 The Pixel detector

The Pixel detector is the sub-detector closest to the interaction point and it has 48.4 cm diameter and approximately 6.2 m length. It consists of three endcap disks and three barrel layers, the innermost of which is only ~ 5 cm away from the beam line. It allows to have uniform coverage in ϕ in the range $|\eta| < 2.5$, and provides the finest granularity, with its 1744 modules consisting of 47232 silicon pixels with a minimum size of $50 \times 400\ \mu m^2$. When charged particles cross the silicon sensors, ionization processes create electron-hole pairs which are collected with an applied electric field and converted into a read-out signal. This charge is recorded locally in the sensor, identifying the position of the particle. The Pixel detector provides on average three measurements per charged particle and has an accuracy of 10 μm in the $r - \phi$ plane and 115 μm along z (barrel) and r (endcap). The innermost layer of the Pixel detector, referred to as the B-layer, is extremely important for the reconstruction of secondary vertices, which can

[1] The radiation length X_0 corresponds to the mean distance over which a high-energy electron loses all but $1/e$ of its energy by bremsstrahlung processes.

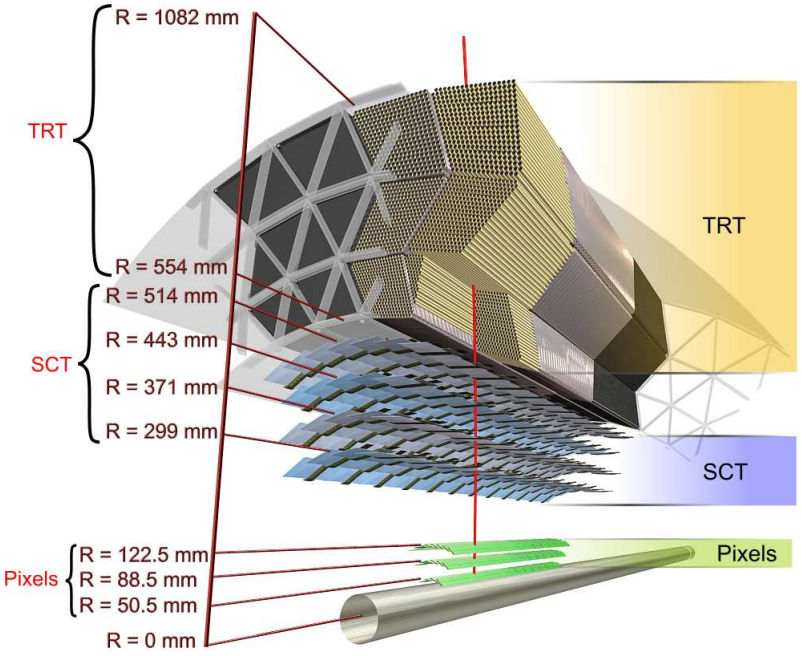

Figure 3.2 Drawing showing the the detector sensors traversed by a charged track of 10 GeV p_T in the barrel of the Inner Detector. The track traverses successively the beam pipe, the three pixel layers, the four SCT double layers, and approximately 36 TRT straws.

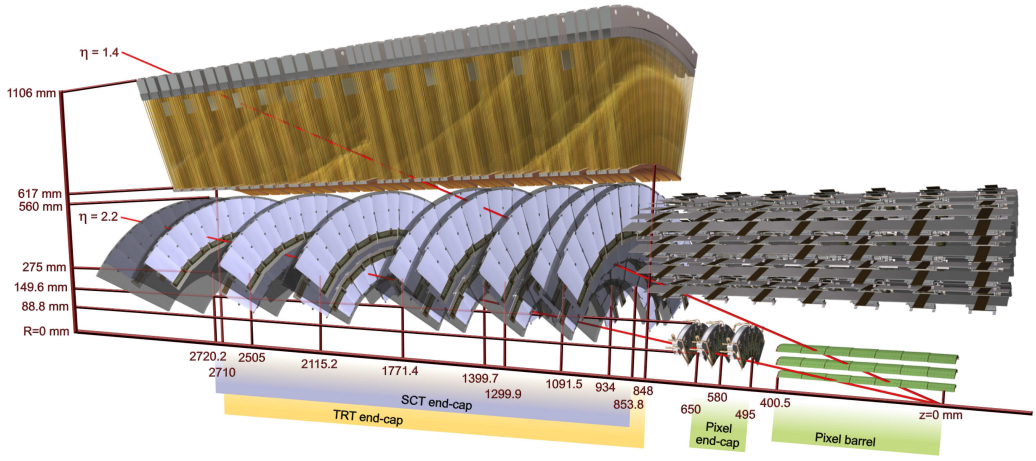

Figure 3.3 Drawing showing the detector elements crossed by two charged particles of 10 GeV p_{T} in the endcap of the ID. A particle at $|\eta| = 1.4$ traverses the beam-pipe, three pixel barrel layers, four SCT disks with double layers of sensors, and approximately 40 straws in the TRT endcap. A particle at $|\eta| = 2.2$ traverses the beam-pipe, only the first layer of the pixel barrel detector, two endcap pixel disks and finally the last four disks of the SCT endcap. The coverage of the endcap TRT does not extend beyond $|\eta| = 2$.

arise from decays of long-lived particles such as B-hadrons, that occur typically within 1-2 cm from the primary interaction vertex.

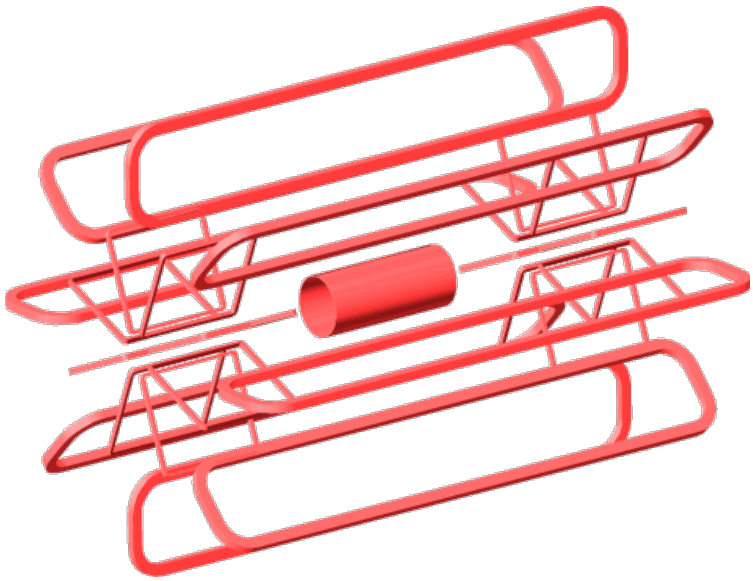

Figure 3.4 The ATLAS magnet system.

3.3.2 The SemiConductor Tracker

The SCT surrounds the Pixel detector, and it consists of four concentric layers in the central region (extending up to $|\eta| < 1.4$) and nine disks in each endcap (extending between $1.1 < |\eta| < 2.5$), inside cylindrical envelopes of 54.9 and 61 cm, respectively. The layout has been designed so that energetic charged particles will pass through at least four layers everywhere in the acceptance region, which extends up-to $|\eta| = 2.5$ (see Figures 3.2 and 3.3) [45]. Each SCT layer is composed of a double layer of silicon microstrips sensors of ~ 6 cm, whose axes are tilted with respect to one another by a 40 mrad stereo angle to provide precision points in both the $R - \phi$ and z coordinates. Two pairs of single-sided microstrips sensors are glued back to back to form each of the 4088 modules. All sensors for the barrel region of the SCT have identical rectangular geometry, with 768 readout strips at a contant 80 μm pitch. The endcap sensors come in five different types, each with trapezoidal geometry. The measured SCT space-point resolution is about 17 μm in the $r - \phi$ plane and 580 μm along the z- and r-directions in the barrel and endcaps, respectively. Both the SCT and the Pixel detector are cooled to temperatures between -5 and -10 °C to limit the effects of radiation damage.

3.3.3 The Transition Radiation Tracker

The TRT is the largest and outermost of the three sub-systems in the ID. It is composed of straw drift tubes, arranged in a barrel and two symmetrical endcap configurations. In the barrel section the straws are aligned parallel to the direction of the beam axis, while in the two endcap sections the straws are arranged in wheels perpendicular to the beam axis, pointing outwards in the radial direction. The TRT extends up to pseudo-rapidity $|\eta| = 2$. The average number of TRT hits on a track is very high, about 34, and the typical position resolution in ϕ is 130 μm.

The TRT operates as a drift chamber: when a charged particle traverses the straw, it ionizes

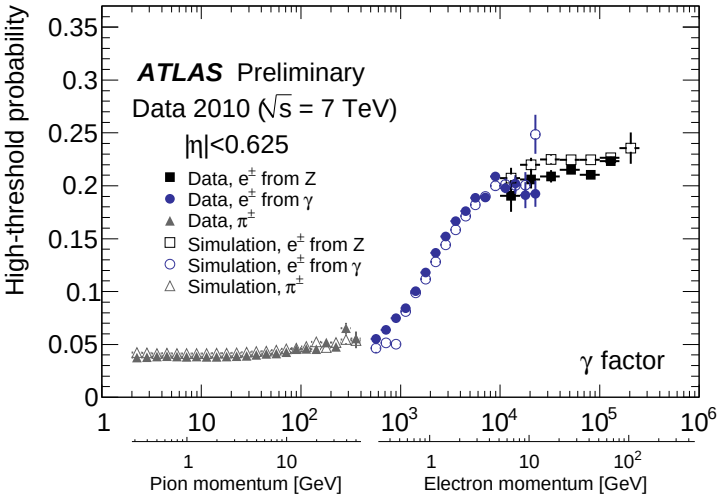

Figure 3.5 Probability of a high threshold TRT hit as a function of Lorentz γ factor in the TRT barrel. The corresponding momentum assuming the pion mass or the electron mass are shown [46].

the xenon gas mixture contained in it. The electrons then drift towards the tungsten gold-plated wire located at the center of the straw and initiate a cascade in the strong electric field, thus producing a detectable electronic signal. The signal on each wire is amplified, shaped and discriminated against two adjustable thresholds, a low threshold (LT) at about 300 eV and a high threshold (HT) at about $6-7$ keV.

In addition to its tracking capabilities, the TRT provides discrimination between electrons and pions over the energy range between 1 and 200 GeV through the detection of transition radiation photons[2]. The probability of emitting such TR photon is a function of the Lorentz factor γ, therefore at a fixed momentum electrons will emit more transition radiation photons than charged hadrons. In order to identify a large energy deposit due to the absorption of a TR photon, the high threshold is used. Figure 3.5 shows the probability of a high threshold TRT hit as a function of the γ factor, calculated using the assumed mass of the candidate (electron or pion) [46, 47]. Particle identification with the TRT is further discussed in Chapter 5.

3.4 The Calorimeter System

The ID is surrounded by a complex calorimeter system which overall extends to $|\eta| < 4.9$. It is designed to measure the energy and position of the particles interacting with the calorimeter material. Except for neutrinos and muons, which escape the calorimeter, these particles are absorbed in the calorimeter material, generating cascade of secondary particles with progressively degraded energies, called showers. The nature of these particle cascades depends on the initial particle passing through the detector. Electrons and photons develop into electromagnetic showers via electron-positron pair production and via bremsstrahlung emissions. Hadrons

[2]Highly relativistic charged particles emit transition radiation (TR) photons when traversing boundaries between materials of different dielectric constants.

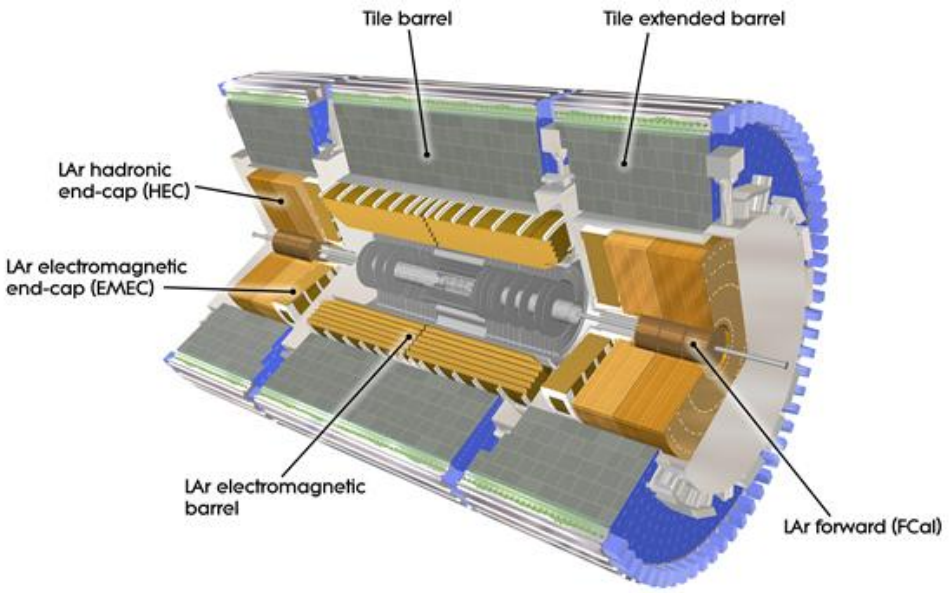

Figure 3.6 Cut-away view of the ATLAS calorimeter system showing its main components [34].

produce hadronic showers which are dominated by successive inelastic nuclear interactions. Different and specialised detectors are used to measure the energy of electromagnetic particles and the energy of hadrons.
An overview of the different sub-detectors is visible in Figure 3.6. The energies of electrons and photons are measured by the liquid-argon (LAr) electromagnetic barrel and end-cap calorimeters. The Tile calorimeters and the LAr hadronic end-cap calorimeter are instead designed to measure the energy of hadrons. Finally, the LAr forward calorimeters provide both electromagnetic and hadronic energy measurements. Some details of the calorimeter sub-systems are given in the following paragraphs.

The ATLAS calorimeters are non compensating, which implies that the calorimeter response to hadronic particles is lower than the response to electromagnetically interacting particles. Not all the energy of an hadronic shower can be detected in the calorimeters, and this is mainly caused by the invisible energy from nuclear breakups and excitation, and by the invisible particles escaping detection. The correct hadronic energy scale is then restored offline, as described in Section 4.3.

The calorimeters have a sampling geometry, in which layers of absorbing passive material with high atomic number are alternated with low density active detector sensors. In this case only a fraction of the energy produced by the particle is measured, and the energy of the full shower has to be inferred. The fine segmentation in the longitudinal and lateral directions allows a measurement of the shower shape and direction variables with good accuracy, and is important for particle identification.

The relative energy resolution in a calorimeter can be parametrised as follows:

$$\frac{\sigma}{E} = \frac{a}{\sqrt{E}} \oplus \frac{b}{E} \oplus c \ , \tag{3.4}$$

where a is the so called stochastic, or sampling term, b is the noise term, and c is the constant term. The stochastic term accounts for statistical fluctuations related to the shower development, to the sampling geometry, and to the absorbing material in front of the calorimeter. It mostly contributes at low energy, where less particles are produced in the cascade and the impact of fluctuations is higher, and it deteriorates as the amount of material in front of the calorimeter increases at larger $|\eta|$. The noise term scales inversely with the particle's energy, and therefore may affect the low-energy performance of the calorimeters. Finally, at higher energies the relative energy resolution tends asymptotically to the constant term.

3.4.1 LAr electromagnetic calorimeter

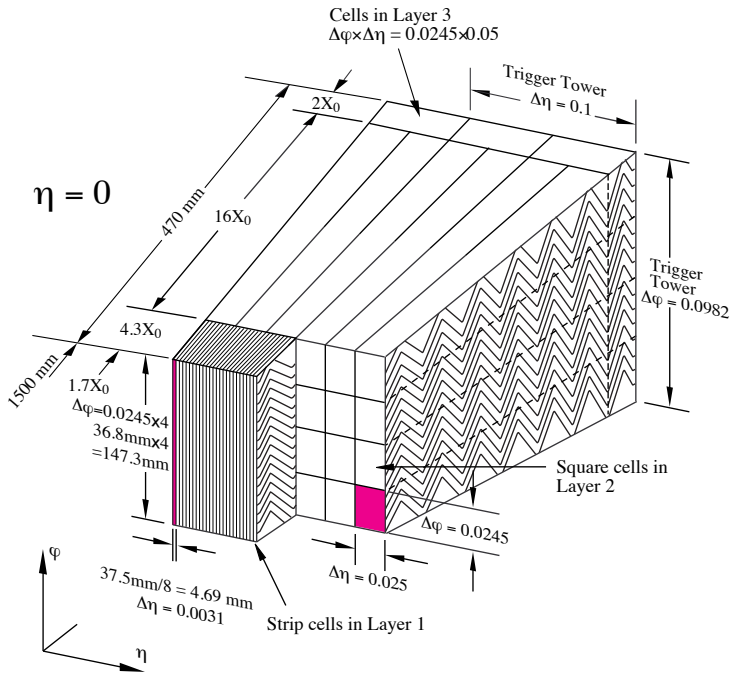

Figure 3.7 Sketch of a section of the LAr EM barrel. The accordion shape of the absorber and the three layers with different granularities are clearly visible [34].

The electromagnetic calorimeter (EM) is a sampling calorimeter using liquid argon as active material and lead as absorbing medium. It consists of a barrel calorimeter covering the range $|\eta| < 1.475$, and two endcap calorimeters which extend from $|\eta| = 1.375$ to $|\eta| = 3.2$. As shown in Figure 3.7, the sampling layers are arranged in an accordion like geometry, ensuring complete and uniform azimuthal coverage and fast readout.
These detectors provide high granularity measurements, particularly in the range $|\eta| < 2.5$, which is crucial for precision physics and particle identification. In this region the calorimeter is segmented into three longitudinal layers with different $\eta - \phi$ granularities. Figure 3.7 shows

a cut-away of the different layers in the EM barrel calorimeter.

The first sampling, also referred to as the strip layer, extends in depth over 4.3 radiation length and is finely granulated in η with strips of dimension $\Delta\eta \times \Delta\phi = 0.003 \times 0.1$. The excellent resolution allows to discriminate against close-by photons coming from pion decays, and against jet background. The choice of a coarser strip size in ϕ than in η is motivated by the fact that showers which start in front of the solenoid are smeared in ϕ by the magnetic field. Therefore, no attempt is made to measure their fine structure in this direction.
The middle calorimeter sampling provides most of the energy measurement, covering 16 radiation length. It has fine segmentation in both η and ϕ, and is organised in cells of $\Delta\eta \times \Delta\phi = 0.025 \times 0.025$. This granularity allows to distinguish electromagnetic showers from showers produced by pions or jets. In combination with the first sampling, this layer also allows the measurement of the electromagnetic shower direction (pointing).
The third sampling, or back layer, adds additional depth to the calorimeter, and has a coarser granularity of $\Delta\eta \times \Delta\phi = 0.050 \times 0.025$. It is used to estimate the longitudinal shower leakage. Finally, an additional presampler located in front of the EM calorimeter is used over the region $|\eta| < 1.8$ to correct for the energy lost in the upstream material. Being used only for energy measurements, its granularity ($\Delta\eta \times \Delta\phi = 0.025 \times 0.1$) is coarser than in the EM calorimeter [48, 49].

The excellent energy resolution, required to achieve a mass resolution of $\sim 1\%$ for the $H \to \gamma\gamma$ and the $H \to ZZ^* \to 4\ell$ channels in the mass region 90–180 GeV, is given by:

$$\frac{\sigma}{E} = \frac{10\%}{\sqrt{E}} \oplus 0.3\% \ . \tag{3.5}$$

The angular resolution of the electromagnetic calorimeter is:

$$\sigma_\eta = \frac{40 \text{ mrad}}{\sqrt{E}}. \tag{3.6}$$

3.4.2 Tile hadronic calorimeter

The ATLAS hadronic calorimetry covers the range $|\eta| < 4.9$ and exploit different technologies and devices as best suited for the varying requirements and radiation environment.
In the region $|\eta| < 1.7$, located just after the EM calorimeter, the Tile calorimeter is used, with its barrel and two extended barrel sections. It is a sampling calorimeter using iron as absorber and scintillating tiles as active material. It is segmented in three layers, the first and the second having a granularity of $\Delta\eta \times \Delta\phi = 0.1 \times 0.1$, and the third being segmented according to $\Delta\eta \times \Delta\phi = 0.2 \times 0.1$.
An important parameter for the hadronic calorimeter is its thickness, which should ensure good containment for hadronic showers and reduce punch-through into the muon system. To achieve this, the total thickness was designed to be 11 interaction lengths [3] at $\eta = 0$, sufficient to reduce

[3] The interaction length λ is defined as the mean free path of a high-energy particle in a material before undergoing inelastic scattering.

the rate of punch-through below the irreducible level of prompt muons, and muons from $\pi^{\pm}$ and $K^{\pm}$ decays [49].

3.4.3 LAr hadronic endcap calorimeter

The hadronic endcap calorimeter (HEC) is a liquid argon sampling calorimeter with flat copper absorber plates. The liquid argon technology has been chosen for its ability to withstand the high radiation environment. The HEC cover the regions of pseudorapity $1.5 < |\eta| < 3.2$, and each endcap calorimeter is structured in two, equal diameter, independent wheels. The granularity of the HEC is $\Delta\eta \times \Delta\phi = 0.1 \times 0.1$ in the region $1.5 < |\eta| < 2.5$, and $\Delta\eta \times \Delta\phi = 0.2 \times 0.2$ beyond.
To ensure total energy containment up to the highest energies, as well as acceptable low background in the muon chambers, the calorimeter thickness is approximately 10 interaction lengths, including the electromagnetic calorimeter in front of the HEC [50].

3.4.4 LAr forward calorimeter

The LAr Forward Calorimeter (FCal) are located between the beam pipe and the LAr endcap calorimeters, and extend the pseudorapidity coverage to $|\eta| = 4.9$. The forward calorimeter accommodates approximately 10 interaction lengths of active detector in a rather short longitudinal space, and it is thus a high density detector. It consists of three longitudinal sections. The first module is optimised for the measurement of electromagnetic objects and uses copper plates as the absorbing material. The other two modules are made mainly of tungsten to optimise both longitudinal and transverse hadronic shower containment in the available space. Behind the last module, an un-instrumented copper-alloy plug provides additional shielding for the muon system [51].

3.5 The Muon Spectrometer

The muon spectrometer forms the outermost part of the ATLAS detector. It was designed to have high-resolution, with stand-alone triggering and momentum measurement capability over a wide range of transverse momentum, pseudorapidity and azimuthal angle.
The muon tracks are deflected in a system of three large superconducting air-core toroid magnets. Over the range $|\eta| \leq 1$, in the barrel region, magnetic bending is provided by a large barrel magnet constructed from eight coils surrounding the hadron calorimeter. For $1.4 \leq |\eta| \leq 2.7$ muon tracks are bent by two smaller end-cap magnets inserted into both ends of the barrel toroid, as shown in Figure 3.4. Finally, in the transition region between $1 \leq |\eta| \leq 1.4$, the magnetic fields generated by the barrel and endcaps toroid overlap, and the deflection is provided by a combination of the two. This magnet configuration provides a field that is mostly orthogonal to the muon trajectories, while minimizing the degradation of resolution due to multiple scattering.
The spectrometer is instrumented with separate-function trigger and high-precision tracking chambers. In the barrel these chambers are arranged in three cylindrical layers around the beam axis, while in the transition and end-cap regions they are installed in three wheels. The

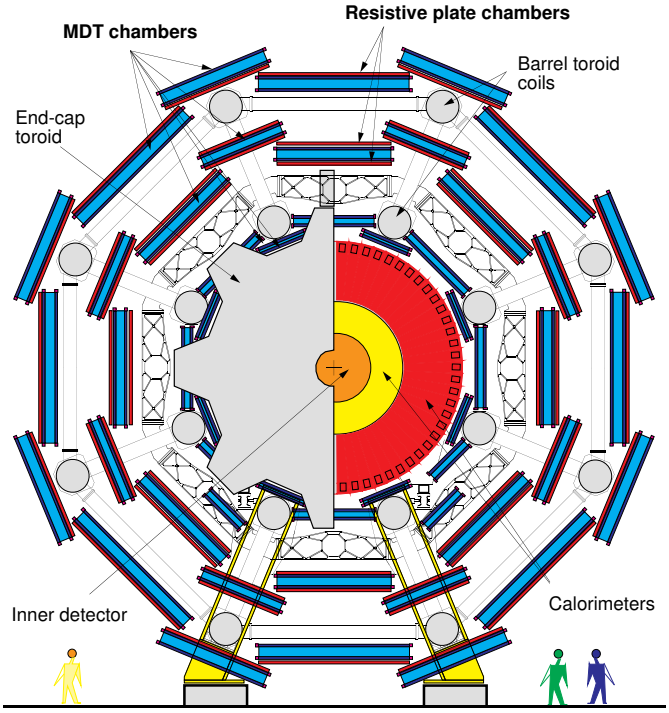

(a)

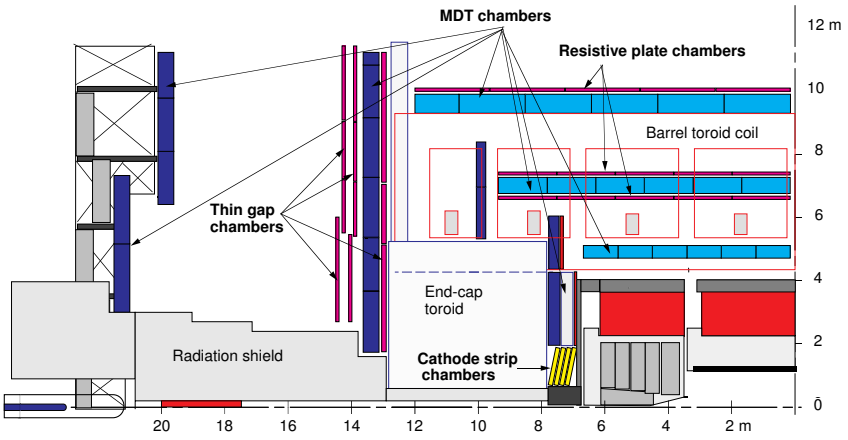

(b)

Figure 3.8 (a) Transverse view of the muon spectrometer. (b) Side view of one quadrant of the muon spectrometer [52].

different layers and wheels are usually referred to as "stations". Figure 3.8(a) and Figure 3.8(b) show a transverse view and the $r - z$ projection of the spectrometer layout, respectively.
The momentum resolution is limited by energy loss fluctuations at small momenta and by detector resolution at high momenta, whereas the multiple scattering effect is approximately momentum-independent. The momentum resolution is typically $2 - 3\%$ over most of the kinematic range apart from very high momenta, where it increases to $\sim 10\%$ at $p_T = 1$ TeV .

3.5.1 Precision chambers

For the precision measurement of muon tracks in the principal bending direction of the magnetic fields, Monitored Drift Tube chambers are used over most of the $\eta-$range. The MDT chambers consist of pressurised drift tubes arranged in two multi-layers of three or four layers, located on either side of a rigid support structure. The single-wire resolution is $\sim 80\mu$m, while per chamber we achieve $\sim 30\mu$m. As shown in Figure 3.8(b), MDT chambers are located both in the barrel and in the endcap regions of the detector, and cover most of the solid angle except in the innermost ring of the inner station of the endcaps, where particle fluxes are highest. In this region, covering the pseudorapidity range $2 \leq |\eta| \leq 2.7$, Cathode Strip Chambers (CSCs) are employed, which provide the finer granularity required to cope with the demanding rate and background conditions.

The CSCs are multi-wire proportional chambers with cathode strip readout, located on four identical planes. The precision coordinate is obtained by measuring the charge induced on the segmented cathode by the avalanche formed on the anode wire. These cathode strips are oriented perpendicular to the anode wires. A measurement of the transverse coordinate is instead obtained from orthogonal strips, i.e. oriented parallel to the anode wires, which form the second cathode of the chamber. The achieved spatial resolution in the bending plane is 60 μm, while it is ~ 5 mm in the orthogonal direction. The spatial resolution of CSCs is sensitive to the inclination of tracks and the Lorentz angle. To minimize degradations of the resolution, they are installed in a tilted position such that infinite-momentum tracks originating from the interaction point are normal to the chamber surface.

3.5.2 Trigger chambers

The trigger system covers the pseudorapidity range $|\eta| \leq 2.4$ and employs two different types of detectors: Resistive Plate Chambers (RPCs) in the barrel and Thin Gap Chambers (TGCs) in the endcap region.

The basic RPC unit is formed by two parallel resistive bakelite plates filled with an ionising gas mixture. The primary ionisation electrons are multiplied into avalanches by a high, uniform electric field. A trigger chamber is made from two independent detector layers, each one read out by two orthogonal series of metal strips. The "η strips", parallel to the MDT wires, provide the bending view of the trigger detector, while the "ϕ strips" are used to measure the second coordinate. The spatial resolution of the RPCs is 10 mm. The timing resolution of 1.5 ns makes the RPC well suited for triggering.

In the endcaps of the muon spectrometer the TGCs provide two distinct functions: the muon trigger capabilities and the measurement of the azimuthal coordinate, to complement the

bending coordinate measured by the MDTs. The TGCs are multiwire proportional chambers operating in a saturated mode. The coordinate in the bending plane is obtained from ionization charges collected on the anode wires, whereas the second coordinate is determined from strips arranged orthogonal to the wires [52, 53].

3.6 Trigger and Data Acquisition System

Most of the physics processes of interest at the LHC have very small cross sections, and a large number of collisions are therefore needed to produce a significant number of these events. At the design parameters of the LHC, a luminosity of 10^{34} cm^2 s^{-1} and beams crossings at an event rate of 40 MHz are expected. As we can only afford to save a few hundred events per second, it is extremely important to perform a real-time event selection to reduce the number of events, while retaining excellent efficiency for the interesting processes. This is achieved by the trigger and data acquisition system, which is always referred to as TDAQ. The system is organised in three levels of increasing complexity and with different time latencies and rates, as shown in Figure 3.9. Each level refines the decision taken by the previous one, and progressively reduces the number of events to an acceptable rate.

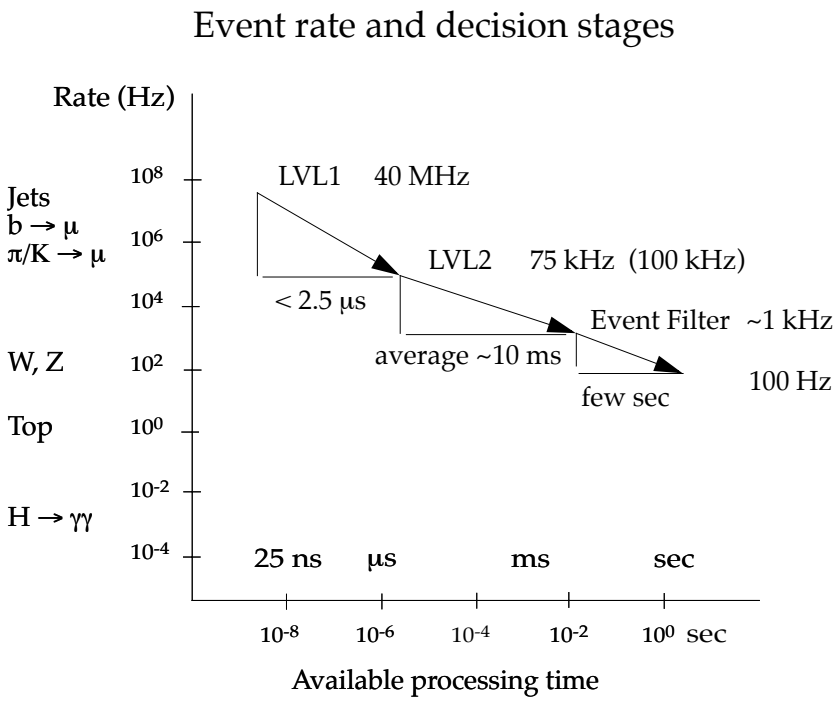

Figure 3.9 The three levels of the ATLAS trigger and their event rates and processing times [54].

The level-1 (L1) trigger is required to provide a decision in less than 2.5 μs and is thus operated directly at a hardware level, using only fast detectors. Information from the ID is not used at this stage, as the track reconstruction would require too much time. The calorimetric

selections are based on reduced coarse granularity information from the electromagnetic and hadronic calorimeters, and events with high p_{T} muons are identified using only the dedicated trigger chambers (RPCs and TGCs). Thanks to this information the L1 trigger is then able to identify geometrical regions of interest (RoI) in terms of $(\eta - \phi)$ coordinates in the detector. The design rate of events accepted by L1 is 75 kHz. If an event is selected by L1, the data are transferred from the front-end electronics of the sub-detectors via Read Out Drivers (RODs), and held temporarily into Read Out Buffers (ROBs) [55].

The RoIs are passed on via the Read Out System (ROS) to the software-based level-2 trigger (L2), which is part of the so-called High Level Trigger (HLT), together with the Event Filter (EF). At this level highly optimised reconstruction algorithms are executed exploiting the full detector granularity and tracking information, but only inside the RoIs. L2 is able to reject fake objects by improving the precision on measured parameters and applying further requirements, such as isolation cuts for muons and loose shower shape and track-cluster matching cuts for electrons, and it is finally expected to reduce the event rate to ~ 1 kHz.

Events that are accepted by L2 are fully assembled and formatted by the Event Builder, which collects the various sub-detector information from the ROSs. Fully built events are then passed to be further processed to the last level of the trigger system, the EF, which has at its disposal the full detector information. Compared to L2, more sophisticated reconstruction and trigger algorithms are used, similar to those executed during offline data reconstruction. The EF also benefits from more detailed calibration and alignment than L2. The latency is of the order of a few seconds [56]. The events accepted by the EF are finally organised into several output streams according to the trigger selection algorithms.

Each trigger consists of a unique combination of L1 item, defining the selection criteria, and trigger chains at L2 and EF. In order to minimise the processing time, each chain is processed in a step-wise manner. At each step, the selection is refined by the readout of increasing amounts of data from the detector, and increasingly complex processing. An event can be rejected at any step if the applied requirements are not satisfied.

Trigger *menus* are full collections of trigger chains and L1 items, and are designed to work in a variety of LHC beam conditions. These conditions may indeed change over time as the operational parameters of the LHC are optimised to provide maximum luminosity to the experiments. On a shorter time scale, the beam conditions vary during an LHC fill cycle. Typically beams are injected in the LHC, accelerated to collision energy and used to collect data for several hours, before being "dumped" by directing them against a target of absorbing material. Due to collisions and other effects, protons are gradually lost from the beam and the luminosity reduces, allowing, for example, the use of additional *end-of-fill* triggers to take advantage of the full L1 bandwidth. Such end-of-fill triggers are used in the analysis described in Chapter 5.
The trigger menu also specifies the prescale factors which can be assigned to given L1 items or HLT chains to reduce their rate. Analogously pass-through factors can be defined which allow to accept events regardless of the trigger decision [57, 58].

The implementation of the main physics triggers used in the analyses presented in this thesis is described in the following sub-sections.

3.6.1 Electron triggers

To identify the RoI position and to compute the cluster E_{T} with a precision of 1 GeV, trigger towers with the reduced granularity of $\Delta\eta \times \Delta\phi \approx 0.1 \times 0.1$ are built at L1 adding up the cells of both the electromagnetic and hadronic calorimeters. EM clusters are then formed by identifying local maxima using a sliding window algorithm based on a 4×4 group of trigger towers. The trigger requirements are satisfied if at least one of the four possible 2×1 or 1×2 combinations of neighbouring trigger towers in the central 2×2 window core exceeds a certain energy threshold. In addition, isolation requirements can be applied to the ring and core cells in the hadronic calorimeter. An illustration of the electromagnetic L1 clustering algorithm can be seen in Figure 3.10.

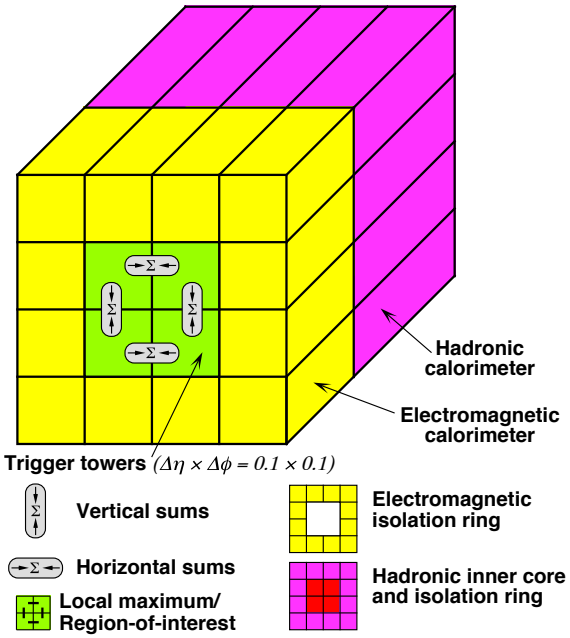

Figure 3.10 Electromagnetic clustering algorithm at L1 [34].

The RoI defining the location of the 2×2 clusters is then passed to the L2 trigger. Due to latency constraints, only the second layer of the electromagnetic calorimeter is used to select the so-called pre-seed, defined as the cell with the largest energy deposition inside a given RoI. The cluster position is calculated from the energy weighted average cell positions in a 3×7 grid around the pre-seed. The clusters are then formed by adding up the energy depositions in 3×7 and 5×5 windows around the cell centres in the barrel and in the endcap EM calorimeters respectively. To refine the selection, cuts on the shower shape variables are applied at this level. In a separate step, L2 also exploits information from the ID, which are first made available at this stage. Fast tracking algorithms, able to fulfill the stringent timing requirements, make use of signals around the L1 RoI from the silicon detectors, and only later extend the tracks to the TRT, if they fall into its acceptance. A minimum track p_{T} of 1 GeV is required.
The electromagnetic clusters and tracks reconstructed at L2 are finally matched based on their $\eta - \phi$ position.

As significantly more time is available at the EF level, more sophisticated clustering and tracking algorithms are executed, which are very similar to those used in the offline electron reconstruction described in Section 4.1. Similar, but typically slightly looser, criteria to those described for the offline electron identification in Section 5.1 are also applied to EF electron candidates [59].

3.6.2 Muon triggers

The muon L1 algorithms search for coincidences of hits in different layers of the dedicated RPC and TGC chambers described in Section 3.5.2. The hit pattern along the muon trajectory is used to estimated the p_{T} of the muons.

At L2 the candidate identified from L1 is refined by using the precision data from the MDTs, presented in Section 3.5.1. Three algorithms are run at this stage. The first one, called standalone algorithm (SA), constructs a track from the MS data within the RoI defined by the L1 seed. In the following step, a fast track combination algorithm (CB) combines the MS tracks with the ones found in the ID in order to improve the resolution of the track parameters. Finally, the isolated muon algorithm incorporates tracking and calorimetric information to find isolated muon candidates.

At the EF, the full information from both the precision and the trigger chambers is accessible. As at L2, a standalone algorithm extrapolates the tracks built in the MS back to the beam line and determines the track parameters at the interaction point. The selected muon candidates are then again combined with an ID track in the so-called "outside-in" strategy. A complementary approach, called "inside-out", runs another algorithm which starts with ID tracks and extrapolates them to the muon detectors [60].

3.7 Offline Data Processing

Once the collected data events are available in the output streams, they are picked up by the offline processing system. Before the properties of physical objects can be reconstructed from the data, detector calibration factors need to be applied. As mentioned in the previous section, the latter are extracted from the express stream shortly after the beginning of a new data-taking run. This early data processing also helps to provide quick feedback on the data quality via offline monitoring tools. The bulk processing of the entire dataset from the physics stream is then launched 36 hours after the end of the run.
The detector calibrations, regarding for example the beamspot position and the identification of noisy detector channels, are uploaded to a detector conditions database. The data quality is then evaluated based on the correct functioning of a given sub-detector or reconstruction algorithm.
The performance of the TDAQ and of the detector systems is also monitored online, and the final "good" or "bad" data-quality decision is formed after combination of the online and offine outputs. The data quality decisions are later propagated to physics analyses through so-called

Good Run Lists (GRLs), which contain luminosity block[4] ranges of detector runs that fulfil the required criteria for a given physics analysis, and account for possible detector inefficiencies.

3.8 SCT Online Monitoring

The monitoring of the correct functioning and performance of the ATLAS detector, both online and offline, is a most important and challenging task. Given their extreme complexity, the monitoring is typically maintained and operated separately for the various sub-detectors. Here, a brief description of the online monitoring of the SCT sub-detector is given, whose maintenance was part of the qualification work conducted by to the author of this thesis to become a member of the ATLAS collaboration.

The online monitoring plays a fundamental role in providing immediate effective feedback of data quality, thus ensuring safe and full exploitation and optimal operation of the SCT. The fastest feedback is provided by the so-called ROS monitoring, which is specific of the SCT system. By directly analysing raw hits from 10% of all level 2 trigger accepted data, this monitoring allows high statistics, minimal trigger bias and fast detector feedback. Histograms showing the number of readout errors, strip hits and simple space-points (identified as a coincidence between hits on the two sides of a module) as a function of time are monitored by shifters and experts, allowing a quick diagnosis of issues during a run.

An illustrative example of the ROS monitoring potential is shown in Figure 3.11, where one can see the hit rates per second for an early 2010 run with one colliding bunch in ATLAS. Prior to the beginning of the run, the noise level is very low, with only $\mathcal{O}(10)$ hits per second. The rate increases to $\mathcal{O}(100)$ after beam injection due to beam background events, and finally reaches $\mathcal{O}(10^3 - 10^4)$ during collisions, remaining stable for over 17 hours. No hits are recorded during the energy ramping up to 2.7 TeV, when the ATLAS triggers are kept on hold. Small effects originating from beam effects or ATLAS data taking changes (e.g. trigger prescale changes), are all visible in the plot. This monitoring is thus also particularly useful for providing fast feedback on unusual and possibly dangerous beam conditions, and was extensively used during LHC commissioning [61, 62].

[4] A luminosity block is a short time interval (order of minutes) during which the data-taking conditions (detector and beam conditions) were approximately stable.

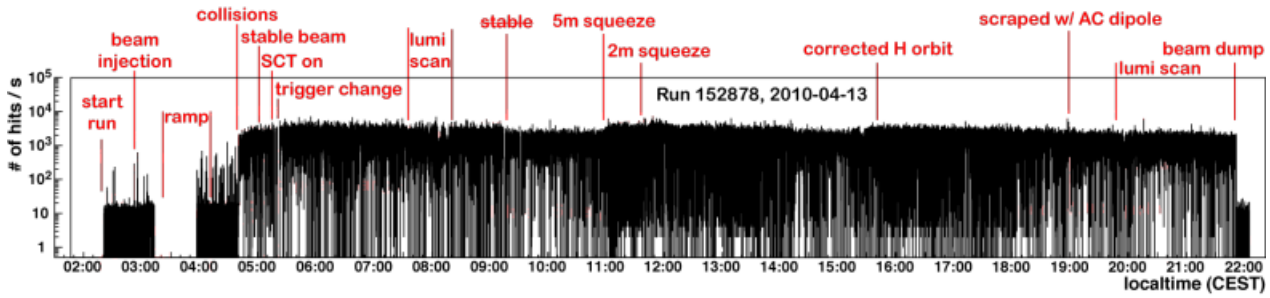

Figure 3.11 Number of hits per second recorded with by the SCT ROS monitoring for a typical long run with one colliding bunch in ATLAS.

Chapter 4

Event reconstruction

The offline reconstruction software converts the raw signals recorded by the detector into collections of measurements associated with the particles produced in the collision. In this chapter the reconstruction of the main physics objects used in the analyses presented in Chapters 6-9 is described. Particular emphasis is given to the electron reconstruction and energy calibration, presented in Section 4.1, to which the author specifically contributed. Sections 4.2 and 4.3 describe the reconstruction of muons and jets, respectively.

4.1 Electron Reconstruction

Owing to its small mass, an electron can loose a significant amount of its initial energy due to bremsstrahlung when interacting with the detector material, and this leads to alterations of the electron's trajectory. The reconstruction scheme used in ATLAS for 2010 and 2011 publications did not include a special treatment to account for these losses, and this resulted in inefficiencies in reconstructing the electron track, as well as in the degradation of the estimated track parameters.
An improved reconstruction scheme was developed and thoroughly studied in ATLAS during 2011 to properly account for bremsstrahlung. Multiple aspects of the reconstruction scheme were revised and improved, as described in full detail in Sections 4.1.1-4.1.5. The author contributed to the validation of the algorithm based on the Gaussian Sum Filter model, which has significantly improved the performance of electron reconstruction, especially in the low-momentum region.

An improved calibration of the electron energy measurements has also been developed for 2012 data, resulting in a sizable reduction of the systematic uncertainties on the energy scales. The new procedure, described in Section 4.1.6, makes use of a new multivariate algorithm called MVA, which has been validated by the author in the context of the $H \to ZZ^* \to 4\ell$ analysis.

After reconstruction, further identification criteria can be applied on electrons to increase the fraction of true signal electrons and reject hadrons that fake the electron signature and non-isolated electrons from, for example, photon conversions to e^+e^- pairs. The discriminating variables and applied selections, as well as the efficiency measurements for these so-called

"menus" will be the subject of Chapter 5.

4.1.1 Electron seed-cluster reconstruction

Electron candidates in the central region of the ATLAS detector ($|\eta| < 2.47$) are reconstructed starting from energy deposits in the EM calorimeter, which are then associated to reconstructed tracks in the ID.
Following the granularity of the EM middle layer, the calorimeter is divided into a grid of $N_\eta \times N_\phi = 200 \times 256$ elements, called towers, of size $\Delta\eta_{\text{tower}} \times \Delta\phi_{\text{tower}} = 0.025 \times 0.025$. The energy of each tower is obtained by summing the energy of the cells in all longitudinal layers (the back, middle and front EM accordion calorimeter layers, and for $\eta < 1.8$ also the presampler detector). If a cell extends across multiple towers, its energy is distributed uniformly among them.
The tower grid is scanned by a *sliding-window* algorithm which searches for seed clusters with total transverse energy above 2.5 GeV. The window size is fixed to 3×5 towers in the $\eta - \phi$ space.
For each seed cluster passing some loose shower shape requirements, a cone, or region-of-interest (ROI), of size $\Delta R = 0.3$ is identified around the seed cluster barycentre. The collection of these EM cluster ROIs is retained for use in the track reconstruction, which is the following step.

4.1.2 Electron track reconstruction

The first stage of track reconstruction is the so-called *pattern recognition*, subsequently followed by a track fit. The scheme used for the 2010 and 2011 data-taking employed the same pattern recognition for all charged particles, with all tracks treated using a pion hypothesis to estimate material effects. In 2012, this standard pattern recognition has been complemented with a modified one which accounts for possible energy losses due to bremsstrahlung allowing at most 30% energy loss at each material surface. If a track falling inside one of the EM cluster ROIs can't be successfully reconstructed using the pion hypothesis, it is retried with the new pattern recognition using an electron hypothesis.
Track candidates are then fitted with the hypothesis used in the pattern recognition, either the pion or the electron one, using the ATLAS Global χ^2 Track Fitter.
Afterwards, the tracks are extrapolated from the end of the ID to the middle layer of the calorimeter, and loosely matched to the seed clusters if they satisfy either of the following requirements:

- The angular distance in ϕ between the track and the cluster is either less than 0.2 on the side the track is bending towards, or less than 0.05 on the opposite side. All tracks but TRT-only ones, i.e. tracks with less than four silicon hits, are also required to be within 0.05 in η of the EM cluster.

- The angular distance in ϕ, after rescaling the track momentum to the measured cluster energy, is either less than 0.1 on the side the track is bending towards, or less than 0.05 on the opposite side. All tracks but TRT-only ones are also required to be within 0.05 in

η of the EM cluster. With this criterium we attempt to recover electrons which have lost a large amount of energy.

At this point all electron-track candidates are identified and a second fit using an optimized electron track fitter, the Gaussian Sum Filter (GSF) algorithm, is performed for all but TRT-only tracks.

4.1.3 The Gaussian Sum Filter algorithm

The track parameters and their corresponding uncertainties are estimated from the track-fitting process. While in the case of muons or pions, a linear least-squares fit using a helical model (including multiple scattering effects) is sufficient to reconstruct the trajectory, this is not the case for electrons, which may suffer from significant energy losses due to bremsstrahlung. A well-known model proposed by Bethe and Heitler in 1934 [63] describes the energy lost by a particle for bremsstrahlung. According to this model, the probability density function to retain a fraction $z = E_f/E_i$ of its initial energy E_i is given by:

$$f(z) = \frac{[-ln(z)]^{a-1}}{\Gamma(a)} \quad \text{with} \quad a = \frac{t}{\ln(2)} \tag{4.1}$$

where t is the thickness of the material traversed by the electron in units of radiation length X_0. At the energies we deal with at the LHC and for large amounts of traversed material (see Figure 4.1), this formula needs to be modified in order to account for additional processes, such as the Landau-Pomeranchuk-Migdal (LPM) or the Ter-Mikaelian effects [64–66]. The resulting probability density function does not have an analytical expression, and numerical implementations are used in simulation programs like GEANT4. It is thus clear that a linear

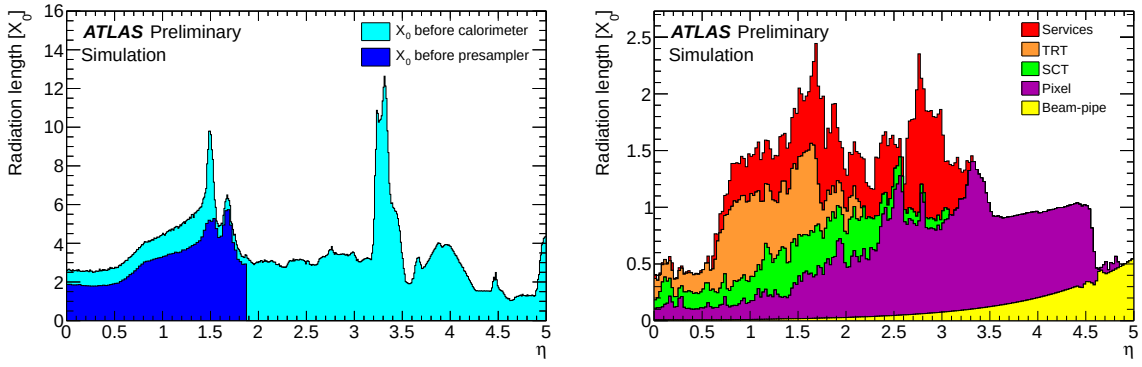

Figure 4.1 Amount of material traversed by a particle as a function of $|\eta|$ in the improved simulation: (left) material in front of the presampler detector and the EM accordion calorimeter, and (right) material up to the ID boundaries. The contributions of the different detector elements, including the services and thermal enclosures are shown separately by filled color areas [67].

description of the electron trajectory would be unsuitable, and that a non-linear fitter is required to provide a better estimation of the track parameters. The GSF algorithm, which is a non-linear generalization of the Kalman filter [68], was developed for this reason. The assumption

behind this algorithm is that the electron's trajectory can be approximated as a weighted sum of Gaussian functions. The experimental noise is split into individual Gaussian components which are processed using the Kalman filter technique. This procedure yields a number of Kalman filters operating in parallel, each representing a different contribution to the full Bethe-Heitler spectrum.

As already mentioned in the previous section, the GSF algorithm is not applied to TRT-only tracks, as no appreciable improvement is observed due to the lower precision of TRT measurements. These tracks and the very rare tracks ($\sim 0.01\%$) which fail the GSF fit maintain the parameters estimated by the Global χ^2 Track Fitter.

The GSF algorithm has been extensively studied and validated on the 2011 data sample and then used for the first time in the $H \to ZZ^* \to 4\ell$ analysis. Since the beginning of 2012 data-taking, the GSF reconstruction algorithm has become part of the standard reconstruction scheme, together with the improved pattern recognition. Section 4.1.5 describes the work done to validate the use of this new algorithm.

4.1.4 Electron candidate reconstruction

Once the electron track parameters have been precisely re-estimated, we proceed with a second track-cluster matching with slightly tighter requirements than the ones used in the previous step. In the first criterium, the distance in ϕ is now required to be 0.1, not 0.2 . Furthermore, TRT-only tracks are required to satisfy the following matching criteria: $|\Delta\eta| < 0.35$ (0.2) in the barrel (endcap), and $|\Delta\phi| < 0.03$ (0.02) on the (opposite) side the track is bending towards.
More that one track can be associated with a given cluster, and selecting the best matching among them is the next step in the reconstruction scheme. This procedure was also improved in 2012 in order to favour the primary electron track in case of cascades due to bremsstrahlung:

1. Tracks with at least one Pixel hit are preferred.

2. In case more than one track with Pixel hits is found, we look at the distance ΔR^{res} between the cluster barycenter and the track extrapolated to the second layer of the calorimeter, having rescaled the track momentum to the measured cluster energy before the extrapolation. If $|\Delta R_i^{\text{res}} - \Delta R_j^{\text{res}}| > 0.01$, where i, j are the tracks indices, then the track with the smaller ΔR^{res} is selected.

3. In case $|\Delta R_i^{\text{res}} - \Delta R_j^{\text{res}}| \leq 0.01$ we consider the distance ΔR between the cluster barycenter and the extrapolated track. If $|\Delta R_i - \Delta R_j| > 0.01$, the track with the smaller ΔR is chosen.

4. Finally, if both $|\Delta R_i^{\text{res}} - \Delta R_j^{\text{res}}| \leq 0.01$ and $|\Delta R_i - \Delta R_j| \leq 0.01$ there is no way to resolve geometrically the ambiguity between the two tracks. The track with more pixel hits (hits in the first layer are given double weight) is then chosen as primary track.

If at least one track is matched to a seed cluster, the latter is rebuilt sequentially in each longitudinal layer starting from the middle layer, following in the strips and pre-sampler, and finally in the back layer. The cluster position is adjusted in each layer to take into account the

distribution of the deposited energy. The cluster size is $N_\eta^{\text{cells}} \times N_\phi^{\text{cells}} = 3 \times 7$ in the barrel region, and $N_\eta^{\text{cells}} \times N_\phi^{\text{cells}} = 5 \times 5$ in the endcaps. These sizes have been optimised to account for the electron energy distribution in the barrel and endcap calorimeters, while minimising the pile-up and noise contributions.

The cluster energy is finally determined by applying correction factors computed by a MC-based calibration scheme, as described in Section 4.1.6.

The overall improvement achieved in 2012 reconstruction scheme thanks to the modified pattern recognition, the optimised electron track fitter, and the new track-cluster matching procedure, can be seen in Figures 4.2. The efficiency of electron reconstruction (including additional requests on track quality, namely that there are at least one hit in the Pixel detector and at least seven hits between Pixel and SCT) for 2011 and 2012 data-taking campaigns are compared. Figure 4.2(a) shows the efficiency as a function of pseudorapidity for electrons with transverse energy between 15 and 50 GeV. Over this E_T range the reconstruction efficiency in 2012 is found to vary from 99% at low η to 97% at high η. The absolute increase in reconstruction efficiency in 2012 as compared to 2011 - for both data and MC - is $\sim 2\%$ in the barrel region and up to 8% at high $|\eta|$ in the endcaps, where bremsstrahlung emissions are higher due to the larger amount of material in front of the calorimeter.

The same reconstruction efficiency viewed as a function of the transverse energy is shown in Figure 4.2(b) for electrons in the central part of the detector ($|\eta| < 2.47$). The efficiency in 2012 is found to be approximately 97% for electrons with $E_{\text{T}} = 15$ GeV, and reaches about 99% at $E_{\text{T}} = 50$ GeV. The average increase in efficiency in 2012 with respect to 2011 results is $\sim 2\%$ for high E_T electrons and up to $\sim 7\%$ for low E_T (< 20 GeV) electrons [69].

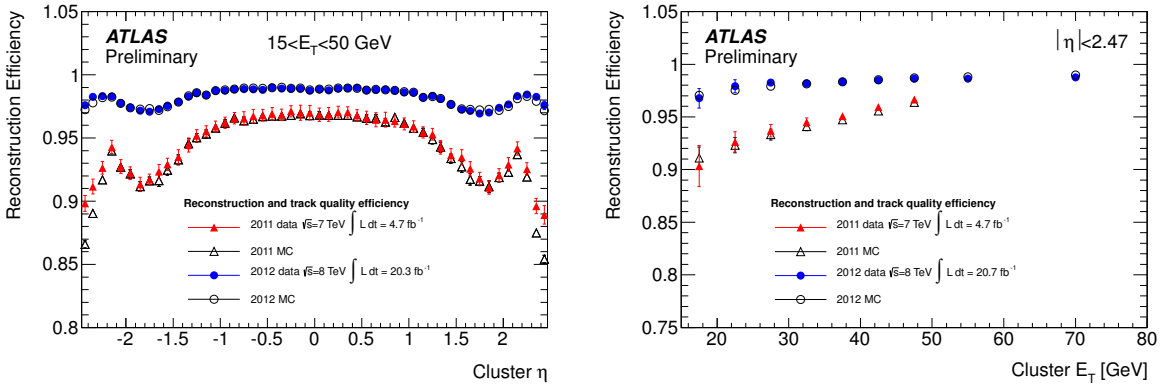

(a) **(b)**

Figure 4.2 Efficiency of electron reconstruction including criteria on track quality shown as a function of η for electrons with E_T between 15 and 50 GeV 4.2(a), and as a function of the E_T for electrons in the with $|\eta| < 2.47$ 4.2(b). Data (filled markers) and MC (open markers) are shown for both 2011 (triangles) and 2012 (circles) data samples.

4.1.5 The GSF algorithm validation

Prior to being used in the default reconstruction scheme for 2012 data-taking, the GSF algorithm was extensively studied on electrons produced in several physics processes, providing

a wide range of electron track momenta. Electrons from $J/\psi \to ee$, $Z \to ee$ and heavy-quark decays were considered, as well as electrons arising from $H \to ZZ^* \to 4\ell$ decays. The author particularly contributed to the validation studies performed on low ($\sim$ 15 GeV) transverse energy electrons from J/ψ events[1], where the greatest improvements are expected.

The goal of the study was to assess the quality of the estimated track parameters using either the standard or the GSF fitting procedure. This was done comparing, for both procedures, the reconstructed quantities of clean, truth-matched electrons, with the corresponding truth values provided by our MC generator.
Since radiative effects appear on the bending plane, the GSF algorithm is expected to improve only the precision on the track parameters belonging to that plane, leaving the track parameters on the longitudinal plane only marginally altered. Among the variables which have been considered for this validation study, only the most relevant three are presented here: the transverse impact parameter significance d_0/σ_{d_0}, the track direction angle ϕ, and the track inverse momentum multiplied by the charge q/p.

d_0/σ_{d_0}

The transverse impact parameter d_0 is the distance on the transverse plane between the track perigee and the primary interaction vertex[2] (i.e. the closest distance in the $x-y$ plane between the track and the beam line), while its significance is defined as the ratio of d_0 over the corresponding error from the track fit. These variables are extremely important for the $H \to ZZ^* \to 4\ell$ analysis, as they allow to separate the final state electrons resulting from the Z decays, whose true d_0 value is zero, from those originating from heavy-quark decays, which are expected to have large d_0 values.
Accounting for the radiative energy losses results in a better estimation of both the transverse impact parameter d_0 and in particular of its relative error. This improvement is clearly visible from Figure 4.3(a), which shows the d_0/σ_{d_0} distribution for both the GSF and standard fitting procedures, as well as the ratio between the two. Particularly important is also the evolution of the d_0/σ_{d_0} resolution with the electron pseudorapidity and transverse momentum, which we studied dividing the distributions in bins of η_{truth} and $p_{\text{T truth}}$ and extracting the widths for each bin. Figures 4.3(b) and 4.3(c) show the d_0/σ_{d_0} resolution as a function of $p_{\text{T truth}}$ and η_{truth} respectively. While the standard tracking results exhibit a clear dependence on η, reflecting the η dependence of the material distribution seen in Figure 4.1, this is no longer visible for GSF-refitted tracks. In addition, a substantial improvement in the resolution of the estimated d_0 significance is achieved over the entire transverse momentum spectrum.

ϕ

Similar conclusions can be drawn from Figure 4.4(a), which shows the difference between the reconstructed value of the track azimuthal angle ϕ, for both GSF and standard fitting

[1] Only results for prompt J/ψ, i.e. directly produced in the primary interaction, are presented. A non-prompt J/ψ sample was also initially studied, and showed very similar results.

[2] The primary vertex is required to have at least three associated tracks having $p_{\text{T}} > 400$ MeV. In case more than one vertex fulfils this criteria, the primary vertex is chosen to be the reconstructed vertex with the highest summed $|{p_{\text{T}}}^2|$ of associated tracks.

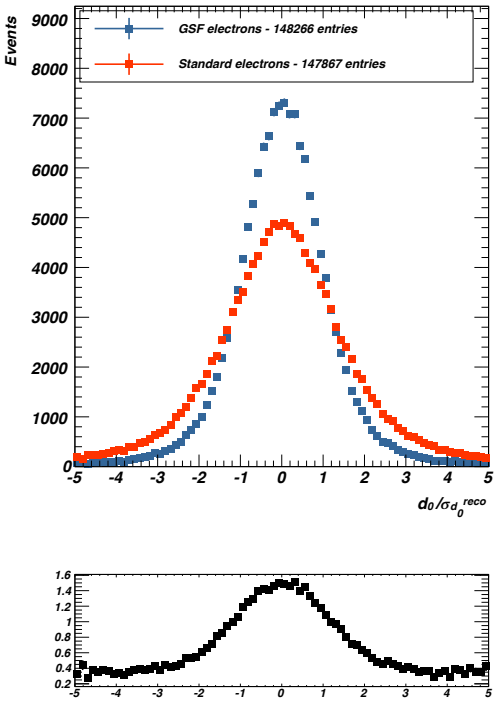

(a)

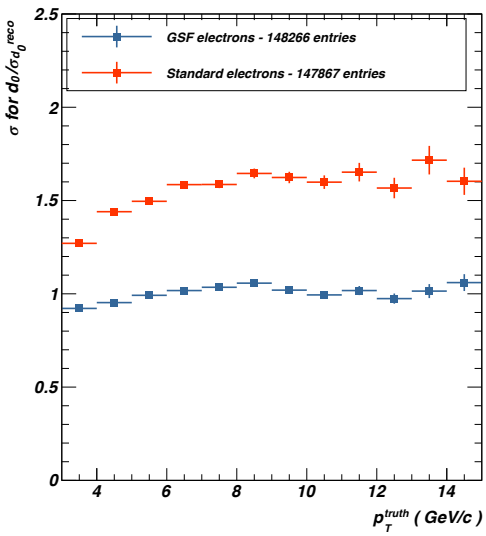

(b)

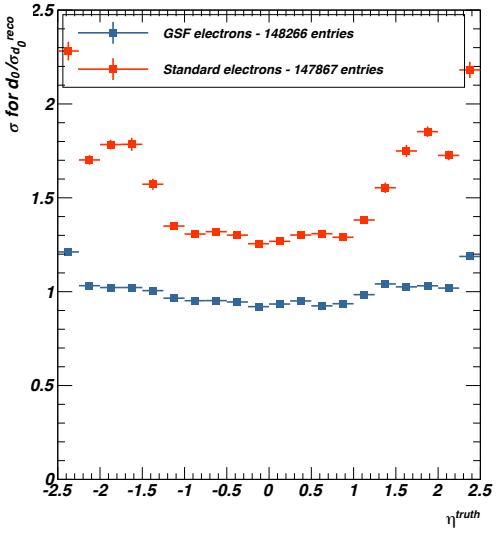

(c)

Figure 4.3 (a) The d_0/σ_{d_0} distribution for both GSF (blue) and standard (red) reconstructed electrons (top panel), and the ratio between the two (lower panel). The resolution of the d_0 significance is shown as a function of the true electron p_{T} (b) and η (c).

procedures, and the corresponding true value ϕ_{truth}. The resolution of the distribution, shown as a function of the electrons' true p_{T} and η in Figures 4.4(b) and 4.4(c), is clearly improved for the GSF refitted tracks, and turn out to be more uniform for different pseudorapidity ranges, indicating a reduced dependence on the amount of the ATLAS tracker material traversed by the electrons.

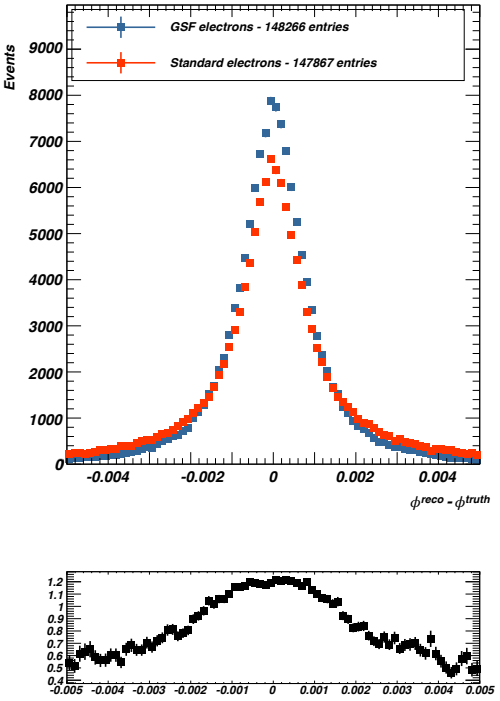

(a)

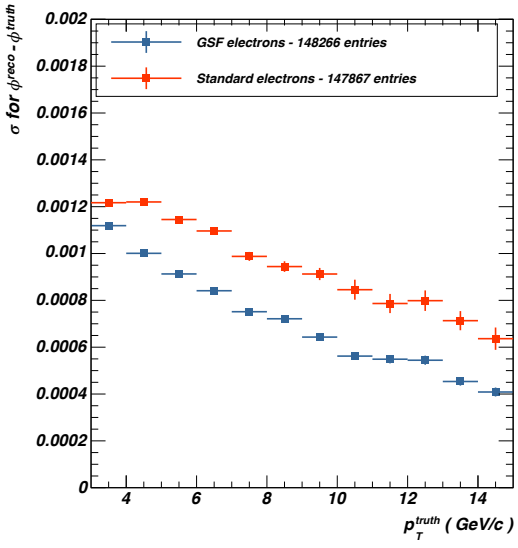

(b)

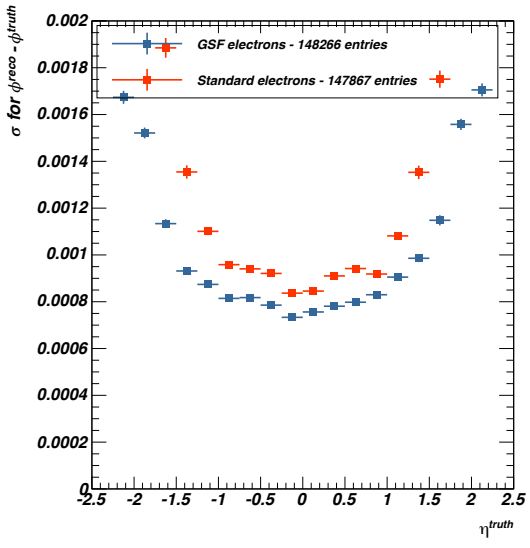

(c)

Figure 4.4 (a) The $\phi^{\text{reco}} - \phi^{\text{truth}}$ distribution for both GSF (blue) and standard (red) reconstructed electrons (top panel), and the ratio between the two (lower panel). The resolution of the d_0 significance is shown as a function of the true electron p_{T} (b) and η (c).

q/p

Finally, the relative bias of the track inverse momentum multiplied by the charge q/p was considered for this study. This is shown for both GSF and standard reconstructed electrons in

Figure 4.5(a). While a perfect recovery of the radiative energy losses is essentially unachievable, a shift of the estimated track inverse momentum towards their true values is clearly visible for GSF electrons. To study the dependence of the bias on the true electron transverse momentum and pseudorapidity, shown in Figures 4.5(b) and 4.5(c), we divided the distributions in bins of η_{truth} and $p_{\text{T truth}}$ and extracted the mean values for each bin. A significant overall improvement is achieved for GSF refitted values.

The improvements on the electron kinematic quantities also lead to an increased accuracy of the parent J/ψ four momentum. As a result, the peak position and the resolution of the J/ψ invariant mass distribution are expected to be more accurate. This is confirmed by the results shown in Figures 4.6 where the invariant mass is displayed, for both standard and GSF electrons, for different regions of the J/ψ rapidity. The shape of the curves is more symmetrical for the GSF refitted electrons, although a tail to the left of the peak remains visible, reflecting the inability of the GSF algorithm to account for bremsstrahlung losses when the photon emission occurs very close to the production vertex. The peak position is closer to the PDG value of the J/ψ mass [70], and the resolution is indeed narrower when using GSF refitting. For both reconstructions, the width of the distributions is strongly dependent on the rapidity, and it is much larger in the forward regions, where the electrons traverse more material and the coverage by the tracking elements is reduced. On the other hand, the peak position is clearly more stable with GSF electrons, and this is an important improvement over the standard reconstruction.

A correct estimation of the uncertainty associated with the mass, $\delta m_{e^+e^-}$, is also extremely important, allowing for example to perform unbinned maximum likelihood fits on the invariant mass (or, say, the vertex position of the J/ψ decay or the pseudo-proper time of the J/ψ candidate) using candidate-by-candidate uncertainties. To assess the validity of this uncertainty, we studied pull distributions in the same rapidity bins as in Figures 4.6. Ideally, we would expect the pulls $(m_{e^+e^-} - m_{J/\psi}^{PDG})\ \delta m_{e^+e^-}$ to be distributed as a Gaussian with $\sigma = 1$ and mean value at zero. The improvements given by the GSF algorithm are clearly visible in Figure 4.7: while the standard pulls are extremely poor, in the GSF case the peaks of the distributions are close to zero and the widths are of the correct order. Moreover, the shape of the GSF pulls is fairly stable in different rapidity regions, demonstrating that the uncertainties are being appropriately modulated to account for the poorer resolution in the forward regions. The GSF algorithm therefore succeeds in providing also a significant improvement in the estimation of the mass uncertainties, indicating a more general improvement on the covariance matrix of the four momentum measurements.

4.1.6 Electron energy calibration

Reconstructed electron and photon clusters are calibrated to correct for the energy lost in the material before entering the calorimeter, for the energy deposited in neighbouring cells, as well as for the energy leaked beyond the calorimeter. Further corrections are applied to account for the variation of the energy response as a function of the electron impact point on the calorimeter, and detector non-uniformities due, for example, to high-voltage problems. A new calibration scheme, sketched in Figure 4.8, was developed in 2012 to address the needs of

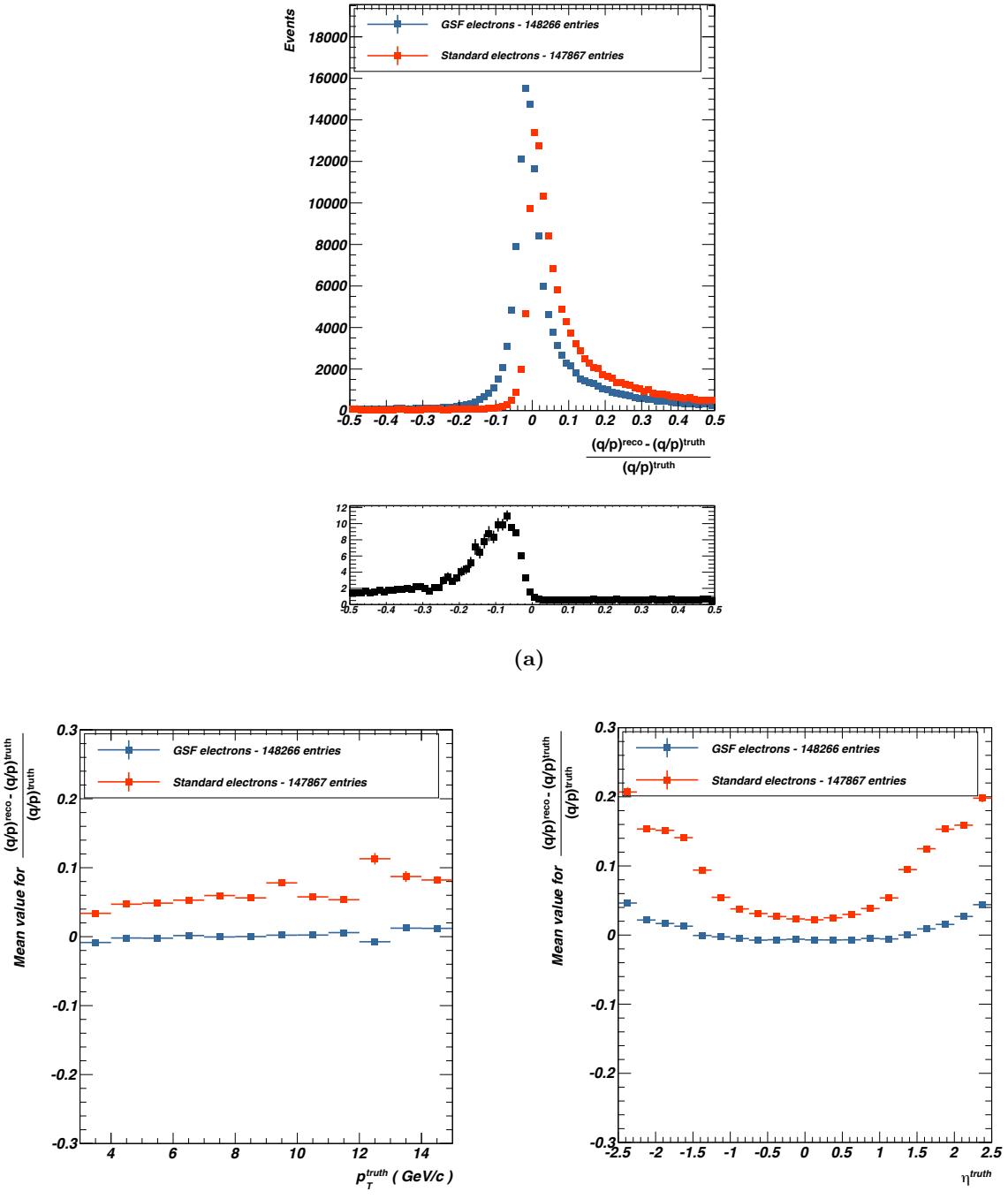

Figure 4.5 (a) The $(q/p^{\text{reco}} - q/p^{\text{truth}})$ / q/p^{truth} distribution for both GSF (blue) and standard (red) reconstructed electrons (top panel), and the ratio between the two (lower panel). The resolution of the d_0 significance is shown as a function of the true electron p_{T} (b) and η (c).

precision measurements involving electrons and photons.

The first step of this procedure is to extract corrections studying simulated electrons. This step strongly relies on a good description of the detector geometry and material distribution. An in-depth investigation of the amount of passive material upstream of the calorimeter, measured

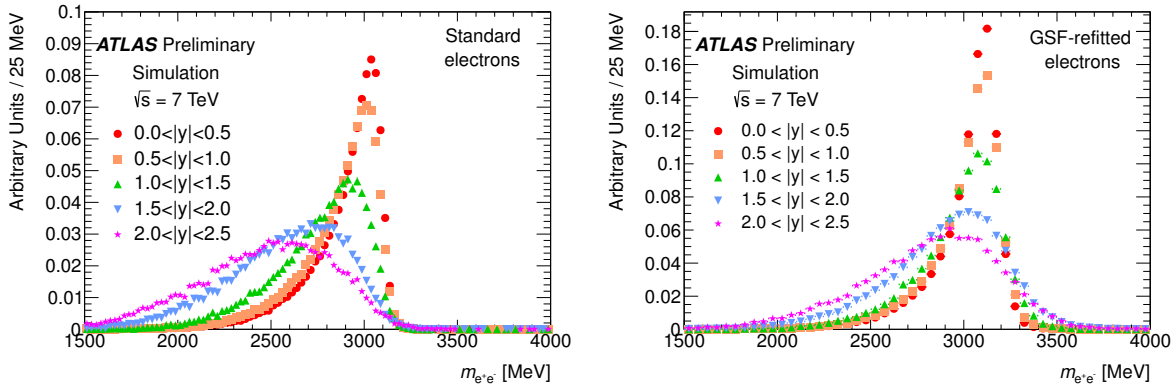

(a) (b)

Figure 4.6 The invariant mass distributions for different ranges of the J/ψ rapidity for the standard (a) and GSF (a) reconstruction of simulated electrons from J/ψ decays. While the widths of the distributions clearly increase in the more forward y regions, the GSF algorithm successfully stabilises the position of the peak [71].

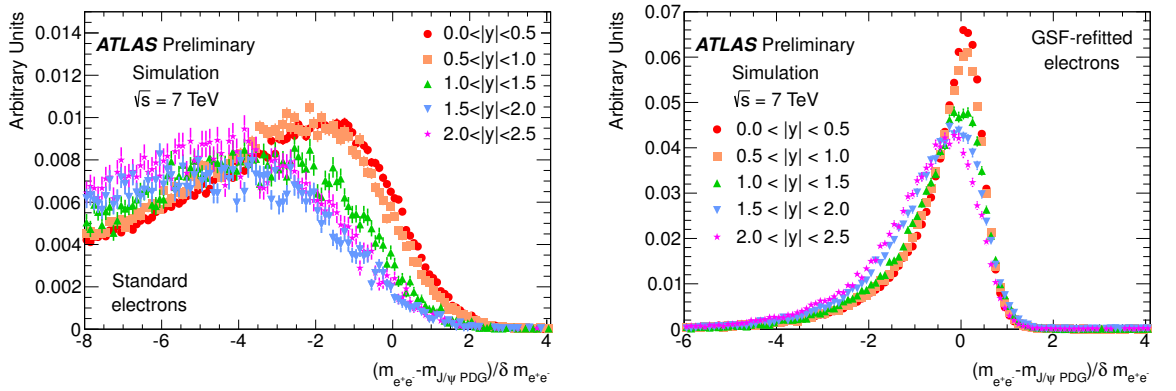

(c) (d)

Figure 4.7 The pull distribution of the di-electron invariant mass, for the standard (a) and GSF (b) reconstruction of simulated electrons from J/ψ decays as a function of the J/ψ rapidity. The results for the GSF are less dependent on rapidity, and far closer to the ideal distribution – a Gaussian function centred at zero with unity width in the core and a tail on the negative side – than those for the standard reconstruction [71].

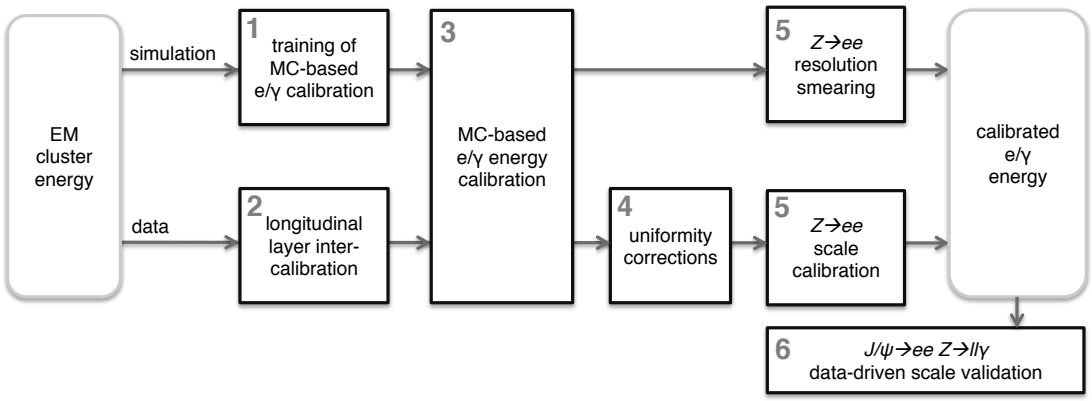

Figure 4.8 Schematic overview of the procedure used to calibrate the energy response of electrons and photons in ATLAS [67].

in data using the ratio of the first-layer energy to the second-layer energy in the longitudinally segmented EM calorimeter ($E_{1/2}$), led to an improved detector description in the GEANT4 simulation, which is currently being used.

The calibration constants are determined using a new multivariate algorithm (MVA)[3], which is optimised separately for electrons, converted and unconverted photons[4]. The quantities used as inputs to the MVA for the electron energy calibration are the total energy measured in the calorimeter, the ratio of the pre-sampler energy to the calorimeter energy, the shower depth, the cluster barycentre pseudorapidity in the ATLAS coordinate system, and the η and ϕ coordinates of the cluster barycentre in the calorimeter frame. The cluster pseudorapidity is included to account for the passive material variations in front of the calorimeter. The barycentre position in the calorimeter frame allows instead to correct for the increase of lateral energy leakage for particles hitting cells close to the edge, as well as for the variation of the response as a function of the particle impact point with respect to the calorimeter absorbers.

Before determining the overall energy scale, the energy scales of the different longitudinal layers have to be intercalibrated (step 2). In particular, the strip-to-middle layer energy scale is corrected, as well as the presampler one, while no dedicated intercalibration of the third EM longitudinal layer is carried out as its contribution is considered to be negligible.

The MC-based e/γ response calibration is then applied to the cluster energies reconstructed both from collision data and MC simulated samples (step 3).

A set of corrections are further implemented to account for measured time-dependent effects and for response details not included in the simulation in specific detector regions (step 4).

Any residual difference in response between data and simulation is corrected for in data using per-electron scale factors derived *in situ* from a large sample of collected $Z \to ee$ events. At the same time, the resolution in data is studied and found to be slightly worse than that in simulation. Appropriate corrections are extracted by adjusting the width of the reconstructed

[3]The new calibration scheme is implemented using the Toolkit for Multivariate Analysis (TMVA) framework [72]. The framework provides a ROOT-integrated machine learning environment for the processing and parallel evaluation of multivariate classification and regression techniques.

[4]We refer to converted photons if they underwent a conversion into an e^+e^- pair in the detector material before entering the calorimeter. Photons which do not undergo such a conversion are referred to as unconverted.

Z mass distribution in MC to match the one in data (step 5).
The calibrated electron energy is finally validated in data using electron candidates from $J/\psi \to ee$ events (step 6). The scale dependence with η and p_{T}, and its associated systematics, are visible from Figure 4.9 for two representative η bins. In all cases, the energy scales lie within the calibration systematic uncertainties.

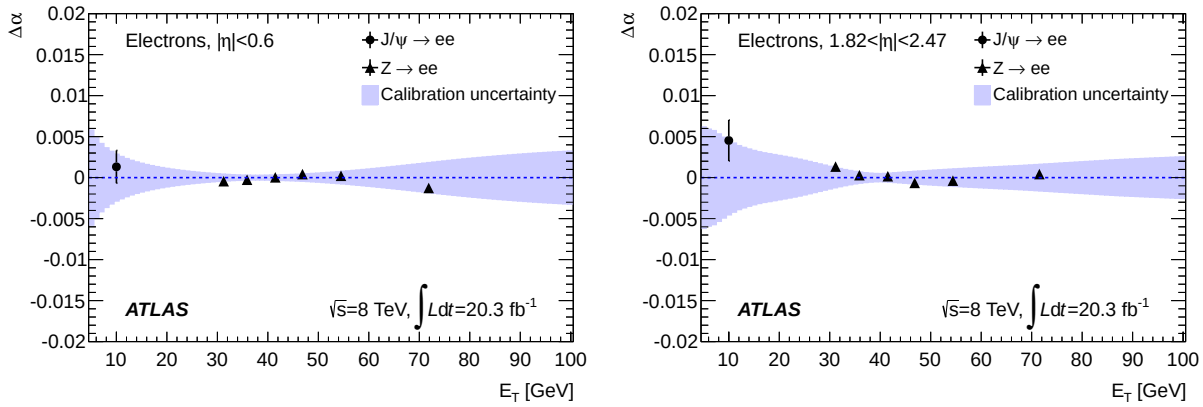

Figure 4.9 Energy scale factors $\Delta\alpha$ obtained after Z-based calibration from the $J/\psi \to ee$ and the E_{T}-dependent $Z \to ee$ analyses, as a function of E_{T} in two representative pseudorapidity bins. The band represents the calibration systematic uncertainty. The error bars on the data points represent the total uncertainty specific to the cross-checking analyses [67].

The resolution curve is shown for electrons in Figure 4.10, as a function of energy for $|\eta| = 0.2$ and $|\eta| = 1.7$. Thanks to the new MVA algorithm, the energy resolution is improved, with

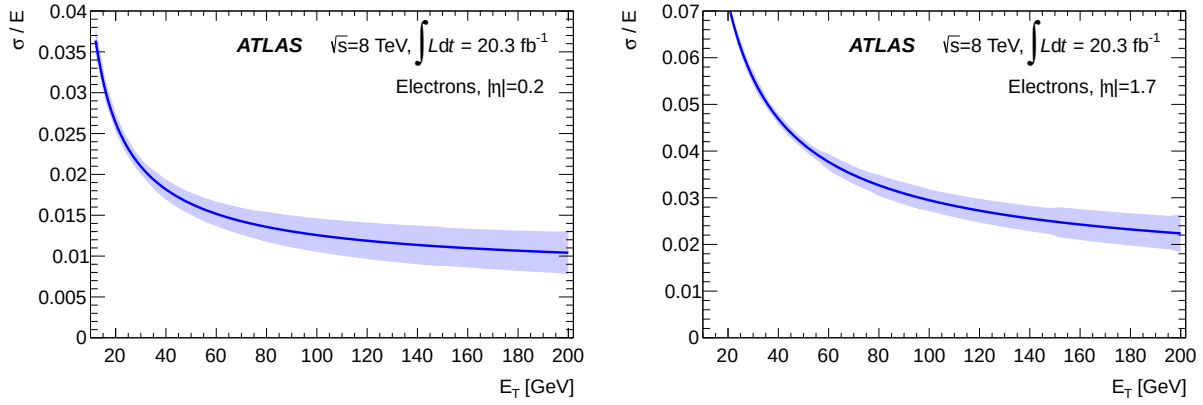

Figure 4.10 Electron energy resolution curve and its uncertainty as a function of E_{T} for $|\eta| = 0.2$ (left) and $|\eta| = 1.7$ (right) [67].

respect to the previous calibration approach, by roughly 10% (20%) for unconverted (converted) photons. For electrons the improvements are less significant, and are approximately a few percent in most of the acceptance region, rising up to 30% in the region with the largest amount of material in front of the calorimeter.

For electrons with $E_T \sim 40$ GeV, the achieved calibration is typically accurate to 0.05%

in most of the detector acceptance, going up to 0.2% in regions with large amounts of passive material, for $1.37 < |\eta| < 1.82$. At $E_T \sim 11$ GeV, the electron energy response uncertainty ranges between 0.4% and 1.1%.
The detector resolution is determined with a relative inaccuracy of less than 10% for electrons up to 60 GeV, rising up to 40% for transverse energies above 500 GeV [67].

4.1.7 Validation of the MVA-based calibration

The new MVA-based calibration procedure has been used for the final Run I ATLAS Higgs mass measurements, obtained from the combination of the $H \to ZZ^* \to 4\ell$ and the $H \to \gamma\gamma$ decay channels. An in depth investigation has been therefore carried out for both channels, to assess the validity of the new corrections. The outcome of the study for the $H \to ZZ^* \to 4\ell$ analysis, which was performed by the author of this thesis, is described in this section.

A signal MC sample with $m_H = 125$ GeV was used in the study, and the entire $H \to ZZ^* \to 4\ell$ selection, described in full detail in Chapter 6, was applied to the events. Higgs boson candidates are formed by selecting two same-flavor, opposite-sign lepton pairs in an event. For each selected quadruplet, the lepton pair with the mass closest to the Z boson mass is identified as the leading dilepton pair and its invariant mass is referred to as m_{12}. The so-called sub-leading pair is instead the one arising from the off-shell Z boson, and its invariant mass is referred to as m_{34}. The three possible cases with $Z \to ee$ decays – four electrons, or two electrons and two muons with the electrons being either the leading or the sub-leading pair – were treated separately.
A truth-matching procedure was applied on the selected electrons, allowing us to pair the electrons' calibrated energies with the corresponding true values. The impact of the new calibration procedure on single electrons was then studied comparing the energy resolutions obtained with the previous calibration (referred to as standard), and the new MVA-based one. Since we are interested in the relative difference, we considered the ratio between the calibrated energy E and its true value E_{truth}. The results, presented for the $4e$ channel in Figure 4.11(a), show a marginal improvement for both the mean and the RMS depending on the channel.
The effect of the calibration on the Higgs candidates can be seen from Figure 4.11(b), which shows the quadrilepton invariant mass for the $4e$ channel. The resolutions are almost the same in the two cases, and only a small improvement is observed in the central value, which is shifted by approximately 700 MeV toward the true value at 125 GeV for the MVA-based calibration.
The improvements due to the new calibration are expected to be more significant for low E_T electrons, and this is indeed confirmed by the results in Figures 4.12(a) and 4.12(b), where the ratios of m_{12} and m_{34} over their true values are plotted, respectively, again for the $4e$ channel. The differences between the standard and the MVA-based calibration are more visible in the m_{34} distribution, reflecting a bigger impact on the sub-leading electrons, which have lower momentum.

It is worth noting that, in the case of the $H \to \gamma\gamma$ decay channel, a much bigger improvement of 10% is observed on the expected mass resolution.

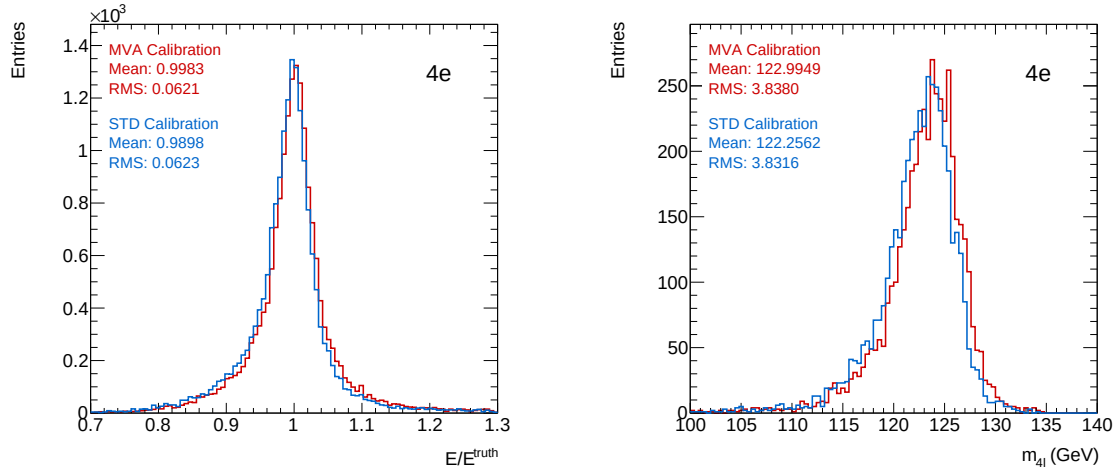

(a) **(b)**

Figure 4.11 (a) The ratio between the electron's calibrated energy E and its true value E_{truth}, and (b) the quadrilepton invariant mass in $H \to ZZ^* \to 4\ell$ events. In both plots, the $4e$ channel is considered. The results obtained using the old (standard) calibration and the new MVA-based one are compared.

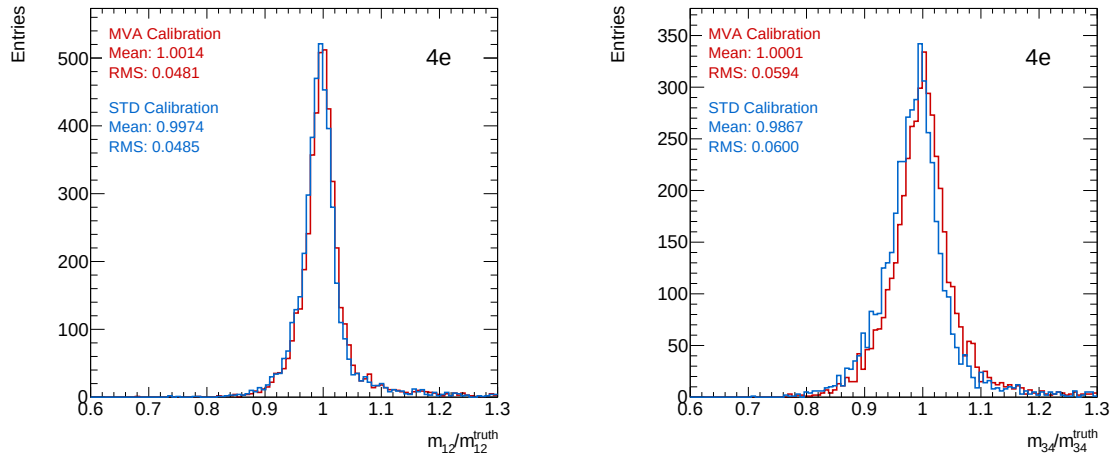

(a) **(b)**

Figure 4.12 The ratios of m_{12} (a) and m_{34} (b) over their true values in $H \to ZZ^* \to 4\ell$ events. In both plots, the $4e$ channel is considered. The results obtained using the old (standard) calibration and the new MVA-based one are compared.

4.2 Muon Reconstruction

Muons are efficiently reconstructed in ATLAS using mainly the precision measurements in the ID and in the MS and, to a lesser extent, from calorimetric deposits. Depending on the available information from the various sub-detectors, muons are reconstructed following four specific strategies leading to different muon classes. "Stand-alone" muons (SA) are reconstructed in the MS only, and their track parameters are estimated by extrapolating the track back to the primary interaction vertex. These kind of muons are used outside the ID coverage ($2.5 < |\eta| < 2.7$). The main type of muons in ATLAS are instead "combined" muons (CB), which are based on the combination of the tracks measured in the ID and in the MS, reconstructed separately. When an ID track matches at least one local track segment in the MDT or CSC chambers, then we can reconstruct "segment-tagged" muons (ST). This class of muons is particularly useful to recover muons falling in MS regions with smaller coverage, or traversing less chambers due to their low momentum. The last type of muons are the "calorimeter-tagged" muons (CaloTag), which are reconstructed matching an ID track with an energy deposit in the calorimeter compatible with a minimum ionizing particle. Although this type has the lowest purity, compared to the other three mentioned above, it allows to recover acceptance in the uninstrumented regions of the MS [73].

Several algorithm chains have been used in ATLAS during Run I to implement the reconstruction strategies described above. For the $H \to ZZ^* \to 4\ell$ analysis presented in this thesis, the so-called STACO [74] chain is used, which is based on the statistical combination of the track parameters of the MS and ID muon tracks using the corresponding covariance matrices. This provides an improved momentum resolution, and allows the rejection of muons from secondary interactions, as well as from π/K in-flight decays.

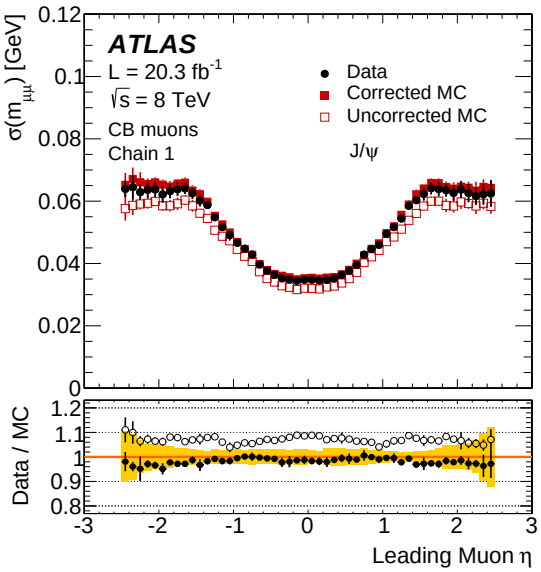

Figure 4.13 Invariant mass resolution for the $J/\psi \to \mu\mu$ resonance. The top panel shows the resolution for data, uncorrected and corrected simulation. In the bottom panel the ratio between data and simulation is shown [73].

Unlike the case of electrons and jets, no further correction is applied on data samples for muons. The ATLAS simulation, on the other hand, includes the best knowledge of the detector geometry, material distribution and modelling of muon interactions available at the time of event generation, and needs additional corrections in order to reproduce the muon momentum scale and resolution observed in data. The p_T of the muons is thus corrected accounting for energy losses, multiple scattering, and detector-related effects as inhomogeneities of the magnetic field and detector misalignments. The corrections are calculated and applied separately for the ID and the MS tracks of a muon, to allow a better understanding of the sources of the corrections. These two tracks are then recombined using a weighted average of the two momenta to obtain the corrected combined muon momentum.
A maximum likelihood fit based on MC templates is used to compare the simulation to the data for $J/\psi \to \mu\mu$ and $Z \to \mu\mu$ candidate events and extract the corrections.

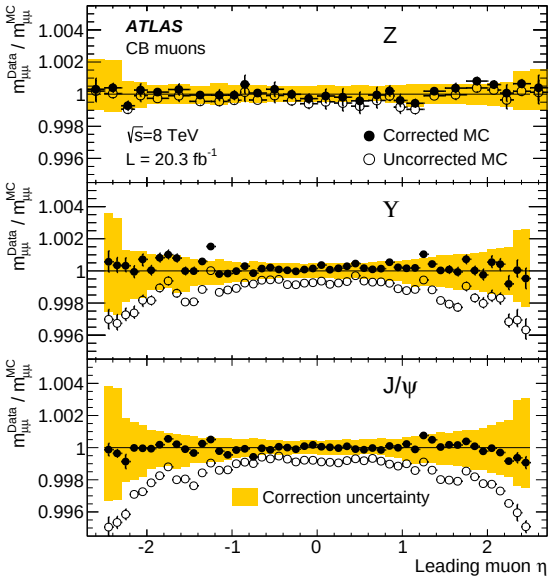

Figure 4.14 Ratio of the measured reconstructed mass between data and both corrected and uncorrected simulation, for three different resonances: Z (top), Υ (centre) and J/ψ (bottom). The yellow band represents the systematic errors associated with the derived corrections [73].

Finally, the J/ψ, Υ, and Z resonances are used to validate the procedure by measuring the muon momentum scale and resolution on both data and simulation with and without corrections. The muon momentum resolution is related to the invariant mass resolution, extracted using analytical fits to $m_{\mu\mu}$, and is found to be between 1.7% and 4% depending on the muon momentum and the detector region. The results obtained using $J/\psi \to \mu\mu$ events for data, uncorrected and corrected simulation are shown in Figure 4.13.
The momentum scale is validated by comparing the peak position of the three resonances. Figure 4.14 illustrates the ratio of the fitted mean mass between data and MC and shows how the scale is well modelled and is within the assigned systematic uncertainties ($\sim 0.05\%$ and $\sim 0.2\%$

in central and forward regions respectively) in the whole p_{T} range [73].

4.3 Jet Reconstruction

Quarks and gluons emerging from proton-proton collisions undergo a process referred to as hadronisation, and manifest themselves as groups of collimated particles in the final state. These particles are collected into physically measurable objects called jets. In order to extract information on the kinematics of the initial particles or partons that participated in the physics processes of interest, jets are fully reconstructed by applying a jet-finding algorithm to calorimeter signals, followed by a calibration step.

Jets are reconstructed in ATLAS starting from different physics objects as inputs to the jet finding algorithms. Topological clusters, or *topoclusters*, are the most frequently used, and consist of groups of calorimeter cells clustered into three-dimensional energy deposits designed to follow the shower development exploiting the longitudinal and transverse calorimeter segmentation. The topocluster finding algorithm is seeded by a cell whose signal-to-noise ratio is above a threshold of 4. Neighboring cells with a signal-to-noise ratio above 2 are collected iteratively, increasing the size of the cluster until no nearest neighbour is found exceeding this threshold. Finally, all surrounding cells are added to the topocluster. In case more than one energy deposition maxima is found in a given cluster, this is split into smaller clusters.

Jets can also be reconstructed from groups of geometrically delimited calorimeter cells, called *towers*. Towers are formed by collecting cells into bins of a regular $\Delta\eta \times \Delta\phi = 0.1 \times 0.1$ grid within the detector acceptance[5]. Depending on the overlap area between the tower bin and the cell, the cell signal or a fraction of it will be summed up to the tower.

Finally, in addition to the calorimeter signals, ATLAS also reconstructs jets using tracks, which provide independent detection of jet activity and measurements of jet properties [34, 75].

Two different inputs from the calorimeters are used for jet-finding: calorimeter towers and topological clusters, or topoclusters.
Towers are formed by collecting cells into bins of a regular $\Delta\eta \times \Delta\phi = 0.1 \times 0.1$ grid within the detector acceptance[6]. Depending on the overlap area between the tower bin and the cell, the cell signal or a fraction of it will be summed up to the tower.
Topoclusters are groups of calorimeter cells clustered into three-dimensional energy deposits that are designed to follow the shower development exploiting the longitudinal and transverse calorimeter segmentation. The topocluster finding algorithm is seeded by a cell whose signal-to-noise ratio is above a threshold of 4. Neighboring cells with a signal-to-noise ratio above 2 are collected iteratively, increasing the size of the cluster until no nearest neighbour is found exceeding this threshold. Finally, all surrounding cells are added to the topocluster. In case more than one energy deposition maxima is found in a given cluster, this is split into smaller clusters.
In addition to the calorimeter signals, ATLAS also reconstructs jets using tracks, which provide

[5] For cells larger than the tower grid element size, the energy contribution of the cell to the tower is weighted by the ratio of the tower bin area over the cell area in η, ϕ.

[6] For cells larger than the tower grid element size, the energy contribution of the cell to the tower is weighted by the ratio of the tower bin area over the cell area in η, ϕ.

independent detection of jet activity and measurements of jet properties [34, 75].

The default jet reconstruction algorithm employed in ATLAS data taking is the anti-k_t algorithm [76], and for the analyses described in this thesis topoclusters have been used as inputs. The anti-k_t algorithm belongs to the class of clustering algorithms, in which one introduces the following "distances" between inputs i and j and between input i and the beam (B):

$$d_{ij} = \min\left(\overline{k}_{t,i}^2, \overline{k}_{t,j}^2\right) \frac{\Delta_{ij}^2}{R^2} \ , \tag{4.2}$$

$$d_{iB} = \overline{k}_{t,i}^2 \ , \tag{4.3}$$

where Δ_{ij} is the radial distance between the two objects, $k_{t,i}$ is the transverse momentum of particle i, and R is the radius parameter of the algorithm. The clustering compares d_{ij} and d_{iB}, and if d_{ij} is found to be the smallest one then i and j are combined, otherwise object i is called a jet and not considered in the next iteration. The distances are recalculated and the procedure is repeated until no inputs are left.
The anti-k_t algorithm is unaffected by the presence of soft particles originating from infrared or collinear emissions; these properties are referred to as infrared and collinear safety.

In non-compensating calorimeters such as the ones in the ATLAS experiment, the response to hadrons is lower than the response to particles interacting electromagnetically. A calibration procedure is therefore needed in order to restore the correct hadronic energy scale starting from the electromagnetic scale (*jet energy scale*). In addition, further corrections need to be applied to take into account other detector-related effects, such as energy leakages outside of the calorimeter and energy losses in passive material.
Corrections as a function of the uncalibrated jet energy and pseudorapidity are applied to jets reconstructed at the electromagnetic scale according to a scheme called EM+JES [75]. Calibration constants are derived from the comparison of the reconstructed jet kinematics to that of the corresponding truth level jet in Monte-Carlo simulation [77, 78].

4.3.1 *b*-tagging

In general, the jet reconstruction algorithms cannot determine the type of parton that initiated a given jet. Jets originating from b-quarks, however, have unique features that allow us to distinguish them from jets generated by lighter quarks or gluons. Bottom-quark flavoured hadrons decay primarily via suppressed weak interactions, and have therefore relatively long lifetimes of ∼1.5 ps. This leads to typical decay lengths of the order of millimetres, thus large enough to be resolved by the Pixel detector. Various algorithms have been developed in ATLAS for the identification of these "b-jets". The common key objects for b-tagging are the calorimeter jets described above, the tracks reconstructed in the inner detector, and the selected primary vertex. The tracks are associated with the reconstructed jet based on their angular distance $\Delta R = \sqrt{\Delta\eta^2 + \Delta\phi^2}$, with specific requirements depending on the selected algorithm. The most discriminating variables resulting from these algorithms, which can be based on impact parameters (IP3D), secondary vertices (SV1), or even on the topology of weak b- and c-hadron

decays (JetFitter), are then combined in artificial neural networks. The most commonly used in ATLAS is the MV1 algorithm, which is based on the combination of IP3D, SV1 and JetFitter. It is trained with b-jets as signal and light-flavour jets (also called "light-jets") as background, and computes a *tag weight* for each jet. Typically fixed cuts, also called *working points*, are applied to the tag weight distribution in order to obtain specified b-jet efficiencies. The performance of the MV1 algorithm has been calibrated at working points corresponding to efficiencies of 60%, 70% and 80% [79].

Chapter 5

Electron Identification

The particles selected by the electron reconstruction algorithms are not only isolated signal electrons, but also background objects including hadrons as well as background electrons coming dominantly from photon conversions and heavy flavour hadron decays. In order to reject as much of these backgrounds as possible while keeping the efficiency for isolated signal electrons high, further selections can be applied on reconstructed electrons. This step is referred to as electron identification, and it is described in some detail in Section 5.1.

While efficiently identifying electrons is clearly very important, it is also crucial to precisely measure this efficiency. Indeed, the accuracy with which the MC-based detector simulation models the electron efficiency plays a fundamental role in cross section measurements and various searches for new physics. In order to achieve reliable physics results, the MC samples are corrected to reproduce the measured data identification efficiencies. A big effort is thus made in ATLAS to provide an accurate efficiency measurement over a broad E_{T} spectrum. A completely new method was developed by the author of this thesis to measure the identification efficiencies addressing the particular complications of low E_{T} electrons. An overview of all the existing and complementary analyses is presented, together with the final efficiency measurements, in Section 5.2, while Section 5.3 is dedicated to the detailed description of the new methodology.

5.1 Electron Identification

The selections used to identify electrons are combined into so-called *menus* with varying levels of background rejections and signal efficiencies. Several measured quantities provided both by the ID and by the calorimeter are used to separate isolated electrons from the background. These discriminating variables, a full list of which can be found in Table 5.1, are exploited either applying rectangular cuts in the cut-based menus, or as inputs to a multivariate algorithm in the likelihood-based (LH) menus. Both techniques are described in detail in Sections 5.1.1 and 5.1.2. Section 5.1.3 presents the isolation cuts that can be used in physics analyses to further discriminate signal electrons from the background [69, 80].

5.1.1 Cut-based identification

Due to its simplicity, the cut-based identification has been used in ATLAS to identify signal electron ever since the beginning of data taking, and were used throughout Run I. Three different

Table 5.1 Definition of electron discriminating variables [69].

Type	Description	Name
Hadronic leakage	Ratio of E_{T} in the first layer of the hadronic calorimeter to E_{T} of the EM cluster (used over the range $\lvert\eta\rvert < 0.8$ and $\lvert\eta\rvert > 1.37$)	R_{Had1}
	Ratio of E_{T} in the hadronic calorimeter to E_{T} of the EM cluster (used over the range $\lvert\eta\rvert > 0.8$ and $\lvert\eta\rvert < 1.37$)	R_{Had}
Third layer of EM calorimeter	Ratio of the energy in the third layer to the total energy	f_3
Middle layer of EM calorimeter	Lateral shower width, $\sqrt{(\Sigma E_i \eta_i^2)/(\Sigma E_i) - ((\Sigma E_i \eta_i)/(\Sigma E_i))^2}$, where E_i is the energy and η_i is the pseudorapidity of cell i and the sum is calculated within a window of 3×5 cells	$\mathrm{w}_{\eta 2}$
	Ratio of the energy in 3×3 cells over the energy in 3×7 cells centered at the electron cluster position	R_ϕ
	Ratio of the energy in 3×7 cells over the energy in 7×7 cells centered at the electron cluster position	R_η
Strip layer of EM calorimeter	Shower width, $\sqrt{(\Sigma E_i (i - i_{\mathrm{max}})^2)(\Sigma E_i)}$, where i runs over all strips in a window of $\Delta\eta \times \Delta\phi \approx 0.0625 \times 0.2$, corresponding typically to 20 strips in η, and i_{max} is the index of the highest-energy strip	$\mathrm{w}_{\mathrm{stot}}$
	Ratio of the energy difference between the largest and second largest energy deposits in the cluster over the sum of these energies	E_{Ratio}
	Ratio of the energy in the strip layer to the total energy	f_1
Track quality	Number of hits in the B-layer (discriminates against photon conversions)	n_{Blayer}
	Number of hits in the pixel detector	n_{Pixel}
	Number of total hits in the pixel and SCT detectors	n_{Silicon}
	Transverse impact parameter	d_0
	Significance of transverse impact parameter defined as the ratio of $d_0$and its uncertainty	d_0/σ_{d_0}
	Momentum lost by the track between the perigee and the last measurement point divided by original momentum	$\Delta p/p$
TRT	Total number of hits in the TRT	n_{TRT}
	Ratio of the number of high-threshold hits to the total number of hits in the TRT	F_{HT}
Track–cluster matching	$\Delta\eta$ between the cluster position in the strip layer and the extrapolated track	$\Delta\eta_1$
	$\Delta\phi$ between the cluster position in the middle layer and the extrapolated track	$\Delta\phi_2$
	Defined as $\Delta\phi_2$, but the track momentum is rescaled to the cluster energy before extrapolating the track to the middle layer of the calorimeter	$\Delta\phi_{Res}$
	Ratio of the cluster energy to the track momentum	E/p
Conversions	Veto electron candidates matched to reconstructed photon conversions	!isConv

menus, or operating points, with increasing background rejection were originally developed: *loose*, *medium* and *tight*[1]. All menus are based on sequential cuts applied on selected variables, but with increasing tightness more variables are added and cuts are tightened on the variables already used in the looser selections. As shown in Figure 5.1, the menus have been improved and adapted during 2011 and 2012 data-taking periods, to cope with the more challenging pile-up conditions (see Figure 2.4).

Furthermore, a new operating point called *multilepton* was developed in 2012 to address the

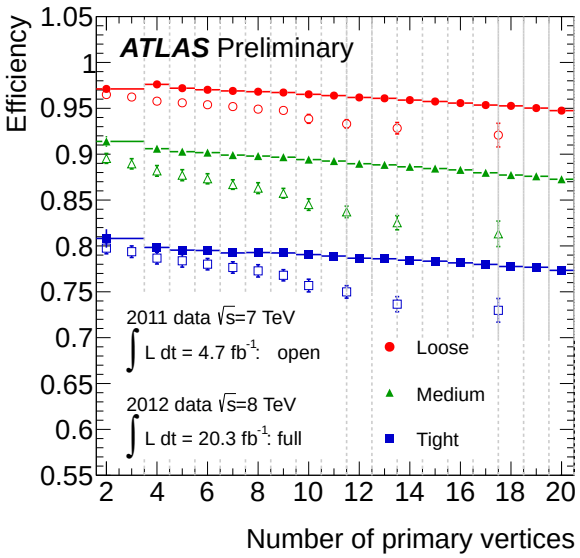

Figure 5.1 Identification efficiency in data for the various cut-based selections measured with 2011 and 2012 data as a function of the number of reconstructed primary vertices [69].

specific needs of low E_{T} electrons in the $H \to ZZ^* \to 4\ell$ analysis. The menu was designed to have similar efficiency as the *loose* operating point, but higher rejection power. As can be seen from Table 5.2, which summarises which variables are used for the different selections, the *multilepton* operating point also exploits the potential of variables measuring Bremsstrahlung effects.

The distributions of a few representative discriminating variables are shown in Figure 5.2 for the four different categories of electrons: isolated electrons, fake electrons from light jets, electrons from photon conversion and heavy quark decays. All menus, including the likelihood-based ones, are optimised separately in bins of $|\eta|$ and E_{T} to account for the different regions of the detector and different detector response depending on the electron energy. The binning used for the cut-based menus is detailed in Tables 5.3 and 5.4.

5.1.2 Likelihood-based identification

Multivariate analysis techniques offer great potential as they allow to simultaneously evaluate several properties when making a selection decision. They have thus been exploited also for electron identification, and, among the different possibilities, a likelihood method has been chosen for its simple construction.

[1]Notice that these criteria are sometimes also referred to as *loose++*, *medium++*and *tight++*.

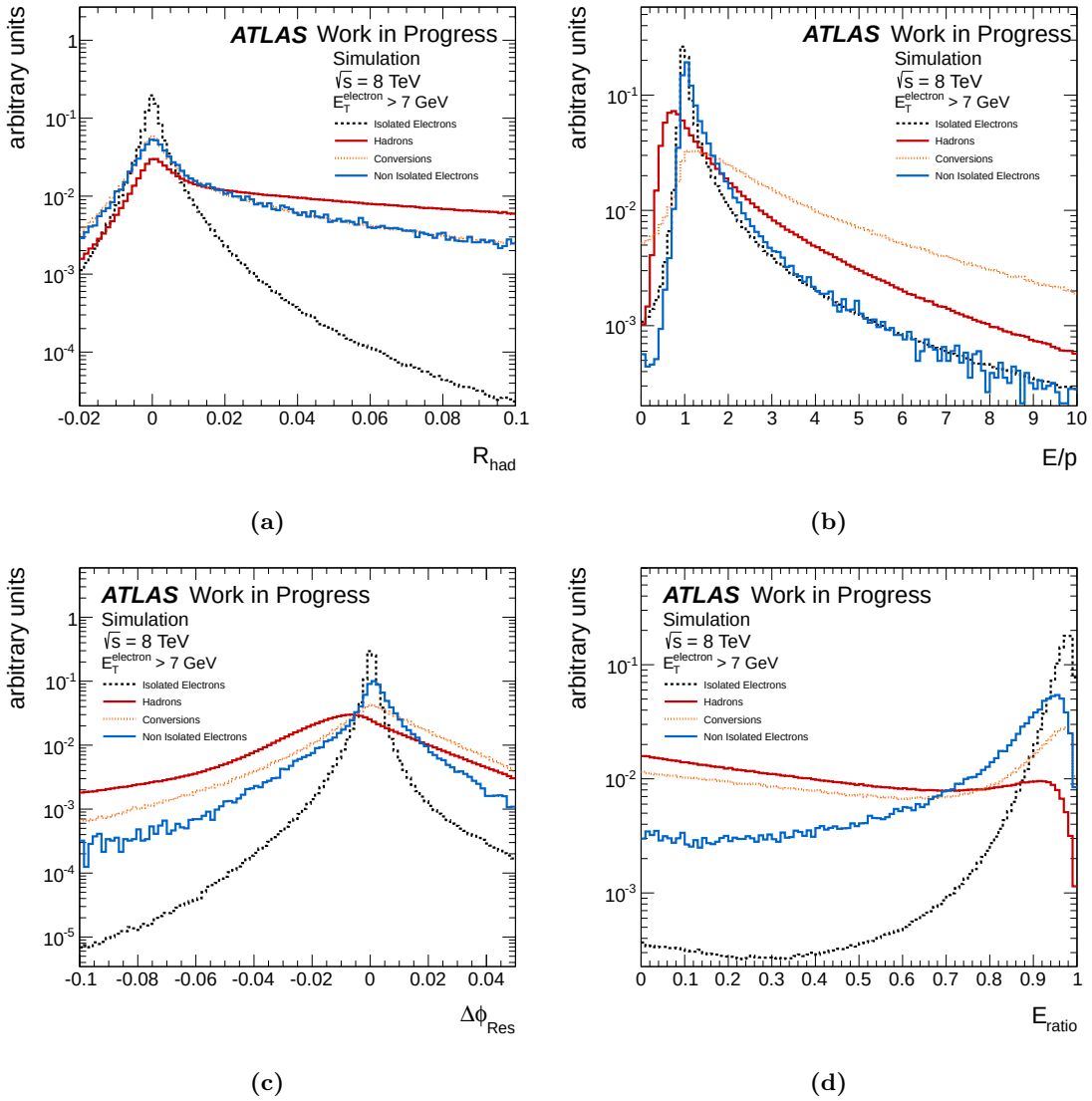

Figure 5.2 The R_{Had} (a), E/p (b), $\Delta\phi_{Res}$ (c) and E_{Ratio} (d) distributions for four different kind of electrons: isolated electrons (dashed black line), fake electrons from light jets (red line), electrons from photon conversion (dotted orange line) and non isolated electrons arising from the heavy quark decays (azure line) [82].

Table 5.2 Variables used in the 2011 and 2012 electron identification menus [81].

	Cut-based 2011			Cut-based 2012				Likelihood 2012		
Name	*loose*	*medium*	*tight*	*loose*	*medium*	*tight*	*multilepton*	LOOSE LH	MEDIUM LH	VERY TIGHT LH
$R_{\mathrm{Had}(1)}$	✓	✓	✓	✓	✓	✓	✓	✓	✓	✓
f_3					✓	✓	✓	✓	✓	✓
$w_{\eta 2}$	✓	✓	✓	✓	✓	✓	✓	✓	✓	✓
R_η	✓	✓	✓	✓	✓	✓	✓	✓	✓	✓
R_ϕ								✓	✓	✓
w_{stot}	✓	✓	✓	✓	✓	✓	✓	✓	✓	✓
E_{Ratio}	✓	✓	✓	✓	✓	✓	✓	✓	✓	✓
f_1								✓	✓	✓
n_{Blayer}		✓	✓		✓	✓	✓	✓	✓	✓
n_{Pixel}	✓	✓	✓	✓	✓	✓	✓	✓	✓	✓
n_{Si}	✓	✓	✓	✓	✓	✓	✓	✓	✓	✓
d_0		✓	✓		✓	✓			✓	✓
d_0/σ_{d_0}									✓	✓
$\Delta p/p$							✓	✓	✓	✓
n_{TRT}			✓		✓	✓	✓	✓	✓	✓
F_{HT}		✓	✓		✓	✓	✓	✓	✓	✓
$\Delta\eta_1$	✓	✓	✓	✓	✓	✓	✓	✓	✓	✓
$\Delta\phi_2$			✓			✓				
$\Delta\phi_{Res}$							✓	✓	✓	✓
E/p			✓			✓				
!isConv			✓			✓				✓

Bin boundaries in $\lvert\eta\rvert$										
Cut-based menus										
0	0.1	0.6	0.8	1.15	1.37	1.52	1.81	2.01	2.37	2.47
LH menus										
0		0.6	0.8	1.15	1.37	1.52	1.81	2.01	2.37	2.47

Table 5.3 Pseudorapidity binning used in electron identification. The binning listed for the LH menus is also used for the signal and background PDFs [69].

The electron likelihood discriminant is constructed by first creating a set of signal and background probability density functions (PDFs) from a list of electron identification variables with power for discriminating signal from background. Variables measuring Bremsstrahlung effects are included (as in the multilepton cut-based selection), as well as additional variables with large overlap between signal and background that prevents the use of explicit cuts. On the other hand, since having a robust four-vector measurement is extremely important, regardless of the likelihood discriminant output, the variables counting the hits on the track are not included in the PDFs, and are instead left as simple cuts.

Based on the PDFs, which are obtained from data, each electron is assigned an overall probability of being either signal or background. These signal and background probabilities are then

Bin boundaries in E_{T} [GeV]												
Cut-based menus												
5		10	15	20		30		40	50	60	70	80	∞
LH menus												
	7	10	15	20	(25)	30	(35)	40	45				∞

Table 5.4 E_{T} binning used in electron identification. Excluding the numbers in parentheses, the binning listed for the LH menus is also used for creating the signal and background PDFs [69].

combined into a discriminant $d_{\mathcal{L}}$:

$$d_{\mathcal{L}} = \frac{\mathcal{L}_S}{\mathcal{L}_S + \mathcal{L}_B}, \qquad \mathcal{L}_S(\mathbf{x}) = \prod_{i=1}^{n} P_{s,i}(x_i) \tag{5.1}$$

where $\mathbf{x}$ is the set of variables associated with an electron, and $P_{s,i}(x_i)$ is the value of the signal probability density function of the i^{th} variable value x_i (similarly, $P_{b,i}(x_i)$ is the background probability function). The choice of the cut value to be applied on the discriminant determines the signal efficiency/background rejection of the likelihood. An example likelihood discriminant output is shown in Figure 5.3 for both signal and background electrons.

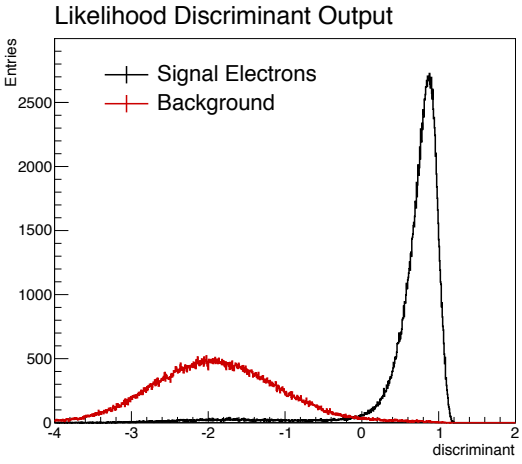

Figure 5.3 An example likelihood discriminant output shown for data signal (black line) and background (red line) electrons.

Three different operating points are available to physics analyses: LOOSE LH, MEDIUM LH and VERY TIGHT LH LH. In terms of electron efficiency these selections roughly match the cut-based counterparts *multilepton*, *medium* and *tight*, but they have an improved rejection of light flavor jets and photon conversions. Each operating point cuts on a different likelihood discriminant, built using a different set of variables. The LOOSE LH selection features variables most useful for discrimination against light-flavor jets, while additional variables are added in the MEDIUM LH and VERY TIGHT LH operating points to further reject the background from heavy-flavor decays and conversions.

Despite the use of different variables for the different operating points, the samples of electrons selected by a tighter LH are almost entirely contained in the samples selected using a looser one.

5.1.3 Electron isolation

Requiring the electrons to be isolated can also help to further discriminate against fake electrons from hadronic jets. Depending on the needs of each specific analysis, different isolation cuts can be applied, but two main classes of variables can be identified.

- Calorimeter-based isolation
  The variables providing the calorimetric isolation are referred to as $E_{\mathrm{T}}^{\mathrm{cone}\Delta R}$, where ΔR is the size of the cone considered around the electron. The isolation is computed by adding up all the transverse energy deposits in the cells contained in the cone, excluding the contribution of the electron itself, contained in the central 5×7 cells. The possible energy leakage from the electron and the effects due to the pile-up are corrected for. The typical cone size used by the physics analyses varies between 0.2 and 0.4.

- Track-based isolation
  The variables providing the track isolation are instead referred to as ${p_{\mathrm{T}}}^{\mathrm{cone}\Delta R}$. In this case the isolation is estimated as the sum of the transverse momenta of all the tracks falling inside the cone, excluding the contribution from the electron itself. To be considered in the calculation, the tracks are required to have $p_{\mathrm{T}} > 1$ GeV, originate from the primary vertex, and have at least four hits between the Pixel and SCT detectors.

5.2 Identification Efficiency Measurements

In order to measure the identification efficiency in different kinematic regions, while at the same time providing overlapping results, the measurements are performed exploiting different resonances - the W, the Z and the J/ψ - as well as complementary methodologies applied on a given resonance. The same technique, referred to as the tag-and-probe method, was however used in each analysis.

As both the data-taking conditions and the identification menus themselves have changed between 2011 and 2012, the efficiency measurements were performed separately for the two data samples. In particular, different methods were exploited in 2011 and 2012 analyses. The $W \rightarrow e\nu$ tag-and-probe method was used in 2011 but then dropped in 2012 because of a high background contamination due to 2012 run conditions. Furthermore, the existing methods making use of $Z \rightarrow ee$ and $J/\psi \rightarrow ee$ tag-and-probe were adapted and improved in 2012, to account for the different data-taking conditions, i.e. background contamination, pile-up effects, and higher available statistics. Finally, a new way to exploit the $Z \rightarrow ee$ tag-and-probe in the lower E_{T} region ($10 < E_{\mathrm{T}} < 15$ GeV) was introduced in 2012, and therefore only included in 2012 final results.

Regarding the identification menus, in 2011 only the cut-based menus *loose*, *medium* and *tight* were used in ATLAS, and the efficiency calculations were thus extracted for these three

selections. In 2012, with the introduction of the new cut-based menu and the LH criteria, the considered menus have increased significantly. Specifically, the following menus were considered: cut-based *loose*, *medium*, *tight*, *multilepton*, and LOOSE LH, MEDIUM LH and VERY TIGHT LH LH. Notice that the original three cut-based menus are not the same for 2011 and 2012, since they were improved during 2012, as described in Section 5.1.1.

An introduction to the tag-and-probe method and a description of general definitions are given in Section 5.2.1, followed by an overview of the $W \to e\nu$, $Z \to ee$ and $J/\psi \to ee$ tag-and-probe methods in Sections 5.2.2, 5.2.3 and 5.2.4, respectively. A complete description of the $J/\psi \to ee$ tag-and-probe method developed by the author is instead given in Section 5.3. Finally, Section 5.2.5 shows the final results obtained in 2011 and in 2012 combining the measurements from the various methods.

5.2.1 The tag-and-probe technique

Measuring the efficiency of a particular selection requires a clean and unbiased sample of signal electrons. A widely used technique to provide such sample is the so-called tag-and-probe method. The idea is to select events with well-known resonances by applying stringent requirements on only one of the particles produced in the decay (called "tag"). The efficiency of a selection can then be determined by applying it directly to the second particle arising from the decay ("probe"), after accounting for residual background contamination. In order not to bias the selected probe sample, each valid combination of electron pairs in the event is considered, i.e. an electron can be considered as a tag in one pair and as a probe in another.

The efficiency to detect an electron in the ATLAS detector may be factorised as a product of different efficiency terms:

$$\varepsilon_{\text{tot}} = \varepsilon_{\text{reconstruction}} \times \varepsilon_{\text{identification}} \times \varepsilon_{\text{trigger}} \times \varepsilon_{\text{additional}} \,. \tag{5.2}$$

The efficiency components are defined and measured in a specific order to preserve consistency. The reconstruction efficiency is measured with respect to the clusters reconstructed in the electromagnetic calorimeter[2]. The term we are particularly interested in, the identification efficiency, is instead determined with respect to reconstructed electron candidates with associated tracks that have at least 1 hit in the Pixel detector and at least 7 hits between Pixel and SCT (these requirements are referred to as "track quality", and are included in the reconstruction efficiency measurement). Trigger efficiencies are then calculated for reconstructed electrons passing a given identification criterion. Finally, the efficiency of any additional selection criteria applied in the analyses, for example on the isolation of electrons, is determined for each analysis separately.

The efficiencies are estimated as the ratio between the number of electrons passing the selection (numerator), over the total number of electrons (denominator). The number of electrons and the level of background are thus estimated separately before applying any selection, at the

[2]Cluster reconstruction is expected to be very efficient for true electrons. In MC simulations, the efficiency is about 95% for electrons with a transverse energy $E_{\text{T}} = 7$ GeV and 99.9% at $E_{\text{T}} = 45$ GeV for $|\eta| < 1.37$.

so-called "probe-level", and after applying the criteria we want to test.

In the identification efficiency measurement, some general requirements on the event properties are applied to reject background events. Only events passing data-quality criteria, concerning in particular the inner detector and the calorimeters, are considered. Moreover, at least one reconstructed primary vertex with a minimum of three associated tracks is required in each event. The electrons are required to be in the central region of the ATLAS detector, i.e. $|\eta| < 2.47$. Finally, the tag-and-probe pairs must also pass requirements on their reconstructed invariant mass, which of course depend on the selected resonance. The remaining background events are estimated using either background template shapes or combined fits of background and signal analytical models to the data. The specific procedure, as well as the variable used to discriminate the signal from the background are different for the various methods, and will be further described below.

The same cuts applied on the data samples are used to select simulated events and compute the associated MC efficiencies. No background subtraction needs to be applied to simulated samples, however the reconstructed electron tracks are required to be matched to a true primary electron within a cone of $\Delta R = 0.2$ (a fraction of the hits are required to be in common between the two tracks). In the matching procedure electrons coming from converted photons that are radiated off an electron originating from the resonance decay are also accepted.

Data-to-MC correction factors

As already stated, in order to provide reliable physics results, we must make sure that the simulation reproduces as closely as possible the efficiencies actually measured in data. Due to small mis-modelling of track properties or shower shapes in the calorimeter, this is never exactly the case and MC samples need to be corrected. Correction factors are defined as the ratio between the efficiency measured in data and the one extracted from the simulation, and are usually referred to as *scale factors*. The electron efficiencies are computed in all methods as a function of the electron energy and pseudorapidity, thus also the scale factor measurements are performed in two-dimensional bins in (E_{T}, η). Any residual effects coming from kinematical differences in the physics processes, for example between the different resonances in our measurements, or between these and the physics of interest in given analyses, are expected to mostly cancel out in the data-to-MC efficiency ratio. For this reason, the combination between the results provided by the different methods is made using the scale factors, rather than the efficiencies themselves.

Determination of central values and uncertainties

For the evaluation of the final results and of the related uncertainties, different variations of each measurement are carried out. Although every method has its own specific set of variations, the common idea behind this approach is to estimate the impact of the analysis choices and of potential imperfections in the background modelling. So, for example, the selection of the tag electron or the background estimation methods are varied in all methods. Obviously, the same variations are applied in data and in MC, and the scale factors are computed separately for each variation first. The final results of a given measurement are then taken to be the average

values of the results from all variations.

The related systematic uncertainty is estimated as the root mean square (RMS) of all variations, with the intention of modelling a 68% confidence interval. If this is not the case, i.e the RMS covers less than 68% of all variations, the uncertainties are appropriately enlarged.

The statistical uncertainty is instead evaluated as the average of the statistical uncertainties over all considered variations. The estimation of the statistical uncertainty on a single variation is calculated following the prescriptions given in [83].

5.2.2 Tag-and-probe with $W \to e\nu$ events

In the case of W tag-and-probe the missing transverse energy corresponding to the neutrino is used to tag the presence of a $W \to e\nu$ decay, and therefore of the produced isolated electron. The use of the missing E_{T} makes this method particularly challenging, due mainly to the high background contamination and the inability to properly reconstruct the resonance mass. Nonetheless, this channel contributes significantly to the overall efficiency determination in 2011 due to its high statistical power. The $W \to e\nu$ tag-and-probe has been used to measure efficiencies for electrons with $E_{\mathrm{T}} > 15$ GeV.

$W \to e\nu$ events are collected with specialised triggers that were run unprescaled in 2011, thanks to the use of the missing transverse momentum $E_{\mathrm{T}}^{\mathrm{miss}}$ significance, x_s[3], which reduces significantly the background.

The isolation distribution of the probes is used to discriminate the signal against the background electrons, which account for 2% to 40% of all the selected events, depending on the probe η and p_{T} . The selected variable is the calorimetric isolation defined in Section 5.1.3, corrected for pile-up and underlying contributions, and normalised to the electron transverse energy: ${E_{\mathrm{T}}}^{\mathrm{cone}\Delta\mathrm{R}}/E_{\mathrm{T}}$, with ΔR being either 0.3 or 0.4[4]. A background template is constructed from the selected probe sample by reversing two of the electron identification criteria, namely the total shower width $\mathrm{w_{stot}}$ and the ratio of high-threshold hits to all TRT hits. The template is then normalised to the probe isolation distribution above a certain threshold, which is assumed to be dominated by background events. Figure 5.4 shows a typical ${E_{\mathrm{T}}}^{\mathrm{cone\ 0.3}}/E_{\mathrm{T}}$ distribution, with the threshold set at 0.4, for the selected probe sample and for the normalised template [81].

5.2.3 Tag-and-probe with $Z \to ee$ events

Tag-and-probe using $Z \to ee$ decays provides a clean sample of isolated electrons, and was used in both 2011 and 2012 to measure efficiencies down to $E_{\mathrm{T}} = 15$ GeV. Below this threshold the background contribution becomes too important, and the simple $Z \to ee$ topology can no longer be used. On the other hand, if we only select the probe electrons arising from the $Z \to ee\gamma$ decay, where one of the two electrons has lost its energy due to final state radiation (FSR), we will have a significantly reduced background contamination at low E_{T}. This additional method was introduced in 2012 to measure efficiencies in the region $10 < E_{\mathrm{T}} < 15$ GeV.

[3] $x_s = E_{\mathrm{T}}^{\mathrm{miss}}/(\alpha(\sqrt{\sum E_{\mathrm{T}} - c}))$, where the sum runs over all energy deposits and the constants α and c are optimised such that the denominator approximates the $E_{\mathrm{T}}^{\mathrm{miss}}$ resolution.

[4] Above $E_{\mathrm{T}} = 45$ GeV the probe electrons tend to be very isolated. The isolation variables are thus normalised to a fix value rather than to the electron transverse energy, in order to maintain sufficient events in the control regions.

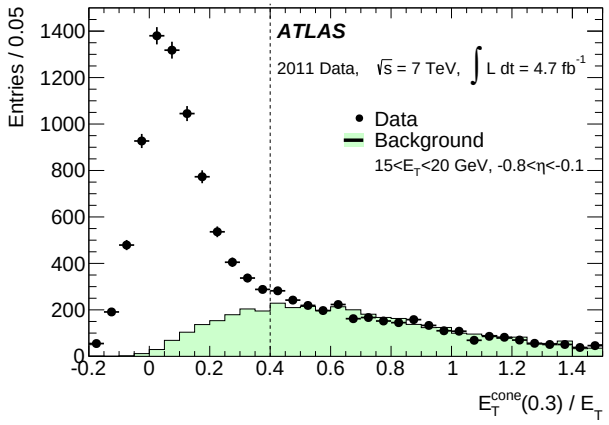

Figure 5.4 Illustration of the background subtraction technique used in the $W \to e\nu$ tag-and-probe in the 15 GeV $< E_{\mathrm{T}} <$ 20 GeV and $-0.8 < \eta < -0.1$ bin. An example of a typical probe ${E_{\mathrm{T}}}^{\mathrm{cone}(0.3)}/E_{\mathrm{T}}$ distribution for a representative (E_{T}, η) bin is shown. The dashed line indicates the threshold chosen to identify the background-only region. The normalised background template is shown in green [81].

$Z \to ee$ events are collected using single-electron triggers, requiring the candidates to pass a minimum E_{T} threshold and strict quality criteria.

Two different variables are used to discriminate signal electrons from the background: the invariant mass of the tag-and-probe pair, as used in the so-called Z_{mass} method, and the isolation distribution, as done in the so-called Z_{iso} method. In the case of $Z \to ee\gamma$ events, the invariant mass of the three objects - the tag electron and photon, and the probe - is considered.

Z_{mass} method

As for the W tag-and-probe, a template fit is used to estimate the background contamination. The templates are built requiring the probes to fail identification and isolation cuts. During 2012 a detailed study was carried out to assess the shape biases of possible background templates, and finally the least biased were chosen. The residual signal contamination in the background templates is accounted for using events from MC simulation.

The normalisation of the templates is determined using a method referred to as side-band method, in which the regions on the sides of the resonance invariant mass peak, where the signal contribution is highly reduced, are exploited.
For what regards the denominator (probe sample with no identification criteria applied yet), the region is normalised to the tag and probe (and the photon in the case of $Z \to ee\gamma$) invariant mass distribution above the Z peak. When we apply an identification selection on the sample, the signal contamination becomes non negligible also in the tails, and a slightly different approach needs to be taken for the numerator. The templates used, as well as the region used for the normalisation, are the same as for the denominator, but the same-sign sample is considered.
Figure 5.5 show the $Z \to ee$ tag-and-probe invariant mass distribution for both the denominator and after applying the *tight* selection for an example bin. Figure 5.6 show the same for the $Z \to ee\gamma$ distribution.

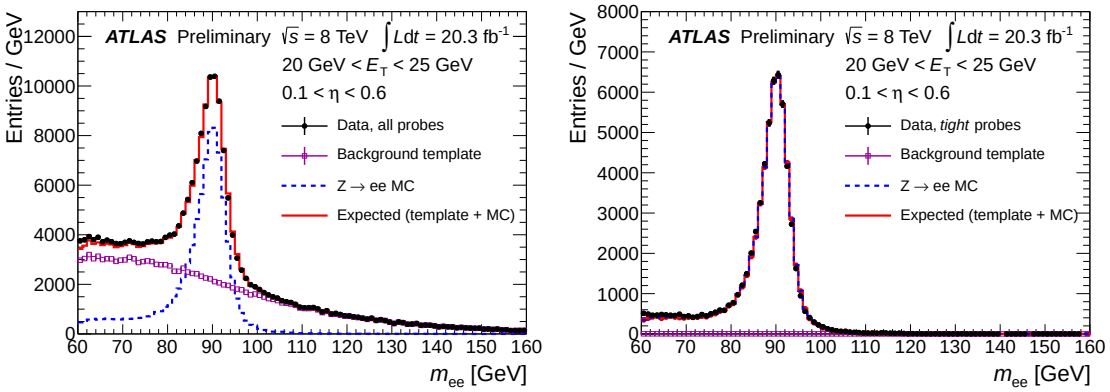

(a) **(b)**

Figure 5.5 Illustration of the background subtraction technique used in the Z_{mass} method in the 20 GeV $< E_{\text{T}} <$ 25 GeV, $0.1 < \eta < 0.6$ bin. The invariant mass distribution is shown at probe level (reconstruction + track quality) (a), and after applying the *tight* selection (b). Black dots represent the selected probes, while the normalised background template, the MC $Z \rightarrow ee$ expectation and their sum are shown by the magenta, dashed blu and red lines, respectively [69].

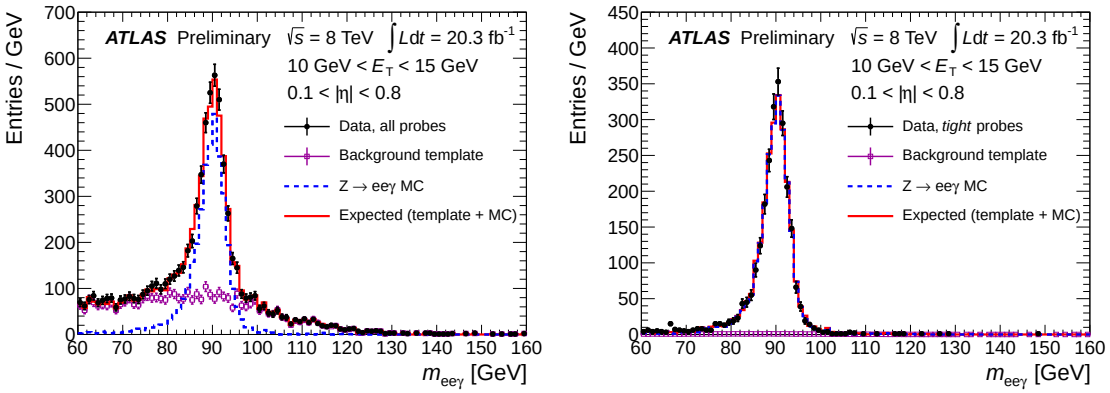

(a) **(b)**

Figure 5.6 Illustration of the background subtraction technique used in the $Z \rightarrow ee\gamma$ method in the 10 GeV ¡ E_{T} ¡ 15 GeV, 0.1 ¡ $|\eta|$ ¡ 0.8 bin. The invariant mass distribution is shown at probe level (reconstruction+track quality) 5.6(a), and after applying the *tight* selection 5.6(b). Black dots represent the selected probes, while the normalised background template, the MC $Z \rightarrow ee\gamma$ expectation and their sum are shown by the magenta, dashed blu and red lines, respectively [69].

Z_{iso} method

The Z_{iso} method uses the isolation distribution of the probe electrons to discriminate against background events. The variable used in 2011 analysis is the same seen for the $W \to e\nu$ tag-and-probe, while in 2012 the absolute ${E_{\text{T}}}^{\text{cone0.3}}$ was used. Once again the background template is built requiring the probes to fail some of the identification cuts. In 2012 the templates were chosen following the results of a study performed to estimate the bias due to the cut inversion and contamination from signal electrons. As done for the W tag-and-probe, the templates are then normalised to the background-dominated upper end of the probe isolation distribution.

Each of the described Z tag-and-probe methods has its own set of variations to assess the systematic uncertainties on the extracted measurements. However, in the E_{T} range where results from both the Z_{mass} and the Z_{iso} methods are available, $E_{\text{T}} > 15$ GeV, the two are treated together as variations of the same measurement. In other words, the two methods are regarded as variations of the background subtraction technique, which indeed follows in the two cases completely different approaches. In the bin $10 < E_{\text{T}} < 15$ GeV, only the $Z \to ee\gamma$ method (among the Z tag-and-probe methods) is available.

5.2.4 Tag-and-probe with $J/\psi \to ee$ events

$J/\psi \to ee$ events are used to measure the electron identification efficiency in the low transverse energy region, from 7 to 20 GeV. At such low energies, the probe sample suffers from a significant background fraction, which is estimated using the reconstructed di-electron invariant mass of the selected tag-and-probe pairs. Furthermore, the J/ψ sample is composed of two contributions. In *prompt production*, the J/ψ meson is produced directly in the proton-proton collision via strong interaction or from the decays of directly produced heavier charmonium states. In *non-prompt production*, the J/ψ mesons are instead coming from b-hadron decays. The electrons arising from the decay of prompt J/ψ particles are expected to be isolated, and therefore to have efficiencies close to those of isolated electrons from other physics processes of interest in the same transverse energy range, such as $H \to ZZ \to 4e$. On the other hand, electrons produced in the busy environment of b-hadron decays are expected to be less isolated and, consequently, have lower efficiencies. The challenge of the $J/\psi \to ee$ tag-and-probe is thus not only to discriminate the J/ψ signal electrons from the background, but also to isolate those electrons coming from promptly produced J/ψ.

Experimentally, the two production modes can be distinguished by measuring the displacement of the $J/\psi \to ee$ vertex with respect to the primary vertex. Due to the long lifetime of b-hadrons, electron pairs from non-prompt J/ψ production will have a measurably displaced vertex, while prompt J/ψ decays will occur at the primary vertex. The fraction of prompt J/ψ particles can thus be inferred from the distribution of the measured distance between the primary vertex and the J/ψ decay vertex. In particular, the variable used to discriminate prompt

and non-prompt production, called *pseudo-proper time*[5] [84], is defined as:

$$\tau = \frac{L_{xy} \cdot m_{\mathrm{PDG}}^{J/\psi}}{{p_{\mathrm{T}}}^{J/\psi}} , \tag{5.3}$$

where L_{xy} measures the displacement of the J/ψ vertex with respect to the primary vertex in the transverse plane[6], while $m_{\mathrm{PDG}}^{J/\psi}$ and ${p_{\mathrm{T}}}^{J/\psi}$ are the mass [70] and the reconstructed transverse momentum of the J/ψ particle, respectively. The pseudo-proper time distribution for prompt and non-prompt signal MC samples is shown in Figure 5.7.

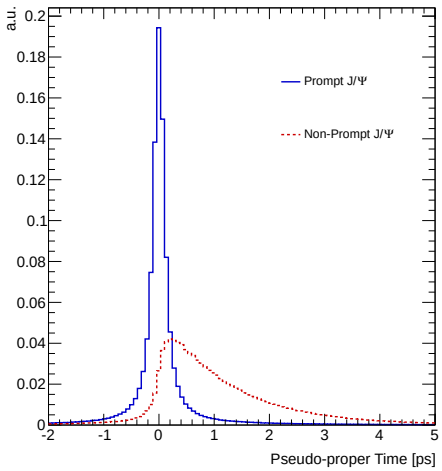

Figure 5.7 Pseudo-proper time distribution of $J/\psi \to ee$ candidates in Monte Carlo simulation for prompt and non-prompt J/ψ production, integrated over $E_{\mathrm{T}} < 25$ GeV and $|\eta| < 2.47$.

Two methods have been used to measure the electron identification efficiency using $J/\psi \to ee$ decays, both in 2011 and in 2012. The *short-τ method* attempts to reduce the non-prompt contribution by only considering events with short pseudo-proper time, thus selecting a sub-sample dominated by prompt J/ψ production. The remaining non-prompt contamination is estimated using MC simulation and the ATLAS measurement of the non-prompt fraction in $J/\psi \to \mu\mu$ events [85].

A more recent method, developed by the author of this Thesis and referred to as *τ-fit method*, uses instead the full τ range, and extracts the non-prompt fraction by directly fitting the pseudo-proper time distribution. As already anticipated, a detailed description of this method is given in Section 5.3.

[5] Since the original b-hadron is not fully reconstructed, we can't measure directly its lifetime. The measured J/ψ transverse momentum and the projection of the J/ψ vertex displacement L_{xy} are instead used to estimate the b-hadron lifetime in the transverse plane, with the formula 5.3. For this reason, the variable is referred to as "pseudo-proper" time.

[6] L_{xy} is estimated from the longitudinal impact parameters of the reconstructed electron tracks with respect to the primary vertex to which the original (non-GSF-refitted) track belongs (i.e. to which it contributes with the largest vertex weight).

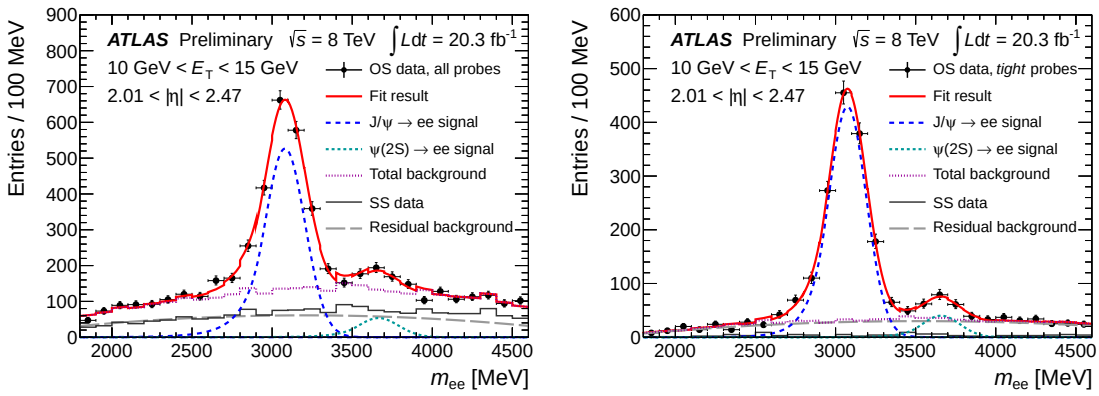

Figure 5.8 Illustration of the background subtraction technique as carried out in the short-τ method. The di-electron invariant mass fit for all probes passing track-quality requirements (left) and for probes passing the cut-based *tight* identification (right) for 10 GeV $< E_{\mathrm{T}} <$ 15 GeV and $2.01 < |\eta| < 2.47$ is shown. Dots with error bars represent the OS tag and probe pairs for data, the fitted J/ψ signal is shown by the dashed blue and the ψ(2S) by the dashed light blue lines (both modelled by a Crystal-Ball function). A background fit is carried out using the sum of the SS distribution (solid gray) from data and a Chebychev polynomial of 2nd order describing the residual background (dashed gray). The sum of the two background contributions is depicted as a purple dotted line. The pseudo-proper time is required to be -1 ps $< \tau <$ 0.2 ps [69].

As done for the two $Z \to ee$ tag-and-probe methods, the $J/\psi \to ee$ methods are regarded as variations of the same measurements, as they are based on the same data samples.

5.2.5 Combination

The measurements obtained from the different methods described above have been combined to extract the final results. As already explained, the residual kinematic differences between the considered processes are expected to cancel out in the data-to-MC correction factors, and the combination is thus performed using the scale factors, rather than the efficiencies. In 2012, the following measurements were considered in the different E_{T} bins, as also visible from the scheme in Figure 5.9:

- 7-10 GeV: $J/\psi \to ee$ (short-τ and τ-fit),
- 10-15 GeV: $J/\psi \to ee$ (short-τ and τ-fit) and $Z \to ee\gamma$,
- 15-20 GeV: $J/\psi \to ee$ (short-τ and τ-fit) and $Z \to ee$ (Z_{mass} and Z_{iso}),
- 20 GeV and above: $Z \to ee$ (Z_{mass} and Z_{iso}).

While in 2011 the $Z \to ee\gamma$ tag-and-probe method was not yet available, the results from the $W \to e\nu$ tag-and-probe were considered in combination with the ones from the $Z \to ee$ tag-and-probe in the region beyond 15 GeV. The distribution of the probes passing the *tight* identification selection are shown as a function of E_{T} for the samples available in 2011 and 2012 in Figures 5.10(a) and 5.10(b), respectively.

Only the E_{T} bins 10-15 GeV and 15-20 GeV (15-20 GeV and 20 GeV and above for 2011) allow a combination of statistically independent measurements.

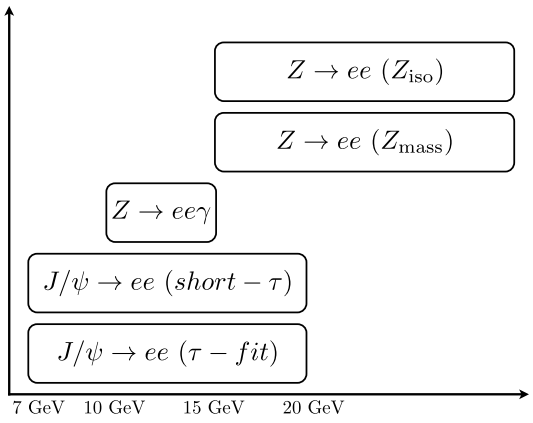

Figure 5.9 Scheme representing the efficiency measurements used for the 2012 combined results.

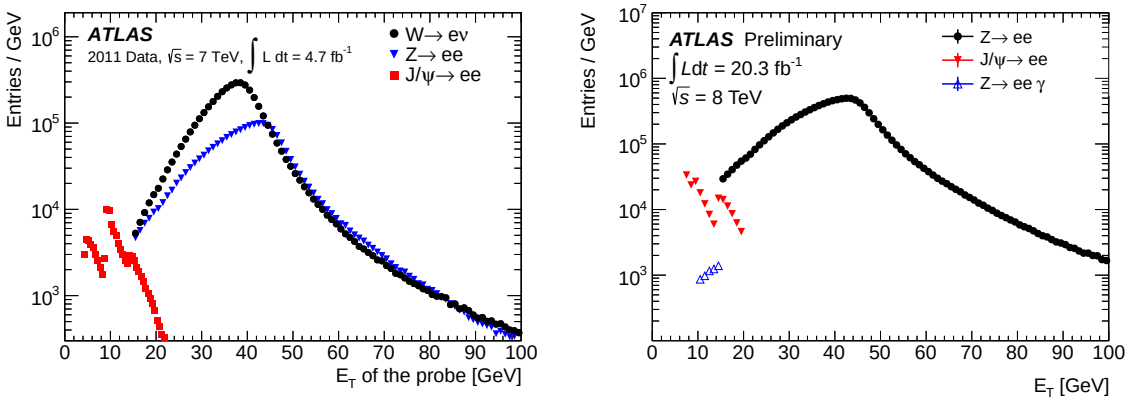

(a) **(b)**

Figure 5.10 Probe electrons passing the *tight* identification criteria as a function of E_{T} for the 2011 (a) and 2012 (b) datasets. In (a) the $W \to e\nu$, $Z \to ee$ and $J/\psi \to ee$ samples are shown, while figure (b) presents the distributions of the $Z \to ee$ $Z \to ee\gamma$ and $J/\psi \to ee$ samples. The non-continuous E_{T} spectrum of the $J/\psi \to ee$ sample is due to the different E_{T} thresholds of the triggers used to collect the sample.

A code originally developed for the HERA experiment was used for the combination in both 2011 and 2012. It extracts the combined scale factor values and their uncertainties by performing a χ^2 fit over all bins, while accounting for the correlations of the systematic uncertainties in the different η and E_{T} bins.

As already mentioned, the final combined scale factor results are used to correct the MC simulation in all physics analyses involving electrons in the final state. For visualisation purposes, the data efficiencies, both combined and from the different measurements, are also derived as the data-to-MC ratios multiplied by the $Z \to ee$ MC efficiency prediction. As already stated, the measurement of both efficiencies and scale factors is double-differential, performed as a function of the probe η and E_{T}.

2011 results

In the low E_{T} region, i.e. $7 < E_{\mathrm{T}} < 20$ GeV, the measurement is driven by the $J/\psi \to ee$ sample, although results from the $W \to e\nu$ and the $Z \to ee$ samples are also included in the combination for the 15-20 GeV bin. In this range, a coarse η binning is used (11 bins in η for $W \to e\nu$ and $Z \to ee$ tag-and-probe, and 6 bins in $|\eta|$ for the $J/\psi \to ee$) due to the limited available statistics. The measurements are limited by the statistical precision, as can be seen from Figure 5.11, and the total uncertainty varies from 3% to 7% in the barrel and in the endcap calorimeter regions, respectively.

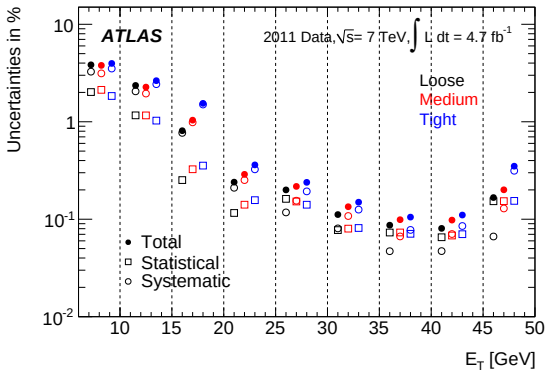

Figure 5.11 Decomposition of the total uncertainty into its statistical and systematic components. The three identification criteria *loose*, *medium* and *tight* are represented by black, red and blue markers, respectively. Error bars indicate the total uncertainties [81].

In the high E_{T} region, ranging between 20 GeV and 50 GeV, the abundant statistics from the $Z \to ee$ and $W \to e\nu$ channels allows the use of a finer η granularity (50 bins). The total uncertainty is generally statistically dominated (see Figure 5.11), and ranges from a few per mil at 35 GeV, to at most 1-2%.

A comparison of the scale factors obtained from the different channels is shown in Figure 5.12 for two illustrative E_{T} bins. The agreement among the channels is in general reasonable, with the most notable discrepancy observed in the 15-20 GeV bin, where the $J/\psi \to ee$ results for central η are lower than for $Z \to ee$ and $W \to e\nu$ with a significance of approximately two standard deviations.

The combined data-to-MC ratios are shown in Figure 5.13 for the E_{T} bins 15-20 GeV and 35-40 GeV. These corrections, applied in all analyses involving electrons, are typically no more than a few percent.

Figure 5.14 illustrates the combined efficiency measurements as a function of η for a few representative E_{T} bins. A slight dependence on the pseudorapidity can be observed, particularly marked for the tighter *medium* and *tight* selection. These shapes reflect well known features of the detector design, as well as the use of different variables and cuts in the selection procedure depending on the η region. A small gap between the calorimeter endcap wheels and in the TRT around $|\eta| \simeq 0$ explains the small drop in efficiency in that region. A larger drop can be observed in the complex transition regions between the barrel and the endcap EM calorimeters, for $1.37 < |\eta| < 1.52$. Finally, in the high η region the efficiencies are lower due to the larger amount of material in front of the endcap calorimeters. Moreover, for $|\eta| > 2$ the TRT information is

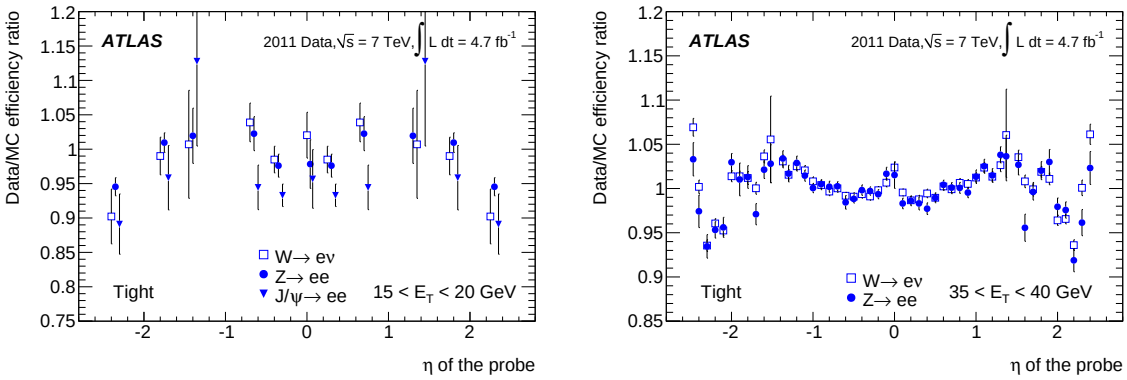

(a) **(b)**

Figure 5.12 Comparison of the scale factors extracted from the various measurements in two E_{T} bins, shown as a function of the tight probe pseudorapidity. In (a), scale factors from $Z \to ee$, $W \to e\nu$, and $J/\psi \to ee$ are compared in the E_{T} range 15-20 GeV. In (b), scale factors from $Z \to ee$ and $W \to e\nu$ are shown in the E_{T} range 35-40 GeV. The error bars correspond to the total uncertainties in each channel [81].

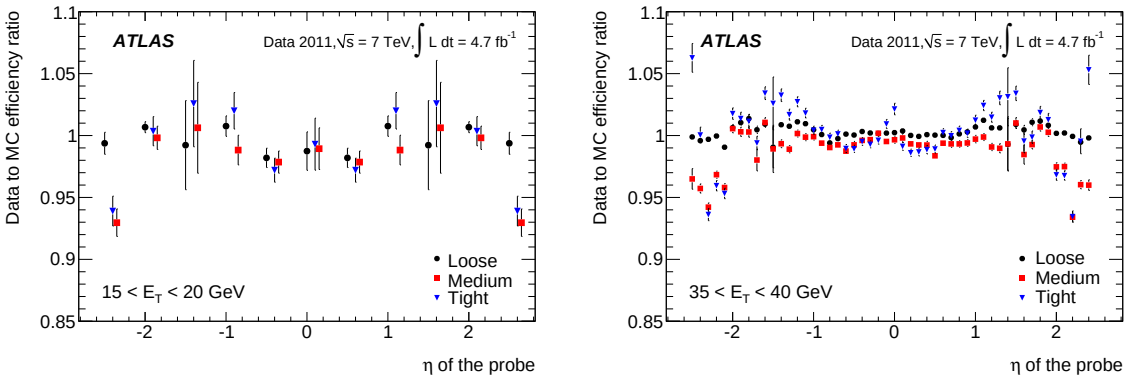

(a) **(b)**

Figure 5.13 Electron identification data-to-MC efficiency ratios for two representative E_{T} bins, the 15-20 GeV in (a) and the 35-40 GeV in (b). The three identification criteria *loose*, *medium* and *tight* are represented by black, red and blue markers, respectively. Error bars indicate the total uncertainties [81].

no longer available, and harder cuts on the shower shape variables need to be applied.

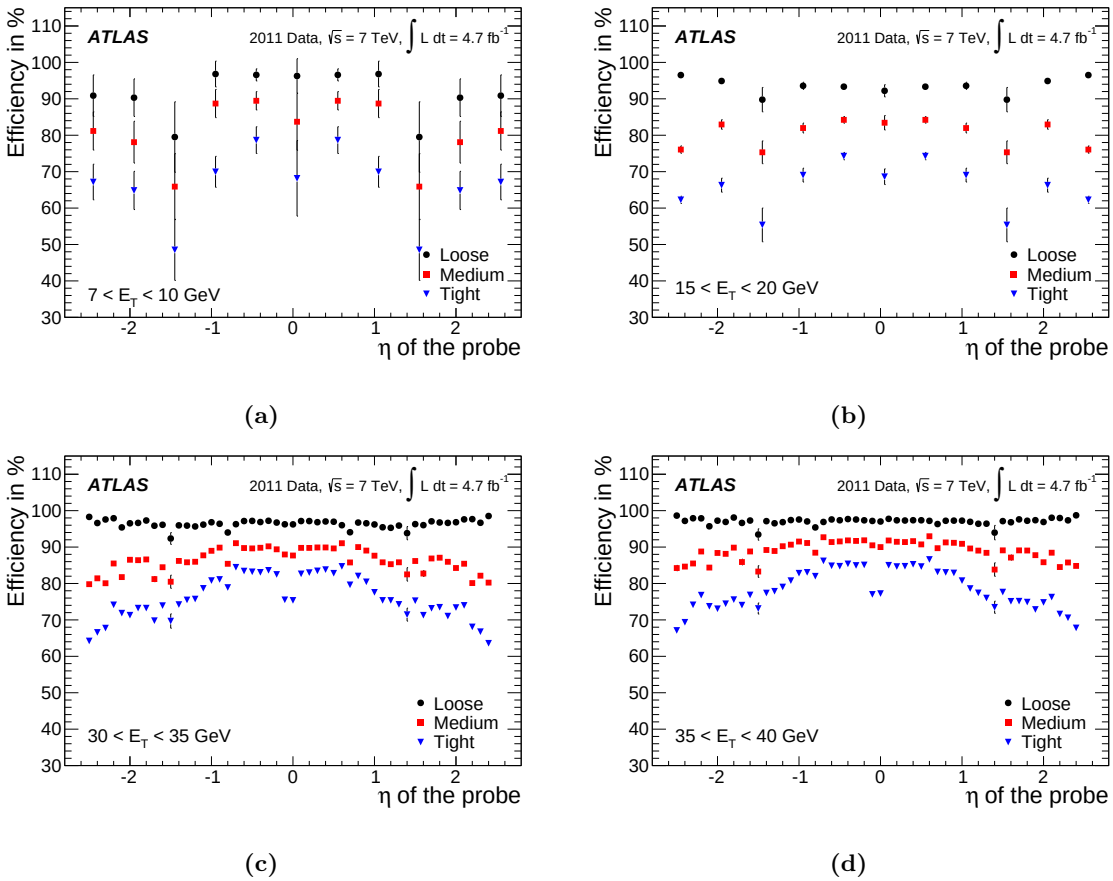

Figure 5.14 Electron identification efficiencies, derived as the combined data-to-MC ratios multiplied by the $Z \to ee$ MC efficiency prediction, as a function of η. Four representative E_{T} bins are shown, namely the 7-10 GeV in (a), the 10-15 GeV in (b), the 30-35 GeV in (c) and the 35-40 GeV in (d). The three identification criteria *loose*, *medium* and *tight* are represented by black, red and blue markers, respectively. Error bars indicate the total uncertainties [81].

The efficiency distributions as a function of E_{T}, integrated over the entire pseudorapidity range, are instead visible in Figure 5.15. The *loose* efficiencies range between approximately 91% and 98% over the whole spectrum, while the *medium* and *tight* selections exhibit a stronger dependence on energy. The *medium* efficiencies improve from about 81% to 92% with the electron increasing energy between 7 GeV and 50 GeV, and the *tight* efficiencies vary from about 67% at 7 GeV to 84% at 50 GeV.

2012 results

The binning used for the efficiency measurements in 2012 is specified in Tables 5.5. As in 2011, the η bins are coarser at low E_{T} due to the lower available statistics in that region. The E_{T} binning, on the other hand, is extended with respect to 2011 and has three additional bins above 50 GeV. The measured efficiencies are also presented as a function of the reconstructed primary vertices in the event, which is a measure of the hadronic activity due to overlapping collisions. Since the size of the $J/\psi \to ee$ sample is not large enough, this measurement is only

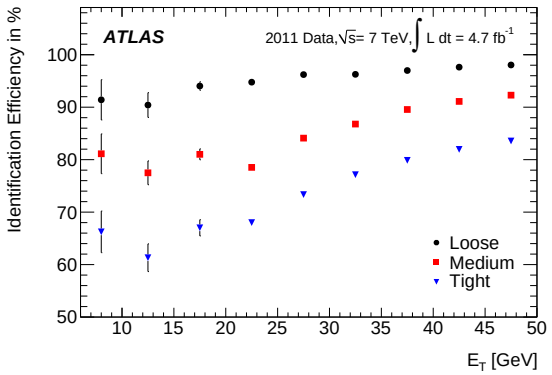

Figure 5.15 Electron identification efficiencies, derived as the combined data-to-MC ratios multiplied by the $Z \to ee$ MC efficiency prediction, as a function of E_{T} [81].

made using electrons with $E_{\mathrm{T}} > 15$ GeV from $Z \to ee$ events with the Z_{mass} method.

Table 5.5 Identification efficiency measurement bins in electron transverse energy, (a), and in pseudorapidity, (b).

Bin boundaries in E_{T} [GeV]												
7	10	15	20	25	30	35	40	45	50	60	80	∞

(a)

Bin boundaries in η																			
Identification efficiency measurement for E_{T} <20 GeV: only absolute η bins																			
										0	0.1		0.8			1.37	1.52		2.01		2.47
All other measurements																			
-2.47	-2.37	-2.01	-1.81	-1.52	-1.37	-1.15	-0.8	-0.6	-0.1	0	0.1	0.6	0.8	1.15	1.37	1.52	1.81	2.01	2.37	2.47

(b)

A comparison of the results obtained from the different channels can be seen in Figure 5.16, for the two bins in which independent measurements overlap. The $Z \to ee$ efficiencies computed from the data-to-MC ratios, extracted with either the J/ψ or the Z tag-and-probe methods, are illustrated in the E_{T} bins 10-15 GeV and 15-20 GeV. The agreement between the independent results is good.

The combined efficiencies in both data and MC can be seen in Figures 5.17 and 5.18, where these results are shown as a function of E_{T}, η and the number of primary vertices. In particular, Figure 5.17 presents the measurements for the four cut-based menus, while the three likelihood-based criteria are overlaid in Figure 5.18. As seen for 2011 results, the identification efficiencies strongly depend on E_{T} and, for the tighter criteria, on η. Their values average between 96% (cut-based *loose*) and 78% (VERY TIGHT LH) for electrons with $E_{\mathrm{T}} > 15$ GeV. The data-to-MC correction factors, which are also illustrated in the lower panels of the figures, are found to be very close to one, demonstrating how the simulation correctly reproduces the data in most cases. Only for the most stringent criteria, and for low E_{T} or high η values, the corrections reach about 10%. After combination, the uncertainties on the scale factors vary between 0.5% and 10%, with the highest uncertainties found in the transition region of the calorimeter, $1.37 < |\eta| < 1.52$.

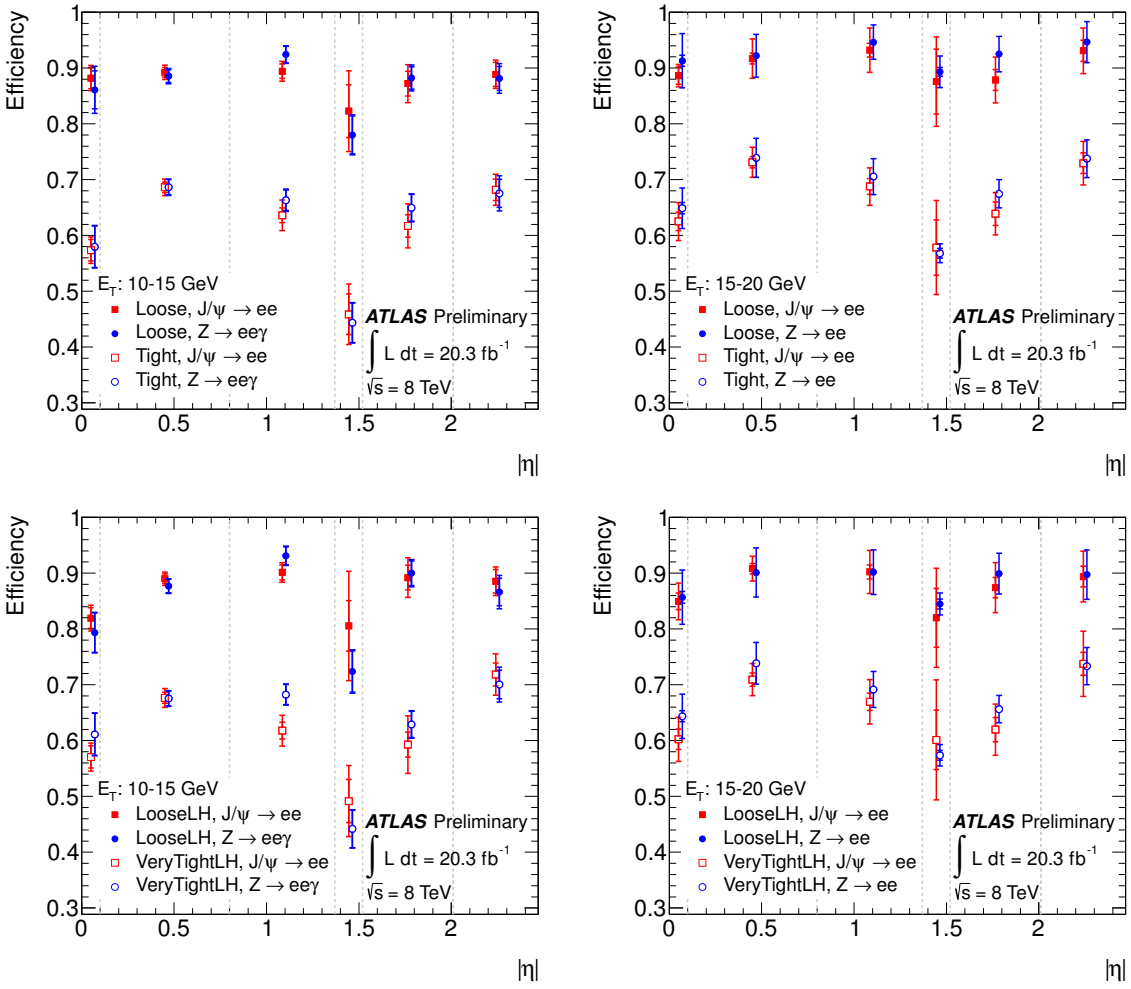

Figure 5.16 Measured identification efficiency as a function of $|\eta|$ for $E_{\mathrm{T}} = 10$ - 15 GeV and $E_{\mathrm{T}} = 15$ - 20 GeV (right), for the cut-based *loose* and *tight* selections (top), and for LOOSE LH and VERY TIGHT LH LH (bottom). The data efficiency is derived by applying the measured data-to-MC efficiency ratios, determined with either the J/ψ or the Z methods, on the MC prediction from $Z \to ee$ decays. The statistical (inner error bars) and the total (outer error bars) uncertainties are shown [69].

Even with the higher statistics available in the 2012 dataset, the statistical component of the uncertainty still represents a significant contribution to the total error.

The behaviour of the identification efficiencies as a function of E_{T} and η show roughly the same trends already seen in the 2011 results. For the tighter criteria, which apply more stringent cuts on a higher number of variables, the overall identification efficiency decreases, while the dependence on E_{T} and η increases, as expected.
The efficiencies rise as a function of E_{T} for all menus, due to the fact that high E_{T} electrons are more easily separated from background objects in many of the discriminating variables. An exception to this trend is given by the 7-10 GeV bin, which instead shows a significant increase in the efficiency, due to some cuts being relaxed in that region. The same happens for the highest E_{T} bin, as the track momentum measurement becomes unreliable at those energies and the E/p cut is dropped. Dedicated studies showed how the MC correction factors computed for electrons above 80 GeV can be safely applied to electrons with energies higher than $E_{\mathrm{T}} = 400$ GeV.
The shape of the efficiencies as a function of η shows, as in 2011, a drop in the efficiencies in the regions around $|\eta| = 0$, in the transition region, and for high $|\eta|$ values.

As shown in Figures 5.17(c) and 5.18(c), the dependence on the number of primary vertices is not well predicted in MC simulation, especially for the tighter menus where it is significantly underestimated. The scale factors, fairly stable for the *multilepton* and *loose* selections, decrease by about 2% for the other cut-based and likelihood operating points when increasing the number of primary vertices from 1 to 30. This discrepancy is primarily caused by the known mis-modelling of the R_{Had}, $\mathrm{w}_{\mathrm{stot}}$ and F_{HT} variables in MC, which affects cut-based and LH selections differently. While cut-based criteria efficiencies are only affected if the mis-modelling occurs next to the cut value, for LH selections a mis-modelling anywhere in the distributions could affect the efficiency.

As already mentioned in Section 5.1.2, the new LH selections were tuned to match the efficiencies of the cut-based counterparts *multilepton*, *medium* and *tight*. Figure 5.19(a), in which the efficiencies of all operating points are overlaid, shows how this is indeed achieved in almost all bins. On the other hand, while the signal efficiencies match, the rejection power of the LH criteria is expected to be higher. This is shown in Figure 5.19(b), which illustrates the ratio of background efficiencies for a LH and the closest-efficiency cut-based selections. The background rejection is clearly improved for the LH selections, which let through only about 40-60% of the background, compared to the cut-based selections. A detailed description of the background efficiency measurement can be found in Ref. [69].

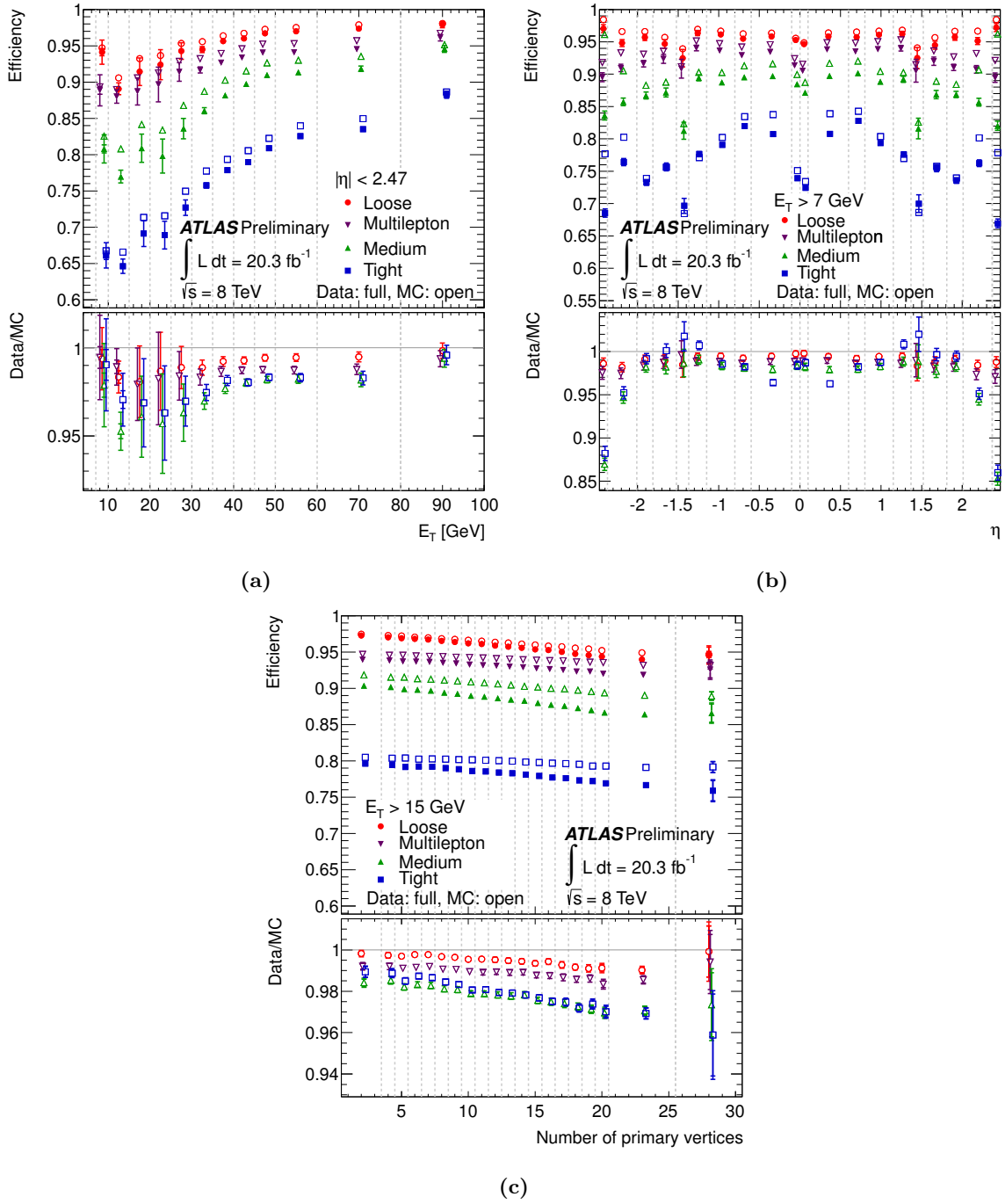

(a) **(b)** **(c)**

Figure 5.17 Identification efficiency in data as a function of E_{T} (a), η (b) and the number of reconstructed primary vertices (c) for the cut-based *loose*, *multilepton*, *medium* and *tight* selections, compared to MC expectation for electrons from $Z \rightarrow ee$ decay. The lower panel shows the data-to-MC efficiency ratios. The statistical (inner error bars) and the total (outer error bars) uncertainties are shown [69].

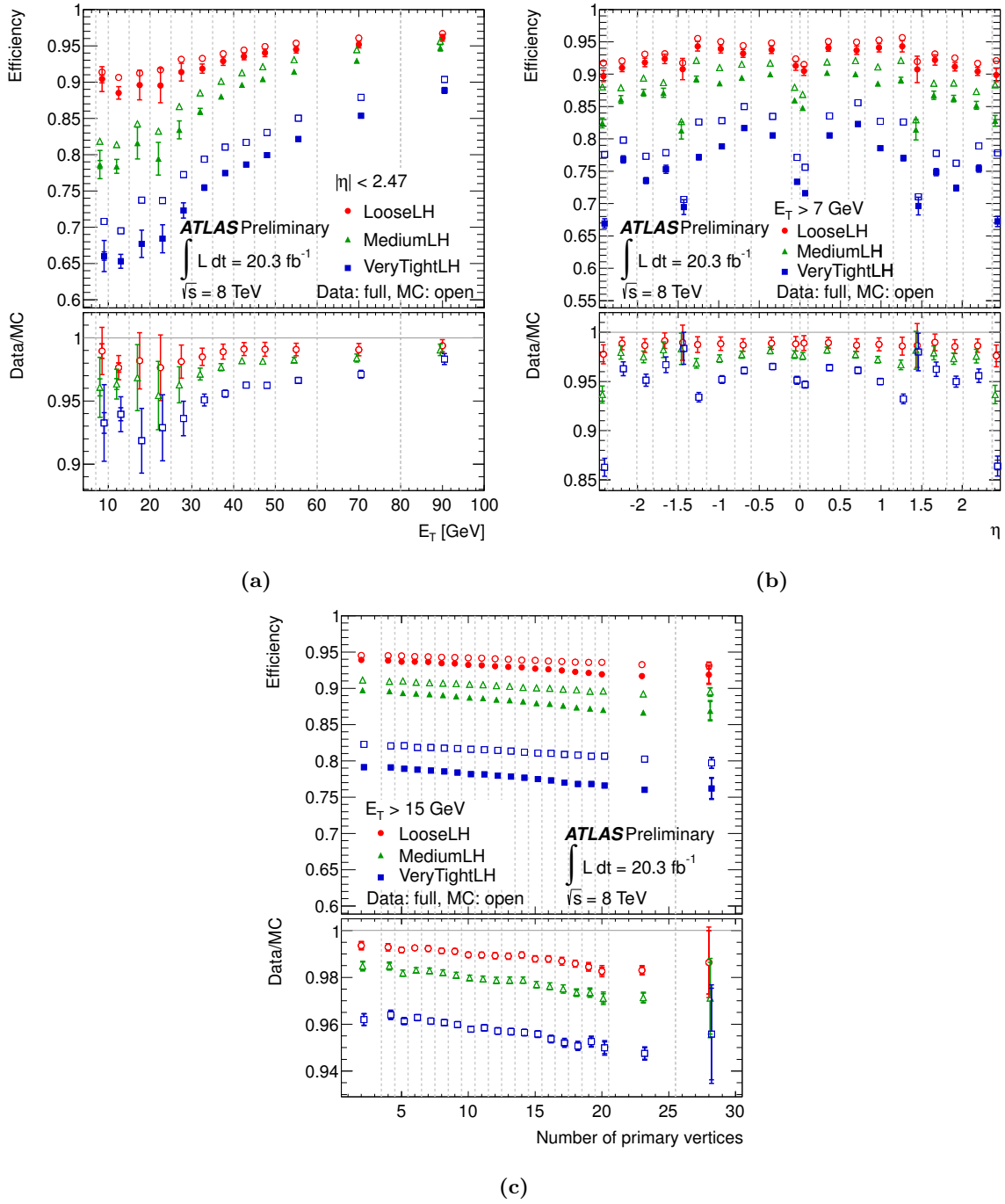

Figure 5.18 Identification efficiency in data as a function of E_{T} (a)), η (b) and the number of reconstructed primary vertices (c) for the LH-based LOOSE LH, MEDIUM LH and VERY TIGHT LH selections, compared to MC expectation for electrons from $Z \to ee$ decay. The lower panel shows the data-to-MC efficiency ratios. The statistical (inner error bars) and the total (outer error bars) uncertainties are shown [69].

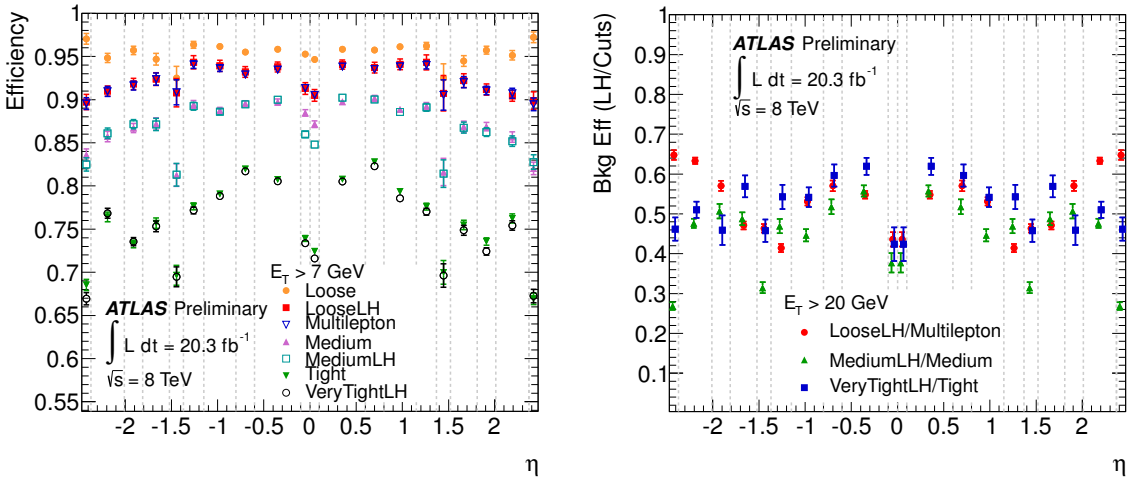

(a) **(b)**

Figure 5.19 (a) The measured identification efficiency for the various cut-based and LH selections is shown as a function of η . (b) The ratio of background efficiencies for a likelihood-based and the closest-efficiency cut-based selections as a function of η, as obtained using an inclusive background sample [69].

5.3 Tag-and-probe with $J/\psi \to ee$ Events: τ-fit Method

As pointed out in Section 5.2.4, there are two $J/\psi \to ee$ tag-and-probe analyses, which mainly differ in the treatment of the prompt and non-prompt components of the J/ψ data sample. The most recent one, referred to as the τ-fit method, was entirely developed by the author of this thesis, and is thus presented in full detail in the remainder of this chapter.

5.3.1 Data selection

Data samples

The 2011 and 2012 analyses are based on the pp collision data collected with the ATLAS detector at a center of mass energy of 7 TeV and 8 TeV, respectively. The data is filtered requiring good data quality, in particular concerning the inner detector and the calorimeters, and the total integrated luminosity corresponds to $\mathcal{L} = 4.7$ fb^{-1} in 2011, and to $\mathcal{L} = 20.3$ fb^{-1} in 2012.

The recorded data both in 2011 and in 2012 are subdivided into several periods corresponding to the changing conditions of the detector, including the trigger menus, as well as the instantaneous luminosity of the LHC.

Triggers

The following dedicated prescaled di-electron triggers were used to collect $J/\psi \to ee$ events, both in 2011 and in 2012:

- e5_tight_e4_etcut_Jpsi

- e5_tight_e9_etcut_Jpsi
- e5_tight_e14_etcut_Jpsi
- e7_tight_e14_etcut_Jpsi (2011 only)
- e9_tight_e4_etcut_Jpsi
- e14_tight_e4_etcut_Jpsi

Here the tag corresponds to the the first trigger object, which is required to pass tight[7] electron identification and an E_{T} threshold cut. The second object, which is a reconstructed electron passing another E_{T} threshold cut, corresponds instead to the probe. An additional cut on the invariant mass of the two objects, $1 < m_{ee} < 5$ (6) GeV, is required to reduce the rate at EF (L2).
These triggers are end-of-fill triggers, and can only be used after the luminosity has dropped during a run. The pile-up rate seen in these $J/\psi \to ee$ events will thus be lower relative to the average for the hard scattering processes in the full run. The discrepancy arising with respect to MC is accounted for, as explained in the Section 5.3.2.

Among the listed triggers, the first three (four in 2011) allow to explore the probe E_{T} spectrum of interest, and the latter two help to populate the low E_{T} probe spectrum. Table 5.6 lists the fraction of events in the 2012 data selected by each trigger as a function of the probe E_{T} bin, after the event selection. While in 2012 all triggers have ran throughout the entire data

J/ψ trigger	5-7 GeV	7-10 GeV	10-15 GeV	15-20 GeV	20-25 GeV
e5_tight_e4_etcut	19.8%	17.5%	8.3%	1.2%	1.3%
e5_tight_e9_etcut	0.0%	0.0%	52.3%	8.5%	7.5%
e5_tight_e14_etcut	0.0%	0.0%	0.0%	85.7%	89.4%
e9_tight_e4_etcut	32.6%	33.2%	17.5%	3.5%	1.8%
e14_tight_e4_etcut	47.6%	49.3%	21.9%	1.1%	0.0%

Table 5.6 Contribution of the different triggers (in %) to the probe sample for each E_{T} bin in the full 2012 dataset.

taking period, in 2011 they were evolving with time. Four data periods can be distinguished, each having the same trigger conditions. A list of the triggers active in the various data periods is given in Table 5.7.

$E_{\mathrm{T}} \times \eta$ binning

Although the final results are only available in the three E_{T} bins between 7 and 20 GeV, the efficiency measurement was performed in 6 E_{T} bins, namely E_{T} = 5–7, 7–10, 10–15, 15–20 and 20–25 GeV. The last bin was only introduced in 2012, but not included in the combination as the measurements never proved to be stable enough. This was related to both the very low statistics and the spacial proximity of the tag and the probe at such high E_{T} values.

[7] The trigger tight selection has some cuts removed as compared to the offline tight selection

Period	First-Last Run	J/ψ trigger (fraction)
1 (B-D)	177986-180481	e5_tight_e4_etcut (44%), e5_tight_e9_etcut (56%)
2 (E-H)	180614-184169	e5_tight_e4_etcut (32%), e5_tight_e9_etcut (57%), e7_tight_e14_etcut (11%)
3 (I-K)	185353-187815	e5_tight_e4_etcut (18%), e5_tight_e9_etcut (35%), e5_tight_e14_etcut (30%), e7_tight_e14_etcut (16%)
4 (L-M)	188902-191933	e5_tight_e4_etcut (20%), e5_tight_e9_etcut (34%), e5_tight_e14_etcut (20%), e9_tight_e4_etcut (19%), e14_tight_e4_etcut (7%)

Table 5.7 Triggers used in each 2011 data period to collect $J/\psi \to ee$ candidates. For each period, the fraction of events collected by each trigger is given in parenthesis.

The lower E_{T} bin, on the other hand, was also present in 2011, even though the lower end was 4 and not 5 GeV. In ATLAS, only electrons with $E_{\mathrm{T}} > 7$ GeV are used in physics analysis, therefore no scale factors are needed below 7 GeV. Nonetheless, the results obtained in the lower E_{T} bin are anyway included in the combination framework and thus influence the measurements in the other bins by accounting for correlations between bins.

For each E_{T} bin, the probe sample is subdivided in six intervals of absolute $|\eta|$, namely 0–0.1, 0.1–0.8, 0.8–1.37, 1.37–1.52, 1.52–2.01 and 2.01–2.47, to account for different regions of the detector. With the higher available statistics in 2012, the possibility of using η bins was also considered, but finally discarded. While no particular asymmetry was in fact observed, having significantly less statistics in the different bins brought to a reduced sensitivity, especially in the transition region and in the endcaps.

The kinematic distributions of E_{T} and η of both tag and probe electrons are shown in Figure 5.20 for the data. The rising fronts on the E_{T} spectra correspond to the thresholds of the various triggers, while the low statistics at large η values are a result of the kinematic cuts applied.

Event selection

The event selection proceeds as follows.

- At least one primary vertex with at least three associated tracks is required to be present in the event.
- Events with at least two electron candidates recorded under fully operational detector conditions are considered. Both electrons must be in the pseudorapidity range of $|\eta| < 2.47$, and a minimum transverse energy of 5 GeV (4 GeV in 2011) is required for each electron.
- The tag is required to match within a cone of $\Delta\mathrm{R} < 0.005$ a trigger electron satisfying the trigger E_{T} threshold and tight ID requirements. The probe should have an E_{T} which is 1 GeV higher than the corresponding trigger E_{T} threshold, and also match a trigger electron satisfying the trigger E_{T} threshold.
- The tag electron is required to satisfy the *tight* ID.

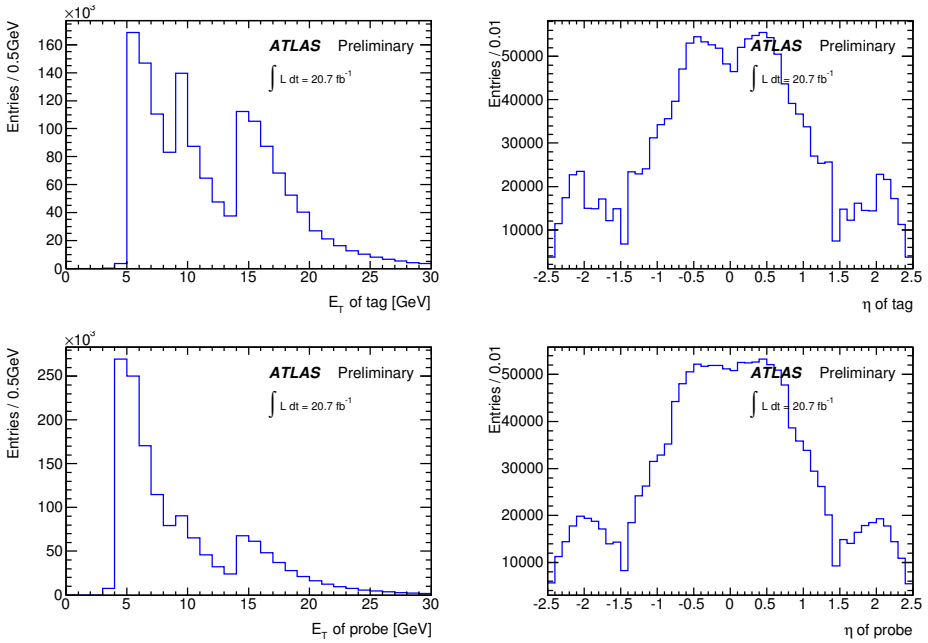

Figure 5.20 The transverse energy E_{T} (left) and the pseudorapidity η (right) spectra for the tag (top) and the probe (bottom) electron candidates for the 2012 $J/\psi \to ee$ data sample. The enhancement at $E_{\mathrm{T}} \approx 4$ GeV for the probes is due to the e5_tight_e4_etcut, e9_tight_e4_etcut and e14_tight_e4_etcut triggers.

- The probe electron must have hits in the Inner Detector, such that $N_{\mathrm{Pixel}} > 0$ and $N_{\mathrm{Pixel+SCT}} > 6$.

- The radial distance in the calorimeter between the clusters of the tag and the probe is required to be $\Delta R^{\mathrm{calo}}_{\mathrm{tag-probe}} > 0.1$. Also, the radial distance in the inner detector between the the tag and the probe is required to be greater than 0.2. These selection cuts ensure that the probe object is not affected by a close-by tag electron and, therefore, prevents a possible bias of the identification efficiency measurement.

In 2011, an additional requirement was applied on the tag electron, which had to satisfy tighter cuts on the F_{HT} variable [8] to reduce the large amount of background. Following a detailed study performed in 2012 on the possible tag selections, this cut was finally removed in the 2012 analysis. The study showed how, by introducing an isolation cut on the tag, rather than the existing tighter TRT cut, we obtain a cleaner sample, better signal/background ratio, while at the same time having less signal losses. In particular, the selected cut applied on the tag in the 2012 analysis is ${p_{\mathrm{T}}}^{\mathrm{cone0.2}}/E_{\mathrm{T}} < 0.15$.

In the 2012 (2011) analysis, about 700,000 (600,000) electron probes are selected for $E_{\mathrm{T}} =$ 7-20 GeV, of which about 190,000 (120,000) pass the *tight* selection, within the wider pseudo-proper time range of (-1, 3) ps and integrated over $|\eta| < 2.47$.

[8] F_{HT} (including outliers) had to be greater than 0.17, 0.19, 0.19, 0.20, 0.22, respectively in the 5 $|\eta|$ bins (0-0.1,0.1-0.8,0.8-1.37,1.37-1.52,1.52-2).

Isolation cuts on probe

Electrons coming from J/ψ decays, even if promptly produced, are in general less isolated than the ones coming from Z or W decays. Also for a data sample enriched with direct decays, isolation variables indicate indeed the presence of additional tracks and energy. This busy environment is not well modelled in the Monte-Carlo, as can be seen from Figure 5.21. An

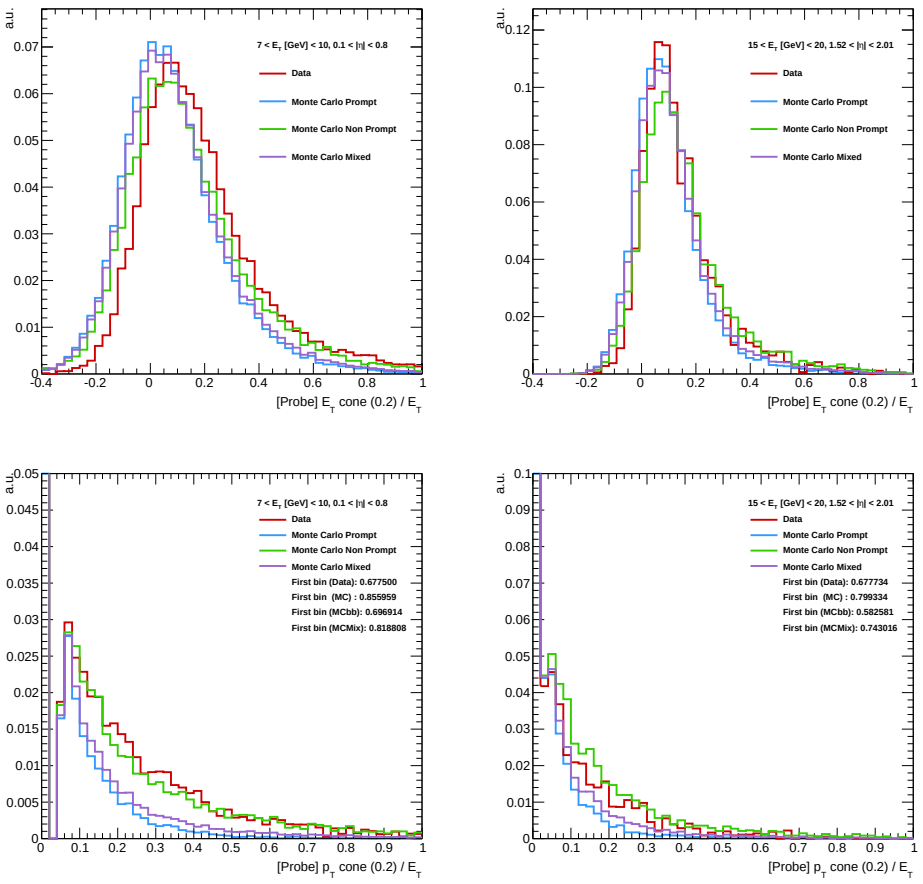

Figure 5.21 Distributions of the isolation variables in 2012 data compared to prompt and non-prompt J/ψ MC and their combination using the measured fractions as described in Section 5.3.3. Both the calorimeter $E_{\mathrm{T}}^{\mathrm{cone0.2}}$ (top) and the track isolation ${p_{\mathrm{T}}}^{\mathrm{cone0.2}}$ (bottom) variables are shown, for probes with $E_{\mathrm{T}} = 7 - 10$ GeV and $|\eta| = 0.1 - 0.8$ (left) and with $E_{\mathrm{T}} = 15 - 20$ GeV and $|\eta| = 1.52 - 2.01$ (right). The first bin has been cut in the plots showing ${p_{\mathrm{T}}}^{\mathrm{cone0.2}}$; its content can be read from the legend. The background is subtracted using the sideband method described in Section 5.3.3.

additional isolation cut is thus applied to the probe, to ensure that the measured efficiencies correspond to well-isolated electrons. To account for any possible bias arising from a particular choice of the isolation cut, several thresholds were considered for both the calorimetric and track isolation variables introduced in Section 5.1.3. In 2011, we have investigated the effects on efficiencies and scale factors when applying four different isolation cuts on the probes:

- ${E_{\mathrm{T}}}^{\mathrm{cone0.2}}/E_{\mathrm{T}} < 0.20$
- ${E_{\mathrm{T}}}^{\mathrm{cone0.2}}/E_{\mathrm{T}} < 0.30$

- ${p_{\mathrm{T}}}^{\mathrm{cone0.2}}/E_{\mathrm{T}} < 0.02$
- ${p_{\mathrm{T}}}^{\mathrm{cone0.2}}/E_{\mathrm{T}} < 0.15$

The loosest and tightest cuts were dropped in 2012, and only one calorimetric and one track isolation cuts were considered:

- ${E_{\mathrm{T}}}^{\mathrm{cone0.2}}/E_{\mathrm{T}} < 0.20$
- ${p_{\mathrm{T}}}^{\mathrm{cone0.2}}/E_{\mathrm{T}} < 0.15$

Other complementary variations were considered in the short-τ method. In both analyses, when applying the calorimetric isolation variable, we also required the tag to be further than $\Delta R^{\mathrm{calo}}_{\mathrm{tag-probe}} = 0.22$ in order to avoid cluster overlaps. The tag track is instead subtracted from the ${p_{\mathrm{T}}}^{\mathrm{cone0.2}}$ variable if it lies within $\Delta R = 0.2$ of the probe.

These isolation criteria are found to have less than 1% effect on the identification efficiency in simulated events.

Pseudo-proper time ranges

In the τ-fit analysis, the pseudo-proper time of the di-electron system is required to be in the range of (-1, 3) ps. This very loose cut (it has a typical efficiency of almost 95% for prompt and 90% for non-prompt J/ψ production) allows fitting this variable to discriminate between prompt and non-prompt J/ψ decays. In the short-τ method described in Section 5.2.4, on the other hand, a hard cut is applied to the pseudo-proper time to reject the non-prompt contribution as much as possible, requiring it to be within (-1, 0.2) or (-1, 0.4) ps. To check for any possible bias or difference arising from the use of different ranges for the pseudo-proper time, in 2012 we have also carried out our analysis in these more restricted τ ranges:

- $-1 < \tau < 0$ ps;
- $-1 < \tau < 0.2$ ps;
- $-1 < \tau < 0.4$ ps.

As we cannot perform a fit on the pseudo-proper time distribution when restricting ourselves to the above ranges, an interpolation is needed for these cases, as will be explained in Section 5.3.3. Notice that in the 2011 analysis only the nominal range $-1 < \tau < 3$ was considered.

5.3.2 Monte Carlo simulation

The $J/\psi \to ee$ events are simulated in 2012 (2011) using Pythia8 (Pythia6) interfaced to Photos, and then processed through a detailed ATLAS detector simulation based on Geant4. In 2011, MC samples are generated to mimic the same period granularity present in the data sample.

The same software used to reconstruct data events is applied on simulated events, which are then corrected to account for known mis-modelings. The energy of the electron candidates is smeared to match the resolution in data, and the MC events are weighted to reproduce the

beam-spot z-distribution.

As the $J/\psi \to ee$ events are collected in data using "end-of-run" triggers, they present different pile-up conditions with respect to other data samples and to simulation (see Figure 5.22). An explicit pile-up reweighing is thus applied to MC using the ratio of the distributions for the measured number of primary vertices seen in data and MC. The overall weight as a function of the number of vertices is also shown in Figure 5.22. Separated samples are generated for

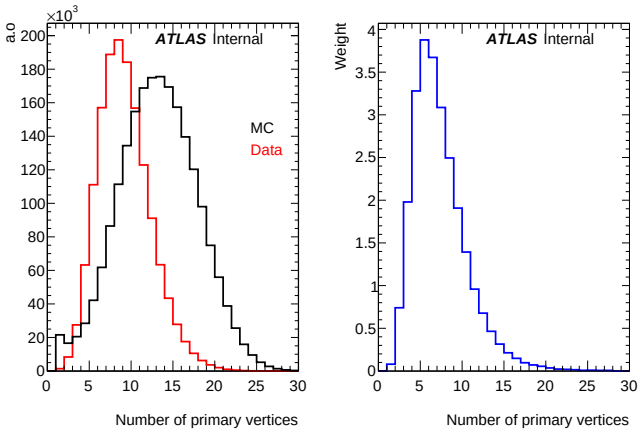

Figure 5.22 Data-MC comparison of the distribution of the number of reconstructed primary vertices for J/ψ events in the 2012 run. The weight distribution used to correct the MC sample is also given.

prompt ($pp \to J/\psi + X$) and non-prompt ($b\bar{b} \to J/\psi + X$) production. MC efficiencies are computed separately from the prompt and the non-prompt J/ψ samples, and then compared directly to the corresponding measurements extracted from data. Since with the τ-fit method the two contributions can be separated in data, there is indeed no need to combine the MC samples as done in the short-τ method.

Different MC samples are also generated with explicit selections on the true value of the electron's transverse energy. Samples with e3e3, e3e8 and e3e13 filter are used, where a filter of eXeY requires two true electrons with ${E_{\mathrm{T}}}^1 > Y$ GeV and ${E_{\mathrm{T}}}^2 > X$ GeV. When computing MC efficiencies, only one sample per each E_{T} bin is considered, rather than adding up the samples, as it was shown that this gives better agreement between data and MC. In particular, the e3e3 sample is used in the 5-7 GeV and in the 7-10 GeV bins, the e3e8 sample in the 10-15 GeV bin, and the e3e13 sample in the 15-20 GeV and in the 20-25 GeV.

All the triggers introduced in the previous section are simulated in each MC sample. As shown in Figure 5.23 for 2012, the efficiencies are found to depend on the trigger. Moreover, due to the prescale applied online, the fraction of events selected by a given trigger is different in data and simulation. For these reasons, the efficiencies are first computed for each trigger separately and then combined together taking into account the corresponding data statistics for each trigger. The same procedure is applied in the 2011 and 2012 analyses, although in the former an additional complication arises from the fact that not all triggers were used in each period, as seen in Table 5.6. The efficiencies are thus computed separately for each period and for each active trigger.

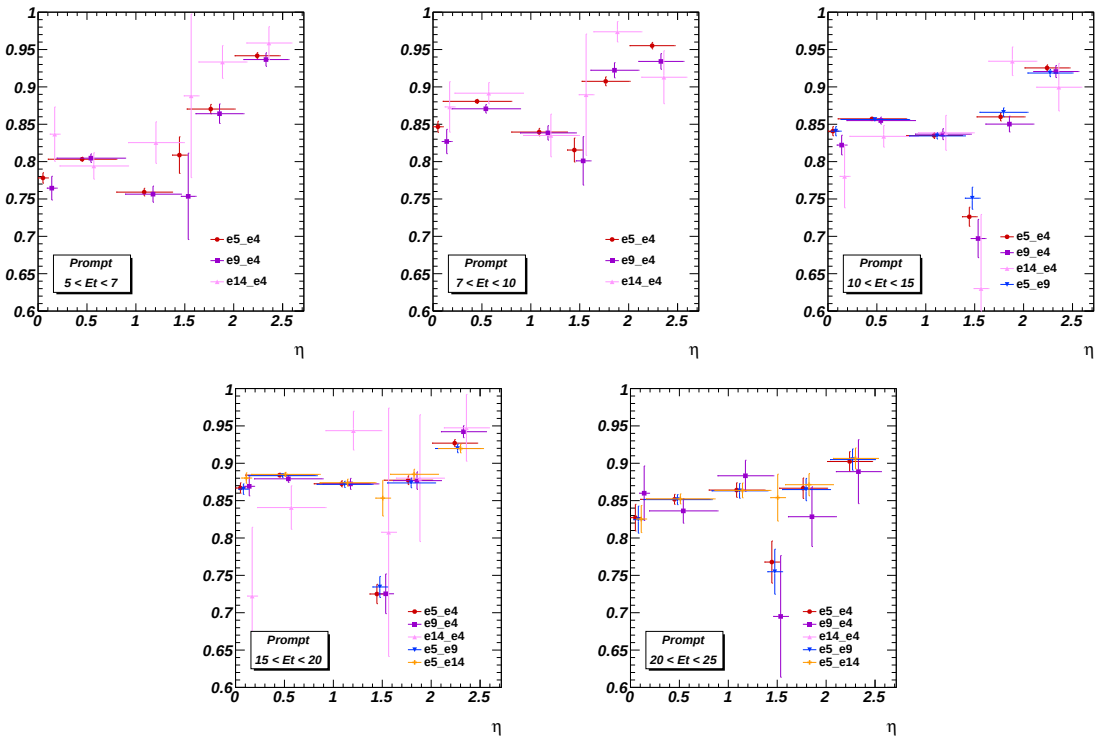

Figure 5.23 MC prompt efficiencies as a function of $|\eta|$ for the *medium* selection for different E_{T} bins and for different triggers. Errors come from the limited statistics only. For a given $E_{\mathrm{min}} < E_{\mathrm{T}} < E_{\mathrm{max}}$ bin, only triggers with a probe E_{T} threshold lower than E_{min} are considered.

5.3.3 Fitting procedure

As already mentioned, the τ-fit method estimates the background contaminations via a fit to the tag-and-probe di-electron invariant mass, and further extracts the non-prompt J/ψ fraction by fitting the pseudo-proper time distribution. To derive efficiencies and scale factors for a pseudo-proper time range (-1, x) ps (where $x = 0, 0.2, 0.4, 3$), the following procedure is applied (see also Figure 5.24):

1. Perform an invariant mass fit in the range (-1, x) ps to extract the signal yield;
2. Perform an invariant mass fit and subsequently a pseudo-proper time fit in the default range of (-1, 3) ps to extract the fraction of promptly produced J/ψ particles in the range (-1, 3) ps;
3. Interpolate the prompt fraction to the range (-1, x) ps using the fitted shapes;
4. Combine this information with the signal yield found at 1, and then compute efficiencies and scale factors.

Invariant mass fit

For each bin, an unbinned maximum likelihood fit is performed on the invariant mass of the two electrons, in the range between 1.8 and 4.6 GeV. In the $20 < E_{\mathrm{T}} < 25$ GeV bin, the range is restricted to 2.3-4.6 GeV because of low statistics in the lower mass tail.

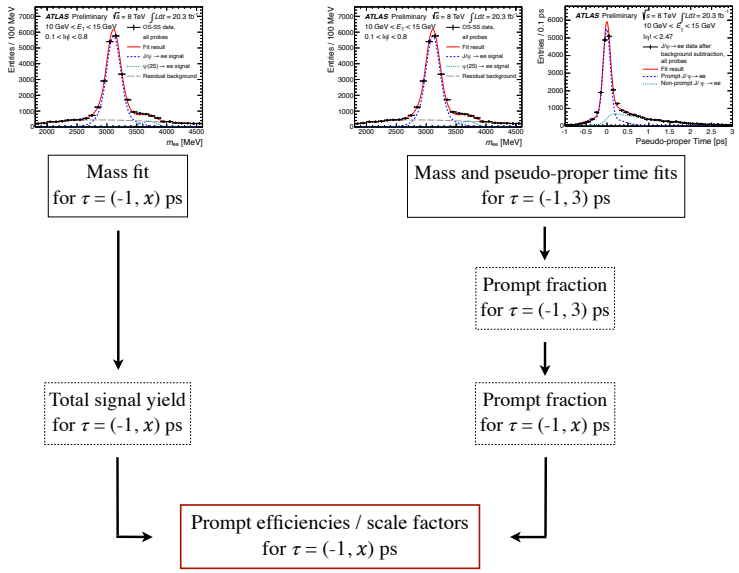

Figure 5.24 Schematic view of the τ-fit method.

The signal contribution coming from J/ψ decays is described in the 2011 analysis using a Crystal Ball function[9]. With the higher statistics available in 2012, this simple function was found to be unsuited to well model the J/ψ dielectron invariant mass distribution, and a Gaussian was added to the Crystal Ball function. The Crystal Ball tail parameters α and η have been fixed to values extracted from a fit to the prompt signal Monte Carlo sample. The same signal function is also used to describe the ψ_{2s} component, which is clearly visible in most of the bins. The mass difference between the J/ψ and the ψ_{2s} is fixed to the PDG value($m_{J/\psi}$ = 3.096 GeV and $m_{\psi_{2s}}$ = 3.686 GeV), and the ratio of ψ_{2s} to J/ψ events is also restricted to be close to the measured value ($\sim$ 0.035) [86]. In the 2012 data sample, the χ_c[10] component is also visible between the J/ψ and the ψ_{2s} resonances in a few bins.

This component is not considered in the baseline fit, but is taken into account by some systematic variations introduced in 2012. The function used to describe the χ_c is again the same used for the J/ψ and the ψ_{2s}.

An important contribution to our background comes from the random combination of two electron candidates not coming from a J/ψ. To subtract these events we apply a weight which is equal to -1 when the electrons have same sign (SS) and to $+1$ when they are oppositely charged (OS). The remaining background events are then described by a Chebychev polynomial of 1st or 2nd order, depending on the considered bin. Thanks to this "weighted" same sign subtraction, as opposed to the use of a same sign template, we are able to perform an unbinned fit to our data. From these fits we extract the signal and background yields in a counting window around the nominal J/ψ mass, between 2.8 and 3.3 GeV. Example fits for the 2012 data sample are shown in Figure 5.25.

The choice of fit region and counting window, as well as the choice of the analytical function

[9]

[10]Notice that the χ_c does not decay directly into electrons, but only via the production of a J/ψ associated with a photon, with a BR of $\sim$ 1%.

to describe the signal and background shapes are varied to estimate the related systematics, as discussed in detail in Section 5.3.4.

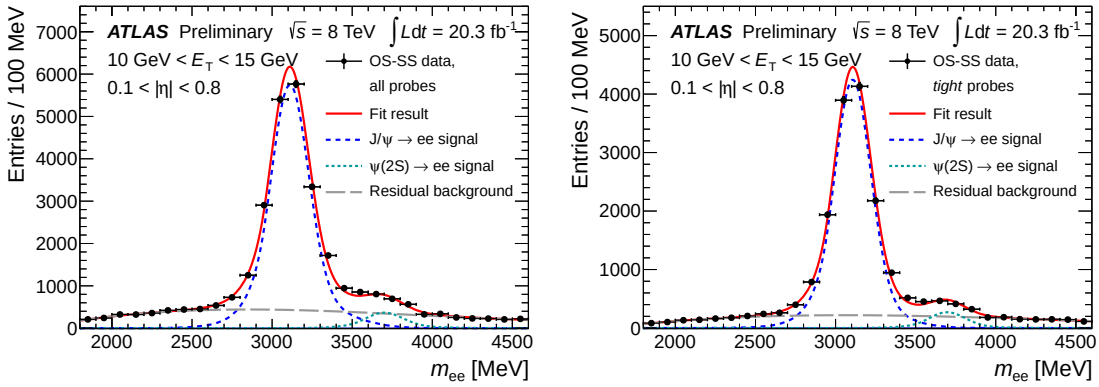

Figure 5.25 Illustration of the background determination for the 2012 J/ψ analysis. The di-electron invariant mass fit for all probes passing track-quality requirements (left) and for probes passing the cut-based *tight* identification (right) for 10 GeV $< E_{\mathrm{T}} <$ 15 GeV and $0.1 < |\eta| < 0.8$ is shown. Dots with error bars represent the OS minus SS data, the fitted J/ψ signal is shown by the dashed blue and the ψ(2S) by the dashed light blue lines (both modeled by Crystal-Ball + Gaussian function). The residual background (Chebychev polynomial of 2nd order) is shown by the dashed gray line [69].

Background subtraction

The pseudo-proper time distribution offers no discrimination power against the background contribution, which is also a mixture of prompt and non-prompt components. The information on the signal and background yields is thus taken from the invariant mass fits. Moreover, the shape of the background is determined using the events that fall into two side-band regions in the invariant mass distributions. During 2011 the side-bands were defined as the regions between $1.8 < m_{ee} < 2.2$ GeV and $4.3 < m_{ee} < 4.6$ GeV. Following the changes in the selection, the side-bands were instead re-defined in 2012 as follows: $2.3 < m_{ee} < 2.5$ GeV and $4.0 < m_{ee} < 4.2$ GeV.

In order to perform an unbinned fit, we again subtract the background events from our sample in a similar way as done for the mass fit, i.e. by weighting our events. We thus compute a weight which is equal to:

- $+1$ for all the events that are in the counting mass window;
- $-(N_{\mathrm{win}} - S_{\mathrm{win}})/N_{\mathrm{SB}}$ for the events in the side-bands;
- 0 elsewhere.

Here N_{win} and N_{SB} are the number of events under the J/ψ peak in the counting window and in the side-bands, while S_{win} is the signal yield extracted from the mass fit in the counting window. After applying these weights to our events, we are left with only the J/ψ signal contribution in our sample.

To make sure that the background is correctly estimated with this procedure, we have performed a closure test (see also Figure 5.26):

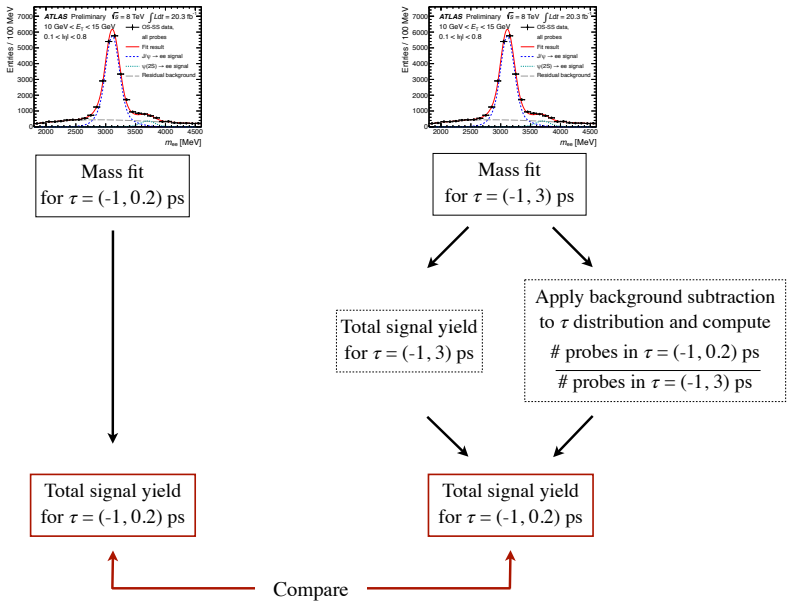

Figure 5.26 Schematic view of the closure test performed on the side-band background subtraction.

1. Perform an invariant mass fit in the range of (-1, 0.2) ps and extract the signal yield S_{02};
2. Perform an invariant mass fit in the default range of (-1, 3) ps and extract the signal yields S_{30};
3. Apply the described background subtraction and consider the τ distribution in the full range of (-1, 3) ps;
4. Extract the fraction of probes in the range of (-1, 0.2) ps to the full range of (-1, 3) ps $f_{02/30}$;
5. Compute an estimate of the signal yield in the the range of (-1, 0.2) ps as $S'_{02} = S_{30} \times f_{02/30}$;
6. Compare the two signal yield estimates S_{02} and S'_{02}.

Figure 5.27 shows the ratio S'_{02} / S_{02} for all E_{T} bins. All measurement are compatible with one within one sigma. Furthermore, a similar behaviour is observed whether we apply an identification menu on the probes or not, thus an even smaller effect on efficiencies and scale factors is observed. Different definitions of the side-bands are considered as variations, as described in Section 5.3.4.

Pseudo-proper time fit

The probability density function for the pseudo-proper time consists of two terms, one for the non-prompt J/ψ contribution from B-hadron decays and the other for the J/ψ mesons from prompt decays:

$$\mathcal{P}_{\mathrm{Signal}} = f \cdot \mathcal{P}_{\mathrm{Prompt}} + (1 - f) \cdot \mathcal{P}_{\mathrm{NonPrompt}} \ , \tag{5.4}$$

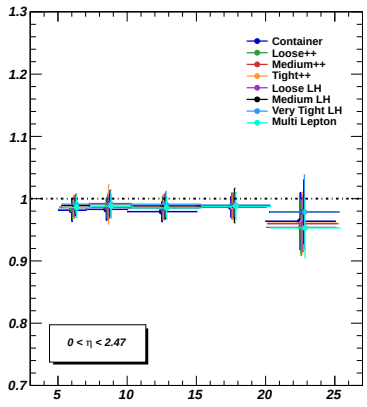

Figure 5.27 Closure test on the background subtraction method, represented here with the ratio between the signal yields S'_{02} and S_{02} for all E_T bins and for all menus. All measurements are compatible with one within one sigma, and the same bias is observed at all levels of identification, resulting in a negligible effect of the final efficiencies.

where f is the fraction we want to extract from the fit. The pseudo-proper time distribution of the J/ψ particles from B-hadron decays is an exponential function convoluted with two gaussians to account for resolution effects. The exponent of the function is fixed to the value extracted from Monte Carlo. Promptly produced J/ψ particles decay at the primary vertex, and their pseudo-proper time distribution is thus simply given by the two resolution gaussians. An unbinned maximum likelihood fit is performed on our data in the τ range between -1 and 3 ps. Example fits are shown in Figure 5.28.

The η dependence of the prompt fraction was studied in data both in 2011 and in 2012, and

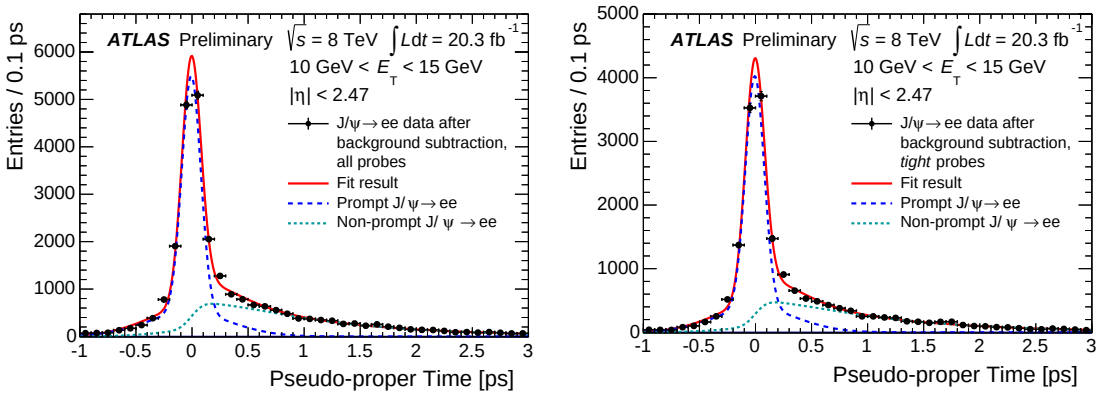

Figure 5.28 Illustration of the pseudo-proper time fit procedure. Probes from the 2012 data sample passing reconstruction + track-quality criteria are shown in the left plot, while the *tight* identification selection in also applied in the right plot. The E_{T} bin 10-15 GeV is considered, and $|\eta|$ is required to be less than 2.47. Dots with error bars represent the OS minus SS data with the residual background subtracted using the m_{ee} distribution side-bands. The signal prompt and non-prompt components are represented by the dashed blue (sum of two Gaussians) and light blue (exponential decay function convoluted with the sum of two Gaussians) lines respectively [69].

found not to be significant, as shown for example in Figure 5.29 for the 2012 analysis. For

our final results the fractions were thus extracted only in 5 E_{T} bins, integrating over the full η range, to profit from larger statistics. The resulting fraction of prompt J/ψ production is shown in Figure 5.30 for the full fit range of (-1,3) ps as well as in the range (-1,0.2) ps, using the 2011 dataset. The fractions are higher in the latter case, and increase when applying tighter identification selections, as expected. The same behaviour has been observed in 2012.

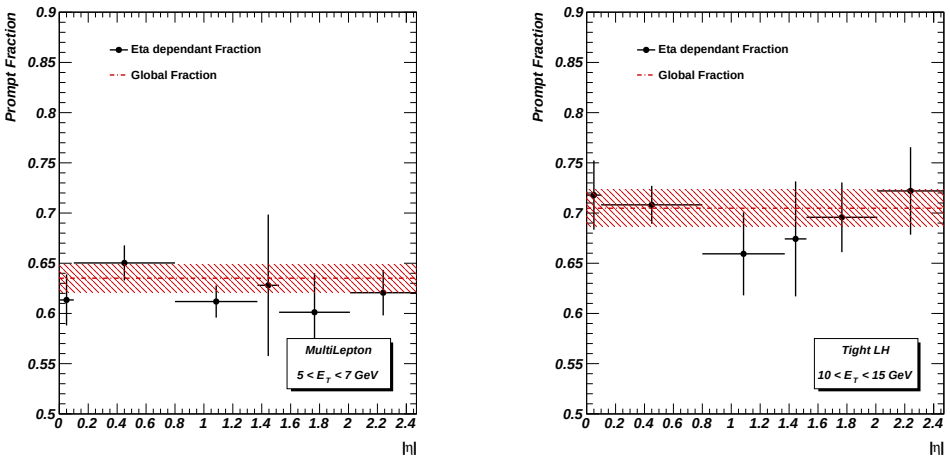

Figure 5.29 Fraction of prompt J/ψ production in 2012 analysis as a function of $|\eta|$ for $E_{\mathrm{T}} = 5 - 7$ GeV and *multilepton* selection (left), and $E_{\mathrm{T}} = 10 - 15$ GeV and VERY TIGHT LH selection (right). Errors include both statistical and systematical uncertainties.

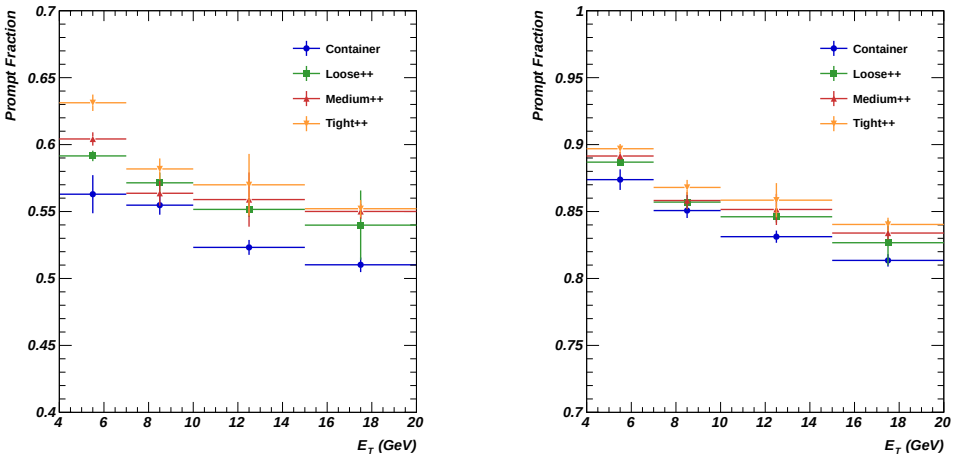

Figure 5.30 Fraction of prompt J/ψ production in 2011 analysis as a function of the probe E_{T} for the pseudo-proper time range of (-1,3) ps (left) and (-1,0.2) ps (right). Results at the denominator level and for the three cut-based identification menus available in 2011 are shown. Errors include statistical uncertainties only.

5.3.4 Systematic variations

To estimate the systematic uncertainty of the measurement, several aspects of the fitting procedure were varied, one at a time. In total 19 and 27 variations of the baseline procedure

described above were considered in 2011 and in 2012 respectively. Unless otherwise stated, the variations described below refer to both analyses.

For the invariant mass fit, the following variations are taken into account:

- the fit range is varied from nominal (1.8 - 4.6 GeV) to 1.5 - 4.6 GeV and 1.6 - 5.0 GeV;
- the counting window is varied from nominal (2.8 - 3.3 GeV) to 2.7 - 3.4 GeV and 2.9 - 3.2 GeV;
- the background shape is varied from nominal (Chebyshev polynomial of 1st or 2nd order) to Chebyshev polynomial of 0th, 1st, or 2nd order and exponential function;
- the tail parameters of the Crystal-Ball function are varied from nominal (both fixed to values extracted from MC) to both left free in the data fit;
- the χ_c component is included in the fit (2012 analysis only);
- the signal function is varied from nominal (Crystal Ball plus Gaussian) to a simple Crystal Ball (2012 analysis only), also for the case where the χ_c component is included.

The measurements are also repeated with modified tag selections. In 2011, the following requirements are applied instead of the nominal selection (tighter TRT and no isolation cuts applied):

- ${p_T}^{\text{cone0.2}}/E_T < 0.20$ after subtracting the probe track when $\Delta R^{\text{track}}_{\text{tag-probe}} < 0.2$;
- $E_T^{\text{cone0.2}}/E_T < 0.15$ and $\Delta R^{\text{calo}}_{\text{tag-probe}} > 0.22$;
- $E_T^{\text{cone0.2}}/E_T < 0.30$ and $\Delta R^{\text{calo}}_{\text{tag-probe}} > 0.22$;

Similarly, in 2012 the nominal selection (${p_T}^{\text{cone0.2}}/E_T < 0.15$, but no tighter TRT cut applied) is varied requiring the tag to pass:

- tighter constraint on the fraction of high-threshold hits in the TRT;
- ${p_T}^{\text{cone0.2}}/E_T < 0.02$ after subtracting the probe track when $\Delta R^{\text{track}}_{\text{tag-probe}} < 0.2$;
- $E_T^{\text{cone0.2}}/E_T < 0.20$ and $\Delta R^{\text{calo}}_{\text{tag-probe}} > 0.22$;
- $E_T^{\text{cone0.2}}/E_T < 0.30$ and $\Delta R^{\text{calo}}_{\text{tag-probe}} > 0.22$;
- no isolation cut.

Finally, the pseudo-proper time fit procedure is also modified in the following ways:

- the fit range is varied from nominal (-1, - 3) ps to (-0.5, - 2.5) ps and (-1.5, 3.5) ps;
- the exponent of the decay function describing the non-prompt contribution is varied from nominal (fixed to values extracted from MC) to left free in the data fit;

- the mean of the Gaussians describing the pseudo-proper time resolution are varied from nominal (fixed to values extracted from MC for the non-prompt, and free for the prompt component) to either both fixed or both left free.

The side-bands definition in 2011 analysis is modified from nominal (1.8 - 2.2 GeV and 4.3 - 4.6 GeV) to:

- 1.8 - 2.1 GeV and 4.2 -4.6 GeV
- 1.8 - 2.3 GeV and 4.4 - 4.6 GeV

while in 2012 it is varied from the nominal (2.3 - 2.5 GeV and 4.0 - 4.2 GeV) to

- 2.1 - 2.3 GeV and 4.0 - 4.2 GeV
- 2.1 - 2.5 GeV and 4.0 - 4.2 GeV
- 2.3 - 2.5 GeV and 4.0 - 4.3 GeV
- 2.3 - 2.5 GeV and 4.2 - 4.4 GeV
- 2.3 - 2.5 GeV and 4.3 - 4.6 GeV

The central values of the measurements are calculated as the mean over all variations, while the systematic errors are estimated as the RMS over all variations. The statistical error is taken as the average of the statistical errors. Variations resulting in the failure of the fit ($\chi^2/dof > 3-5$ depending on the η bin and the fit type) are excluded from the average. Pathological cases where the efficiency is greater than one are also excluded from our measurement. The stability of the results is illustrated in Figure 5.31, where the scale factors for all variations are shown for *loose* and VERY TIGHT LH in two example bins.

5.3.5 Efficiency and scale factor results

As already explained in Section 5.3.1, a number of different isolation cuts on the probe were considered, together with the case in which no isolation is instead applied. Moreover, in 2012, the analysis was repeated for four different pseudo-proper time ranges, as described in Section 5.3.1. This led to 5 different isolation configurations in 2011, and 12 configurations in 2012, each arising from the combination of a given isolation cut and a given pseudo-proper time range. For each of these configurations, we have provided a full set of efficiency and scale factor measurements, each including all the systematic variations described above. It is thus possible to compare the results obtained with different probe isolation and τ settings.

In Figure 5.32 we compare the scale factors[11] (2012 analysis) at a given isolation cut on the probe ($p_{\mathrm{T}}{}^{\mathrm{cone0.2}}/E_{\mathrm{T}} < 0.15$) for different pseudo-proper time ranges. Both statistical and systematic uncertainties are shown for each configuration. It appears that, while in some complicated bins (as in the transition region, for example) there is a difference between the various ranges, no specific trend is in general visible.

[11] Notice that, unless specifically stated, we always refer to scale factors and efficiencies extracted for electrons arising from prompt J/ψ decays.

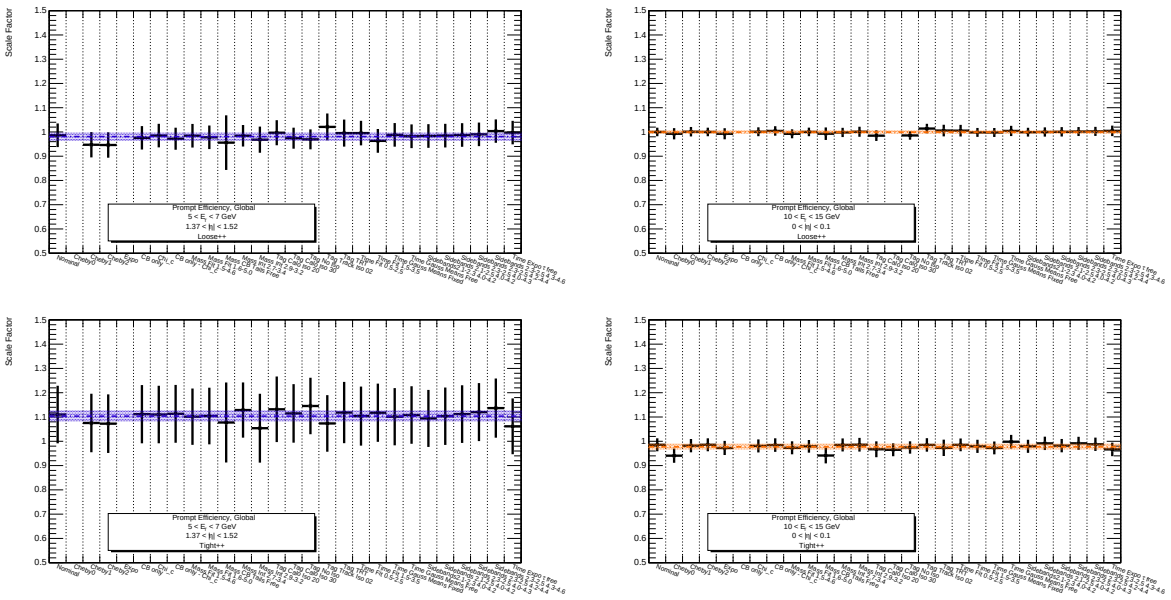

Figure 5.31 Scale factor results for all variations considered in 2012 analysis. Two representative identification menus are shown, *loose* (left) and *tight* (right), for the pseudo-proper time range of (-1,3) ps, and for E_{T}=5-7 GeV and $|\eta| = 1.37 - 1.52$ (top) and for E_{T}=10-15 GeV and $|\eta| = 0 - 0.1$ (bottom). The error bars on the individual scale factor measurements are statistical only. The coloured bands illustrate the RMS of the variations around their mean value. Missing measurements correspond to discarded variations (see text). The stability of the measurements is clearly visible in all plots.

In Figure 5.33 we compare instead the scale factors (2012 analysis) obtained at a given pseudo-proper time range, $-1 < \tau < 3$ ps, for different isolation cuts. In general scale factors are higher (closer to 1) when isolation on the probe is applied. The same trend has been observed in 2011.

Being able to separate the prompt and non-prompt contributions in data implies that, not only we are able to provide efficiencies and scale factors for clean prompt J/ψ electrons, but also that we can compare them to the measurements extracted for non-prompt electrons. These electrons, produced in the busy environment of b-hadron decays, are expected to be less isolated and, consequently, have lower efficiencies with respect to prompt electrons. This trend is indeed observed, and visible for example in Figure 5.34 where data and MC efficiencies are shown together for both the prompt and the non-prompt 2011 samples, for all identification menus and for all bins.

The 2012 measured scale factors using the short-τ and the τ-fit methods (also referred to as short-lifetime and lifetime-fit methods, respectively) are compared in Figure 5.35. These results arise from combining together some of the available configurations for a given method. For the short-τ results, all the variations with isolation requirements, as well as two choices of the pseudo-proper time range, namely $-1 < \tau < 0.2$ ps and $-1 < \tau < 0.4$ ps, are combined together. In the case of the τ-fit method, all the examined isolation cuts on the probe are again considered, and two possibilities regarding the pseudo-proper time range are compared: either combining $-1 < \tau < 0.2$ ps and $-1 < \tau < 0.4$ ps as above, or $-1 < \tau < 0.2$ ps and

$-1 < \tau < 3$ ps, with the latter including events from the full pseudo-proper time range. A nice agreement is observed for the two methods.

As mentioned in Section 5.2.4, being based on the the same data-sample, the two J/ψ methods are not included into the combination framework as independent measurements, but rather combined together as systematic variations of the same measurement.
In the combinations leading to the final 2011 and 2012 scale factor measurements, all the configurations with different isolation requirements on the probe were included for the two methods. Moreover, for 2012 final results, the $-1 < \tau < 0.2$ ps and $-1 < \tau < 0.4$ ps ranges were considered for the short-τ method, while for the τ-fit method the $-1 < \tau < 0.2$ ps and $-1 < \tau < 3$ ps ranges were used to cover possible biases from the truncated pseudo-proper time distribution.

After combination of the two methods, a precision better than 2% (4%) is achieved in the challenging lowest E_{T} region (7-10 GeV) on the efficiency measurement for the LOOSE LH (*loose*) identification menu used in the $H \to ZZ^* \to 4\ell$ analysis in 2012 (2011).

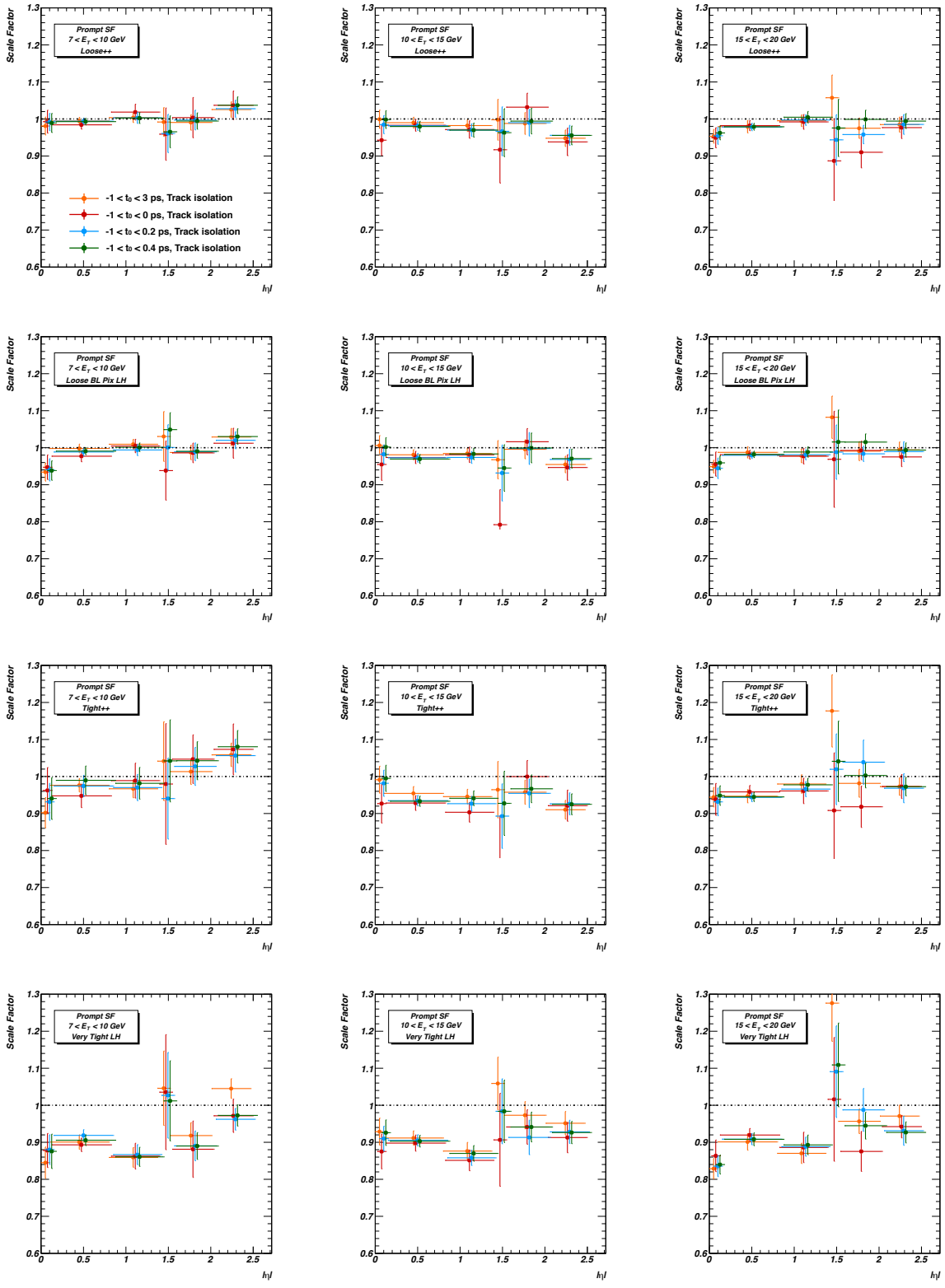

Figure 5.32 Identification efficiency scale factors as a function of $|\eta|$ for a given isolation cut on the probe ($p_{\mathrm{T}}{}^{\mathrm{cone0.2}}/E_{\mathrm{T}} < 0.15$) and for different E_{T} bins: 7-10 GeV (first column), 10-15 GeV (second column), 15-20 GeV (third column). Results obtained for the considered pseudo proper time ranges are overlaid: (-1, 3) ps, (-1, 0) ps, (-1, 0,2) ps, (-1, 0.4) ps are indicated by orange, red, azure and green markers, respectively.

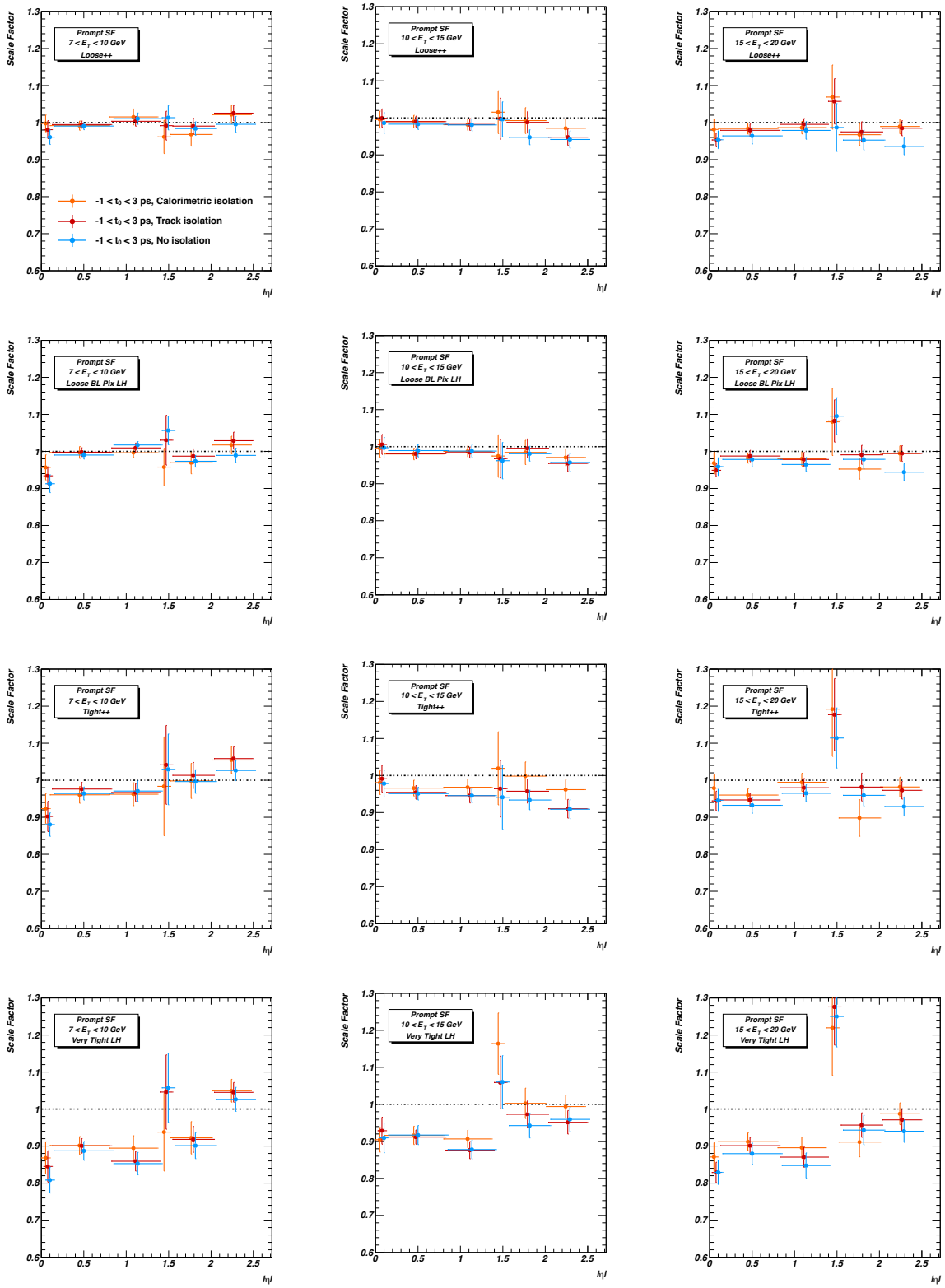

Figure 5.33 Identification efficiency scale factors as a function of $|\eta|$ for a given pseudo-proper time range ($-1 < t_0 < 3$ ps) and for different E_{T} bins: 7-10 GeV (first column), 10-15 GeV (second column), 15-20 GeV (third column). Results obtained when applying a calorimetric isolation cut on the probe ($E_{\mathrm{T}}^{\mathrm{cone0.2}}/E_{\mathrm{T}} < 0.20$), a track isolation cut on the probe ($p_{\mathrm{T}}^{\mathrm{cone0.2}}/E_{\mathrm{T}} < 0.15$), or no isolation cut at all, are shown in orange, red and azure markers, respectively.

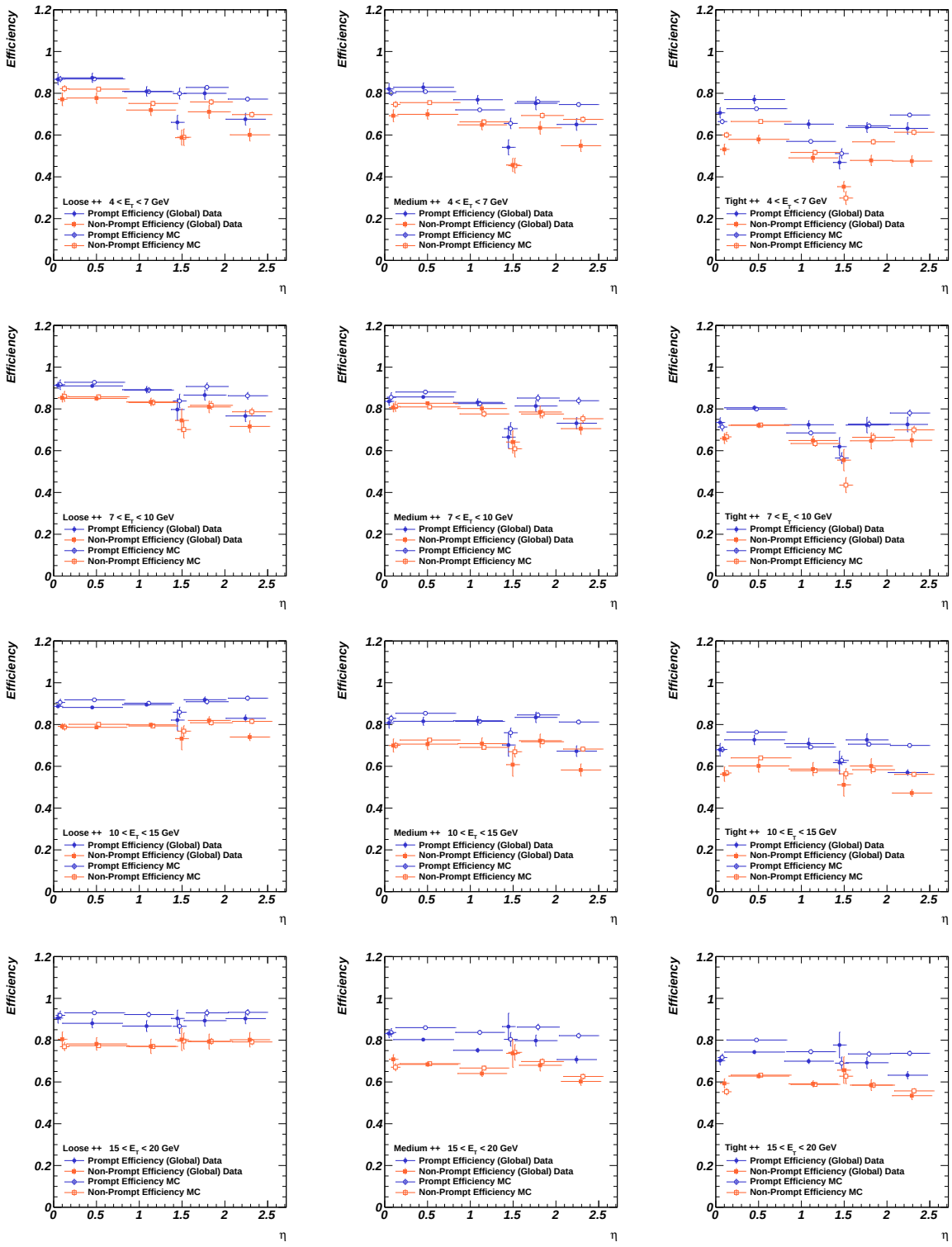

Figure 5.34 Identification efficiency measured by the τ-fit method in 2011 for prompt (blue) and non-prompt (orange) components separately, compared to the MC predictions (empty markers), as a function of $|\eta|$ for the three cut based selections and the different E_{T} bins (row 1) 4-7 GeV, (row 2) 7-10 GeV, (row 3) 10-15 GeV, (row 4) 15-20 GeV. Results for the nominal variation are shown, thus errors include statistical uncertainties only.

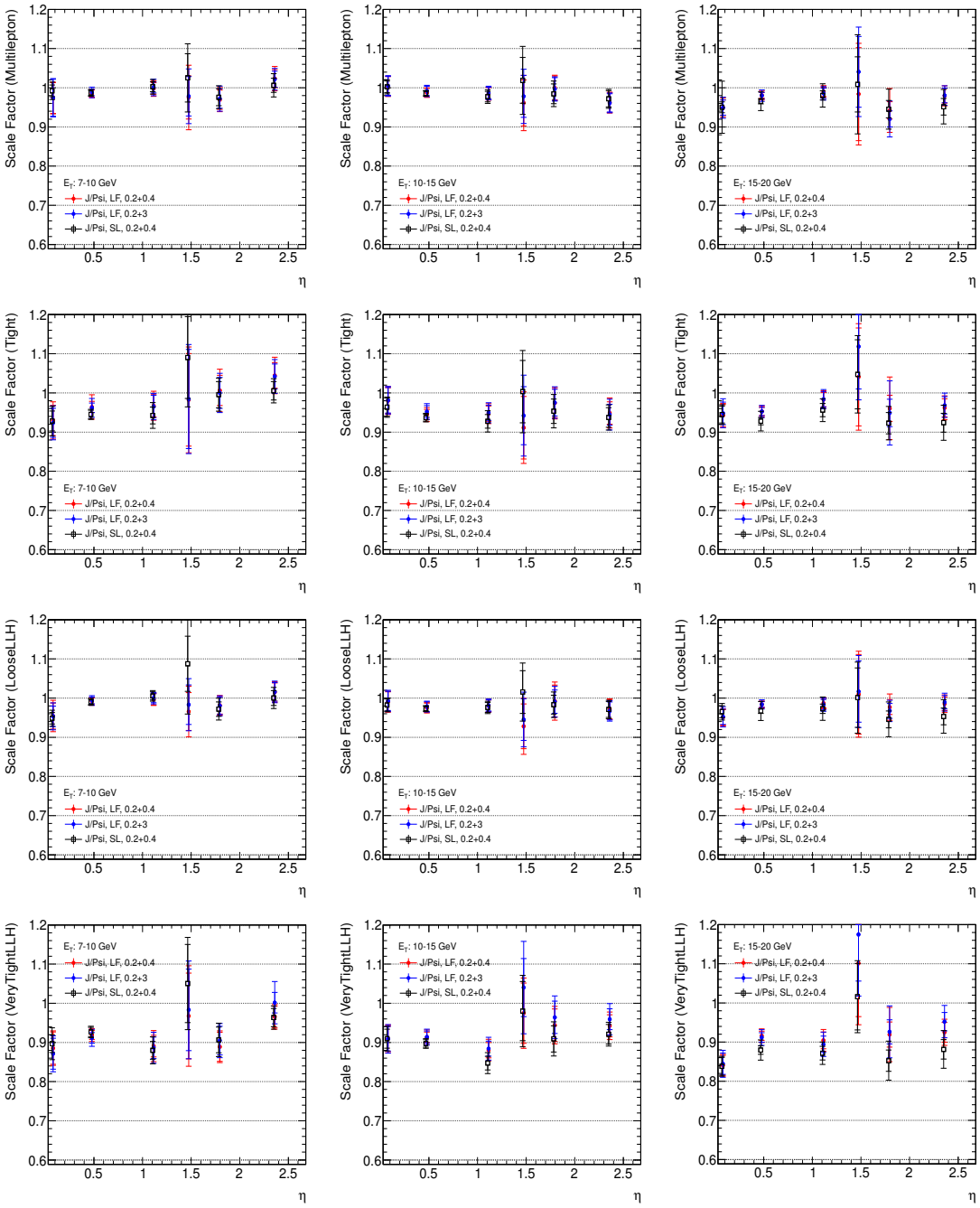

Figure 5.35 Measured scale factors as a function of $|\eta|$ for E_{T} = 7-10, 10-15, and 15-20 GeV (from left to right) for different identification menus: *multilepton*, *tight*, LOOSE LH, and VERY TIGHT LH (from top to bottom). The results of the short-lifetime ("SL") and the lifetime-fit ("LF") methods are compared. Inner error bars are statistical, while the outer bars indicate the full statistical plus systematic errors. In the case of the short-lifetime method selection variations with $-1 < \tau < 0.2$ ps and $-1 < \tau < 0.4$ ps, and all the variations with isolation requirement are combined together. For the lifetime-fit method two possibilities are compared: either considering $-1 < \tau < 0.2$ ps and $-1 < \tau < 0.4$ ps as above, or $-1 < \tau < 0.2$ ps and $-1 < \tau < 3$ ps with the latter including events from the full pseudo-proper time range. In both possibilities, all the variations with isolation requirement are included.

Chapter 6

$H \to ZZ^* \to 4\ell$ Analysis: Event Selection

The final chapters of this thesis discuss the measurement of the properties of the Higgs boson in the decay channel $H \to ZZ^* \to 4\ell$, and the work done by the author within this analysis. Despite its relatively low cross section, compared to the $H \to \gamma\gamma$ and $H \to WW^* \to \ell\nu\ell\nu$ channels, the $H \to ZZ^* \to 4\ell$ decay is universally known as the golden channel, as it offers a clean signature and a high signal-to-background ratio, as well as the capability to fully reconstruct the final state. The study of the $H \to ZZ^* \to 4\ell$ decay channel indeed provided a unique opportunity in the search for the Higgs boson and, after a new particle was discovered, it allowed to confirm its SM-like nature by precisely measuring its properties.

The author of this thesis has been involved in the $H \to ZZ^* \to 4\ell$ analysis since the time of the discovery. However, only the most recent results in terms of mass, production rates, and fiducial and differential cross section measurements are described here.
This part of the thesis is organised in four chapters, where the first two address those aspects of the analysis which are mostly common to all the measurements. The simulation samples and the analysis selection are presented in the remainder of this chapter, while the evaluation of the background sources, to which the author significantly contributed, are described separately in Chapter 7.

The final ATLAS Run 1 measurements of the Higgs boson mass, production and couplings in the decay channel $H \to ZZ^* \to 4\ell$ are presented in Chapter 8. The updated mass measurement, improved with respect to the previous result [1] also thanks to the improvements in the electron reconstruction, identification and energy calibration described in Chapters 4 and 5, is discussed in detail. The mass measurement obtained from the combination of the $H \to ZZ^* \to 4\ell$ and $H \to \gamma\gamma$ results [2] is only briefly presented.
The method adopted to extract the mass measurement simultaneously provides a measure of the production rate relative to the SM expectation, the signal strength μ, which is also presented. The Higgs couplings are instead tested by studying the production rates with events categorised according to the characteristics of the different production modes. This categorised analysis allows to place constraints on possible deviations from the expected couplings of the SM Higgs boson.

Finally, Chapter 9 presents a newly published measurement of the fiducial and differential

cross sections of Higgs boson production in the $H \to ZZ^* \to 4\ell$ decay channel based on the 8 TeV data sample. Fiducial cross sections are quoted in order to minimise the model dependence of the acceptance corrections related to the extrapolation to phase-space regions not covered by the detector. The measured fiducial cross sections are also corrected for detector effects to be directly compared to theoretical calculations. The differential measurements are performed in several observables related to the Higgs boson production and decay. The author of this thesis has contributed to these results with the measurement of the fiducial cross section and the estimation of the background related systematic uncertainties for both the fiducial and differential measurements.

The remainder of this chapter is organised as follows: Section 6.1 describes the datasets and simulated samples used to model signal and background events. A study on the different ZZ^* MC generators, performed by the author of this thesis, is also presented in this Section. Section 6.2 illustrates the triggers used in the analysis, while Section 6.3 describes the reconstruction of the various objects present in our final state. The selection applied on the samples to isolate the signal region is finally presented in Section 6.4, while the further categorisation aiming at differentiating the Higgs candidates according to their production mechanism is illustrated in Section 6.4.1.

6.1 Data and Simulated Samples

6.1.1 Data samples

The data samples used for the mass, production and coupling measurements correspond to an integrated luminosity of 4.5 fb^{-1} at a center-of-mass energy of 7 TeV, and to 20.3 fb^{-1}at a center-of-mass energy of 8 TeV, collected in the years 2011 and 2012, respectively. Only the 8 TeV data sample is used for the fiducial and differential cross sections measurements. A few important parameters describing the differences between the data-taking conditions during the 2011 and 2012 campaigns are summarised in Table 6.1.

Table 6.1 Differences between 2011 and 2012 data-taking campaigns.

Year	Energy ($\sqrt{s}$)	Peak luminosity	Pile-up ($<\mu>$)	Data	Data taking efficiency	Data quality efficiency
2011	7 TeV	3.65 $\times 10^{33}$cm^{-2}s^{-1}	9.1	4.5 fb^{-1}	~96.5%	~89.9%
2012	8 TeV	7.73 $\times 10^{33}$cm^{-2}s^{-1}	20.3	20.3 fb^{-1}	~95.5%	~95.3%

6.1.2 Monte Carlo samples

Monte Carlo signal samples

The POWHEG-BOX MC event generator [87, 88] is used to model the $H \to ZZ^* \to 4\ell$ signal, providing separate calculations for the gluon fusion (ggF) and vector-boson fusion (VBF) production mechanisms with matrix elements up to next-to-leading order (NLO). A reweighing

of the Higgs boson transverse momentum in the ggF process is applied, following the calculation in [89, 90], which includes QCD corrections up to next-to-next-to-leading order (NNLO) and QCD soft-gluon resummations up to next-to-next-to-leading logarithm (NNLL). The effects of non-zero quark masses are also taken into account [91]. POWHEG-BOX is interfaced to PYTHIA8.1 [92,93] for showering and hadronisation, which in turn is interfaced to PHOTOS [94,95] for QED radiative corrections in the final state. The production of the Higgs boson in association with a vector boson, $pp \to WH$ or $pp \to ZH$ (VH), as well as the associated production with a top quark pair, $pp \to t\bar{t}H$ ($t\bar{t}H$), is simulated using PYTHIA8.1. The production of a Higgs boson in association with a b quark pair ($b\bar{b}H$) is included in the signal yield assuming the same signal efficiency as for the ggF production, while the m_{H} dependence is assumed to be equal to that for the $t\bar{t}H$.

The Higgs boson production cross sections and decay branching ratios, as well as their uncertainties, are taken from [96, 97].
The cross sections for the gluon-fusion process have been calculated to NLO [98–100] and to NNLO [101–103] in QCD, and they include QCD soft-gluon resummations calculated in the NNLL approximation for the ggF process [104]. NLO electroweak radiative corrections are also taken into account [105, 106]. These results are compiled in [107–109] assuming factorisation between QCD and EW corrections.
The VBF cross section is calculated using full QCD and EW corrections up to NLO [110–112], and approximate NNLO QCD [113].
The cross sections for the associated WH/ZH production processes are calculated at NLO [114] and at NNLO [115] in QCD, and NLO EW radiative corrections are applied [116].
The cross sections for the $t\bar{t}H$ production process is estimated up to NLO in QCD [117–120].

The Higgs boson decay widths for the WW and the ZZ four-lepton final states are predicted by PROPHECY4F [121, 122], which includes the complete NLO QCD+EW corrections as well as interference effects between identical final-state fermions. The $H \to ZZ^* \to 4\ell$ branching ratios are obtained combining PROPHECY4F results to the ones from HDECAY [123], which is used to simulate the other Higgs boson decay widths, e.g. $\gamma\gamma$, $\tau\tau$, $b\bar{b}$, etc. In Table 6.2 we summarise the production cross sections and branching ratios for $H \to ZZ^* \to 4\ell$ used to normalise the signal MC samples for several values of the Higgs boson mass.

The QCD scale uncertainties for $m_{\mathrm{H}} = 125$ GeV [96] amount to $+7\%$ and -8% for the ggF process, between $\pm 1\%$ to $\pm 2\%$ for the VBF and VH production processes, and $+4\%$ and -9% for the associated $t\bar{t}H$ production process. The uncertainties on the production cross section due to uncertainties on the parton distribution function (PDF) and the strong coupling constant, α_s, is $\pm 8\%$ for $gg \to H$ processes and $\pm 4\%$ for $q\bar{q} \to H$ processes, estimated according to the prescription in [124] and by using the PDF sets of CTEQ [125], MSTW [126] and NNPDF [127]. The PDF uncertainties of processes with identical initial states are assumed to be 100% correlated, regardless of their being signal or background [128].

Monte Carlo background samples

The continuum $(Z^{(*)}/\gamma^*)(Z^{(*)}/\gamma^*)$ background, referred to as ZZ^* hereafter, is modelled using POWHEG-BOX [129] for $q\bar{q} \to ZZ$, and GG2ZZ [130] for $gg \to ZZ$. The PDF+α_s and QCD

scale uncertainties are parametrised as functions of $m_{4\ell}$ following the recommendations in [97]. For the ZZ^* background at $m_{4\ell} = 125$ GeV, the quark-initiated (gluon-initiated) processes have a QCD scale uncertainty of $\pm 5\%$ ($\pm 25\%$), and $\pm 4\%$ ($\pm 8\%$) for the PDF and α_s uncertainties, respectively.

The production of a Z boson associated with jets is simulated using ALPGEN [131] and is divided into two sources: Z+light jets and $Z + b\bar{b}$. The former includes $Z + c\bar{c}$ in the massless c-quark approximation and $Z + b\bar{b}$ with $b\bar{b}$ from parton showers, while the latter uses matrix-element calculations to account for the b-quark mass. The double counting of identical jets produced via the matrix-element calculation and the parton shower is removed using the MLM [132] matching scheme. However, this scheme is not implemented for b-jets. Therefore, $b\bar{b}$ pairs with separation $\Delta R \equiv \sqrt{(\Delta\phi)^2 + (\Delta\eta)^2} > 0.4$ between the b-quarks are taken from the matrix-element calculation, while for $\Delta R < 0.4$ the parton-shower $b\bar{b}$ pairs are used. In this search the Z+jets background is normalised using control samples from data. For comparison between data and simulation, the NNLO QCD FEWZ [133, 134] and NLO QCD MCFM [135, 136] cross section calculations are used to normalise the simulations for inclusive Z boson and $Z + b\bar{b}$ production, respectively.

The $t\bar{t}$ background is modelled using POWHEG-BOX interfaced to PYTHIA8.1 for parton shower and hadronisation, PHOTOS for QED radiative corrections and TAUOLA [137, 138] for the simulation of τ lepton decays.

Finally, SHERPA [139] is used for the simulation of WZ production.

Generated events are processed through the ATLAS detector simulation [140] within the GEANT4 framework [141]. Additional pp interactions in the same and nearby bunch crossings are included in the simulation. The simulation samples are weighted to reproduce the distribution of the mean number of interactions per bunch crossing observed in data.

m_H [GeV]	$\sigma(gg \to H)$ [pb]	$\sigma(qq' \to Hqq')$ [pb]	$\sigma(q\bar{q} \to WH)$ [pb]	$\sigma(q\bar{q} \to ZH)$ [pb]	$\sigma(q\bar{q}/gg \to b\bar{b}H/t\bar{t}H)$ [pb]	$B(H \to ZZ^* \to 4\ell)$ [10^{-3}]
$\sqrt{s} = 7$ TeV						
123	15.6 ± 1.6	1.25 ± 0.03	0.61 ± 0.02	0.35 ± 0.01	0.26 ± 0.04	0.103 ± 0.005
125	15.1 ± 1.6	1.22 ± 0.03	0.58 ± 0.02	0.34 ± 0.01	0.24 ± 0.04	0.125 ± 0.005
127	14.7 ± 1.5	1.20 ± 0.03	0.55 ± 0.02	0.32 ± 0.01	0.23 ± 0.03	0.148 ± 0.006
$\sqrt{s} = 8$ TeV						
123	19.9 ± 2.1	1.61 ± 0.05	0.74 ± 0.02	0.44 ± 0.02	0.35 ± 0.05	0.103 ± 0.005
125	19.3 ± 2.0	1.58 ± 0.04	0.70 ± 0.02	0.42 ± 0.02	0.33 ± 0.05	0.125 ± 0.005
127	18.7 ± 1.9	1.55 ± 0.04	0.67 ± 0.02	0.40 ± 0.02	0.32 ± 0.05	0.148 ± 0.006

Table 6.2 Calculated SM Higgs boson production cross sections for gluon fusion, vector-boson fusion and associated production with a W or Z boson or with a $b\bar{b}$ or $t\bar{t}$ pair in pp collisions at $\sqrt{s}$ of 7 TeV and 8 TeV. The quoted uncertainties correspond to the total theoretical systematic uncertainties calculated by adding in quadrature the QCD scale and PDF+α_s uncertainties. The decay branching ratio (B) for $H \to 4\ell$ (with $\ell = e, \mu$), is reported in the last column.

Studies on ZZ^* background MC generators

The main purposes of the study presented here have been the improvement of our understanding of the ZZ^* background simulation and the reduction of the related uncertainties, through comparison of the performance of different MC generators.

In the SM, events with two Z bosons decaying into four leptons can be produced at leading order (LO) from a pair of quarks or gluons, via the three possible Feynman diagrams displayed in Figure 6.1. The $q\bar{q} \to ZZ^*$ diagram in 6.1(a) is referred to as singly-resonant (or s-channel), while the one in 6.1(b), is called doubly-resonant (or t-channel).

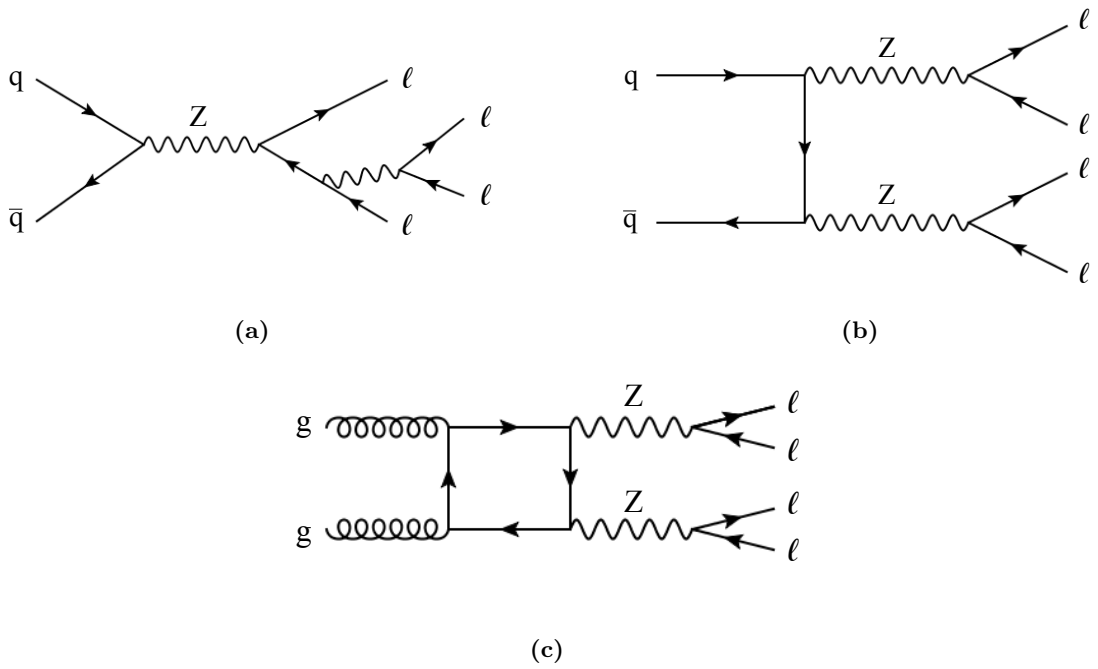

Figure 6.1 Feynman diagrams representing the SM processes in which two Z bosons decaying into four leptons can be produced. The quark-initiated diagram in (a) is referred to as singly-resonant (or s-channel), while the one in (b), is called doubly-resonant (or t-channel). The diagram in 6.1(c) is instead called gluon fusion production.

At the time of the study, which was made at the beginning of the 2012 data taking campaign, the ZZ^* background was generated using PYTHIA, which does not include the singly resonant diagram, nor the gluon fusion production (6.1(c)), and only uses LO calculations for the doubly-resonant contribution. The inclusive total cross section and the shape of the m_{ZZ^*} spectrum had to be thus normalised using a k-factor taken from the MCFM prediction, including both $q\bar{q}$ annihilation at QCD NLO and gluon fusion. A resulting 15% theoretical uncertainty was applied to the analysis published in September 2011 [142].

A new implementation of the vector-boson pair production process at NLO was provided afterwards in POWHEG-BOX [129], with the Z/γ^* interference and the singly-resonant ($Z \to 4\ell$) contributions properly included, and the interference terms arising from identical leptons in the final state also considered.

The use of this generator would clearly improve the modelling of the ZZ^* background in our analysis, and its performance were hence studied and compared to that of PYTHIA.

The $gg \to ZZ^*$ contribution, not included in POWHEG-BOX, was instead studied using GG2ZZ,

which computes the $gg \to ZZ^*$ at LO, corresponding to order α_s^2, compared to α_s^0 for the LO $q\bar{q} \to ZZ^*$.
For the sake of completeness, SHERPA was also considered in the comparison, which includes all four-lepton final states at LO. As for PYTHIA, a k-factor from MCFM is used to normalise the cross section.

The study was made using truth information at generator level as well as at particle level. In the former case, the truth objects are taken as they are generated in the various samples, while in the latter case the particles undergo energy losses when traversing the detector. It is possible to recombine the photons emitted by the "bare" leptons with the final state lepton, and in this case we refer to "dressed" particles. All photons found in a cone of $\Delta R = 0.1$ around the leptons are considered in this "dressing" procedure.
The event selection is made requiring four final-state leptons, either electrons or muons, with $p_{\mathrm{T}} > 7$ GeV and $|\eta| < 2.7$. Leptons coming from the same Z boson are paired together. The mass of both Z bosons are required to be within 15 and 115 GeV, and m_Z is required to be within 66 and 106 GeV for at least one Z. Finally, the invariant mass of the four leptons is required to be above 40 GeV[1].

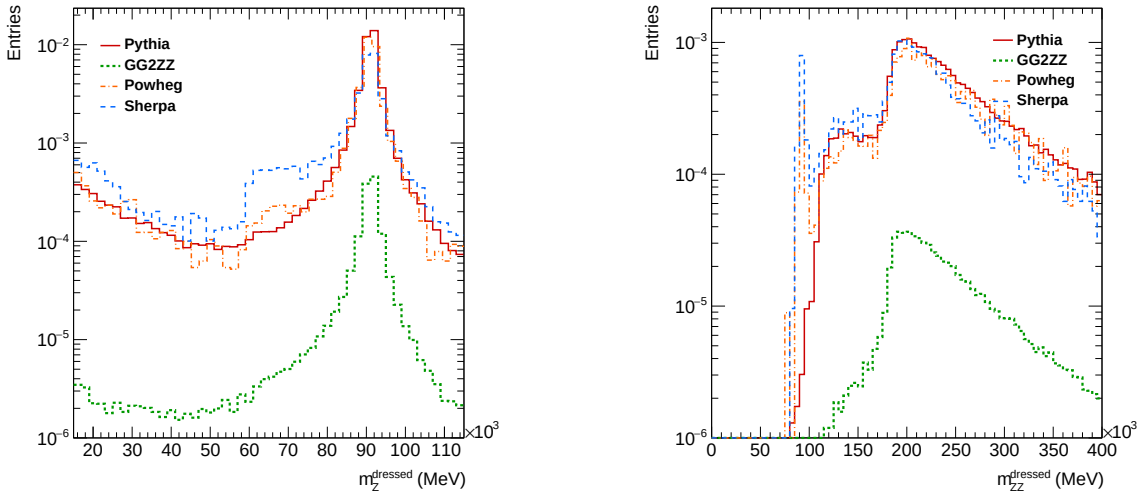

(a) **(b)**

Figure 6.2 The dilepton (a) and four-lepton (b) invariant masses are shown for different MC generators: PYTHIA (red), GG2ZZ (green), POWHEG-BOX (blue), and SHERPA (orange). The four momenta of dressed leptons are used to compute both quantities. All distributions are normalised according to the cross sections and filter efficiencies of each sample.

The dilepton and four-lepton invariant mass distributions are shown in Figure 6.2 for all the considered generators. In this case, the four momenta of dressed leptons are used to compute both quantities. All distributions are normalised according to the cross sections and filter efficiencies of each sample, which explains why the GG2ZZ contribution is much smaller with respect to the others.

[1]The applied kinematics cuts follow the ones used in the analysis at the time of the study.

The relatively small differences in the $m_{\ell\ell}$ distributions between PYTHIA, POWHEG-BOX and SHERPA come from the different levels of calculation, from the gluon contribution – included in the k-factors applied on PYTHIA and SHERPA but not in POWHEG-BOX –, and from the specific filter cuts used to generate the samples. As already mentioned, another important difference is the lack of the singly-resonant $q\bar{q}$ diagram in PYTHIA, which is clearly visible when looking at the $m_{4\ell}$ distribution in 6.2(b).

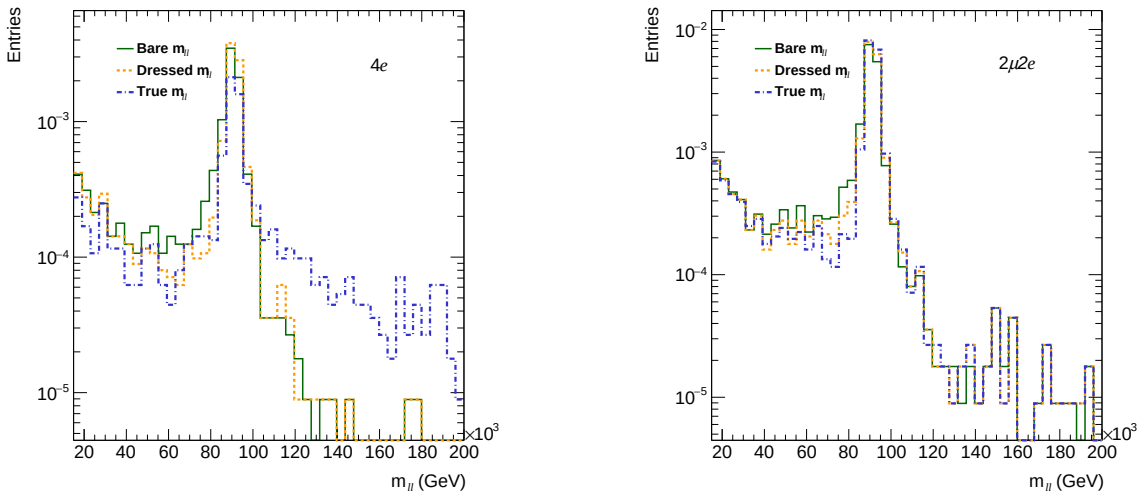

(a) **(b)**

Figure 6.3 The dilepton invariant mass distribution, as obtained with POWHEG-BOX, is shown when considering exclusively final states with four electrons (a), or with two electrons and two muons (b). The green, orange and blue line represent the results obtained by taking directly the true Z mass, or computing it from the four momenta of bare or dressed leptons.

Figure 6.3 shows instead a particular feature of the POWHEG-BOX generator, which was identified as a result of this study. The $m_{\ell\ell}$ distribution is again shown, but this time only for POWHEG-BOX, and considering exclusively final states with four electrons (6.3(a)), or final states with two electrons and two muons (6.3(b)). The results obtained by computing the invariant mass from the four momenta of true, bare or dressed leptons are compared. The cut on $m_{\ell\ell}$ is released from 115 to 200 GeV. An important disagreement in the high $m_{\ell\ell}$ region between the true mass curve and the other two is clearly visible in the $4e$ plot. The origin of this particular behaviour was investigated by the authors of POWHEG-BOX code, and found to be related to interference effects between identical leptons. When the interference among four electrons or muons in the final state is taken into account, it is in fact no longer possible to assign the pairs of leptons to a specific Z, and the truth information is thus no longer accurate. This effect, which is hence linked to having four identical leptons in the final state, has no impact on the case of mixed channels, as can indeed be seen from Figure 6.3(b).
While this effect prevents any truth study based on $4e$ and 4μ events, it is an unavoidable aspect of the underlying physics described by the generator, and has no effect on the analysis. It was therefore finally decided to adopt POWHEG-BOX for the modelling of the ZZ^* background, as seen in the previous section. The related uncertainties, also illustrated in Section 6.1.2, are

substantially reduced with respect to the values assigned when using PYTHIA.

6.2 Trigger Selection

Four-lepton events were selected using single-lepton and dilepton triggers. Due to the increasing instantaneous luminosity, the p_{T} and E_{T} thresholds were raised between 2011 and 2012 for both single and dilepton triggers. An additional dimuon asymmetric trigger with different thresholds on the two muons' p_{T} was introduced in 2012. The applied thresholds are summarised in Table 6.3.
The trigger efficiency for events passing the final analysis selection is always above 97%, and close to 100% in the case of four electrons in the final state for both 7 TeV and 8 TeV data.
In the event selection, reconstructed objects are required to match the ones that fired the trigger. In particular, the events are considered if either a reconstructed lepton matches the single lepton trigger object, or two leptons match the di-lepton trigger objects.

Table 6.3 Single lepton and dilepton trigger p_{T} and E_{T} thresholds (for muons and electrons respectively) during 2011 and 2012 data-taking.

	$\sqrt{s} = 7$ TeV	$\sqrt{s} = 8$ TeV
Single lepton triggers		
muon	18 GeV	25 GeV
electron	20→22 GeV	24 GeV
Dilepton triggers		
di-muon (symmetric)	10-10 GeV	13-13 GeV
di-muon (asymmetric)	-	8-18 GeV
di-electron	12-12 GeV	12-12 GeV
electron-muon	6-8 GeV	8-12 GeV

6.3 Object Reconstruction and Identification

6.3.1 Electron reconstruction and identification

In 2012, electron candidates are reconstructed according to the standard scheme described in Chapter 4, which includes, together with the improved pattern recognition, also the new optimised electron track fitter. The GSF algorithm was included in the default reconstruction scheme only in 2012, but thanks to the validation studies described in Section 4.1.5 it could be already used in the $H \to ZZ^* \to 4\ell$ for the 2011 data sample.

In order to maintain large acceptance and good discrimination, the identification selection is kept "loose". The cut-based *loose* selection is used in 2011, while the improved likelihood-based LOOSE LH selection is applied in 2012.

In both data samples the electron cluster energy is corrected following the new calibration scheme described in Section 4.1.6. As seen from the studies discussed in Section 4.1.7, the use of this improved procedure in our analysis brings marginal improvements upon the energy resolution. On the other hand, it resulted in a significant reduction in the overall energy scale

uncertainty – for $|\eta| < 1.37$ the uncertainty is reduced, for example, from 0.4% to 0.04% for electrons of $E_{\mathrm{T}} = 40$ GeV – and has an important impact on the systematic uncertainty of the Higgs boson mass measurement.
In addition, a combined fit of the cluster energy and track momentum is applied to electrons with E_{T} below 30 GeV when the cluster E_{T} and the track p_{T} agree within their uncertainties. The combined fit improves the resolution of $m_{4\ell}$ for the $4e$ and $2\mu 2e$ final states by about 4%.

6.3.2 Muon reconstruction and identification

All four muon types introduced in Section 4.2 – i.e. combined, standalone, segment-tagged and calorimeter-tagged muons – are used in the analysis. Nevertheless, at most one standalone or calorimeter-tagged muon is accepted in the event, due to the higher fake rate associated to these muon types. For all but standalone muons, which fall outside the ID acceptance, the inner detector tracks are required to have a minimum number of associated hits in each sub-detector to ensure good track reconstruction. Standalone muons are instead required to have hits in each of the three stations they traverse.

6.3.3 Final-state radiation recovery

Final-state radiation photons are recovered and included into the four-lepton measurement. Both collinear ($\Delta R_{\mathrm{cluster},\mu} \leq 0.15$) and non-collinear ($\Delta R_{\mathrm{cluster},\ell} > 0.15$) photons are searched for and associated with muons[2] in the first case, and with either muons or electrons in the second case. The collinear photons are required to have a transverse energy of $E_{\mathrm{T}} > 1.5$ GeV and a fraction of the total energy deposited in the front sampling layer of the calorimeter greater than 0.1. If more than one collinear photon is found, only the one with the highest E_{T} is kept. Non-collinear photons must have $E_{\mathrm{T}} > 10$ GeV, be isolated (E_{T} below 4 GeV within a cone of size $\Delta R = 0.4$, excluding the photon itself), and satisfy strict ("tight") identification criteria [143]. Again, only the highest-E_{T} non-collinear photon is retained.

At most one FSR photon is used per event, with priority given to collinear photons. Figure 6.4 shows the invariant mass distributions for $Z \to \mu\mu$ where either a collinear (6.4(a)) or a non-collinear (6.4(b)) FSR photon is found. The distributions are shown before and after the FSR recovery, for both data and simulation. In both figures, the improvement on the invariant mass distribution is clearly visible. About 70% (60%) of collinear (non-collinear) FSR photons are recovered within the selected fiducial region, with a purity of about 85% (>95%).

6.3.4 Jet reconstruction

Jets are reconstructed using the anti-kt algorithm introduced in Section 4.3, with a distance parameter R = 0.4.
To reduce the number of jet candidates originating from pile-up vertices, at least 50% (75% for 2011 data) of the summed scalar p_{T} of the tracks associated with a jet is required to come from tracks originating from the primary vertex (as defined in the following section). This cut is only applied to jets with $p_{\mathrm{T}} < 50$ GeV and falling within the ID acceptance ($|\eta| < 2.4$).

[2] Photons collinear to electrons are included in the calorimeter shower.

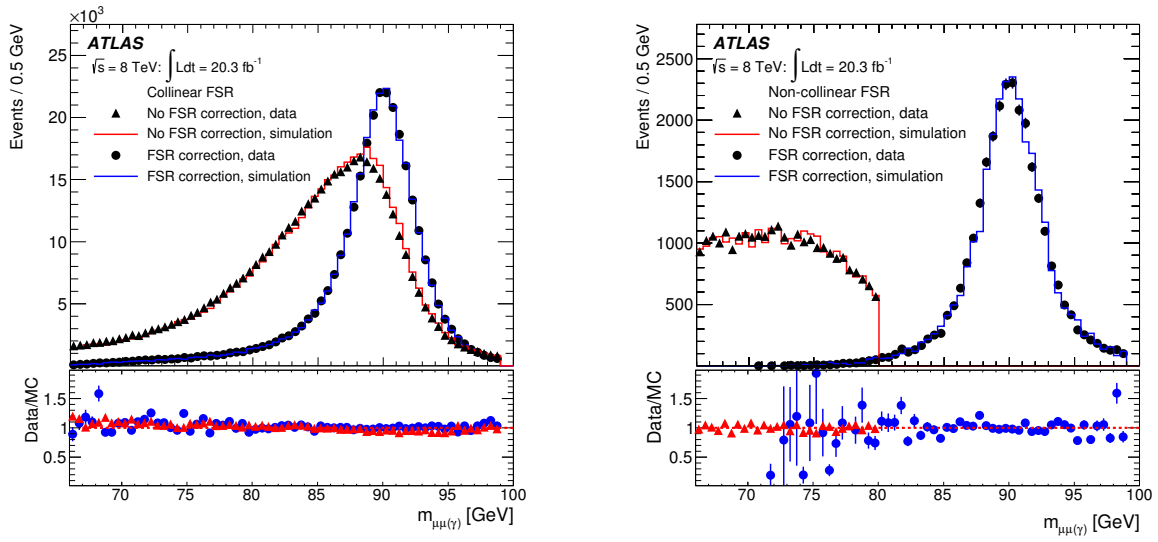

(a) **(b)**

Figure 6.4 The invariant mass distributions of $Z \to \mu\mu(\gamma)$ events in data is shown before (filled triangles) and after (filled circles) collinear (6.4(a)) and non-collinear (6.4(b)) FSR recovery is applied. The prediction of simulation is shown before correction in red, and after correction in blue [4].

6.4 Event Selection

Events in data are selected using the standard GRL for physics analysis, which requires all detector components to be operating correctly. Furthermore, events are required to have at least one vertex with three associated tracks having $p_{\mathrm{T}} > 400$ MeV. In case more than one vertex fulfils this criteria, the primary vertex is chosen to be the reconstructed vertex with the highest summed $|{p_{\mathrm{T}}}^2|$ of associated tracks.

Higgs candidates are formed by selecting two same-flavour, opposite-sign lepton (SFOS) pairs in an event. Each lepton track is required to have a longitudinal impact parameter, z_0, less than 10 mm away from the primary vertex. Additionally, events with cosmic muons are rejected by requiring the transverse impact parameters of the muon tracks, d_0, to be less than 1 mm with respect to the primary vertex. These selections are clearly not applied to standalone muons, that have no ID track.

Electrons are required to have $E_{\mathrm{T}} > 7$ GeV and to be measured in the pseudorapity range $|\eta| < 2.47$, while muons must satisfy $p_{\mathrm{T}} > 6$ GeV and be measured within $|\eta| < 2.7$.

Depending on the selected leptons, multiple quadruplets are possible within a single event, and the quadruplet selection is done separately according to their channel: 4μ, $2\mu 2e$, $2e2\mu$ and $4e$. In the $2\mu 2e$, $2e2\mu$, the first two leptons represent the leading lepton pair, which will be defined shortly.

Within one quadruplet, the first, the second and the third most energetic leptons are required to have $p_{\mathrm{T}} > 20$ GeV, $p_{\mathrm{T}} > 15$ GeV and $p_{\mathrm{T}} > 10$ GeV, respectively.

The lepton pair with mass closest to the Z boson mass is identified as the leading di-lepton and its invariant mass, m_{12}, is required to be between 50 GeV and 106 GeV. Among the remaining lepton pairs, the one closest in mass to the Z boson is selected as sub-leading di-lepton, provided that its invariant mass, m_{34}, is in the range $m_{\mathrm{min}} < m_{34} < 115$ GeV. The value of m_{min}

depends on the reconstructed invariant mass of the lepton quadruplet, and it is equal to 12 GeV for $m_{4\ell} < 140$ GeV, it rises linearly to 50 GeV at $m_{4\ell} = 190$ GeV and remains constant at 50 GeV for $m_{4\ell} > 190$ GeV.
In the case in which more than one quadruplet passes the above selection, the one corresponding to the channel with the highest expected signal rate is chosen, i.e., in the order: 4μ, $2e2\mu$, $2\mu2e$ and $4e$. At this stage, only one quadruplet per event is considered.
The four leptons forming the quadruplet are required to be spatially well separated: a radial distance of at least $\Delta R = 0.10$ ($\Delta R = 0.20$) is required between same flavour (different flavour) leptons. To exclude events containing $J/\psi \to \ell\ell$ decays, in the case of $4e$ or 4μ quadruplets the event is removed if an alternative opposite-charge same-flavour di-lepton pair is found to have an invariant mass below 5 GeV.
The Z+jets and $t\bar{t}$ background contributions are further reduced by applying requirements on the impact parameter significance, as well as on the track and calorimeter-based isolation of the leptons. The transverse impact parameter significance is required to be $d_0/\sigma_{d_0} < 6.5$ for electrons, and $d_0/\sigma_{d_0} < 3.5$ for muons. The measured impact parameter of electrons is affected by Bremsstrahlung and consequently has a broader distribution. The normalised track isolation, defined in this case in a cone of $\Delta R = 0.2$ and divided by the lepton p_{T}, is required to be smaller than 0.15 for all leptons in the quadruplet. Analogously, the normalised calorimetric isolation in a cone of 0.2 must be smaller than 0.2 (0.3) for electrons in 2012 (2011), while for muons it is required to be smaller than 0.3 (0.15 for standalone muons). For both the track and calorimetric isolations any contributions arising from other leptons in the quadruplet are subtracted.

FSR photons are searched for in the event, as discussed in Section 6.3.3, and at most one is added to the 4ℓ system. The FSR correction can be applied only to the leading dilepton, with priority given to collinear photons associated with the leading dimuon. For the photon to be included in the invariant mass calculation, the leading dimuon mass must be in the range 66-89 GeV, and $m_{\mu\mu\gamma}$ must be below 100 GeV. If these requirements are not fulfilled, non-collinear FSR photons are considered, and the one with the highest E_{T} is added, as long as $m_{\ell\ell} < 81$ GeV and $m_{\mu\mu\gamma} < 100$ GeV. The expected fraction of collinear (non-collinear) corrected events is 4% (1%).

For the 7 TeV data sample, the combined signal reconstruction and selection efficiency for $m_H = 125$ GeV is 39% for the 4μ channel, 25% for the $2e2\mu/2\mu2e$ channels and 17% for the $4e$ channel. Thanks to the improvements described in Chapters 4 and 5 in the electron reconstruction and identification, the efficiencies for the 8 TeV data sample are increased to 27% for the $2e2\mu/2\mu2e$ channels and to 20% for the $4e$ channel.

Finally, we can improve the invariant mass resolution by taking advantage of the fact that the first lepton pair is predominantly produced in the decay of an on-shell Z boson. The four-momenta of the leading dilepton are thus recomputed by means of a Z-mass-constrained kinematic fit. A Breit-Wigner function is used to describe the Z line shape, convoluted with a single Gaussian modelling the lepton momentum response function, with the Gaussian width set to the expected resolution for each lepton. The improvement on the $m_{4\ell}$ resolution is about 15%.

Figure 6.5 shows the $m_{4\ell}$ distribution for a simulated sample at $m_H = 125$ GeV, before (6.5(a)) and after (6.5(b)) applying the Z-mass constraint for the $4e$ channel. The width of the reconstructed Higgs mass for $m_H = 125$ GeV is 1.6 GeV and 2.2 GeV for the 4μ and the $4e$ final states respectively, and it is dominated by the experimental resolution. According to the Standard Model prediction, the natural width of the Higgs boson is approximately 4 MeV.

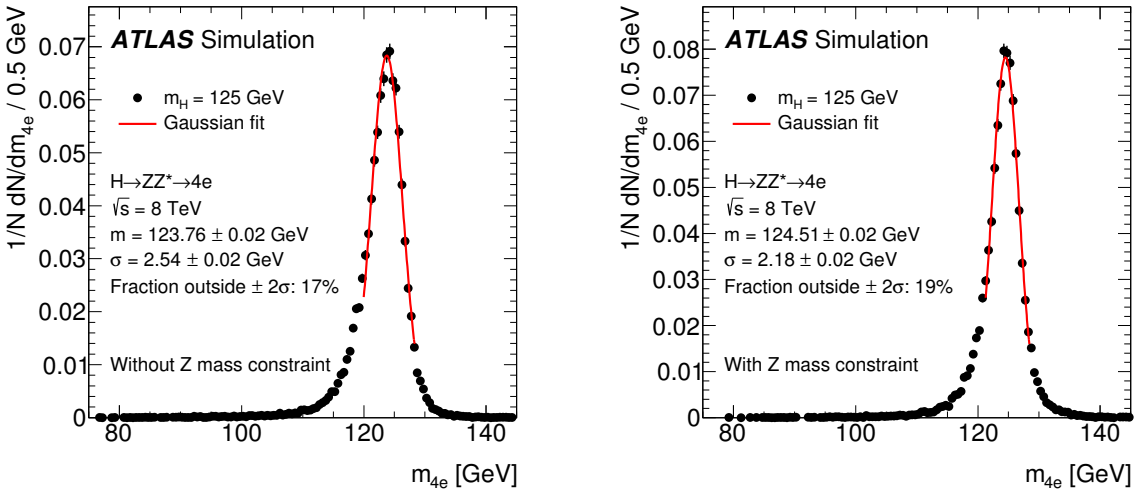

(a) **(b)**

Figure 6.5 Invariant mass distribution for a simulated signal sample with $m_H = 125$ GeV before (a) and after (b) the Z-mass constraint for the $4e$ channel. Superimposed is the Gaussian fit to the $m_{4\ell}$ after correction for final-state radiation. [4].

6.4.1 Event categorisation

The events satisfying the above criteria are subsequently categorised according to their production mechanism to provide a measurement of the Higgs couplings.
Depending on other event characteristics, each $H \to ZZ^* \to 4\ell$ candidate is assigned to one of four categories: *VBF enriched*, *VH-hadronic enriched*, *VH-leptonic enriched* and *ggF enriched*. Figure 6.6 illustrates schematically the event categorisation flow. The expected yields at $m_H = 125$ GeV from each production mechanism falling inside each category are shown in Table 6.4, for the Higgs boson production and ZZ^* background events.

Events are first considered for the *VBF enriched* category by requiring the presence of two high-p_{T} jets. A pre-selection is applied on all jets in our samples, which are required to have $p_{\mathrm{T}} > 25(30)$ GeV for $|\eta| < 2.5$ ($2.5 < |\eta| < 4.5$). Furthermore, in order to avoid double counting, jets are discarded if they are found to be within a cone of $\Delta R = 0.2$ around an electron satisfying the analysis selection criteria. If more than two jets in the event fulfil these requirements, the two highest-p_{T} jets are selected as VBF jets. To increase the purity of this category, only events where the invariant mass of the dijet system, m_{jj}, is greater than 130 GeV are selected. These cuts lead to a signal efficiency of approximately 55% and to a residual contamination from ggF events of about 58%, as shown in Table 6.4. The sensitivity is then improved thanks to a multivariate discriminant used in the couplings fit, as will be described

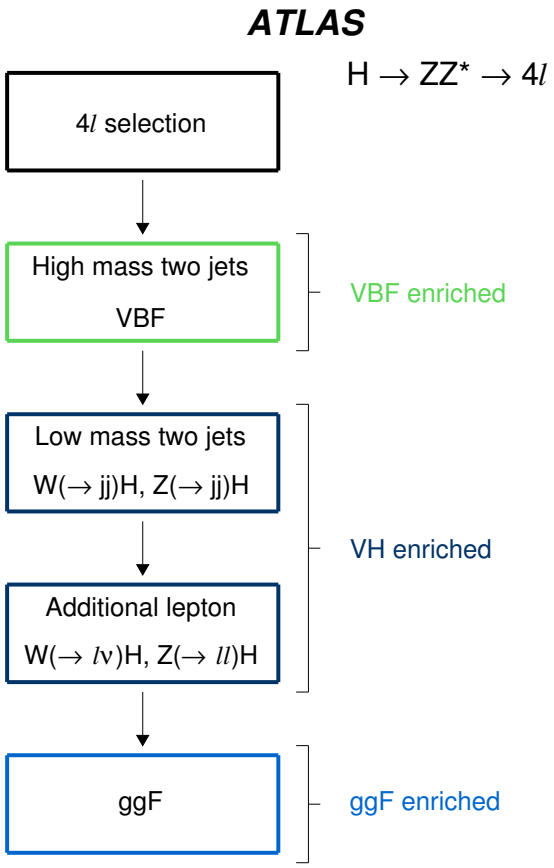

Figure 6.6 Schematic view of the event categorisation. Events are required to pass the four-lepton selection, and then they are assigned to one of four categories which are tested sequentially: *VBF enriched*, *VH-hadronic enriched*, *VH-leptonic enriched* and *ggF enriched* [4].

in Section 8.1.2.

Events which are not selected for the *VBF enriched* category are considered for the *VH-hadronic enriched* category. This category collects those events in which the Higgs boson is produced in association with a Z or a W, subsequently decaying into hadrons. Experimentally, this results in the presence of two jets with m_{jj} peaking either at the W or at the Z mass value. A cut on the invariant mass of the dijet system is thus applied, which is required to be within 40 and 130 GeV, as presented in Figure 6.7. A specific multivariate discriminant, presented in Section 8.1.2, is also developed for the *VH-hadronic enriched* category and used directly in the selection. After applying the cut on the discriminant output weight, the overall signal efficiency is about 25%. Events failing to satisfy the above criteria are next considered for the *VH-leptonic*

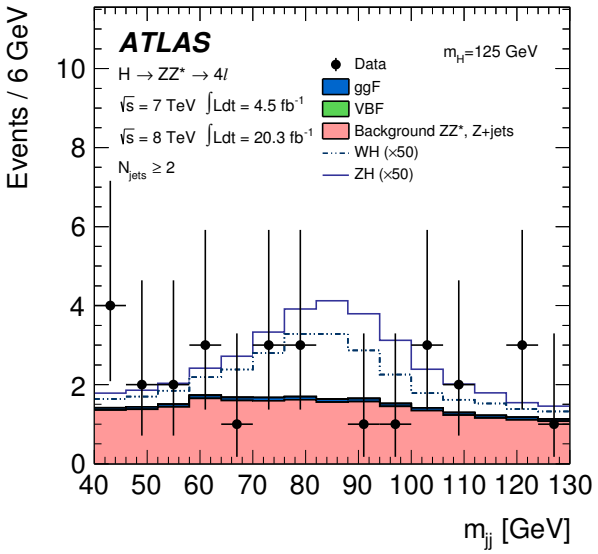

Figure 6.7 Distributions of the dijet invariant mass for the events with at least two jets for the data (filled circles), the expected signal (solid and dashed histograms) and the backgrounds (filled histograms). The WH and ZH hadronic signals are scaled by a factor 50 and the ZH distribution is added on top of the WH distribution [4].

enriched category. In this case, the associated vector boson decays leptonically, thus we look for at least one lepton in the event, in addition to those forming the Higgs candidate, with $p_{\mathrm{T}} > 8$ GeV and satisfying the same lepton requirements. For this category the signal efficiency is very high, and amounts to approximately 90% and 100% depending on whether a W or a Z boson is produced.

Finally, if an event has not been assigned to any of the previously described categories, it is assigned to the *ggF enriched* category.

Table 6.4 The expected number of events in each category (*ggF enriched*, *VBF enriched*, *VH-hadronic enriched* and *VH-leptonic enriched*), after all analysis criteria are applied, for each signal production mechanism (ggF/$b\bar{b}H/t\bar{t}H$, VBF, VH) at $m_H = 125$ GeV, for 4.5 fb^{-1}at $\sqrt{s} = 7$ TeV and 20.3 fb^{-1}at $\sqrt{s} = 8$ TeV. The requirement $m_{4\ell} > 110$ GeV is applied [4].

Category	$gg \to H, q\bar{q}/gg \to b\bar{b}H/t\bar{t}H$	$qq' \to Hqq'$	$q\bar{q} \to W/ZH$
	$\sqrt{s} = 7$ TeV		
ggF enriched	2.06 ± 0.25	0.114 ± 0.005	0.067 ± 0.003
VBF enriched	0.13 ± 0.04	0.137 ± 0.009	0.015 ± 0.001
VH-hadronic enriched	0.053 ± 0.018	0.007 ± 0.001	0.038 ± 0.002
VH-leptonic enriched	0.005 ± 0.001	0.0007 ± 0.0001	0.023 ± 0.002
	$\sqrt{s} = 8$ TeV		
ggF enriched	12.0 ± 1.4	0.52 ± 0.02	0.37 ± 0.02
VBF enriched	1.2 ± 0.4	0.69 ± 0.05	0.10 ± 0.01
VH-hadronic enriched	0.41 ± 0.14	0.030 ± 0.004	0.21 ± 0.01
VH-leptonic enriched	0.021 ± 0.003	0.0009 ± 0.0002	0.13 ± 0.01

Chapter 7

$H \to ZZ^* \to 4\ell$ Analysis: Background Estimation

The estimation of the different background sources contaminating our signal region is a fundamental part of the analysis, and is described in detail in this chapter.
The background processes to be considered in the $H \to ZZ^* \to 4\ell$ analysis are the ZZ^* SM production, which has the same topology as the signal process and is thus referred to as irreducible background, and the reducible background from Z+jets, top quark pair production and WZ production.

The ZZ^* background is a well-known process leading to good quality and well-isolated final-state leptons, and can thus be reliably estimated from MC. The analysis selection is applied on the ZZ^* sample introduced in Section 6.1.2, normalised to the theoretical SM NLO predictions.

For the evaluation of the more complicated Z+jets and $t\bar{t}$ backgrounds, data-driven methods are instead used. Since the composition of these reducible backgrounds strongly depends on the flavour of the sub-leading leptons, the $\ell\ell + ee$ and $\ell\ell + \mu\mu$ final states are treated separately. The methods developed for the two cases are described in Sections 7.1 and 7.2 respectively, with special emphasis given to the part regarding the $\ell\ell + ee$ background estimation, to which the author of this thesis contributed significantly.
The small contribution coming from the WZ reducible background is either estimated from simulation or included in the data-driven estimations, as will be discussed later in this chapter.
As done throughout the entire analysis, the 2011 and 2012 datasets have been considered separately. Unless otherwise specified, we generally refer to results obtained with the 2012 sample, which was used to develop and test all the described methods. The final background estimations are of course given for both datasets.

7.1 $\ell\ell + \mu\mu$ Background

In $\ell\ell + \mu\mu$ final state events, the main background contribution comes from Z+jets which in this case mostly consists of $Z + b\bar{b}$ events with heavy-flavor semileptonic decays and, to a lesser extent, of Z+light jets with subsequent π/K in-flight decays. The top quark production also brings a small contribution to the background.
The number of background events is estimated from an unbinned maximum likelihood fit,

performed simultaneously to four orthogonal control regions (CR), each of them providing information on one or more of the background components. The four control regions are built by relaxing the impact parameter significance and isolation selections on the sub-leading muons, and are designed to minimise contamination from the Higgs boson signal and from the ZZ^* background. More specifically, they are defined as follows:

- *Inverted d_0 significance CR (enhanced in $Z + b\bar{b}$ and $t\bar{t}$).* Candidates are required to pass the analysis event selection, but no isolation requirement is applied on the subleading muons and at least one of the two muons must fail the d_0 significance requirement. This control region is enriched in $Z + b\bar{b}$ and $t\bar{t}$ events, as b-quark mesons are characterised by large values of d_0 significance.

- *Inverted isolation CR (enhanced in Z+light jets and $t\bar{t}$).* Candidates are required to pass the analysis event selection, including the d_0 significance selection, but at least one of the two sub-leading muons must fail the isolation requirement. Relative to the previous one, this control regions aims at enhancing the Z+light jets over the $Z + b\bar{b}$ component, but the $t\bar{t}$ background also contributes significantly.

- *$e\mu + \mu\mu$ CR (enhanced in $t\bar{t}$).* Candidates are required to pass the analysis event selection, but the leading di-lepton is required to be an electron-muon pair. No d_0 significance and isolation requirements are applied on the sub-leading muons, which are also allowed to be equally or oppositely charged. Events with a Z boson decaying into e^+e^- or $\mu^+\mu^-$ pair of leptons are vetoed by applying a requirement on the mass. This control region is dominated by $t\bar{t}$ events.

- *Same-sign sub-leading dilepton CR.* Candidates are required to pass the analysis event selection, but the sub-leading muons are not required to pass either the isolation or the d_0 significance selections, while they are required to have same charge. This control region is not dominated by a specific background, but still provides additional information to constrain the different components.

The expected composition of the reducible background components for each control region is shown in Table 7.1. The contribution from ZZ^* andWZ production are estimated, for each control region, from simulation.
A fifth control region is also defined by applying the analysis event selection except for the isolation and impact parameter requirements to the sub-leading dilepton pair. The fit results are expressed in terms of yields in this reference control region. The ratios of the number of events in the fit control regions to the number of events in the reference control region are taken from MC simulation, and treated as parameters in the combined fit.

The observable chosen for the fit is the leading di-lepton m_{12} distribution, which peaks at the Z mass for the resonant Z+jets component and has a broad distribution for the non-resonant $t\bar{t}$ component. The $t\bar{t}$ background is modelled by a second-order Chebychev polynomial, while a Breit-Wigner convoluted with a Crystal Ball is used to describe the Z+jets component (the same shape is used for both the heavy and light flavour components). The shape parameters are derived from simulation, and constrained in the combined fit to be the same, within the

Table 7.1 Expected contribution of the $\ell\ell + \mu\mu$ reducible background sources in each of the control regions.

	Control region			
Background	Inverted d_0	Inverted isolation	$e\mu + \mu\mu$	Same-sign
$Zb\bar{b}$	$32.8 \pm 0.5\%$	$26.5 \pm 1.2\%$	$0.3 \pm 1.2\%$	$30.6 \pm 0.7\%$
Z + light-flavor jets	$9.2 \pm 1.3\%$	$39.3 \pm 2.6\%$	$0.0 \pm 0.8\%$	$16.9 \pm 1.6\%$
$t\bar{t}$	$58.0 \pm 0.9\%$	$34.2 \pm 1.6\%$	$99.7 \pm 1.0\%$	$52.5 \pm 1.1\%$

Table 7.2 Data-driven $\ell\ell + \mu\mu$ background estimates for the $\sqrt{s} = 7$ TeV and $\sqrt{s} = 8$ TeV data, expressed as yields in the reference control region, for the combined fit and fits to the individual control regions. In the individual control regions only the total Z+jets contribution can be determined, while the $e\mu + \mu\mu$ control region is only sensitive to the $t\bar{t}$ background. The statistical uncertainties are shown [4].

Reducible background yields for 4μ and $2e2\mu$ in reference control region				
Control region	$Zb\bar{b}$	Z + light-flavor jets	Total Z + jets	$t\bar{t}$
Combined fit	159 ± 20	49 ± 10	208 ± 22	210 ± 12
Inverted impact parameter			206 ± 18	208 ± 23
Inverted isolation			210 ± 21	201 ± 24
$e\mu + \mu\mu$			–	201 ± 12
Same-sign dilepton			198 ± 20	196 ± 22

uncertainties, in each of the control regions. The results of the combined fit in the four control regions are shown in Figure 7.1, along with the individual background components, while the event yields in the reference control region are summarised in Table 7.2. To validate the fit method, the maximum likelihood fit was also applied to the individual control regions, yielding estimates compatible to those of the combined fit, as visible in Table 7.2.

The estimated yields in the reference control region are extrapolated to the signal region by multiplying each background component by the probability of satisfying the isolation and impact parameter significance requirements, estimated from simulation. The use of MC events is here motivated by the fact that the various background components are treated separately, and it wouldn't be possible in data to obtain control regions sufficiently pure in each component. The systematic uncertainties associated to these transfer factors arise mostly from the size of the simulated samples, and it is equal to 6% for $Z + b\bar{b}$, 60% for Z+light jets and 16% for $t\bar{t}$. These simulation-based efficiencies are then validated with data using events with $Z \to \ell\ell$ candidates and one additional muon. Based on the observed data/simulation agreement an additional systematic uncertainty of 1.6% is added.
The final background estimates in the 4μ and in the $2e2\mu$ final states are summarised in Table 7.3, separately for the 2011 and the 2012 datasets. Statistical and systematic uncertainties are shown, with the latter including both the uncertainties related to the transfer factors and the ones related to the fit.

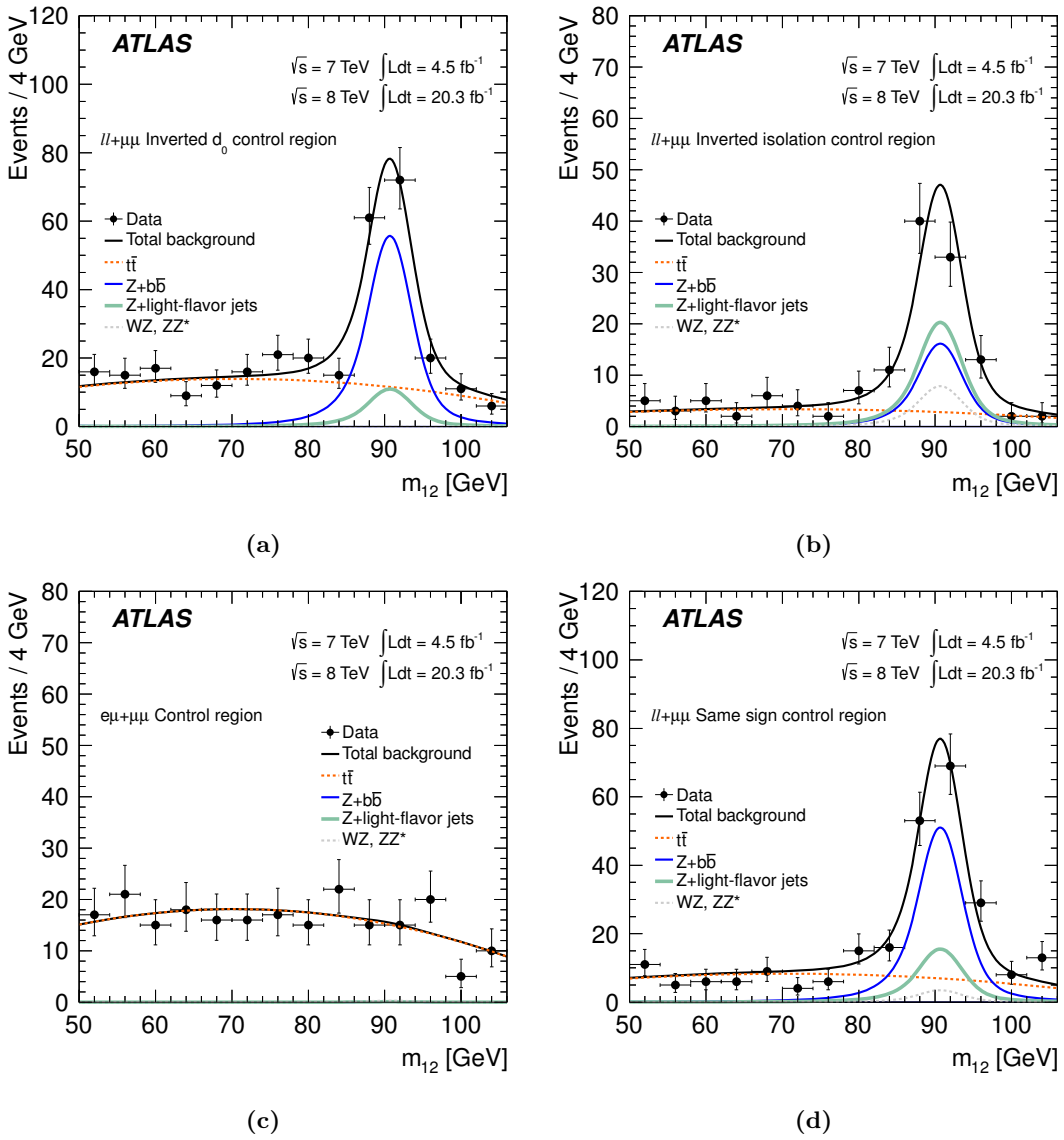

Figure 7.1 The observed m_{12} distributions (filled circles) and the results of the maximum likelihood fit are presented for the four control regions: ((a)) inverted requirement on impact parameter significance, ((b)) inverted requirement on isolation, ((c)) $e\mu$ leading dilepton and ((d)) same-sign subleading dilepton. The fit results are shown for the total background (black line) as well as the individual components: Z+jets decomposed into $Z + b\bar{b}$ (blue line) and Z+light-flavor jets (green line), $t\bar{t}$ (dashed red line), and the combined WZ and ZZ (dashed gray line), which are estimated from simulation [4].

Table 7.3 Estimates of the $\ell\ell + \mu\mu$ background in the signal region for the full $m_{4\ell}$ mass range, for the $\sqrt{s} = 7$ TeV and $\sqrt{s} = 8$ TeV data. The Z+jets and $t\bar{t}$ background estimates are both data-driven, while the WZ contribution is taken from simulation. The decomposition of the Z + jets background in terms of the $Z + b\bar{b}$ and the Z+light jets contributions is also provided [4].

Background	4μ	$2e2\mu$
	$\sqrt{s} = 7$ TeV	
Z + jets	$0.42 \pm 0.21(\text{stat}) \pm 0.08(\text{syst})$	$0.29 \pm 0.14(\text{stat}) \pm 0.05(\text{syst})$
$t\bar{t}$	$0.081 \pm 0.016(\text{stat}) \pm 0.021(\text{syst})$	$0.056 \pm 0.011(\text{stat}) \pm 0.015(\text{syst})$
WZ expectation	0.08 ± 0.05	0.19 ± 0.10
	Z + jets decomposition	
$Zb\bar{b}$	$0.36 \pm 0.19(\text{stat}) \pm 0.07(\text{syst})$	$0.25 \pm 0.13(\text{stat}) \pm 0.05(\text{syst})$
Z + light-flavor jets	$0.06 \pm 0.08(\text{stat}) \pm 0.04(\text{syst})$	$0.04 \pm 0.06(\text{stat}) \pm 0.02(\text{syst})$
	$\sqrt{s} = 8$ TeV	
Z + jets	$3.11 \pm 0.46(\text{stat}) \pm 0.43(\text{syst})$	$2.58 \pm 0.39(\text{stat}) \pm 0.43(\text{syst})$
$t\bar{t}$	$0.51 \pm 0.03(\text{stat}) \pm 0.09(\text{syst})$	$0.48 \pm 0.03(\text{stat}) \pm 0.08(\text{syst})$
WZ expectation	0.42 ± 0.07	0.44 ± 0.06
	Z + jets decomposition	
$Zb\bar{b}$	$2.30 \pm 0.26(\text{stat}) \pm 0.14(\text{syst})$	$2.01 \pm 0.23(\text{stat}) \pm 0.13(\text{syst})$
Z + light-flavor jets	$0.81 \pm 0.38(\text{stat}) \pm 0.41(\text{syst})$	$0.57 \pm 0.31(\text{stat}) \pm 0.41(\text{syst})$

7.2 $\ell\ell + ee$ Background

Three main sources of background for sub-leading electron pairs can be identified: light-flavour hadrons misidentified as electrons, photon conversions to electron-positron pairs, and non-isolated electrons arising from heavy-flavour semi-leptonic decays. Several methods have been developed to estimate these background contributions to our signal region, all of which make use of control regions obtained by relaxing or inverting the selection on one $(3\ell + X)$ or both $(Z + XX)$ electrons in the sub-leading pair. These control regions, which will be introduced in full detail in the following sections, are used to estimate the yields of the different background components, but may suffer from low statistics. The efficiencies needed to extrapolate the background sources from the control regions into the signal region are instead extracted from abundant control regions denoted as $Z + X$, built by requiring the presence of a Z boson and only one additional object with released selection.

By applying a truth-matching procedure, the electron candidates in simulated events can be classified into: isolated electrons (e), light jets faking an electron (f), photon conversions (γ), and electrons from heavy-flavour quark decays (q).
Furthermore, electron candidates can be categorised, both in data and in MC, based on reconstruction discriminating variables. Two categories can be identified in this case:

- **Electron (E)**. A first requirement on the ratio of the energy in the strip layer of the LAr calorimeter to the total energy is applied ($f_1 > 0.1$). Moreover, in order to reduce the contamination from photon conversions, the electron tracks are required to have a hit in

the b-layer, if such is expected. Finally, for $|\eta| < 2$ the fraction of high-threshold hits in the TRT detector F_{HT} is required to be higher than 0.1. For $|\eta| > 2$ a cut on the energy shower shape distribution is applied ($R_\phi > 0.9$).

- **Fakes (F)**. All candidates not passing the E category requirements are classified as F.

Three independent methods have been developed to estimate the reducible background events, all of which are described in the remainder of this chapter following an historical approach. The so-called "reco-truth unfolding" method and the "$3\ell + X$" method are illustrated in Sections 7.2.1 and 7.2.2, respectively. The third and last method, referred to as "transfer factor method with b-enriched $Z + X$" and illustrated in Section 7.2.3, was entirely developed by the author of this thesis, and succeeds, by solving the remaining problems in the previously developed methods, in estimating the background using only data events. The same idea at the heart of this new method was also used for the definition of a particular control region, enhanced in $b \to e$, which brought a significant improvement on the results of both the "reco-truth" and the "$3\ell + X$" methods. This control region is described in Section 7.2.4.

7.2.1 Reco-truth unfolding method

This method uses a $Z + XX$ control region, with the full analysis selection applied on the leading dilepton, and the subleading leptons passing all criteria but electron identification, isolation and impact parameter significance. More specifically, a relaxed version of the electron identification is applied, referred to as Relaxed LOOSE LH. Since no inverted cut is applied, the control region in this case also includes events from the irreducible ZZ^* background, as well as signal $H \to ZZ^* \to 4\ell$ events, which will have to be subtracted from the final estimation.
Thanks to the previously introduced reconstruction-based categorisation, the yields of the four possible categories, EE, FF, EF and FE[1] are estimated in the $Z + XX$ control region using data. For the extrapolation of these background yields to the signal region, we then need to compute the efficiency for the different categories to survive the remaining analysis cuts, and this is done using the $Z + X$ control region.
An important complication arises at this point from the differences in the composition between the $Z + X$ and $Z + XX$ control regions. This originates directly from the definition of the two samples, the first requiring a single *e-like* object on top of the Z, and the second requiring two *e-like* particles. In the latter case, more non-isolated electrons from heavy-flavour decays will be selected, as demonstrated from the numbers in Table 7.4. The truth composition of the reconstruction categories (fraction of the truth categories for each reconstruction category) is shown for simulated events in both control regions, and the disagreement is clearly visible.
Due to these differences in the composition, the efficiencies extracted from the $Z + X$ control region can't be directly applied to the $Z + XX$ sample. In this method, this complication is dealt with using simulated samples for both control regions, and proceeding as follows:

1. Extract efficiencies for each reco-truth category (Ee, Ef, Eq, Eγ, and the same for F) from the simulated $Z + X$ sample;

[1] The subleading leptons are ordered based on their p_{T} value.

Table 7.4 Truth composition of the reconstruction categories (fraction of events in the truth categories for each reconstruction category) in the $Z + X$ and $Z + XX$ simulated samples used in the reco-truth unfolding method. For the $Z + XX$ control region, the two Xs are counted separately. Truth categories are indicated with italic letters, whilst capital letters are used to indicate reconstruction categories.

	e	q	γ	f
		$Z + X$		
E	0.013 ±0.003	0.181 ±0.001	0.225 ± 0.150	0.582 ±0.170
F	0.001 ±0.000	0.0179 ±0.020	0.061 ±0.010	0.920 ±0.007
		$Z + XX$		
E	0.031±0.001	0.335±0.006	0.178±0.008	0.457±0.010
F	0.001 ±0.000	0.047 ±0.002	0.055±0.002	0.893±0.005

Table 7.5 Truth composition of the reconstruction categories (number of events in the truth categories for each reconstruction category) in the $Z + XX$ simulated samples used in the reco-truth unfolding method. Truth categories are indicated with italic letters, whilst capital letters are used to indicate reconstruction categories.

	$Z + XX$															
	ee	eq	$e\gamma$	ef	qq	$q\gamma$	qf	$\gamma\gamma$	γf	ff	qe	γe	fe	γq	fq	$f\gamma$
EE	130.3	4.5	1.8	4.5	44.4	11.7	44.3	8.2	20.1	52.4	1.0	0.4	0.7	10.6	17.9	17.7
FE	16.6	0.4	0.2	0.5	5.7	1.9	4.4	1.8	11.1	100.8	0.1	0.1	2.3	5.4	39.1	34.2
FF	3.6	0.5	0.1	2.5	1.2	0.4	21.9	1.5	31.3	371.3	0.0	0.0	0.6	0.9	18.2	21.3
EF	25.5	1.1	0.7	17.2	9.9	4.8	132.9	1.1	82.5	167.0	0.3	0.0	1.5	0.9	4.2	7.5

2. Starting from these numbers, compute the efficiencies for each of the 4×16 reco-truth category (EEee, EEff, etc.) in the simulated $Z + XX$ sample;

3. Weight the $Z + XX$ efficiencies with the corresponding reco-truth composition (computed from the numbers in Table 7.5), and compute an averaged value of the truth efficiencies for each of the reconstruction categories (EE, EF, FE and EE);

4. Apply these efficiencies to the yields obtained in the $Z + XX$ control region in data.

The kinematical differences between the two control regions are accounted for by computing the efficiencies in bins of η and p_{T}.
Possible discrepancies in the efficiencies between data and MC are instead accounted for in step 1 by applying corrections extracted from specific $Z + X$ control regions, modified in order to enhance only one background component. More details regarding these control regions will be given in the following section, as well as in Section 7.2.4.

By excluding the truth electron fraction (ee) in the efficiency calculation in step 3, only a negligible contribution from signal events is left in the control region. The residual contamination from ZZ^* events is estimated by applying the described method to the simulated ZZ^* sample, and then subtracted from the final result.

The final background estimation is presented in Table 7.6. The systematic uncertainties are dominated by statistical fluctuations in the efficiency and composition MC tables, and from the

data/MC efficiency corrections.

A variation of this method, following the same conceptual strategy but a slightly different procedure, is also used to estimate the background contribution. A different control region is chosen, defined starting from the inclusive $Z + XX$ – in which identification, isolation and d_0/σ_{d_0} cuts are relaxed on both subleading electrons – and requiring the two X to fail one of the previously relaxed cuts. This control regions is conventionally referred to as $Z + \overline{X}\,\overline{X}$.
Moreover, the inclusive reco-truth composition used in step 3 to weight the efficiencies, are instead computed in bins of η and p_{T} in order to better account for kinematical differences between $Z + X$ and $Z + \overline{X}\,\overline{X}$.
Finally, to deal with the consequent reduced statistics, due to both the different choice of the control region and the introduction of the binning, these reco-truth composition weights are computed considering the two Xs of the $Z + XX$ control region separately. In other words, only 8 weights were extracted (w_{eE}, w_{eF}, etc.), rather than the 64 computed from Table 7.5 (w_{eeEE}, w_{eeFF}, etc.).

The results obtained from this measurement are also reported in Table 7.6.

Table 7.6 Summary of the $\ell\ell + ee$ data-driven background estimates for the $\sqrt{s} = 7$ TeV and $\sqrt{s} = 8$ TeV data in the full $m_{4\ell}$ mass range. The "†" symbol indicates the estimates used for the background normalisation, while the other estimates are used as cross-checks. Both statistical and systematic uncertainties are shown. The SS data full analysis is limited to the region of $m_{4\ell}$ below 160 GeV to avoid a ZZ^* contribution; this region contains 70% of the expected background [4].

Method	$\sqrt{s} = 7$ TeV data	$\sqrt{s} = 8$ TeV data
	$2\mu 2e$	
$\ell\ell + XX$ reco-truth	$2.8 \pm 0.4 \pm 1.0$	$2.9 \pm 0.3 \pm 0.3$
$\ell\ell + XX$ reco-truth (variation)	$2.2 \pm 0.3 \pm 1.1$	$2.5 \pm 0.1 \pm 0.9$
$3\ell + X^{\dagger}$	$2.9 \pm 0.5 \pm 0.5$	$2.9 \pm 0.3 \pm 0.6$
$\ell\ell + XX$ transfer factor b-enriched	$2.8 \pm 0.5 \pm 0.8$	$3.2 \pm 0.2 \pm 0.9$
$2\mu 2e$ SS data full analysis	1	2
	$4e$	
$\ell\ell + XX$ reco-truth	$2.6 \pm 0.4 \pm 0.9$	$2.8 \pm 0.3 \pm 0.3$
$\ell\ell + XX$ reco-truth (variation)	$2.0 \pm 0.3 \pm 0.9$	$2.4 \pm 0.1 \pm 0.9$
$3\ell + X^{\dagger}$	$3.3 \pm 0.5 \pm 0.5$	$2.9 \pm 0.3 \pm 0.5$
$\ell\ell + XX$ transfer factor b-enriched	$3.4 \pm 0.9 \pm 0.8$	$2.9 \pm 0.2 \pm 0.8$
$4e$ SS data full analysis	2	2

7.2.2 $3\ell + X$ method

The background composition problem encountered in the previous method can be simplified by relaxing the selection on one single electron, rather than on both the sub-leading ones. This is done in the $3\ell + X$ control region, which includes data that has quadruplets built as for the full analysis, with the exception that the standard selection is applied only to the three highest-p_{T} leptons. The fourth electron is instead only required to pass the standard silicon hits requirements ($n_{\mathrm{Silicon}} > 6$ and $n_{\mathrm{Pixel}} > 1$), while the electron identification, isolation and d_0 significance selection criteria are not applied. In order to suppress the ZZ^* contribution, which, as already explained, is estimated separately from MC, we only select same-sign sub-leading electrons. A residual small ZZ^* contribution (5%) survives the SS selection, and is subtracted at a later stage from the final estimate.

As the composition problem is now limited to one X, the yields of the different background components, f, γ and q, can be extracted by means of a two-dimensional fit. Two discriminating variables are used to perform the fit: the number of hits in the innermost layer of the pixel detector, n_{Blayer}, and the ratio of high-threshold TRT hits, F_{HT}, which is however only in available in the region $|\eta| < 2$. Since most photons convert after the b-layer, the former variable allows the separation of γ from f and q, while on the other hand, jets faking electrons will have a lower F_{HT} compared to conversions and heavy-flavour electrons.
Both variables are fit using template distributions for each background component, visible in Figure 7.2. In order to improve the statistics, these templates are extracted from the $Z + X$ control region in MC, built requiring an on-shell reconstructed Z boson and an additional electron candidate satisfying the standard silicon hits requirements. Moreover, the template shapes are assumed to be independent of the channel and have been obtained adding together the $2\mu 2e$ and $4e$ final states.
Due to its very low contribution in the $3\ell + X$ CR (less than 2%), the yield of the heavy flavour component is constrained to the value predicted by MC. However, the observed discrepancies between data and simulation need to be accounted for by applying appropriate correction factors. These correction factors were extracted by the author of this thesis from a specific control region enriched in electrons from heavy flavour decays, described in detail in Section 7.2.4.
The results of the simultaneous fit, which are performed separately for the two channels, are shown in Figure 7.3 for the $2\mu 2e$ and $4e$ final states combined. The *sPlot* method [144] is used to derive the contributions from the different background sources as a function of the electron p_{T}. The *sPlot* tool is used to assign a weight to each event for each of the components included in the fit model, which correspond to the probability of that background event being f, γ or q.

Once again, in order to extrapolate the f, γ and q backgrounds from the $3\ell + X$ control region to the signal region, we need to compute the efficiency for the different components to survive the full analysis selection. As already mentioned, the abundant $Z + X$ control region is used to extract these efficiencies, and simulated events are used in this method as in the previous one. The efficiencies are estimated in p_{T} bins for the fake and the conversion components, and inclusively for the heavy flavour q component due to lack of statistics.
As done for the reco-truth method, the observed discrepancies in the efficiencies between data and MC are accounted for by applying corrections extracted from specific $Z + X$ control regions,

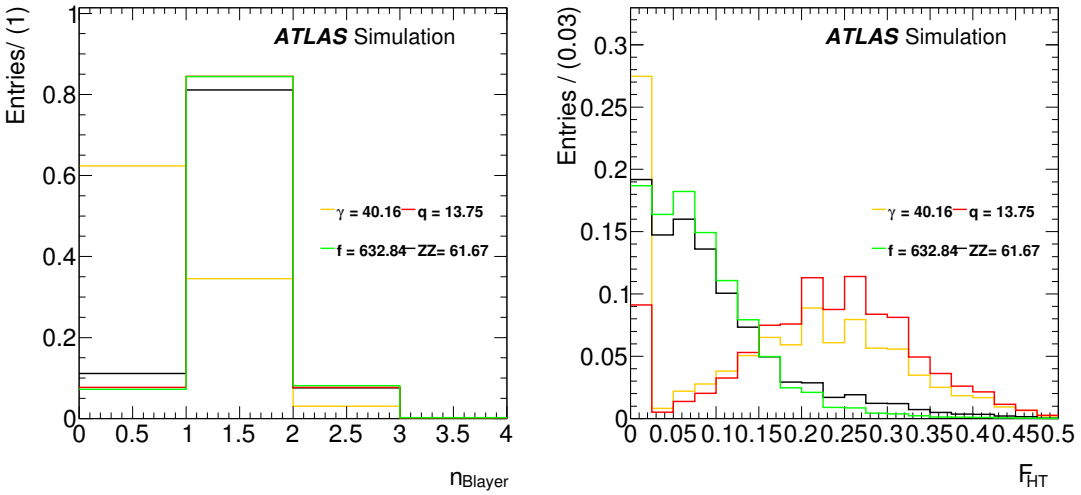

(a) **(b)**

Figure 7.2 Distributions of n_{Blayer} (a) and F_{HT} (b) for the different sources of background (γ,f,q) extracted from the $Z + X$ control region using simulation. The distributions are normalised to unity and obtained from the two $\ell\ell + ee$ final states together. The ZZ^* component has been taken from the $3\ell + X$ control region, and it is mainly composed of fakes. The numbers in the legend represent the expected yields as predicted by MC simulation of the various background sources in the $3\ell + X$ control region.

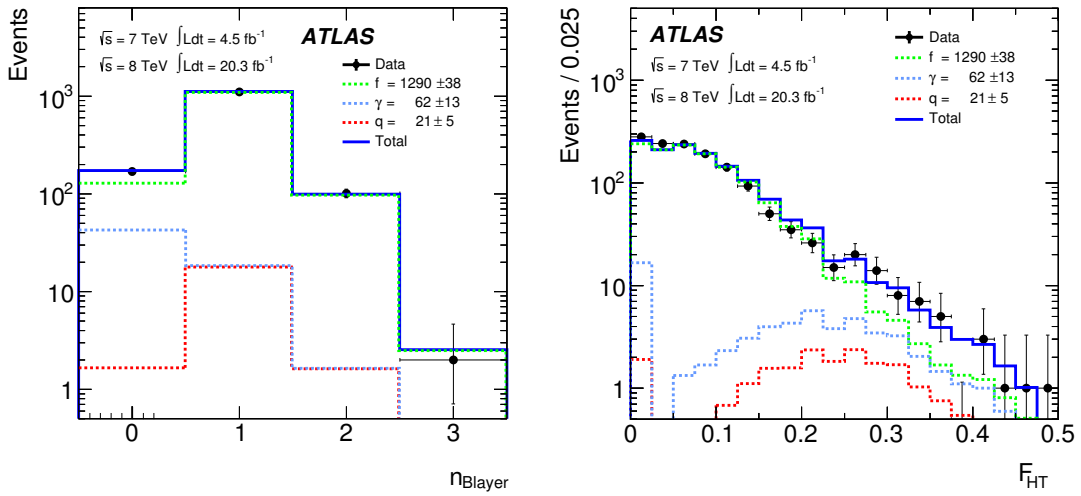

(a) **(b)**

Figure 7.3 The results of the simultaneous fit to n_{Blayer} (a), and F_{HT} (b), for the background components in the $3\ell + X$ control region. The fit is performed separately for the $2\mu 2e$ and $4e$ channels and summed together in the present plots. The data are represented by the filled circles, while the green, blue and red dashed histograms represent the f, γ and q components respectively. The total background is given by the solid blue histogram [4].

where the selection is modified to enhance only one background component. A γ enriched control region is defined requiring no hits in the first pixel layer ($n_{\text{Blayer}} = 0$) and $F_{\text{HT}} > 0.15$. The simulation is found to model well the efficiency of the γ component, to within approximately 10%. Correction factors between 1.6 and 2.5 are instead found for the f component, from a control region built requiring at least one b-layer hit. For the q component, the control region described in Section 7.2.4 is used, and the efficiency is found to be well reproduced by simulation. An additional correction derived from MC equal to OS/SS ≈ 1.7 is applied for the heavy-flavour background, as this component is expected to be affected by the same-sign requirement.

The background yields in the signal regions are finally estimated using transfer factors computed combining the corrected efficiencies with the weights provided by the *sPlot* fit. The final estimations in the $2\mu 2e$ and $4e$ channels, obtained after removing the residual ZZ^* background using MC, are presented in Table 7.6. The systematic uncertainty on the final estimates is dominated by the simulation efficiency corrections, corresponding to 30%, 20%, 25% uncertainties for f, γ, q, respectively.

7.2.3 Trasfer factor method with b-enriched $Z + X$ control region

As already pointed out, the estimation of the electron background is complicated by the presence of different kind of objects in our control regions. The experimental properties and the reliability of MC simulation are in fact different for isolated electrons, light jets faking electrons, electrons from photon conversion and electrons from heavy flavour hadron decays. Moreover, the proportions of the various components differ significantly between the $Z + X$ and $Z + XX$ control regions, and this has prevented from using data rather than simulated events in the reco-truth method introduced in Section 7.2.1.
As seen in Table 7.4, the heavy flavour component is in particular always lower in the $Z + X$ control region than in the $Z + XX$ one. A possible approach to the problem is thus to reduce this discrepancy by enriching the $b \to e$ component in the $Z + X$ control region. This is done by adding requirements on the presence of a b-jet. As explained in Section 4.3, jets originating from b-quarks have unique features, that allow us to identify them in the event using specific algorithms. In this analysis, we have used the official MV1 b-tagger algorithm [79], which assigns a weight to each jet representing the probability of that jet originating from a b quark. Typically, physics analyses make use of fixed cuts, called working points, applied on the b-tagger output weight distribution in order to obtain specific b-jet efficiencies. In this case, the idea is instead to find the appropriate cut on the MV1 output to "tune" our $Z + X$ sample composition to be as close as possible to the $Z + XX$ composition.

Starting from a $Z + X$ control region with relaxed cuts on the X (cuts on isolation and impact parameter significance are relaxed, and a looser version of the identification criteria is applied), we have studied two possible strategies to build our $b \to e$ enriched control region:

– **Events with b-tagged jets**

When a b-tagged jet is found in one of our events, that event is likely to be a $Z + b\bar{b}$ one. To enrich our $Z + X$ sample in $b \to e$ we can then proceed as follows:

- look for jets in the event;

- if a jet is b-tagged, flag the event and all the electrons in it as b-matched.

– **Electrons matched to b-tagged jets**

In this case we want to match directly our subleading electrons with b-tagged jets. The procedure is the following:

- look for jets in a cone of $\Delta R = 0.4$ around the electron;
- if more than one jet is found in the cone, select the one with smallest ΔR;
- if the jet is b-tagged, the electron is flagged as b-matched.

The latter possibility, called "per-electron" matching, leads to very high heavy flavour components in our control region, and was discarded in this study because it never resulted in a composition matching the $Z + XX$ one. On the other hand, as we will see in Section 7.2.4, this strategy proved very useful in the definition of the control region with enhanced $b \to e$, already mentioned in the previous sections, where the objective is indeed to obtain the highest possible heavy flavour component. In the following, only the first algorithm, which we will refer to as the "per-event" matching algorithm, is thus considered.

The available working points supported by central performance measurements in ATLAS for the MV1 tagger are the following:

- 80% b-tagging efficiency: $MV1 > 0.39$
- 70% b-tagging efficiency: $MV1 > 0.8119$
- 60% b-tagging efficiency: $MV1 > 0.9867$

While the last two cuts lead once again to heavy flavour components higher than the $Z + XX$ ones, we did consider the first one in our study, together with a number of other possible cuts, namely $MV1 > 0.07, 0.08, 0.1, 0.2, 0.3$. We also compared to the case where no cut is applied, which corresponds to the standard $Z + X$ control region used in the other $H \to ZZ^* \to 4\ell$ background estimation methods. Table 7.8 shows the truth composition of the reconstruction categories for the $Z + X$ control regions obtained with these different choices of the MV1 cut. Table 7.9 shows instead the composition of the two different $Z + XX$ control regions we have considered: in the first case at least one X is required to fail one of the previously relaxed cuts, while in the second case both X are required to fail a cut. The first control region is referred to as $Z + \overline{X}X$, while the latter, already introduced in Section 7.2.1, is denoted by $Z + \overline{X}\,\overline{X}$. The observed number of events in the inclusive $Z + XX$ control region, as well as in the two $Z + \overline{X}X$ and $Z + \overline{X}\,\overline{X}$ control regions are shown in Table 7.10.

Table 7.7 Control regions definition.

$Z + XX$	Full selection on leading dilepton, subleading leptons pass all criteria but ID, isolation and d_0/σ_{d_0}.
$Z + \overline{X}X$	Same as $Z + XX$, but at least one X is required to fail one cut among ID, isolation and d_0/σ_{d_0}.
$Z + \overline{X}\,\overline{X}$	Same as $Z + XX$, but both Xs are required to fail one cut among ID, isolation and d_0/σ_{d_0}.
$Z + X$	Full selection on leading dilepton. One additional lepton with $p_{\mathrm{T}} > 7$ GeV required.

By comparing the two composition tables, Table 7.8 and 7.9, one can see how the heavy flavour component in both $Z + XX$ control regions is in very good agreement with the one in

the $Z + X$ control region built requiring $MV1 > 0.20$. The same applies to the f component, which is much closer for the $Z + X$ control region built with $MV1 > 0.20$, rather than for the standard $Z + X$ with no b-matching requirements.

Table 7.8 Truth composition of the reconstruction categories (fraction of the number of events in the truth categories for each reconstruction category) for the $Z + X$ control regions obtained with different choices of the MV1 cut (no cut, 0.07, 0.08, 0.1, 0.2, 0.3, 0.39). Truth categories are indicated with italic letters, whilst capital letters are used to indicate reconstruction categories.

	e		***q***		γ		***f***	
	$4e$	$2\mu 2e$	$4e$	$2\mu 2e$	$4e$	$2\mu 2e$	$4e$	$2\mu 2e$
				$Z + X$ with no cut on MV1				
E	0.010 ± 0.000	0.006 ± 0.000	0.135 ± 0.001	0.130 ± 0.001	0.213 ± 0.003	0.222 ± 0.002	0.642 ± 0.004	0.642 ± 0.004
F	0.001 ± 0.000	0.000 ± 0.000	0.013 ± 0.000	0.012 ± 0.000	0.055 ± 0.001	0.055 ± 0.001	0.931 ± 0.004	0.932 ± 0.003
				$Z + X$ with MV1 > 0.07				
E	0.011 ± 0.001	0.006 ± 0.000	0.176 ± 0.002	0.184 ± 0.002	0.225 ± 0.003	0.241 ± 0.003	0.588 ± 0.005	0.568 ± 0.005
F	0.001 ± 0.000	0.000 ± 0.000	0.017 ± 0.000	0.019 ± 0.000	0.062 ± 0.001	0.065 ± 0.001	0.919 ± 0.004	0.916 ± 0.005
				$Z + X$ with MV1 > 0.08				
E	0.011 ± 0.001	0.006 ± 0.000	0.205 ± 0.002	0.242 ± 0.002	0.237 ± 0.004	0.269 ± 0.004	0.548 ± 0.005	0.483 ± 0.005
F	0.001 ± 0.000	0.001 ± 0.000	0.021 ± 0.001	0.029 ± 0.001	0.069 ± 0.001	0.084 ± 0.002	0.908 ± 0.005	0.886 ± 0.006
				$Z + X$ with MV1 > 0.1				
E	0.011 ± 0.001	0.006 ± 0.000	0.224 ± 0.002	0.260 ± 0.003	0.240 ± 0.004	0.270 ± 0.004	0.525 ± 0.005	0.464 ± 0.005
F	0.001 ± 0.000	0.001 ± 0.000	0.024 ± 0.001	0.032 ± 0.001	0.072 ± 0.002	0.086 ± 0.002	0.903 ± 0.005	0.881 ± 0.006
				$Z + X$ with MV1 > 0.2				
E	0.010 ± 0.001	0.005 ± 0.000	0.277 ± 0.003	0.301 ± 0.003	0.238 ± 0.004	0.259 ± 0.005	0.474 ± 0.006	0.435 ± 0.006
F	0.001 ± 0.000	0.001 ± 0.000	0.032 ± 0.001	0.039 ± 0.001	0.075 ± 0.002	0.087 ± 0.002	0.891 ± 0.006	0.873 ± 0.007
				$Z + X$ with MV1 > 0.3				
E	0.008 ± 0.001	0.004 ± 0.000	0.387 ± 0.004	0.399 ± 0.004	0.206 ± 0.005	0.215 ± 0.005	0.398 ± 0.006	0.382 ± 0.007
F	0.001 ± 0.000	0.000 ± 0.000	0.051 ± 0.001	0.056 ± 0.001	0.070 ± 0.003	0.078 ± 0.003	0.878 ± 0.009	0.865 ± 0.009
				$Z + X$ with MV1 > 0.39				
E	0.009 ± 0.001	0.004 ± 0.000	0.423 ± 0.005	0.434 ± 0.004	0.194 ± 0.005	0.196 ± 0.005	0.374 ± 0.007	0.365 ± 0.007
F	0.001 ± 0.000	0.000 ± 0.000	0.058 ± 0.001	0.062 ± 0.002	0.067 ± 0.003	0.076 ± 0.003	0.874 ± 0.009	0.862 ± 0.009

Table 7.9 Truth composition of the reconstruction categories (fraction of the number of events in the truth categories for each reconstruction category) for the two considered $Z + XX$ control regions: $Z + \overline{X}X$ and $Z + \overline{X}\overline{X}$. Truth categories are indicated with italic letters, whilst capital letters are used to indicate reconstruction categories.

	e		***q***		γ		***f***	
	$4e$	$2\mu 2e$	$4e$	$2\mu 2e$	$4e$	$2\mu 2e$	$4e$	$2\mu 2e$
				$Z + \overline{X}X$				
E	0.004 ± 0.000	0.003 ± 0.000	0.280 ± 0.010	0.286 ± 0.010	0.186 ± 0.014	0.173 ± 0.014	0.530 ± 0.023	0.539 ± 0.023
F	0.001 ± 0.000	0.001 ± 0.000	0.029 ± 0.003	0.031 ± 0.003	0.059 ± 0.006	0.049 ± 0.005	0.911 ± 0.025	0.920 ± 0.024
				$Z + \overline{X}\overline{X}$				
E	0.067 ± 0.002	0.061 ± 0.001	0.274 ± 0.008	0.288 ± 0.009	0.184 ± 0.013	0.174 ± 0.013	0.475 ± 0.020	0.477 ± 0.020
F	0.012 ± 0.001	0.009 ± 0.000	0.034 ± 0.003	0.036 ± 0.003	0.059 ± 0.006	0.053 ± 0.005	0.895 ± 0.023	0.902 ± 0.023

These tables are of course built using simulated $Z + X$ and $Z + XX$ samples, but we have

Table 7.10 Observed number of events in the inclusive $Z + XX$ control region, as well as in the two control regions with inverted cuts, $Z + \overline{X}X$ and $Z + \overline{X}\,\overline{X}$.

Events in $Z + XX$		
	$4e$	$2\mu 2e$
EE	195 ± 14	220 ± 15
EF	245 ± 16	263 ± 16
FE	145 ± 12	163 ± 13
FF	261 ± 16	290 ± 17
Tot	846 ± 29	936 ± 31
Events in $Z + \overline{X}X$		
	$4e$	$2\mu 2e$
EE	138 ± 12	151 ± 13
EF	235 ± 15	257 ± 16
FE	135 ± 12	151 ± 13
FF	259 ± 16	289 ± 17
Tot	767 ± 28	848 ± 29
Events in $Z + \overline{X}\,\overline{X}$		
	$4e$	$2\mu 2e$
EE	100 ± 10	100 ± 10
EF	192 ± 14	209 ± 15
FE	118 ± 11	131 ± 12
FF	246 ± 16	270 ± 16
Tot	656 ± 26	710 ± 27

also studied the compositions in data by looking at the population of different reconstruction categories. For example we can compute the fractions of reconstructed electron-like objects (E-like) in the different $Z + X$ control regions, and compare them with the ones in the two $Z + XX$ control regions. The results of this study are summarised in Tables 7.11 and 7.12. From here, one can clearly see how the fractions in the $Z + X$ with no b-tagging requirements are considerably lower than the ones in $Z + \overline{X}X$ and $Z + \overline{X}\overline{X}$, while the latter is quite close to the $Z + X$ with $MV1 > 0.30$ and $MV1 > 0.20$.

Additionally, we can as well exploit the b-matching selection to define a "B" (heavy flavour-like)

Table 7.11 Fraction of E-like events for the $Z + X$ control regions obtained with different choices of the MV1 cut (no cut, 0.07, 0.08, 0.1, 0.2, 0.3, 0.39).

E / (E+F) in $\boldsymbol{Z + X}$		
	$4e$	$2\mu 2e$
no MV1 cut	0.316 ± 0.001	0.313 ± 0.001
$\boldsymbol{MV1 > 0.07}$	0.332 ± 0.002	0.336 ± 0.001
$\boldsymbol{MV1 > 0.08}$	0.347 ± 0.002	0.367 ± 0.002
$\boldsymbol{MV1 > 0.1}$	0.355 ± 0.002	0.374 ± 0.002
$\boldsymbol{MV1 > 0.2}$	0.375 ± 0.002	0.388 ± 0.002
$\boldsymbol{MV1 > 0.3}$	0.407 ± 0.003	0.413 ± 0.003
$\boldsymbol{MV1 > 0.39}$	0.417 ± 0.003	0.421 ± 0.003

Table 7.12 Fraction of E-like events for two different $Z + XX$ control regions: $Z + \overline{X}X$ and $Z + \overline{X}\overline{X}$.

E / (E+F) in $\boldsymbol{Z + XX}$		
	$4e$	$2\mu 2e$
$\boldsymbol{Z + \overline{X}X}$	0.425 ± 0.013	0.423 ± 0.012
$\boldsymbol{Z + \overline{X}\overline{X}}$	0.392 ± 0.014	0.382 ± 0.013

reconstruction category. In this case, we proceed as follows:

1. we build the $Z + X$ control region requiring the X to be b-matched (per-event matching, using different MV1 cuts for systematic studies)

2. we select, from the b-enriched $Z + X$ sample of step 1 and from the $Z + XX$ sample, a sub-sample of events in which X is b-matched (per-electron matching, $MV1 > 0.98$)

Notice that, while no ambiguity arises in the event categorisation when considering only the E and the F category, which are mutually exclusive by definition, this is no longer the case when the additional B category is included. Three possible strategies for categorising the events are possible, as shown in Figure 7.4. The impact of choosing different strategies was found to be of the order of a few percent, and finally the first strategy was chosen for our studies.

Once the B category is defined, we can thus proceed computing the fractions of B-like events as done for the E category, and compare the results for the various control regions, as shown

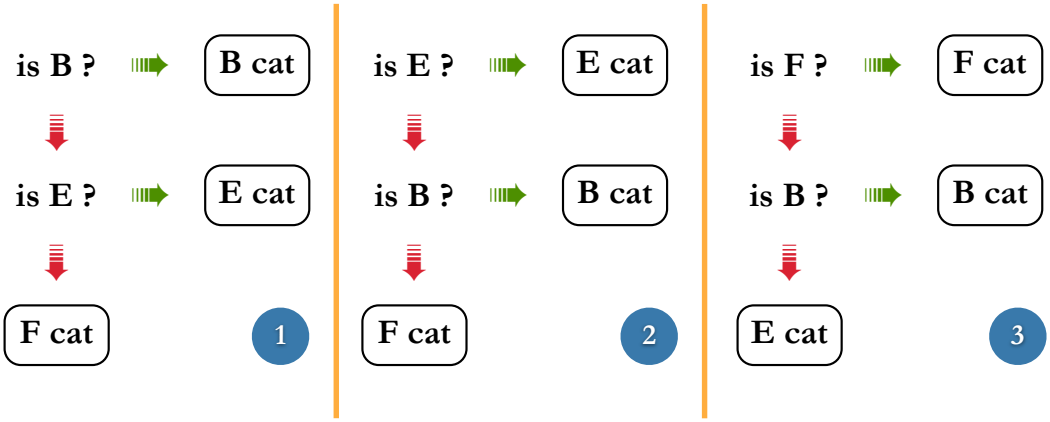

Figure 7.4 Possible strategies for categorising the selected events into E-like, F-like and B-like.

in Tables 7.13 and 7.14. Once again, while there is a clear mismatch between the fraction in the standard $Z + X$ and in the two $Z + XX$ control regions, the latter agree very well with the values obtained for the $Z + X$ with $MV1 > 0.2$.

Table 7.13 Fraction of B-like events for the $Z + X$ control regions obtained with different choices of the MV1 cut (no cut, 0.07, 0.08, 0.1, 0.2, 0.3, 0.39).

B / (E+F+B) in $Z + X$		
	$4e$	$2\mu 2e$
no MV1 cut	0.038 ± 0.001	0.036 ± 0.001
$MV1 > 0.07$	0.054 ± 0.001	0.057 ± 0.001
$MV1 > 0.08$	0.067 ± 0.001	0.083 ± 0.001
$MV1 > 0.1$	0.076 ± 0.001	0.094 ± 0.001
$MV1 > 0.2$	0.101 ± 0.001	0.116 ± 0.001
$MV1 > 0.3$	0.168 ± 0.002	0.174 ± 0.002
$MV1 > 0.39$	0.192 ± 0.002	0.196 ± 0.002

Table 7.14 Fraction of B-like events for two different $Z + XX$ control regions: $Z + \overline{X}X$ and $Z + \overline{X}\overline{X}$.

B / (E+F+B) in $Z + XX$		
	$4e$	$2\mu 2e$
$Z + \overline{X}X$	0.102 ± 0.008	0.110 ± 0.008
$Z + \overline{X}\overline{X}$	0.107 ± 0.009	0.111 ± 0.008

Overall, the best choice seems to be using $Z + X$ with an $MV1 > 0.20$ cut applied and the $Z + \overline{X}\overline{X}$ control region, while the other options are considered in the estimation of the related systematic uncertainty.

We can now extract from our $Z + X$ sample in data the efficiencies to pass the isolation, impact parameter significance and electron ID selections applied in the standard analysis, with

respect to the relaxed selection used to define the control regions. These efficiencies, which in this method are evaluated in bins of p_{T}, η, for each channel ($4e$ or $2\mu 2e$) and reconstruction category (E, F), are then used to extract the transfer factors, according to the following formula:

$$TF = \frac{\varepsilon_{X_3} \cdot \varepsilon_{X_4}}{(1-\varepsilon_{X_3})(1-\varepsilon_{X_4})} \tag{7.1}$$

where ε_{X_3} and ε_{X_4} are the efficiencies assigned to the two X, with $p_{\mathrm{T}X_3} > p_{\mathrm{T}X_4}$. This transfer factor formula is derived for the specific $Z + \overline{X}\overline{X}$ control region, where both X are required to fail a cut, and it is different for other control regions. The formula used for the $Z + \overline{X}X$ is for example:

$$TF = \frac{\varepsilon_{X_3} \cdot \varepsilon_{X_4}}{1-(\varepsilon_{X_3} \cdot \varepsilon_{X_4})} \tag{7.2}$$

The efficiencies extracted from our $Z + X$ with $MV1 > 0.2$ data sample are shown in Table 7.15 integrated over p_{T} and η, and compared to the corresponding values from MC.

Table 7.15 Efficiencies to pass the isolation, impact parameter and electron ID selections, extracted from the $Z + X$ control region. Results obtained from data and simulated events are shown.

Efficiencies to pass relaxed cuts		
Data $Z + X$ sample		
	$4e$	$2\mu 2e$
E	0.104 ± 0.002	0.106 ± 0.002
F	0.025 ± 0.001	0.029 ± 0.001
MC $Z + X$ sample		
	$4e$	$2\mu 2e$
E	0.089 ± 0.002	0.087 ± 0.002
F	0.021 ± 0.001	0.023 ± 0.001

The estimated number of background events in the signal region is finally obtained by applying the transfer factors to the events in the $Z + XX$ control region.
To avoid having any remaining events from the irreducible ZZ^* background, the same procedure is applied using ZZ MC for the $Z + XX$ control region, and the final result is then subtracted from our estimation.
In $Z + \overline{X}\overline{X}$ specifically, the contribution from WZ background, which we would like to include in our reducible background estimation, is instead heavily suppressed. In order to take this into account, we first subtract any remaining contribution as we do for the ZZ^* background, and then add the prediction obtained by applying the full selection on WZ MC. This correction does not apply in the case of $Z + \overline{X}X$, which contains most of the WZ background contribution.

Study on Jet p_{T} cut

It should be noted that all available jets, with p_{T} down to 10 GeV, are used in this method. As only jets with $p_{\mathrm{T}} > 20$ GeV are typically used in ATLAS physics analyses, the effect of including jets below 20 GeV was thoroughly studied. The composition of the $Z + X$ control region was estimated again considering only jets with $p_{\mathrm{T}} > 20$ GeV, and then compared to the numbers in Tables 7.8. No significant differences were observed. The same conclusion was drawn by comparing various $Z + X$ distributions, as for example the b-tagger output weight and the η distributions, shown in Figure 7.5(a) and 7.5(b), respectively. A discrepancy was instead observed for the low-p_{T} bins in the efficiencies to pass the isolation, impact parameter significance and electron ID selections, which are shown, in p_{T} bins of the X, in Table 7.16. Numbers obtained for the $Z + X$ sample, with and without including jets below 20 GeV, and for the $Z + \overline{X}X$ control region are compared. In order not to bias the results, for this comparison we used the $Z + \overline{X}X$ control region where we only considered the X not failing the identification, isolation and d_0/σ_{d_0} requirements. In other words, if X_3 fails the requirements, then X_4 enters the efficiency calculation, and viceversa. As can be seen, the efficiencies in the lower p_{T} bins are significantly lower when only selecting jets with $p_{\mathrm{T}} > 20$ GeV, and are further away from the ones in the $Z + \overline{X}X$ sample. This effect seems to be related to the fact that, by removing jets below 20 GeV, we are selecting less isolated objects, as confirmed by the calorimetric isolation distributions shown in Figure 7.6.

Finally, our studies showed how the inclusion in our procedure of jets with p_{T} down to 10 GeV not only does not bias the method, but actually provides a $Z + X$ sample with isolation properties closer to the $Z + XX$ control region.

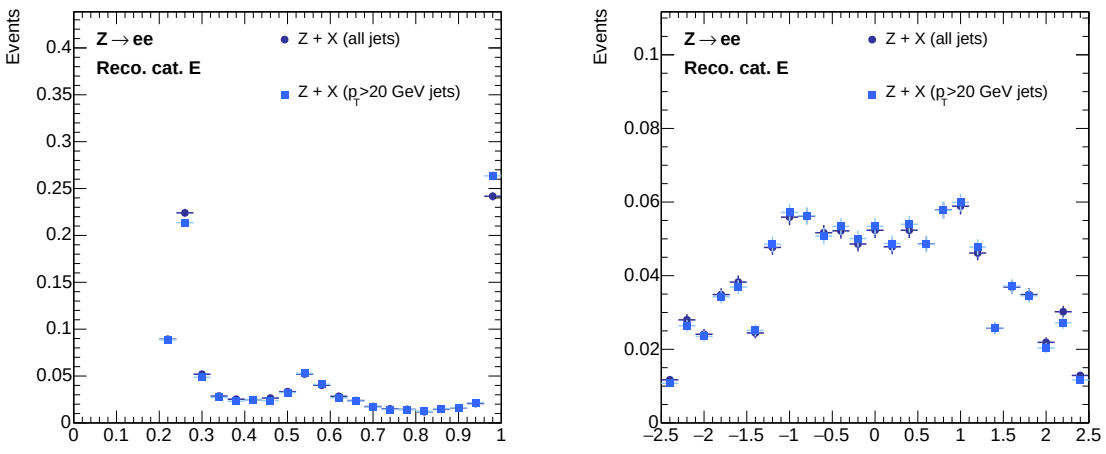

(a) **(b)**

Figure 7.5 (a) The b-tagger output weight and (b) the η distributions for the $Z + X$ sample with (blue circles) and without (light blue squares) including jets below 20 GeV. Results are shown for the $4e$ channel, and for E-like events.

Table 7.16 The efficiencies to pass the isolation, impact parameter significance and electron ID selections applied in the standard analysis. Numbers are obtained from the $Z + X$ data sample, with and without including jets with $p_{\mathrm{T}} < 20$ GeV, and for the $Z + \overline{X}X$ control region. The efficiencies are shown in bins of the X p_{T}, separately for the $4e$ and the $2\mu 2e$ channels.

	$Z + X$ All jets	$Z + X$ Jets > 20 GeV	$Z + \overline{X}X$
	$4e$ | $2\mu 2e$	$4e$ | $2\mu 2e$	$4e$ | $2\mu 2e$
	$7 < p_{\mathrm{T}} < 8$ GeV		
E	0.096 ± 0.006 | 0.117 ± 0.007	0.067 ± 0.006 | 0.069 ± 0.006	0.09 ± 0.04 | 0.09 ± 0.04
F	0.023 ± 0.002 | 0.026 ± 0.002	0.017 ± 0.002 | 0.014 ± 0.002	0.018 ± 0.013 | 0.017 ± 0.012
	$8 < p_{\mathrm{T}} < 9$ GeV		
E	0.088 ± 0.006 | 0.106 ± 0.007	0.065 ± 0.006 | 0.066 ± 0.006	0.09 ± 0.04 | 0.13 ± 0.05
F	0.024 ± 0.002 | 0.029 ± 0.003	0.017 ± 0.002 | 0.017 ± 0.002	0.000 ± 0.000 | 0.009 ± 0.009
	$9 < p_{\mathrm{T}} < 12$ GeV		
E	0.107 ± 0.006 | 0.110 ± 0.006	0.092 ± 0.005 | 0.090 ± 0.006	0.12 ± 0.03 | 0.12 ± 0.03
F	0.026 ± 0.002 | 0.027 ± 0.002	0.019 ± 0.002 | 0.019 ± 0.002	0.053 ± 0.016 | 0.032 ± 0.012
	$12 < p_{\mathrm{T}} < 20$ GeV		
E	0.093 ± 0.006 | 0.103 ± 0.006	0.091 ± 0.006 | 0.108 ± 0.006	0.11 ± 0.02 | 0.16 ± 0.03
F	0.024 ± 0.003 | 0.038 ± 0.004	0.024 ± 0.003 | 0.041 ± 0.004	0.047 ± 0.016 | 0.026 ± 0.011
	$p_{\mathrm{T}} > 20$ GeV		
E	0.130 ± 0.008 | 0.110 ± 0.008	0.123 ± 0.009 | 0.104 ± 0.008	0.26 ± 0.04 | 0.28 ± 0.04
F	0.040 ± 0.006 | 0.039 ± 0.006	0.042 ± 0.006 | 0.033 ± 0.006	0.07 ± 0.03 | 0.10 ± 0.03

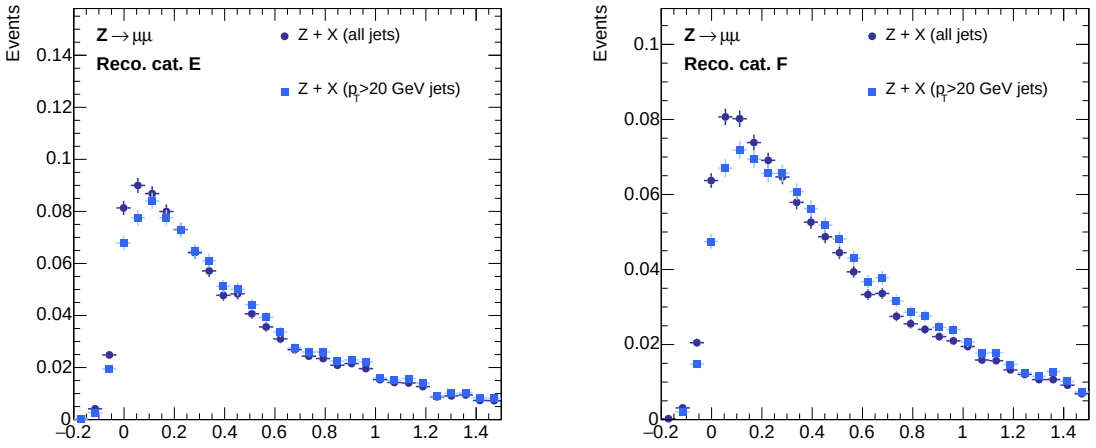

(a) **(b)**

Figure 7.6 The calorimetric isolation distribution for the $Z + X$ sample with (blue circles) and without (light blue squares) including jets below 20 GeV. Results are shown for the $2\mu 2e$ channel, and for (a) E-like and (b) F-like events.

Closure test with MC

In order to further test the internal consistency of the method, we performed a closure test using MC. The number of reducible background events obtained by applying the analysis selection to our MC samples is compared to the estimation that the described method provides when applied on MC. The results, shown in Table 7.17 with their statistical uncertainly only, are indeed compatible. The high uncertainty on the MC events in the signal region is due to the very low statistics available for the Z+jets sample.

Table 7.17 Closure test using MC. The number of reducible background events, obtained by applying the analysis selection to our MC samples, is compared to the estimation obtained by using our data-driven method on MC events. Only statistical uncertainties are shown.

	$4e$	$2\mu 2e$
MC events in signal region	1.4 ± 1.5	2.9 ± 1.1
Data-driven method on MC events	2.0 ± 0.1	2.3 ± 0.1

Systematic Uncertainties

Four different sources of systematic uncertainties were considered in our measurement:

– ***b*-tagging selection**
We vary the definition of the $Z + X$ control region, and therefore its composition, by taking the maximum difference between the central value ($MV1 > 0.2$) and the estimates obtained with all considered MV1 cuts between 0.07 and 0.39.

– **$Z + XX$ control region**
We vary the definition of the $Z + XX$ control region by taking the difference between $Z + \overline{X}X$ and ($Z + \overline{X}\overline{X}$ + WZ MC).

– **Reco categorization**
We consider the difference between the central value, obtained by categorising $Z + X$ and $Z + XX$ events into E-like and F-like objects, and the estimate obtained by introducing the B-like category in the binning. In order to do this, we follow the same procedure used to perform the test on the B-like composition, explained earlier in this section. Table 7.18 shows the truth composition of the reconstruction categories for both the $Z + X$ and the $Z + \overline{X}\overline{X}$ control regions. The compositions are in reasonable agreement and we achieve a high b-purity.

– **Jets p_{T} cut**
As explained earlier in this section, the use of jets with $p_{\mathrm{T}} < 20$ GeV in our method has shown no particular bias, and actually improve the composition agreement between the $Z + X$ and the $Z + XX$ control regions. Nonetheless, as these jets are not typically used in ATLAS we conservatively assign as systematic uncertainty the difference between the central value, and the estimate we obtain considering only jets with $p_{\mathrm{T}} > 20$ GeV.

Table 7.18 Truth composition of the reconstruction categories (fraction of the number of events in the truth categories for each reconstruction category) for $Z + X$ and $Z + \overline{X}\overline{X}$ control regions when three reconstruction categories are defined. An $MV1 > 0.2$ cut is applied in the $Z + X$ selection, and an $MV1 > 0.98$ cut is then used to define the B category for both $Z + X$ and $Z + \overline{X}\overline{X}$. Truth categories are indicated with italic letters, whilst capital letters are used to indicate reconstruction categories.

	e		***q***		***γ***		***f***	
	$4e$	$2\mu 2e$	$4e$	$2\mu 2e$	$4e$	$2\mu 2e$	$4e$	$2\mu 2e$
				$\boldsymbol{Z + X}$				
E	0.012 ± 0.001	0.006 ± 0.000	0.191 ± 0.003	0.202 ± 0.003	0.269 ± 0.005	0.301 ± 0.006	0.528 ± 0.007	0.491 ± 0.007
F	0.001 ± 0.000	0.001 ± 0.000	0.023 ± 0.001	0.027 ± 0.001	0.077 ± 0.002	0.090 ± 0.002	0.899 ± 0.007	0.882 ± 0.007
B	0.000 ± 0.000	0.000 ± 0.000	0.648 ± 0.007	0.644 ± 0.007	0.037 ± 0.003	0.034 ± 0.003	0.32 ± 0.01	0.32 ± 0.01
				$\boldsymbol{Z + \overline{X}\overline{X}}$				
E	0.005 ± 0.001	0.003 ± 0.000	0.18 ± 0.01	0.18 ± 0.01	0.210 ± 0.016	0.199 ± 0.016	0.61 ± 0.03	0.62 ± 0.03
F	0.001 ± 0.000	0.001 ± 0.000	0.018 ± 0.002	0.021 ± 0.002	0.059 ± 0.006	0.049 ± 0.005	0.92 ± 0.03	0.93 ± 0.03
B	0.000 ± 0.000	0.000 ± 0.000	0.67 ± 0.03	0.665 ± 0.023	0.051 ± 0.011	0.034 ± 0.009	0.279 ± 0.023	0.30 ± 0.03

The different systematic uncertainties are summarised in Table 7.19. The uncertainty related

Table 7.19 Contribution of the different systematic uncertainty sources to the final background estimate uncertainty.

Systematic source	$4e$		$2\mu 2e$	
b-tagging	0.328	(11.4%)	0.355	(11.2%)
$Z + XX$ control region	0.352	(12.2%)	0.201	(6.3%)
Reco categorization	0.068	(2.7%)	0.097	(3.1%)
Jets $p_{\mathrm{T}} > 20$ GeV	0.569	(19.7%)	0.806	(25.5%)

to the jets p_{T} cut could be removed if jets below 20 GeV become widely used in ATLAS in the future. This would result in a significant reduction of the total systematic uncertainty, which is indeed dominated by this contribution.

Impact of b-tagging efficiency scale factors

As mentioned earlier in this section, the most common MV1 operating points are the ones corresponding to 60%, 70% and 80% b-tagging efficiencies, and for these values data/MC efficiency scale factors are available, to account for any mis-modelling present in simulation. On the contrary, no scale factors are available for the various MV1 cuts used in this method, and therefore they are not applied to our MC samples. As the method is completely data-driven, and simulation is only used for the composition tables involved in the $Z + X$ "tuning" procedure, we expect the effect of not applying scale factors to be negligible. To confirm this assumption, we used the scale factors for a new operating point, corresponding to 85% b-tagging efficiencies, which were preliminarily made available at the time of this study. The relative cut on the MV1 output, which is 0.1644, is included among the ones used in the method and sufficiently close

to the baseline cut, and could thus be used to test the effect of the scale factors on the samples composition. Since no scale factors are available for jets below 20 GeV, we assigned the same scale factors computed for the lowest p_{T} bin, with doubled uncertainty.
Figure 7.7 shows the composition of the $Z + X$ control region as obtained when requiring $MV1 > 0.1644$, and when applying or not the data/MC scale factors on the samples. The values obtained when scaling the scale factors up and down with their uncertainties are also shown. As can be clearly seen, the variation on the composition due to the scale factors are very small, and covered by our systematic variations, represented in the plot by the compositions obtained with all other considered MV1 cuts. No additional systematic uncertainty was thus added.

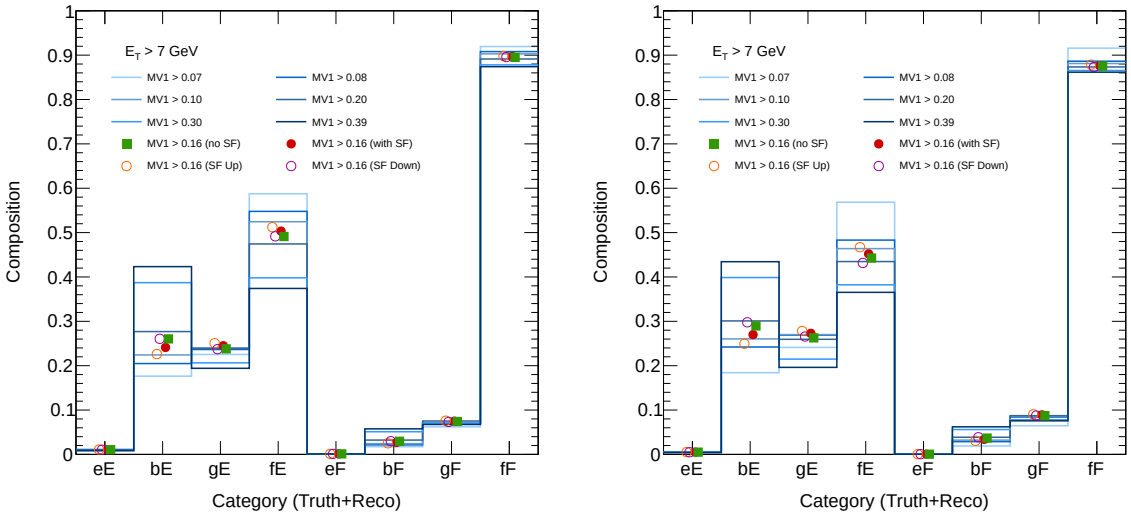

(a) **(b)**

Figure 7.7 Truth composition of the reconstruction categories for the $Z + X$ control region when requiring various MV1 cuts for the $4e$ (a) and for the $2\mu 2e$ (b) channels. Each column represents the fractions of events in one truth category (first letter) for a specific reconstruction category (second letter). For $MV1 > 0.1644$, the results obtained when applying (red filled circle) or not (green filled square) the data/MC scale factors on the samples are compared. The values obtained when scaling the scale factors up and down (empty circles) with their uncertainties are also shown.

Results

Finally, the reducible background estimations for the 2012 dataset are:

$$\mathbf{2\mu 2e}: \; 3.2 \pm 0.2 \text{ (stat.)} \; \pm 0.9 \text{ (syst.)}$$
$$\mathbf{4e}: \; 2.9 \pm 0.2 \text{ (stat.)} \; \pm 0.8 \text{ (syst.)}$$

While for the methods described in Sections 7.2.1 and 7.2.2 the procedure had to be simplified when applied to 2011 data sample due to lack of statistics, the exact same procedure illustrated up-to now was followed to estimate the reducible background contributions to the 2011 dataset.

The different event selection applied to 7 TeV data, in particular regarding the different electron ID menu, led to different compositions in our control regions, so that the "tuning" procedure of the $Z + X$ had to be re-optimised. The same MV1 cuts were studied, together with both $Z + XX$ control regions, and finally it was chosen to use a cut value of 0.15 and $Z + \overline{X}\overline{X}$ as baseline.

The estimated reducible background yields for the 2011 dataset are the following:

$$\mathbf{2\mu 2e}: \ 2.8 \pm 0.5 \text{ (stat.)} \ \pm 0.8 \text{ (syst.)}$$
$$\mathbf{4e}: \ 3.4 \pm 0.9 \text{ (stat.)} \ \pm 0.8 \text{ (syst.)}$$

The final results for both 2011 and 2012 are also summarised in Table 7.6, together with the estimations obtained using the other described methods. As one can see, the various results are in good agreement among each other, and the size of the associated uncertainties are comparable. In this regard it should be noted that the definition of a b-enriched $Z + X$ control region in data, described in detail in the following section, has allowed to quantify and correct the disagreement between data and MC for the heavy flavour component, leading to a significant reduction of the uncertainties on both the reco-truth unfolding and the $3\ell + X$ methods. In particular, an improvement of approximately 10% with respect to the previous results is achieved on the $3\ell + X$ method (see Section 7.2.4), which is used for the background normalisation in the fit to extract the Higgs mass. The transfer factor method represents a fundamental cross check to these results, as it provides the only completely data-driven estimation of the reducible backgrounds.

7.2.4 b-enriched $Z + X$ control region

As seen in Sections 7.2.1 and 7.2.2, both the $3\ell + X$ and the reco-truth unfolding methods extrapolate the background yields to the signal region by means of efficiencies computed from simulated $Z + X$ events. To account for MC mismodelling, these efficiencies are corrected for using data-to-MC efficiency scale factors, which are obtained from control regions in data where only one component is enhanced.

Moreover, in the $3\ell + X$ simultaneous fit, the heavy flavour yield, which is heavily suppressed in this control region, has to be constrained to the value predicted by MC. The existing discrepancies in the heavy flavour contribution between data and simulation, which will be shortly demonstrated, need to be also accounted for by applying appropriate correction factors.

These normalisation factors, as well as the efficiency scale factors for the q component, are extracted from a data control region enriched in $b \to e$, whose definition is based on the same b-matching algorithms described in the previous section. Both strategies, the "per-event" and the "per-electron" matchings, have been considered for this study, and all the three official MVA working points were tested. The standard $Z + X$ selection was used, with an additional cut on the missing transverse energy ($E_{\mathrm{T}}^{\mathrm{miss}} < 25$ GeV), meant to suppress the contribution from WZ events.

Once again we studied the truth composition of the reconstruction categories for the various $Z + X$ CR from MC, the objective being this time to select the one with the highest q purity.

These compositions are shown in Table 7.20, from which one can see how the amount of events categorised as q is high when we focus on the E-like component, while this is not the case for the F-like category, still completely dominated by light jets faking an electron. It was therefore decided to only consider for our purposes, events with b-matched X categorised as E-like. The table also shows, as expected, that the purities are higher when we require the b-jet to be directly matched to the X ("per-electron" match) and for tighter MV1 cuts.
The selected $Z + X$ control region is thus defined as follows:

- the X is required to be matched to at least one jet within a cone of $\Delta R = 0.4$;
- if more than one jet is found, the one with smallest ΔR is chosen;
- the jet is required to be b-tagged, with an MV1 output higher than 0.9867 (60% b-tagging efficiency);
- the X is required to be E-like, according to the definition described in Section 7.2.

The achieved purity for this control region is about 83%.

Table 7.20 Truth composition (fraction of the number of events in the truth categories for each reconstruction category) of different $Z + X$ control regions, obtained with the "per-electron" and "per-event" matching algorithms, and with different b-tagging efficiencies. In the control region built with the "per-electron" matching and 60% b-tagging efficiency we achieve q purities higher than 80%.

	e		q		γ		f	
	$4e$	$2\mu 2e$	$4e$	$2\mu 2e$	$4e$	$2\mu 2e$	$4e$	$2\mu 2e$
				60% b-tagging efficiency, "per-electron" matching				
E	0	0	0.832 ± 0.010	0.833 ± 0.010	0.040 ± 0.004	0.038 ± 0.004	0.129 ± 0.007	0.130 ± 0.008
F	0	0	0.262 ± 0.008	0.265 ± 0.008	0.032 ± 0.005	0.028 ± 0.004	0.706 ± 0.026	0.707 ± 0.025
				70% b-tagging efficiency, "per-electron" matching				
E	0	0	0.758 ± 0.009	0.754 ± 0.008	0.081 ± 0.005	0.079 ± 0.005	0.161 ± 0.007	0.167 ± 0.007
F	0	0	0.195 ± 0.006	0.200 ± 0.006	0.046 ± 0.005	0.051 ± 0.005	0.759 ± 0.021	0.750 ± 0.020
				80% b-tagging efficiency, "per-electron" matching				
E	0.003 ± 0.001	0.001 ± 0.000	0.557 ± 0.006	0.551 ± 0.006	0.200 ± 0.007	0.204 ± 0.007	0.241 ± 0.007	0.244 ± 0.007
F	0.001 ± 0.001	0	0.107 ± 0.003	0.101 ± 0.003	0.086 ± 0.005	0.096 ± 0.005	0.806 ± 0.014	0.803 ± 0.013
				60% b-tagging efficiency, "per-event" matching				
E	0.006 ± 0.001	0.003 ± 0.000	0.744 ± 0.008	0.750 ± 0.008	0.058 ± 0.004	0.055 ± 0.004	0.192 ± 0.008	0.192 ± 0.008
F	0.001 ± 0.000	0.001 ± 0.000	0.170 ± 0.005	0.187 ± 0.006	0.044 ± 0.005	0.043 ± 0.004	0.785 ± 0.019	0.770 ± 0.019
				70% b-tagging efficiency, "per-event" matching				
E	0.007 ± 0.001	0.003 ± 0.000	0.649 ± 0.007	0.647 ± 0.007	0.097 ± 0.005	0.095 ± 0.005	0.248 ± 0.007	0.254 ± 0.008
F	0.001 ± 0.000	0	0.120 ± 0.003	0.132 ± 0.004	0.051 ± 0.004	0.053 ± 0.004	0.827 ± 0.015	0.814 ± 0.015
				80% b-tagging efficiency, "per-event" matching				
E	0.009 ± 0.001	0.004 ± 0.000	0.423 ± 0.005	0.434 ± 0.004	0.194 ± 0.005	0.196 ± 0.005	0.374 ± 0.007	0.365 ± 0.007
F	0.001 ± 0.000	0	0.058 ± 0.001	0.062 ± 0.002	0.067 ± 0.003	0.076 ± 0.003	0.874 ± 0.009	0.862 ± 0.009

The effect of increasing purity is also clearly visible in data from Figure 7.8, which shows the d_0 significance distribution for the $Z + X$ control region obtained with "per-event" matching and 80% b-tagging efficiency (7.8(a)), and for the selected $Z + X$ control region (7.8(b)). The shape is indeed much broader when the percentage of electrons coming from a heavy quark decay is higher.

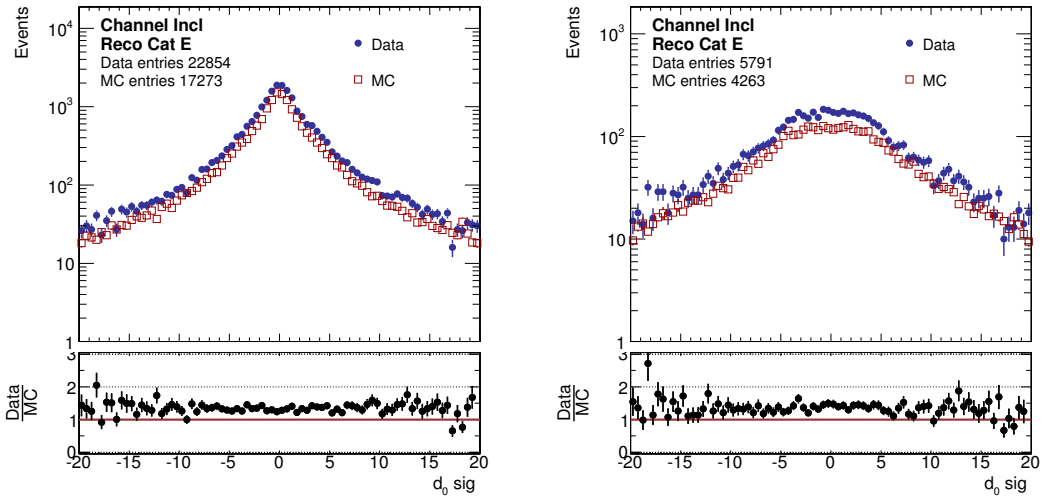

(a) **(b)**

Figure 7.8 d_0 significance distribution (integrated over η and p_{T}) for the $Z + X$ control regions obtained with "per-event matching" and 80% b-tagging efficiency (a), and for the selected one ("per-electron" matching and 60% b-tagging efficiency) (b). The plots are done inclusively for the two $4e$ and $2\mu 2e$ final states.

Figure 7.8, as well as Figure 7.9, also show a clear discrepancy between data and simulation, in which the total number of events is always lower than in data. The ratio between the yields in data and MC for different p_{T} bins are shown in Table 7.21, and represent the normalisation factors used in the $3\ell + X$ method.
Thanks to the introduction of these correction factors in the fitting procedure, the statistical uncertainty on the final results obtained with the $3\ell + X$ method has been reduced by approximately 10% with respect to the previous result. Prior to the estimation of the correction factors, a conservative uncertainty was indeed assigned to account for the unknown level of discrepancy, resulting in a statistical component of the uncertainty of approximately 20% [2], to be compared with the current 10%.

The data-to-MC ratio of the efficiencies to pass the relaxed requirements (electron identification, isolation and d_0/σ_{d_0}) are instead illustrated in bins of p_{T} in Table 7.22. The results are compatible with one for all p_{T} bins.

The systematic uncertainties were computed, both for the normalisation factors and for the efficiency scale factors, by taking the differences between the central values and the results obtained using different $Z + X$ control region. Only the control regions with q purity higher than 70% were considered for this purpose (i.e. the control regions obtained with 60% and 70%

[2] Previous results lead for the final estimation, to $2.6 \pm 0.5 \pm 0.5$ and $2.6 \pm 0.5 \pm 0.4$ for the $2e2\mu$ and the $4e$ channel, respectively.

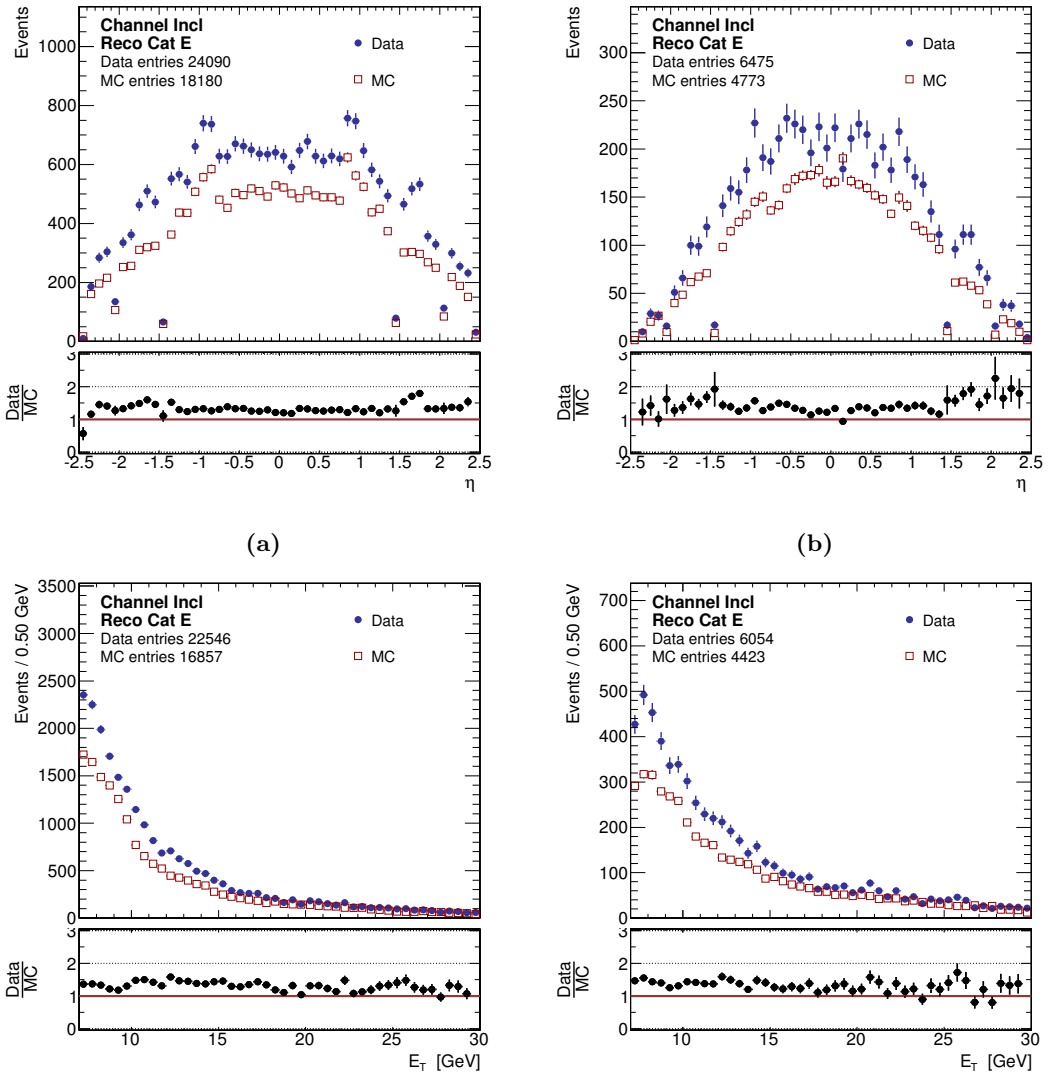

Figure 7.9 η and p_{T} distributions for the $Z + X$ control regions obtained with "per-event matching" and 80% b-tagging efficiency ((a), (c)), and for the selected one ("per-electron" matching and 60% b-tagging efficiency) ((b), (d)). The plots are done inclusively for the two $4e$ and $2\mu 2e$ final states.

b-tagging efficiencies with "per electron" matching, and the one obtained with 60% efficiency and "per-event" matching). The difference between the central values and the results obtained when using only jets with $p_{\mathrm{T}} > 20$ GeV is also taken into account.

Table 7.21 Number of events in data over number of events in MC for different p_{T} bins, obtained from the b-enriched $Z + X$ control region.

Normalisation Factors		
	$4e$	$2\mu 2e$
$7 < p_{\mathrm{T}} < 10$ GeV	1.43 ± 0.05 (stat.) ± 0.05 (syst.)	1.39 ± 0.05 (stat.) ± 0.04 (syst.)
$10 < p_{\mathrm{T}} < 15$ GeV	1.46 ± 0.05 (stat.) ± 0.10 (syst.)	1.38 ± 0.05 (stat.) ± 0.07 (syst.)
$p_{\mathrm{T}} > 15$ GeV	1.29 ± 0.05 (stat.) ± 0.03 (syst.)	1.21 ± 0.04 (stat.) ± 0.04 (syst.)
Inclusive	1.39 ± 0.03 (stat.) ± 0.03 (syst.)	1.33 ± 0.03 (stat.) ± 0.04 (syst.)

Table 7.22 Data/MC efficiency scale factors in different p_{T} bins obtained from the b-enhanced control region.

Efficiency Scale Factors	
$7 < p_{\mathrm{T}} < 10$ GeV	0.99 ± 0.08 (stat.) ± 0.11 (syst.)
$10 < p_{\mathrm{T}} < 15$ GeV	0.95 ± 0.09 (stat.) ± 0.11 (syst.)
$p_{\mathrm{T}} > 15$ GeV	0.96 ± 0.11 (stat.) ± 0.22 (syst.)

7.3 Shape of the Reducible Background Contributions

In order to extract the shape and normalisation of the reducible backgrounds in the mass fit region, which is defined between 110 and 140 GeV, the $m_{4\ell}$ distributions of these backgrounds are needed. In the case of $\ell\ell + \mu\mu$ backgrounds this distribution is taken from simulation, and the relative uncertainty is established varying the track isolation and impact parameter significance selections. Data control regions are instead used for the $\ell\ell + ee$ background shape, with distributions reweighed using the transfer factors described above to match the kinematics of the signal region. The shape used in the mass fit is taken from the $3\ell + X$ sample, while the related uncertainty is taken as the difference between the shapes obtained with the reco-truth and the transfer factor methods.

The smoothed $m_{4\ell}$ shapes of both the $\ell\ell + \mu\mu$ and the $\ell\ell + ee$ reducible backgrounds are shown in Figure 7.10(a) in the full mass range, and in Figure 7.10(b) in the mass fit range.

The same procedure is applied in the differential cross-section analysis to estimate the uncertainty on the shape of the reducible background contributions to the distributions of the variables of interest. An additional uncertainty on the ZZ and WZ contributions is also considered in this case, for the jet related variables. The simulation predictions used in the estimation are compared to the data in the region $m_{4\ell} > 190$ GeV, where the ZZ background process is dominant, and systematic uncertainties are applied to account for the shape differences.

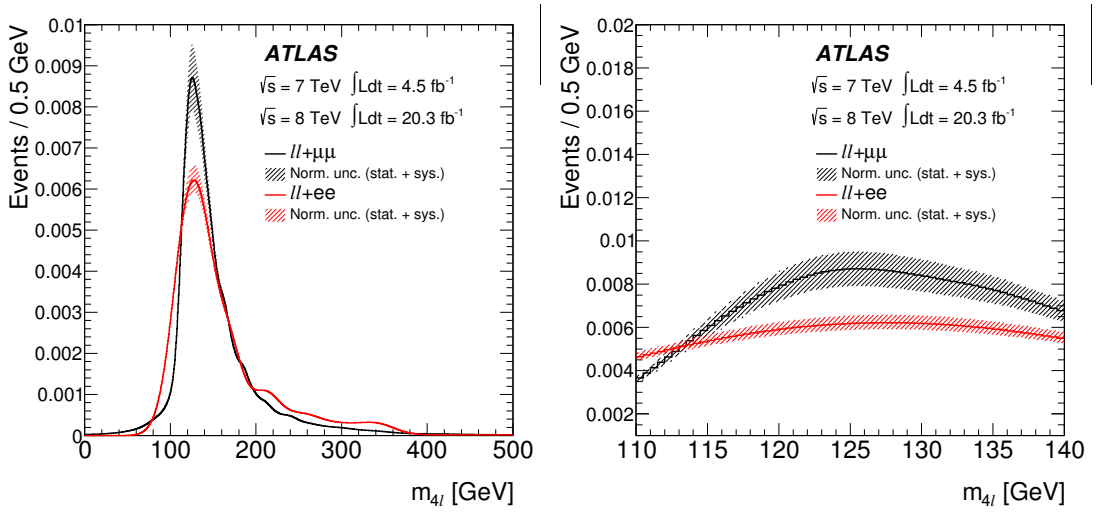

Figure 7.10 Reducible background shape in the $\ell\ell + \mu\mu$ and $\ell\ell + ee$ final states for (a) the full mass range, and (b) the fit range $110 < m_{4\ell} < 140$ GeV.

7.4 Background for Categories

For the evaluation of the reducible backgrounds in the categorised analysis, the fractions of the background contributions to each production category are extracted from simulation. These fractions are then applied to the background estimates seen in Tables 7.3 and 7.6, to give the background contamination in each category, as shown in Table 7.23. The procedure was validated extracting the fractions from the $3\ell + X$ data control region as well, and comparing the results with the fractions obtained from MC. The observed differences are included in the systematic uncertainty. Due to the poor statistics of the MC samples available for 2011, the same fractions extracted using 2012 simulated samples are also applied for 2011.

The expected ZZ^* background is taken from simulation for each production category, and shown in Table 8.4.

Table 7.23 Summary of the reducible background estimates for the data recorded at $\sqrt{s} = 7$ TeV and $\sqrt{s} = 8$ TeV in the full $m_{4\ell}$ mass range. The quoted uncertainties include the combined statistical and systematic components.

Channel	*ggF enriched*	*VBF enriched*	*VH-hadronic enriched*	*VH-leptonic enriched*
		$\sqrt{s} = 7$ TeV		
$\ell\ell + \mu\mu$	0.98 ± 0.32	0.12 ± 0.08	0.04 ± 0.02	0.004 ± 0.004
$\ell\ell + ee$	5.5 ± 1.2	0.51 ± 0.6	0.20 ± 0.16	0.06 ± 0.11
		$\sqrt{s} = 8$ TeV		
$\ell\ell + \mu\mu$	6.7 ± 1.4	0.6 ± 0.6	0.21 ± 0.13	0.003 ± 0.003
$\ell\ell + ee$	5.1 ± 1.4	0.5 ± 0.6	0.19 ± 0.15	0.06 ± 0.11

Chapter 8

Measurement of the Higgs Boson Mass and Couplings

This chapter presents the final ATLAS Run 1 results of the Higgs boson mass, production and couplings measurements in the decay channel $H \to ZZ^* \to 4\ell$.

Section 8.1 describes the multivariate discriminants used to improve the analysis sensitivity, while the signal and background modelling used in the mass and signal strength measurements, as well as in the categorised analysis, are presented in Section 8.2. The systematics uncertainties affecting the various measurements are discussed in Section 8.3, and the results are finally presented in Section 8.4.

8.1 Multivariate Discriminants

The analysis sensitivity is improved by employing three multivariate discriminants to distinguish between the different classes of four-lepton events. The first one is used to increase the discrimination of the ZZ^* background against the Higgs signal. The other two, already mentioned in Section 6.4.1, are instead used in the categorised analysis to separate the VBF- and VH-produced Higgs boson signal from the ggF one in the *VBF enriched* and *VH-hadronic enriched* categories. All three discriminants are based on boosted decision trees (BDT) [145].

8.1.1 BDT for ZZ^* background rejection

$H \to ZZ^* \to 4\ell$ and ZZ^* background events exhibit differences in their kinematics which can be exploited to better distinguish them, and are in this case incorporated into a BDT discriminant (BDT_{ZZ^*}). All events passing the inclusive event selection are considered in the training, which is done using simulated samples of ggF signal production, and $q\bar{q} \to ZZ^*$ background events. An additional cut on the four-lepton invariant mass is applied, which is required to be within 115 and 130 GeV. This particular asymmetric range with respect to the Higgs mass was chosen such that 95% of the signal would be included, and to account for residual FSR and Bremsstrahlung effects.

The discriminating variables used as inputs to the BDT training are the transverse momentum of the four-lepton system ${p_{\mathrm{T}}}^{4\ell}$, the pseudorapidity of the four-lepton system $\eta^{4\ell}$, and a matrix-

element-based kinematic discriminant (D_{ZZ^*}). The latter is defined as follows:

$$D_{ZZ^*} = \ln\left(\frac{|\mathcal{M}_{\text{sig}}|^2}{|\mathcal{M}_{ZZ}|^2}\right), \tag{8.1}$$

where $\mathcal{M}_{\text{sig}}$ and $\mathcal{M}_{\text{ZZ}}$ correspond to the matrix element for the signal process and the ZZ^* background process, respectively, both computed at leading order using MadGraph5 [146]. The SM hypothesis of a scalar boson with spin-parity $J^P = 0^+$ is used to evaluate the matrix element for the Higgs, whose mass is assumed to be equal to $m_{4\ell}$.
The distributions of the three discriminating variables are compared for the ggF signal and the ZZ^* background in Figures 8.1(a)-(c). The BDT_{ZZ^*} output distribution is instead shown in Figure 8.1(d).

As will be discussed in Sections 8.2, the BDT_{ZZ^*} output is used in the two-dimensional model built to measure the Higgs boson mass, the inclusive signal strength and the individual signal strengths per production mode.

8.1.2 BDT for categorisation

For the event categorisation, two separate BDT classifiers were developed to discriminate against the dominant ggF production: one for the VBF production (BDT_{VBF}) and another for the VH production, with the vector boson decaying hadronically (BDT_{VH}). In both cases the Higgs candidates are accompanied by two high-p_{T} jets, and the same discriminating variables are used: the invariant mass of the dijet system m_{jj}, the pseudorapidity separation between the two jets $|\Delta\eta_{jj}|$, the transverse momentum of each jet, and the pseudorapidity of the leading jet. Fully simulated four-lepton Higgs boson signal events produced through ggF and VBF (VH, with the vector boson decaying hadronically) are used for the training of the BDT_{VBF}(BDT_{VH}) discriminant.

The distributions of the five discriminating variables are compared for the ggF and the VBF signals in Figures 8.2(a)-(e). As expected, when considering the VBF production of a Higgs boson, the di-jet system has a high invariant mass and the two jets are emitted in the forward region with a considerable $|\Delta\eta_{jj}|$ separation between them. In the case of ggF events, on the contrary, the jets are more centrally produced, and have a smaller invariant mass and $|\Delta\eta_{jj}|$ separation. The output distributions of BDT_{VBF} for VBF and ggF events, as well as for the ZZ^* background are shown in Figure 8.2(f).

For the VH production mode, the main difference with respect to ggF events is observed in the m_{jj} distribution, which peaks at the Z/W mass, while the other variables have less discrimination power. The BDT_{ZZ^*} output distribution can be seen in Figure 8.3.

As mentioned in Section 6.4.1, the BDT_{VBF} output is used as an observable together with the $m_{4\ell}$ distribution in a maximum likelihood fit for the VBF category, while the BDT_{VH} output is used as a selection requirement (< -0.4) for the event to be classified in the *VH-hadronic enriched* category.

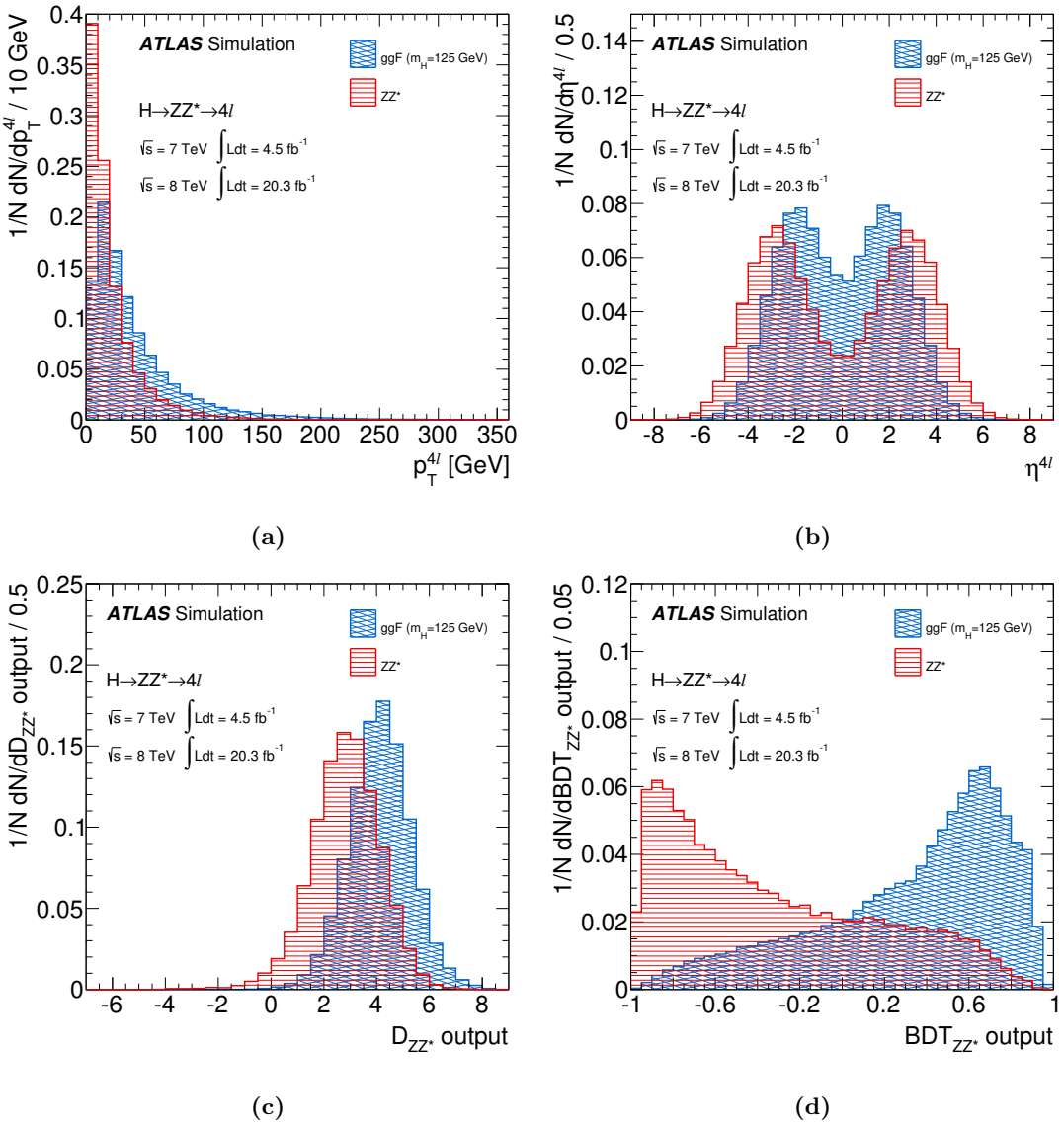

Figure 8.1 The ggF Higgs signal (blue) and the ZZ^* background (red) distributions of the three variables used for the training of the BDT_{ZZ^*} classifier are shown: ${p_{\mathrm{T}}}^{4\ell}$ (a), $\eta^{4\ell}$ (b), and the D_{ZZ^*} output (c). The BDT_{ZZ^*} output distribution is shown in (d). All histograms are normalised to the same area [4].

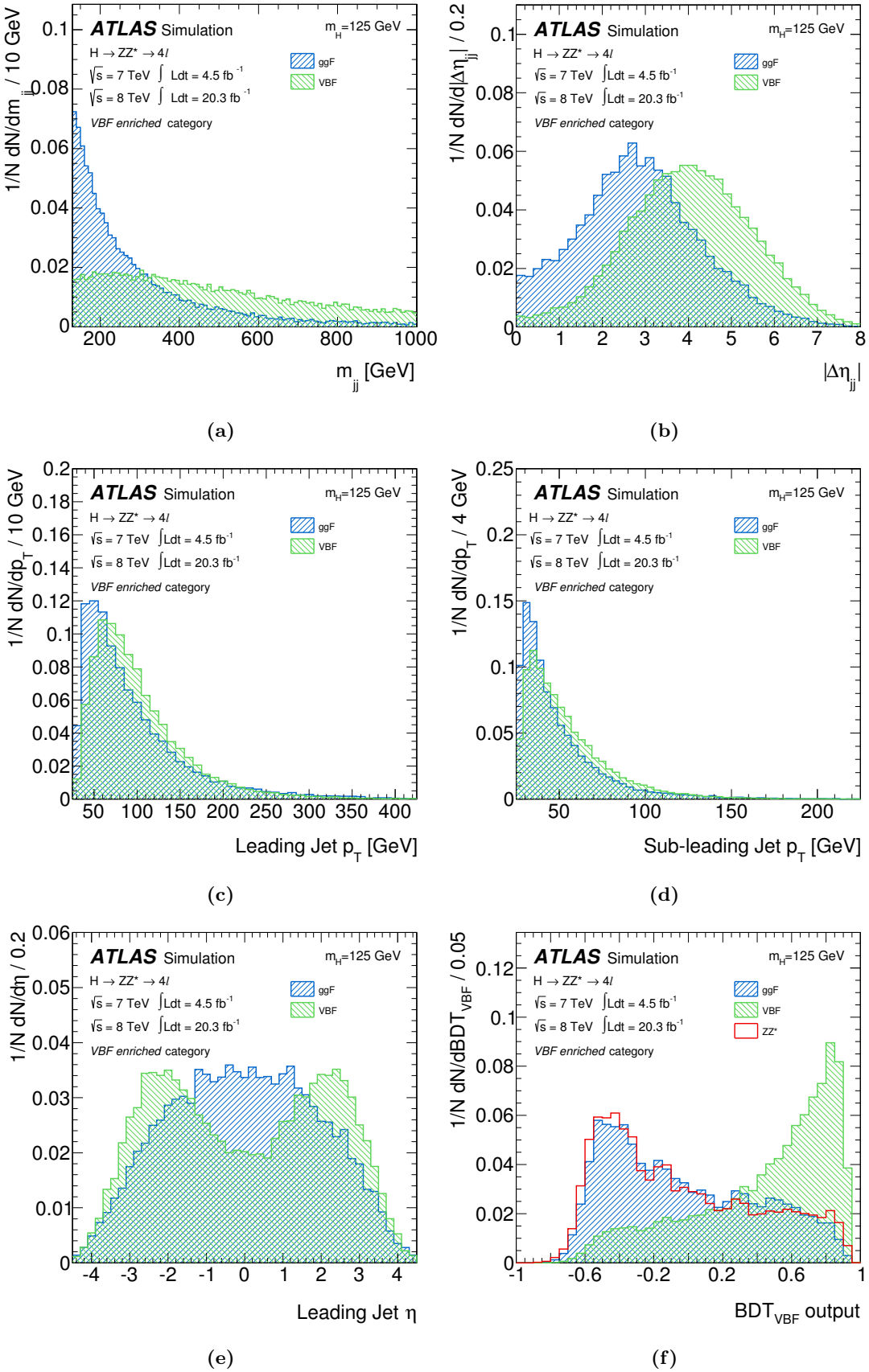

Figure 8.2 The distributions of the five discriminating variables used in the training of the $\mathrm{BDT_{VBF}}$ are shown: the dijet invariant mass (a), the dijet η separation (b), the leading jet p_{T} (c), the subleading jet p_{T} (d), and the leading jet η (e). The distributions are shown for ggF (blue) and VBF (green) events. The $\mathrm{BDT_{VBF}}$ output distribution is shown in (f), also for ZZ^* events (red). All histograms are normalised to the same area [4].

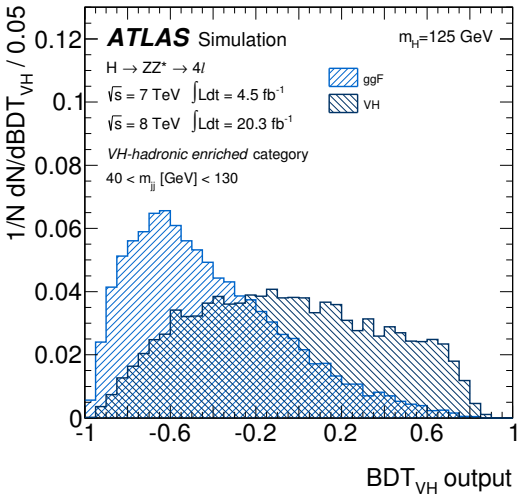

Figure 8.3 $\mathrm{BDT_{VH}}$ discriminant output for the *VH-hadronic enriched* category for VH (dark blue) and ggF (blue) events.

8.2 Signal and Background Modelling

8.2.1 Signal and background modelling for the inclusive analysis

Three different parametrisations of the signal and background were developed for the measurement of the Higgs boson mass and signal strength. The two-dimensional (2D) fit to the $m_{4\ell}$ and the $\mathrm{BDT_{ZZ^*}}$ output distributions, providing the smallest expected uncertainty among the different methods, is chosen as the baseline. The one-dimensional (1D) fit to the $m_{4\ell}$ distribution, used in the previous measurement [1, 28], is used as a cross-check. The third method, not described here, uses per-event resolution and was chosen as baseline method to set an upper limit on the Higgs boson total width. This measurement, which exploits interference effects between signal and background in the $H \to ZZ$ high-mass off-peak region (above $2m_Z$), is discussed elsewhere [147].

Both the 1D and the 2D signal models rely on smooth distributions obtained using a kernel density estimation method [148] from fully simulated events. The simulated samples used to create these templates are generated at 15 different m_H values in the range 115-130 GeV, and normalised to the expected SM cross-section times branching ratio [96] to derive the expected signal yields after acceptance and selection. The extracted templates are then parametrised as functions of m_H using B-spline interpolation [149]. The $m_{4\ell}$ range used for the fit is 110 GeV to 140 GeV.

The probability density function for the signal in the 2D fit is:

$$\begin{aligned}\mathcal{P}(m_{4\ell}, O_{\mathrm{BDT}_{ZZ^*}} \mid m_H) &= \mathcal{P}(m_{4\ell} \mid O_{\mathrm{BDT}_{ZZ^*}},\ m_H)\ \mathcal{P}(O_{\mathrm{BDT}_{ZZ^*}} \mid m_H) \\ &\simeq \left(\sum_{n=1}^{4} \mathcal{P}_n(m_{4\ell} \mid m_H)\theta_n(O_{\mathrm{BDT}_{ZZ^*}})\right) \mathcal{P}(O_{\mathrm{BDT}_{ZZ^*}} \mid m_H),\end{aligned} \tag{8.2}$$

where θ_n defines four equal-sized bins for the value of the $\mathrm{BDT_{ZZ^*}}$ output ($O_{\mathrm{BDT}_{ZZ^*}}$), and $\mathcal{P}_n$ represents the 1D probability density function of the signal in the corresponding $\mathrm{BDT_{ZZ^*}}$ bin.

The variation of the $m_{4\ell}$ shape within a single $\mathrm{BDT}_{\mathrm{ZZ}^*}$ bin is found to be negligible, thus no bias is introduced by the binning approximation.
The probability density function for the background, $\mathcal{P}_{\mathrm{bkg}}(m_{4\ell}, O_{\mathrm{BDT}_{ZZ^*}})$, is derived from simulation for the ZZ^* and the $\ell\ell+\mu\mu$ backgrounds, and with data-driven techniques for the $\ell\ell+ee$ reducible background. The probability densities in the $\mathrm{BDT}_{\mathrm{ZZ}^*}-m_{4\ell}$ plane for the Higgs signal at $m_H = 125$ GeV, the ZZ^* and the reducible backgrounds are shown in Figure 8.4. The separation between the signal and the background provided by the $\mathrm{BDT}_{\mathrm{ZZ}^*}$ is clearly appreciable, and its inclusion in the fit brings about a reduction of approximately 8% on the statistical uncertainty for the mass and inclusive signal strength measurements with respect to the 1D method.

Both the 1D and the 2D models are built using the $m_{4\ell}$ distribution after applying the Z-mass constraint to m_{12}, as described in Section 6.4. The $m_{4\ell}$ distribution for a simulated signal sample with $m_H = 125$ GeV is shown in Figure 8.5, with both the FSR correction and the Z-mass constraint applied, for the 4μ, $4e$ and $2e2\mu/2\mu2e$ channels. The width of the reconstructed Higgs boson, which is expected to be dominated by the experimental resolution[1], ranges between 1.6 GeV for the 4μ final state, and 2.2 GeV for the $4e$ final state.

The $m_{4\ell}$ and the $O_{\mathrm{BDT}_{ZZ^*}}$ data distributions for eight sets of events, one for each final state and data-taking year, are fitted simultaneously using an unbinned maximum likelihood assuming the described signal and background models.
The likelihood function $\mathcal{L}$, which depends on both m_H and μ, is defined as:

$$\mathcal{L}(m_H, \mu, \boldsymbol{\theta}) = \prod_{i}^{\text{year}} \prod_{j}^{\text{final state}} \text{Poisson}(N_{ij}|\mu \cdot S_{ij}(m_H, \boldsymbol{\theta}) + B_{ij}(\boldsymbol{\theta})) \cdot \prod_{k=1}^{N_{ij}} \mathcal{F}_{ij}((m_{4\ell}, O_{\mathrm{BDT}_{ZZ^*}})_k, m_H, \mu, \boldsymbol{\theta}) \,. \tag{8.3}$$

The first term of the likelihood represents the product of the Poisson probability of observing N_{ij} events in each of the eight sets, given the expectation for the signal S_{ij} and the background B_{ij}. The second term is the product of the values of the probability density $\mathcal{F}_{ij}$ for all events, constructed using both the signal and background models described above. The symbol $\boldsymbol{\theta}$ represents the set of nuisance parameters used to model the effect of systematic uncertainties described in the following section.

The statistical treatment of the data is described in [150, 151]. The confidence intervals are based on the profile likelihood ratio $\Lambda(\boldsymbol{\alpha})$, which depends on one or more parameters of interest $\boldsymbol{\alpha}$, such as the Higgs boson mass m_H or the signal strength, as well as on the nuisance parameters $\boldsymbol{\theta}$:

$$\Lambda(\boldsymbol{\alpha}) = \frac{\mathcal{L}(\boldsymbol{\alpha}, \hat{\hat{\boldsymbol{\theta}}}(\boldsymbol{\alpha}))}{\mathcal{L}(\hat{\boldsymbol{\alpha}}, \hat{\boldsymbol{\theta}})}. \tag{8.4}$$

The likelihood fit to the data is then performed for the parameters of interest, which depend on the test under consideration. $\hat{\hat{\boldsymbol{\theta}}}$ corresponds to the value of $\boldsymbol{\theta}$ which maximises $\mathcal{L}$ for the specified $\boldsymbol{\alpha}$, while $\hat{\boldsymbol{\theta}}$ denotes the unconditional maximum likelihood estimate of the nuisance parameters, i.e. where the likelihood is maximised for both $\boldsymbol{\theta}$ and $\boldsymbol{\alpha}$. In particular, the profile

[1] The natural width of a SM Higgs boson with m_H around 125 GeV is approximately 4 MeV

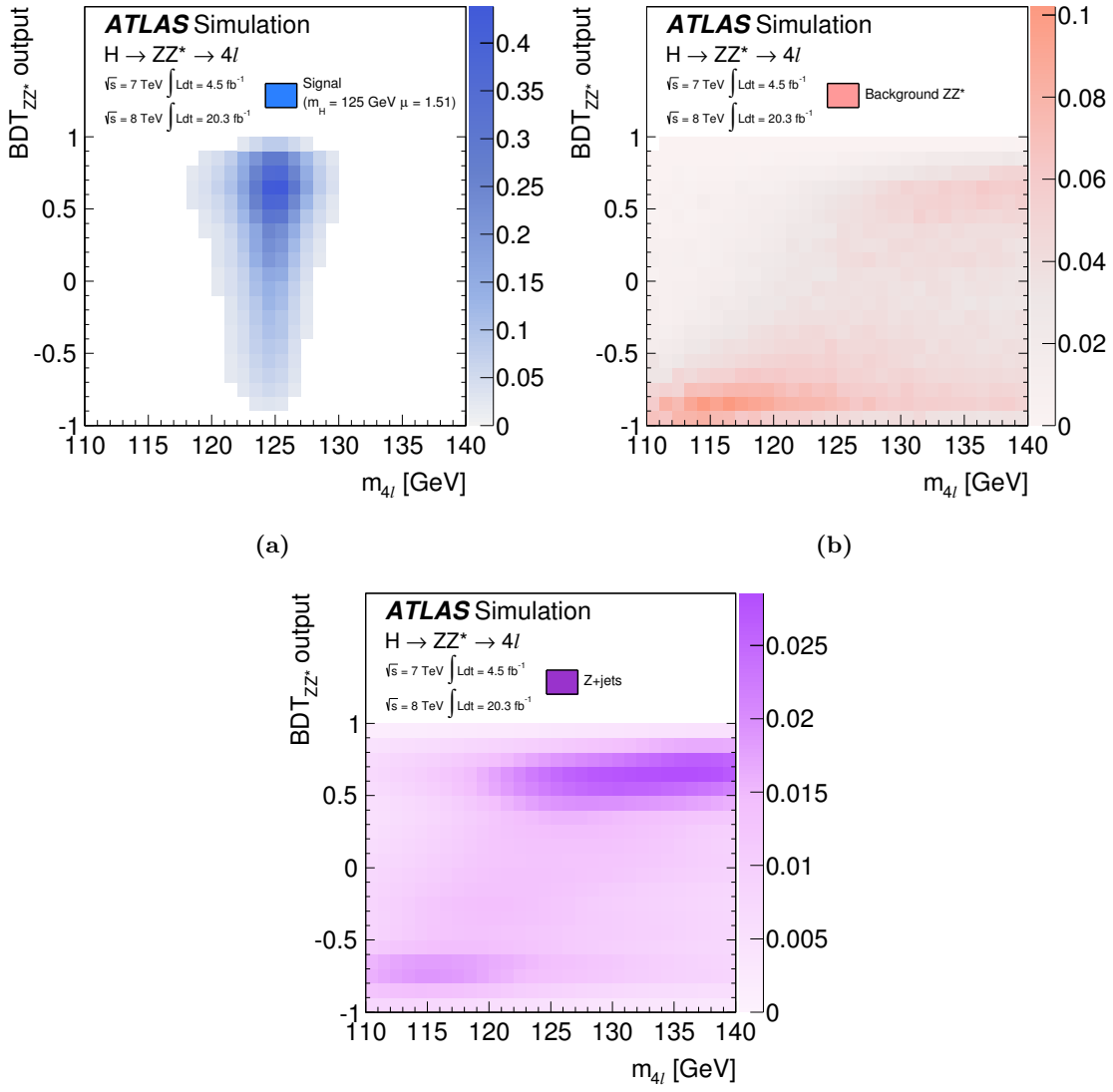

Figure 8.4 Probability density for the signal and the different backgrounds normalized to the expected number of events for the 2011 and 2012 data sets, summing over all the final states. The signal distribution $\mathcal{P}(m_{4\ell}, \mathrm{BDT_{ZZ^*}} \mid \mathrm{m_H})$, assuming $m_H = 125$ GeV, is shown in (a), and the ZZ^* and reducible background distributions $\mathcal{P}(m_{4\ell}, \mathrm{BDT_{ZZ^*}})$ are shown in (b) and (c), respectively [4].

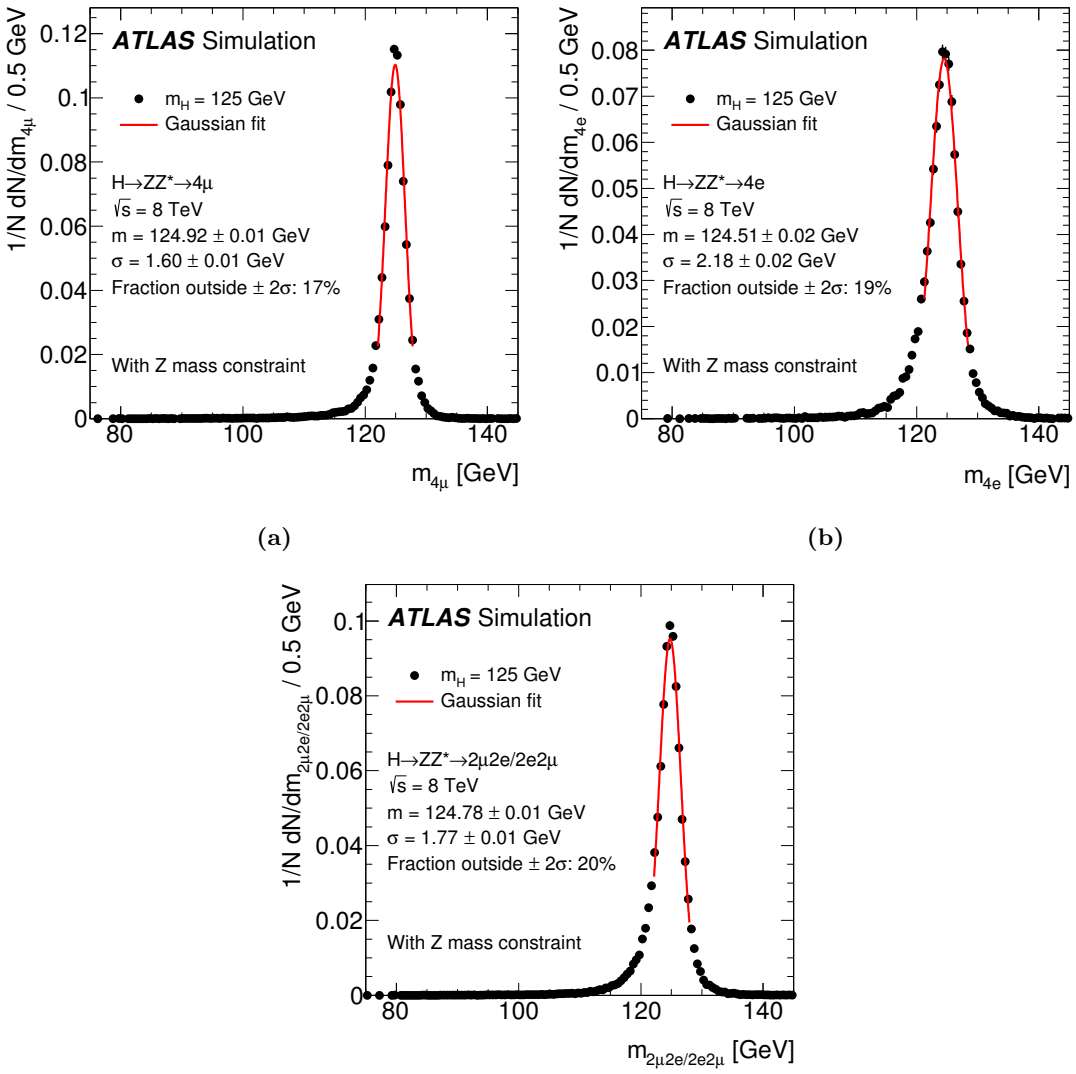

Figure 8.5 Invariant mass distribution for a simulated signal sample with $m_H = 125$ GeV in the 4μ (a), $4e$ (b) and $2e2\mu/2\mu2e$ (c) channels. The Gaussian fit to the $m_{4\ell}$ peak, after the correction for final-state radiation and the Z-mass constraint, is superimposed.

likelihood ratio used for the Higgs boson mass and signal strength measurements are defined as follows:

$$\Lambda(m_H) = \frac{\mathcal{L}(m_H, \hat{\hat{\mu}}(m_H), \hat{\hat{\boldsymbol{\theta}}}(m_H))}{\mathcal{L}(\hat{m}_H, \hat{\mu}, \hat{\boldsymbol{\theta}})} \quad \text{and} \quad \Lambda(\mu) = \frac{\mathcal{L}(\mu, \hat{\hat{\boldsymbol{\theta}}}(\mu))}{\mathcal{L}(\hat{\mu}, \hat{\boldsymbol{\theta}})}, \tag{8.5}$$

where the signal strength is treated as a parameter of interest in the profile likelihood ratio for m_H, while that for μ is evaluated for a fixed value of m_H.

8.2.2 Signal and background modelling for the categorised analysis

In the categorised analysis, the Higgs candidates identified applying the inclusive event selection are further grouped into four categories, according to their production mode. The objective of the analysis is the measurement of the signal strength for the different production modes. More specifically, a common signal strength, $\mu_{ggF+b\bar{b}H+t\bar{t}H}$, is considered for the gluon fusion and for the very small $t\bar{t}H$ and $b\bar{b}H$ production, as the latter two haven't been directly observed yet, and because in the SM the two production modes scale with the $q\bar{q}H$ ($q = b$, t) coupling. Similarly, a common signal strength, μ_{VBF+VH}, is assigned to the VBF and VH production modes, as they scale with WH/ZH gauge couplings in the SM.

A probability density is assigned to each of the categories defined in Section 6.4.1. For the *VBF enriched* category, a two dimensional probability density is built factorising the $\mathrm{BDT_{VBF}}$ and the $m_{4\ell}$ distributions. The factorisation is possible since the $\mathrm{BDT_{VBF}}$ dependance on $m_{4\ell}$ is negligible for both signal and background, as is the $\mathrm{BDT_{VBF}}$ dependance on the Higgs mass, which is in fact neglected in the probability density. Thanks to the inclusion of the $\mathrm{BDT_{VBF}}$ in the *VBF enriched* category, the expected uncertainty on μ_{VBF+VH} is reduced by approximately 25%.

For the two *VH-hadronic enriched* and *VH-leptonic enriched* categories, included separately in the model, unlike in the previous publications, a simple one-dimensional fit on $m_{4\ell}$ is performed. Their inclusion in the model brings the improvement on μ_{VBF+VH} to $\sim 35\%$.

Finally, in the *ggF enriched* category the same 2D model defined in Eq. 8.2 is used.

8.3 Systematic Uncertainties

This section discusses the systematic uncertainties affecting our measurements. The uncertainties related to the mass measurement, to the signal strength measurements and to the event categorisation are described separately, in Sections 8.3.1, 8.3.2, and 8.3.3, respectively.

8.3.1 Systematic uncertainties in the mass measurement

The main sources of systematic uncertainties on the mass measurement are the electron energy scale and the muon momentum scale, described in Sections 4.1.6 and Sections 4.2, respectively.

The electron energy calibration is typically known with a precision of less than 0.1% for $|\eta| < 1.2$ and $1.8 < |\eta| < 2.47$, and of a few per mille in regions with larger amounts of passive material [67]. This translates, for the final state involving electrons, into an uncertainty on the

measured Higgs boson mass of ±0.04%, ±0.025% and ±0.04% for the $4e$, $2e2\mu$ and $2\mu2e$ channels, respectively. When combining all final states together, the contribution from the energy scale to the uncertainty on the mass measurement is ±0.01%.
Similarly, the final states involving muons are affected by the uncertainties on the muon momentum scale, which are about ±0.04% in the barrel region and reach ±0.2% for $|\eta| > 2$, in the transverse momentum range of 6-100 GeV [73]. The resulting uncertainties on the Higgs boson mass are estimated to be ±0.04%, ±0.015% and ±0.02% for the 4μ, $2e2\mu$ and $2\mu2e$ channels, respectively. In this case, the contribution to the uncertainty on the mass measurement when all final states are combined is higher, and equal to ±0.03%, due to larger weight assigned to muon channels in the combined mass fit.

Uncertainties related to background contamination and final-state QED radiation modelling are negligible compared to the sources described above.

8.3.2 Systematic uncertainties in the inclusive signal strength measurement

The expected impact of the main systematic uncertainties affecting the inclusive signal strength measurement are summarised in Table 8.1. These include the uncertainties on the trigger, reconstruction and identification efficiencies of electrons, described in Chapter 5, and of muons [69, 73, 81]. A small uncertainty is also assigned to the efficiency of the isolation and impact parameter requirements of the analysis, in order to account for the disagreement between data and simulation. This uncertainty is only applied for low E_{T} electrons ($E_{\mathrm{T}} < 15$ GeV), while it is found to be negligible for high-E_{T} electrons and muons.
As seen in Chapter 7, systematic uncertainties are also assigned to the data-driven estimates of the reducible background yields, and their impact on the signal strength is visible in Table 8.1 for the various channels.

The overall uncertainty on the integrated luminosity for the complete 2011 dataset is ±1.8% [152]. The uncertainty on the integrated luminosity for the 2012 dataset is ±2.8%, and it is derived following the same methodology as that used in 2011, from a preliminary calibration of the luminosity scale with beam-separation scans.

Among the theory-related systematic uncertainties discussed in Section 6.1.2, the three most important ones are summarised in Table 8.1. The uncertainty on the QCD scale is found to be the dominant one, followed by the uncertainty on the parton distribution function and the strong coupling constant.

8.3.3 Systematic uncertainties in the event categorisation

The systematic uncertainties affecting the yields from the different processes contributing to the various categories are reported in Table 8.2, expressed as fractional uncertainties on the expected yields.

The uncertainty on the theoretical cross section predictions, dominant for the ggF production mode in all four categories, is mainly arising from the requirement on the jet multiplicity applied in the *VBF enriched* and the *VH-hadronic enriched* categories [6, 153]. Even though no such requirements are applied in the *VH-leptonic enriched* and *ggF enriched* categories, they are also affected by this uncertainty due to event migrations.

Source of uncertainty	4μ	$2e2\mu$	$2\mu2e$	$4e$	combined
Electron reconstruction and identification efficiencies	–	1.7%	3.3%	4.4%	1.6%
Electron isolation and impact parameter selection	–	0.07%	1.1%	1.2%	0.5%
Electron trigger efficiency	–	0.21%	0.05%	0.21%	<0.2%
$\ell\ell + ee$ backgrounds	–	–	3.4%	3.4%	1.3%
Muon reconstruction and identification efficiencies	1.9%	1.1%	0.8%	–	1.5%
Muon trigger efficiency	0.6%	0.03%	0.6%	–	0.2%
$\ell\ell + \mu\mu$ backgrounds	1.6%	1.6%	–	–	1.2%
QCD scale uncertainty					6.5%
PDF, α_s uncertainty					6.0%
$H \to ZZ^*$ branching ratio uncertainty					4.0%

Table 8.1 The expected impact of the systematic uncertainties on the signal yield, derived from simulation, for $m_H = 125$ GeV, are summarised for each of the four final states for the combined 4.5 fb^{-1} at $\sqrt{s} = 7$ TeV and 20.3 fb^{-1} at $\sqrt{s} = 8$ TeV. The symbol "–" indicates that the systematic uncertainty does not contribute to a particular final state. The last three systematic uncertainties apply equally to all final states. All uncertainties have been symmetrized [4].

The *VBF enriched* and the *VH-hadronic enriched* categories are also affected by the uncertainty on the potential mismodelling of the underlying event, which is estimated using $Z \to \mu\mu$ simulated events by applying the selection for the *VBF enriched* (or *VH-hadronic enriched*) category and taking the difference of the efficiencies with and without multiparton interactions.

The main experimental systematic uncertainties are given by the uncertainty on the jet energy scale [77], which again affects all categories and is equal to approximately ±10%, ±8%, ±1.5% and ±1.5% for the *VBF enriched*, *VH-hadronic enriched*, *VH-leptonic enriched* and *ggF enriched* categories, respectively.
The much smaller uncertainty on the jet energy resolution is also taken into account [78].

Finally, for the *VH-leptonic enriched* category the same uncertainties described in the previous section for the four leptons of the Higgs decay are considered for the additional lepton.

8.4 Results

8.4.1 Results of the inclusive analysis

Table 8.3 shows the number of expected signal and background events in the inclusive analysis for each of the four decay channels. The total number of expected events is also shown, and compared to the number of observed candidates in the mass window of 120–130 GeV. The signal and ZZ^* background expectations are normalised to the SM expectation, while the data-driven estimates described in the previous chapter are used to normalise the reducible backgrounds. The number of signal expected events are given also in the full mass range, with no selection on $m_{4\ell}$. The results are shown for the 2011 and 2012 datasets separately, and for the full combined sample. A clear improvement in the signal-to-background ratio for the $4e$ and $2\mu2e$ channels can be seen between the 7 and 8 TeV samples, mostly due to the new electron

Process	$gg \to H, q\bar{q}/gg \to b\bar{b}H/t\bar{t}H$	$qq' \to Hqq'$	$q\bar{q} \to W/ZH$	ZZ^*
VBF enriched category				
Theoretical cross section	20.4%	4%	4%	8%
Underlying event	6.6%	1.4%	–	–
Jet energy scale	9.6%	4.8%	7.8%	9.6%
Jet energy resolution	0.9%	0.2%	1.0%	1.4%
Total	23.5%	6.4%	8.8%	12.6%
VH-hadronic enriched category				
Theoretical cross section	20.4%	4%	4%	2%
Underlying event	7.5%	3.1%	–	–
Jet energy scale	9.4%	9.3%	3.7%	12.6%
Jet energy resolution	1.0%	1.7%	0.6%	1.8%
Total	23.7%	10.7%	5.5%	12.9%
VH-leptonic enriched category				
Theoretical cross section	12%	4%	4%	5%
Leptonic VH-specific cuts	1%	1%	5%	–
Jet energy scale	8.8%	9.9%	1.7%	3.2%
Total	14.9%	10.7%	6.6%	5.9%
ggF enriched category				
Theoretical cross section	12%	4%	4%	4%
Jet energy scale	2.2%	6.6%	4.0%	1.0%
Total	12.2%	7.7%	5.7%	4.1%

Table 8.2 Systematic uncertainties on the expected yields from various processes contributing to the *VBF enriched*, *VH-leptonic enriched*, *VH-hadronic enriched* and *ggF enriched* categories, expressed as fractional uncertainties on the yields. The different uncertainties are added in quadrature. The symbol "–" indicates that the uncertainties can be considered negligible. All uncertainties have been symmetrized [4].

identification described in Chapter 5. The overall signal-to-background ratio for the combined sample is 1.6.

The FSR corrections described in Section 6.4 are applied to 10 events in the full mass region – in good agreement with the expected number of 11 events – and to 3 events in the mass range 120-130 GeV. Among these, 8 (1) events are corrected for collinear FSR, and 2 (2) are corrected for non-collinear FSR in the full mass range (in the 120-130 mass window).

The expected $m_{4\ell}$ distribution for the backgrounds and the signal hypothesis are compared to the combined $\sqrt{s} = 7$ TeV and $\sqrt{s} = 8$ TeV data in Figure 8.6, in both the mass ranges 80–170 GeV and 80–600 GeV. The Higgs signal is shown for $m_H = 125$ GeV and normalised to $\mu = 1.51$, corresponding to the μ measurement for the $H \to ZZ^* \to 4\ell$ final state, described below, scaled to this mass by the expected variation in the SM Higgs boson cross section times the branching ratio. The peak of the singly-resonant ZZ^* production is clearly visible in both plots. From Figure 8.6(b) one can see the threshold of the ZZ production above 180 GeV. The narrow Higgs mass peak around 125 GeV is also evident.

The invariant mass distribution in the (m_{12}, m_{34}) plane, as well as its projections, are shown in Figure 8.7. The Z-mass constrained kinematic fit is not yet applied for these distributions.

Figure 8.8(a) shows the distribution of the BDT_{ZZ^*} output versus $m_{4\ell}$ for the reconstructed

Table 8.3 The number of expected signal and background events for a $m_H = 125$ GeV hypothesis is shown in the first four columns. All numbers are estimated in the mass window 120–130 GeV, with the exception of the signal expectation, which is also given in the full mass range. The signal and ZZ^* background expectations are normalised to the SM expectation, while the reducible backgrounds are normalised to data-driven estimates. The fifth column shows the signal-to-background ratio (S/B), and the total number of expected and observed events are given in the last two columns. The results are shown for 4.5 fb^{-1} at $\sqrt{s} = 7$ TeV and 20.3 fb^{-1} at $\sqrt{s} = 8$ TeV as well as for the combined sample [4].

Final state	Signal full mass range	Signal	ZZ^*	Z+jets, $t\bar{t}$	S/B	Expected	Observed
			$\sqrt{s} = 7$ TeV				
4μ	1.00 ± 0.10	0.91 ± 0.09	0.46 ± 0.02	0.10 ± 0.04	1.7	1.47 ± 0.10	2
$2e2\mu$	0.66 ± 0.06	0.58 ± 0.06	0.32 ± 0.02	0.09 ± 0.03	1.5	0.99 ± 0.07	2
$2\mu2e$	0.50 ± 0.05	0.44 ± 0.04	0.21 ± 0.01	0.36 ± 0.08	0.8	1.01 ± 0.09	1
$4e$	0.46 ± 0.05	0.39 ± 0.04	0.19 ± 0.01	0.40 ± 0.09	0.7	0.98 ± 0.10	1
Total	2.62 ± 0.26	2.32 ± 0.23	1.17 ± 0.06	0.96 ± 0.18	1.1	4.45 ± 0.30	6
			$\sqrt{s} = 8$ TeV				
4μ	5.80 ± 0.57	5.28 ± 0.52	2.36 ± 0.12	0.69 ± 0.13	1.7	8.33 ± 0.6	12
$2e2\mu$	3.92 ± 0.39	3.45 ± 0.34	1.67 ± 0.08	0.60 ± 0.10	1.5	5.72 ± 0.37	7
$2\mu2e$	3.06 ± 0.31	2.71 ± 0.28	1.17 ± 0.07	0.36 ± 0.08	1.8	4.23 ± 0.30	5
$4e$	2.79 ± 0.29	2.38 ± 0.25	1.03 ± 0.07	0.35 ± 0.07	1.7	3.77 ± 0.27	7
Total	15.6 ± 1.6	13.8 ± 1.4	6.24 ± 0.34	2.00 ± 0.28	1.7	22.1 ± 1.5	31
			$\sqrt{s} = 7$ TeV and $\sqrt{s} = 8$ TeV				
4μ	6.80 ± 0.67	6.20 ± 0.61	2.82 ± 0.14	0.79 ± 0.13	1.7	9.81 ± 0.64	14
$2e2\mu$	4.58 ± 0.45	4.04 ± 0.40	1.99 ± 0.10	0.69 ± 0.11	1.5	6.72 ± 0.42	9
$2\mu2e$	3.56 ± 0.36	3.15 ± 0.32	1.38 ± 0.08	0.72 ± 0.12	1.5	5.24 ± 0.35	6
$4e$	3.25 ± 0.34	2.77 ± 0.29	1.22 ± 0.08	0.76 ± 0.11	1.4	4.75 ± 0.32	8
Total	18.2 ± 1.8	16.2 ± 1.6	7.41 ± 0.40	2.95 ± 0.33	1.6	26.5 ± 1.7	37

candidates used in the fit. As expected, an excess of events with high $O_{\mathrm{BDT}_{ZZ^*}}$ is found for $m_{4\ell}$ close to 125 GeV, compatible with the Higgs signal hypothesis at that mass. Figures 8.8(b) and 8.8(c) show instead the BDT_{ZZ^*} output distribution for candidates in the mass window 120–130 GeV and the $m_{4\ell}$ distribution for events with $O_{\mathrm{BDT}_{ZZ^*}} > 0$. The latter condition maximises the expected significance for a SM Higgs boson with a mass of about 125 GeV, and indeed this can be appreciated by comparing this $m_{4\ell}$ distribution to the one in Figure 8.6(a), where no requirement on the $O_{\mathrm{BDT}_{ZZ^*}}$ is applied.

The significance of the excess of observed signal events is quantified by means of the local p_0-value, which represents the probability to obtain, in the background only hypothesis, a test statistics more signal-like than the one observed in data. The asymptotic approximation [154] is used in the calculation of the local p_0-value, which is shown as a function of m_H in Figure 8.9, for the 2011 and 2012 datasets separately and for the combined sample. The 2D fit with no selection on the BDT_{ZZ^*} output is used, with $m_{4\ell}$ fixed either to the mass measured for this channel, or to the value obtained from the combination of the $H \to ZZ^* \to 4\ell$ and $H \to \gamma\gamma$ mass measurements [2]. The significance associated to the corresponding p_0-values is equal to 8.2 and 8.1 standard deviations, respectively. The expected significance at these two masses is 5.8 and

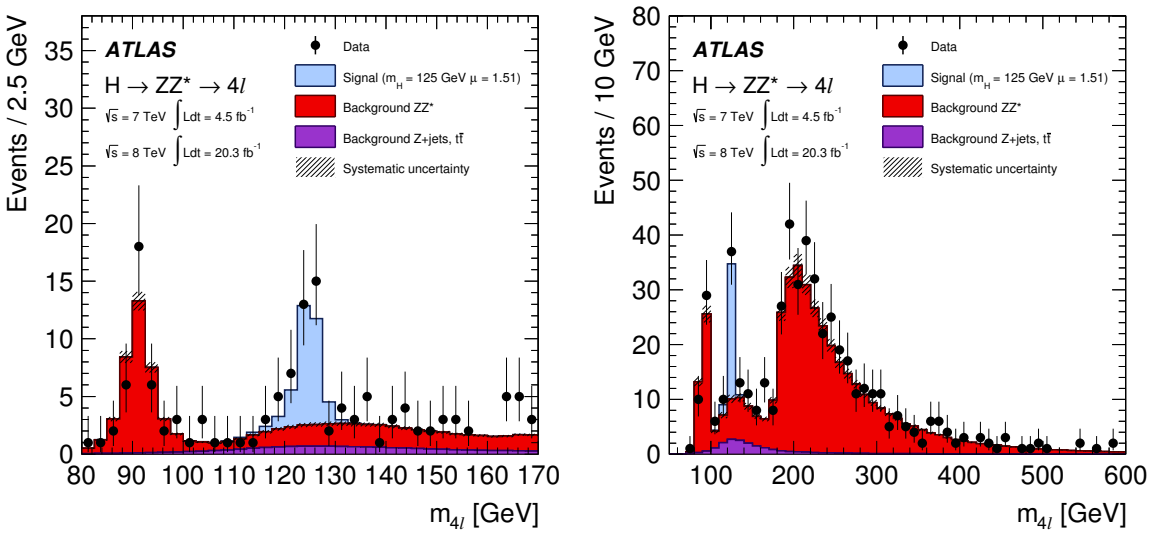

(a) (b)

Figure 8.6 The $m_{4\ell}$ distribution of the combined $\sqrt{s} = 7$ TeV and $\sqrt{s} = 8$ TeV data (filled circles) compared to the expected signal and background contributions (filled histograms). The invariant mass ranges 80-170 GeV (a) and 80-600 GeV (b) are shown. The Higgs signal is shown for $m_H = 125$ GeV and normalised to $\mu = 1.51$ (see text). The irreducible and reducible backgrounds are drawn separately, with red and violet histograms, respectively. The systematic uncertainty associated with the total background contribution is represented by the hatched areas [4].

6.2 standard deviations.

Mass and inclusive signal strength measurements

The Higgs boson mass measured in the $H \to ZZ^* \to 4\ell$ decay channel, obtained using the 2D method described in Section 8.2, is:

$$m_H = 124.51 \ \pm 0.52 \ (\text{stat}) \pm 0.04 \ (\text{syst}) \ \text{GeV} \tag{8.6}$$

where the first error represents the statistical uncertainty and the second the systematic uncertainty. The systematic uncertainty is obtained from the quadrature subtraction of the fit uncertainty evaluated with and without the systematic uncertainties fixed at their best fit values. With the improved uncertainties on the electron and muon energy scales, the mass uncertainty given above is predominantly statistical with a nearly negligible contribution from systematic uncertainties. The other methods described in Section 8.2, 1D and per-event resolution, yield similar results for the Higgs boson mass [2].

Figure 8.10(a) shows the scan of the profile likelihood, $-2\ln\Lambda(m_H)$, as a function of m_H for each one of the four channels separately, as well as for their combination. The signal strength and all the nuisance parameters are profiled in the scan, i.e. allowed to float to the values that maximise the likelihood. The compatibility among the mass measurements from the four final

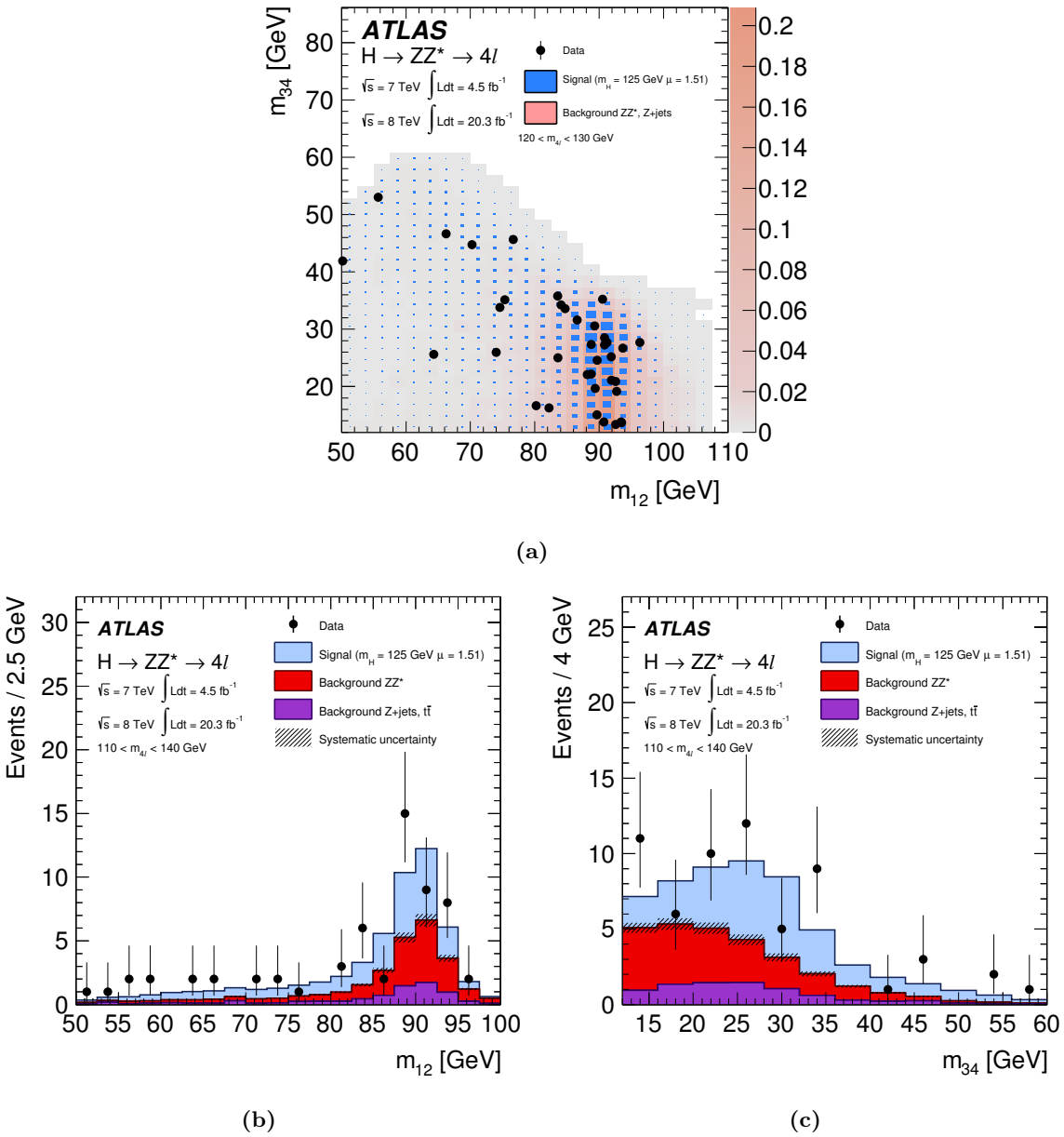

Figure 8.7 The expected and observed (filled circles) distributions of the reconstructed dilepton masses within $120 < m_{4\ell} < 130$ GeV are shown in the m_{34} – m_{12} plane in (a). The Higgs signal expectation (blue), shown for $m_H = 125$ GeV and normalised to $\mu = 1.51$ (see text), and the total background (pink) are superimposed, where the box size (signal) and color shading (background) represent the relative density. The projected distributions for m_{12} and m_{34} are plotted in (b) and (c), respectively, for events in the fit range $110 < m_{4\ell} < 140$ GeV. The signal expectation is represented as blue histograms, while the irreducible and reducible backgrounds are drawn separately with red and violet histograms, respectively. The systematic uncertainty associated to the total background contribution is represented by the hatched areas. In all three plots, the combined $\sqrt{s} = 7$ TeV and $\sqrt{s} = 8$ TeV data sample is used [4].

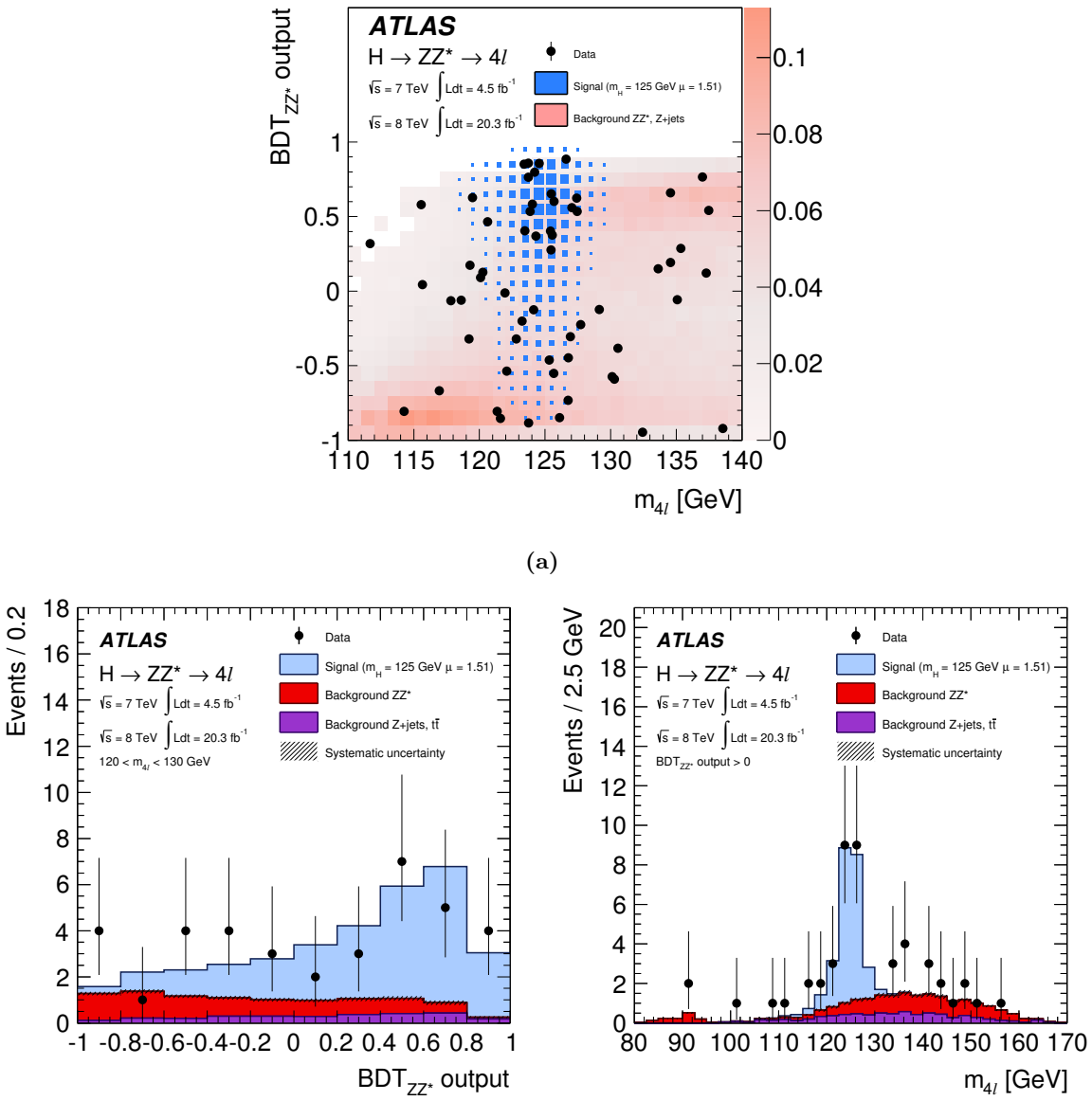

Figure 8.8 The distribution of observed (filled circles) and expected events is shown in (a) in the $\mathrm{BDT}_{ZZ^*} - m_{4\ell}$ plane, within the mass range $110 < m_{4\ell} < 140$ GeV. The Higgs signal expectation (blue), shown for $m_H = 125$ GeV and normalised to $\mu = 1.51$ (see text), and the total background (pink) are superimposed, where the box size (signal) and color shading (background) represent the relative density. The BDT_{ZZ^*} distribution in the range $120 < m_{4\ell} < 130$ GeV, and the $m_{4\ell}$ distribution with the additional requirement that the BDT_{ZZ^*} be positive, are plotted in (b) and (c), respectively. The signal expectation is represented as blue histograms, while the ZZ^* and the Z+jets plus $t\bar{t}$ backgrounds are drawn separately with red and violet histograms, respectively. The systematic uncertainty associated to the total background contribution is represented by the hatched areas. In all three plots, the combined $\sqrt{s} = 7$ TeV and $\sqrt{s} = 8$ TeV data sample is used [4].

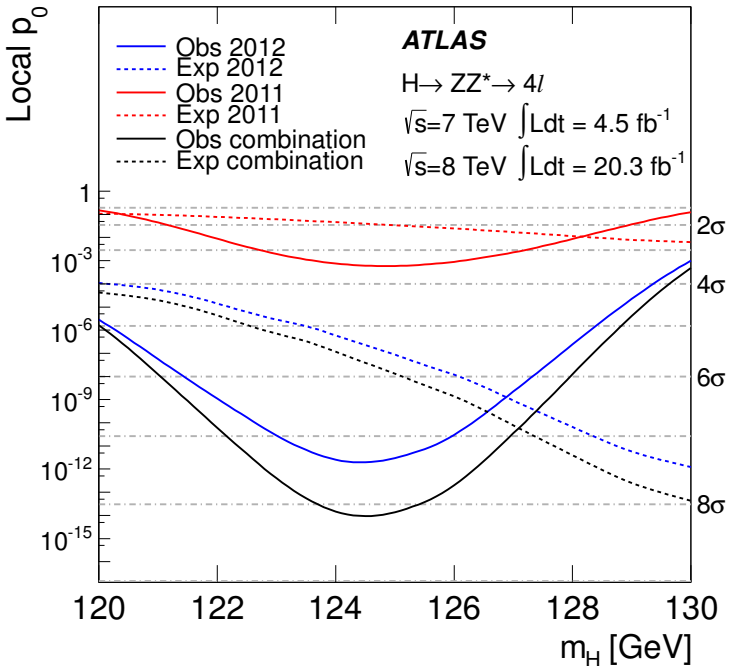

Figure 8.9 The observed local p_0-value for the combination of the 2011 and 2012 datasets (solid black line) as a function of m_H; the individual results for $\sqrt{s} = 7$ TeV and 8 TeV are shown separately as red and blue solid lines, respectively. The dashed curves show the expected median of the local p_0-value for the signal hypothesis with signal strength $\mu = 1$, when evaluated at the corresponding m_H. The horizontal dot-dashed lines indicate the p_0-values corresponding to local significances [4].

states is estimated using a χ^2 test to be approximately 20%. Moreover, the scan obtained for the combination of the channels is shown with and without systematic uncertainties included. The two lines essentially overlap, showing again how the mass measurement is completely statistically dominated.

The measured signal strength at $m_H = 124.51$ is $\mu = 1.66\ ^{+0.39}_{-0.34}\ (\text{stat})^{+0.21}_{-0.14}\ (\text{syst})$, consistent with the SM expectation of one.

The best fit values of μ and m_H are shown in Figure 8.10(b), as well as the profile likelihood ratio contours in the $m_H - \mu$ plane corresponding to the 68% and 95% confidence level intervals.

The mass measurement in Eq. 8.6 can be compared to the previously reported result [1] $m_H = 124.3^{+0.6}_{-0.5}\ (\text{stat})^{+0.5}_{-0.3}\ (\text{syst})$ GeV, which was obtained using the 1D model. The difference between the measured values arises primarily from the changes in the electron calibration and identification, the introduction of the combined track momentum and cluster energy fit, as well as the recovery of non-collinear FSR photons.

The Higgs boson mass obtained from the combination of the results measured in the $H \to ZZ^* \to 4\ell$ and the $H \to \gamma\gamma$ channels is:

$$m_H = 125.36\ \pm 0.37\ (\text{stat}) \pm 0.18\ (\text{syst})\ \text{GeV}\ . \tag{8.7}$$

At this mass value, the signal strength measured in the $H \to ZZ^* \to 4\ell$ is found to be $\mu = 1.50^{+0.35}_{-0.31}\ (\text{stat})^{+0.19}_{-0.13}\ (\text{syst})$.

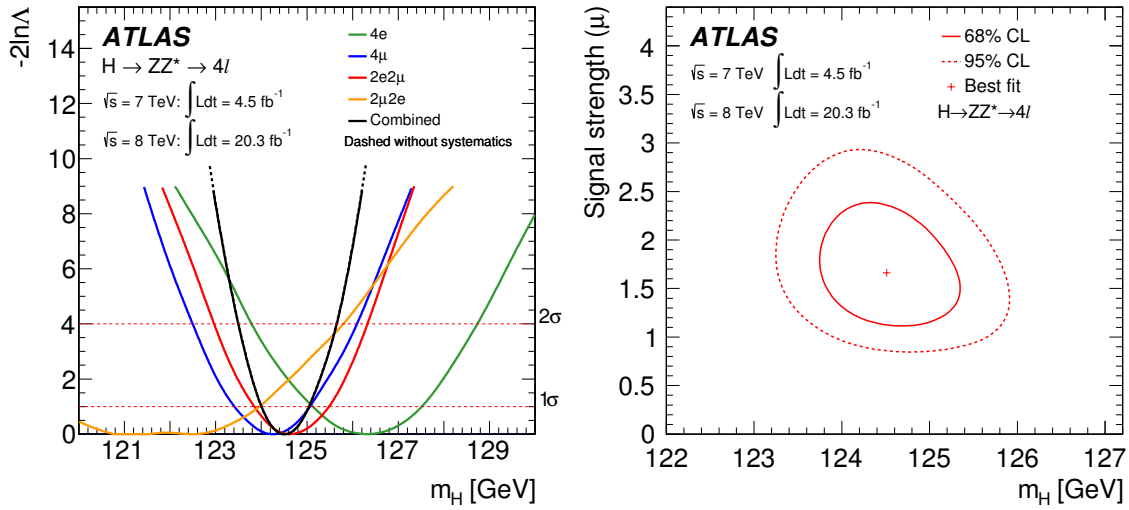

(a) (b)

Figure 8.10 (a) Scan of the profile likelihood as a function of m_H for the individual channels ($4e$, green line; 4μ, blue line; $2e2\mu$, red line; $2\mu2e$, yellow line) as well as for their combination (black lines); the scan for the combination of all channels is shown both with (solid line) and without (dashed line) systematic uncertainties. The signal strength and all the nuisance parameters are profiled in the fit. (b) The 68% and 95% confidence level (CL) contours in the $\mu - m_H$ plane for the inclusive analysis. For both plots, the combined 7 TeV and 8 TeV sample is used.

8.4.2 Coupling studies

The total numbers of expected and observed events in each of the categories defined in 6.4.1 are summarised in Table 8.4 for the full 2011 and 2012 combined sample. The expected yields are also given for different production modes, with the ggF, $b\bar{b}H$ and $t\bar{t}H$ merged together, and for the ZZ^* and reducible backgrounds. The estimates are given for both the $m_{4\ell}$ mass range 120–130 GeV and for $m_{4\ell}$ above 110 GeV.

Three events are observed in the *VBF enriched* category in the mass window 120–130 GeV, one of them having a $\mathrm{BDT_{VBF}}$ output above zero: $m_{4\ell}$ =123.4 GeV and a $\mathrm{BDT_{VBF}}$ output value of 0.7. The expected number of events in the *VBF enriched* category with a $\mathrm{BDT_{VBF}}$ output above zero is 1.26 ± 0.15, half of which is expected to come from a true VBF signal, approximately 35% from ggF production, and the rest from background contamination. The $m_{4\ell}$ and $\mathrm{BDT_{VBF}}$ output distributions are shown in the full mass range and for $110 < m_{4\ell} < 140$ GeV for the *VBF enriched* category in Figure 8.11. The signal purity, defined as $S/(S+B)$, is instead shown as a function of the $\mathrm{BDT_{VBF}}$ output in Figure 8.12, in the mass fit range 110–140 GeV. Two curves are superposed, the first one representing the purity of all Higgs signal production mechanism relative to the ZZ^* and reducible backgrounds, and the second one showing the purity for VBF events relative to the other production modes. The Higgs signal purity is found to be always above 50%, reaching 95% close to $\mathrm{BDT_{VBF}} = 1$. The VBF signal purity on the other hand reaches 50% for $\mathrm{BDT_{VBF}} \simeq 0.6$, and it is equal to approximately 78% at $\mathrm{BDT_{VBF}} = 1$.

No events are found for the *VH enriched* categories in the 120-130 GeV range, either in the hadronic or in the leptonic ones, while 0.8 and 0.1 were expected in the *VH-hadronic enriched*

Table 8.4 Expected and observed yields in the *VBF enriched*, *VH-hadronic enriched*, *VH-leptonic enriched* and *ggF enriched* categories. The expected yields are given for the different production modes (the ggF, $b\bar{b}H$ and $t\bar{t}H$ are combined together) and the ZZ^* and reducible background for 4.6 fb^{-1} at $\sqrt{s} = 7$ TeV and 20.3 fb^{-1} at $\sqrt{s} = 8$ TeV. The estimates are given for both the $m_{4\ell}$ mass range 120-130 GeV and for $m_{4\ell}$ above 110 GeV [4].

Enriched	Signal				Background		Total	Observed
category	$ggF + b\bar{b}H + t\bar{t}H$	VBF	VH-hadronic	VH-leptonic	ZZ^*	Z + jets, $t\bar{t}$	expected	
$120 < m_{4\ell} < 130$ GeV								
VBF	1.18 ± 0.37	0.75 ± 0.04	0.083 ± 0.006	0.013 ± 0.001	0.17 ± 0.03	0.25 ± 0.14	2.4 ± 0.4	3
(BDT$_{\rm VBF} > 0$)	0.48 ± 0.15	0.62 ± 0.04	0.023 ± 0.002	0.004 ± 0.001	0.06 ± 0.01	0.10 ± 0.05	1.26 ± 0.15	1
VH-hadronic	0.40 ± 0.12	0.034 ± 0.004	0.20 ± 0.01	0.009 ± 0.001	0.09 ± 0.01	0.09 ± 0.04	0.80 ± 0.12	0
VH-leptonic	0.013 ± 0.002	< 0.001	< 0.001	0.069 ± 0.004	0.015 ± 0.002	0.016 ± 0.019	0.11 ± 0.02	0
ggF	12.8 ± 1.3	0.57 ± 0.02	0.24 ± 0.01	0.11 ± 0.01	7.1 ± 0.2	2.7 ± 0.4	23.5 ± 1.4	34
$m_{4\ell} > 110$ GeV								
VBF	1.4 ± 0.4	0.82 ± 0.05	0.092 ± 0.007	0.022 ± 0.002	20 ± 4	1.6 ± 0.9	24. ± 4.	32
(BDT$_{\rm VBF} > 0$)	0.54 ± 0.17	0.68 ± 0.04	0.025 ± 0.002	0.007 ± 0.001	8.2 ± 1.6	0.6 ± 0.3	10.0 ± 1.6	12
VH-hadronic	0.46 ± 0.14	0.038 ± 0.004	0.23 ± 0.01	0.015 ± 0.001	9.0 ± 1.2	0.6 ± 0.2	10.3 ± 1.2	13
VH-leptonic	0.026 ± 0.004	< 0.002	< 0.002	0.15 ± 0.01	0.63 ± 0.04	0.11 ± 0.14	0.92 ± 0.16	1
ggF	14.1 ± 1.5	0.63 ± 0.02	0.27 ± 0.01	0.17 ± 0.01	351. ± 20	16.6 ± 2.2	383. ± 20	420

and the *VH-leptonic enriched*, respectively.
The expected and observed yields in the mass range above 110 GeV agree well with each other, and are dominated by the ZZ^* background contribution in all categories.

The measurement of the inclusive signal strength described in the previous section can be extended to a measurement of the signal strengths for specific production modes. As discussed in Section 8.2.2, the ggF, $b\bar{b}H$ and $t\bar{t}H$ mechanism are considered together, and the same is done with the VBF and VH modes. This is equivalent to measuring the couplings for the "fermionic" and "bosonic" production modes separately. More specifically, $\mu_{\rm ggF+b\bar{b}H+t\bar{t}H} \times B/B_{\rm SM}$ and $\mu_{\rm VBF+VH} \times B/B_{\rm SM}$ are measured, where $B/B_{\rm SM}$ is the scale factor of the branching ratio with respect to the SM value. This factor is included since, with the $H \to ZZ^* \to 4\ell$ analysis only, we cannot resolve the source of potential deviations from the SM expectation between production and decay.

The models described in Section 8.2.2 are used in the fit, and the Higgs mass is fixed to the best available ATLAS measurement, which is the $H \to ZZ^* \to 4\ell$ and $H \to \gamma\gamma$ combined value in Eq. 8.7. Figure 8.13(a) shows the best fit value for $\mu_{\rm ggF+b\bar{b}H+t\bar{t}H} \times B/B_{\rm SM}$ versus $\mu_{\rm VBF+VH} \times B/B_{\rm SM}$ with the profile likelihood ratio contours corresponding to the 68% and 95% confidence levels. The measured values for $\mu_{\rm ggF+b\bar{b}H+t\bar{t}H} \times B/B_{\rm SM}$ and $\mu_{\rm VBF+VH} \times B/B_{\rm SM}$ are respectively:

$$\begin{aligned} \mu_{\rm ggF+b\bar{b}H+t\bar{t}H} \times B/B_{\rm SM} &= 1.66\ ^{+0.45}_{-0.41}\ (\text{stat})\ ^{+0.25}_{-0.15}\ (\text{syst}) \\ \mu_{\rm VBF+VH} \times B/B_{\rm SM} &= 0.26\ ^{+1.60}_{-0.91}\ (\text{stat})\ ^{+0.36}_{-0.23}\ (\text{syst}). \end{aligned} \tag{8.8}$$

The fit to the categories can also be constrained to extract a single overall signal strength for the $H \to ZZ^* \to 4\ell$ final state, which is equal to $1.44^{+0.34}_{-0.31}\ (\text{stat})^{+0.21}_{-0.11}\ (\text{syst})$ at $m_H = 125.36$ GeV. This value was used as input to the combination performed on the results available in ATLAS

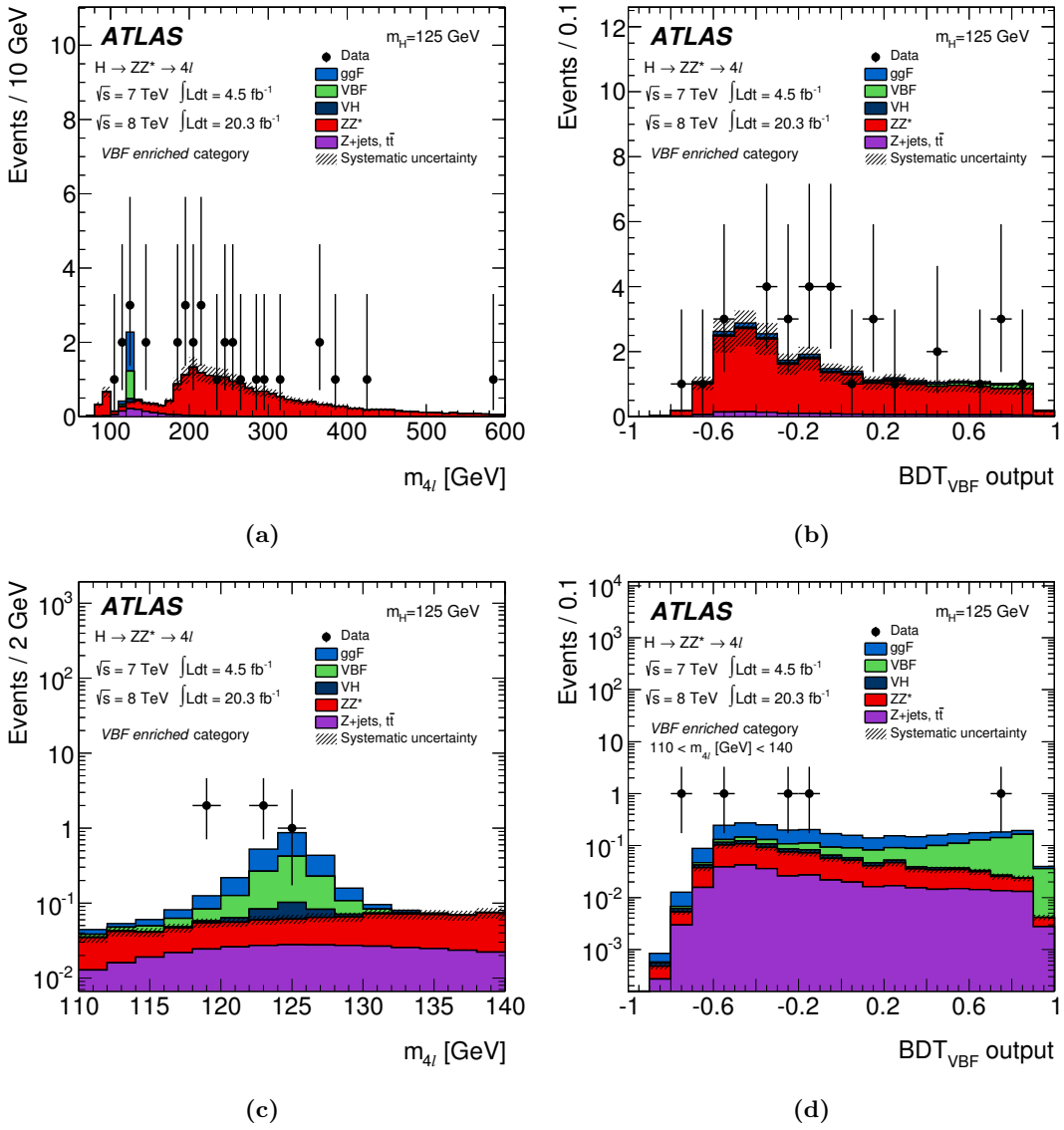

Figure 8.11 Distributions of the observed and expected signal and background events for the *VBF enriched* category for (a) $m_{4\ell}$ and (b) the $\mathrm{BDT_{VBF}}$ output in the full mass range, and for (c) $m_{4\ell}$ and (d) the $\mathrm{BDT_{VBF}}$ output in the fit mass range $110 < m_{4\ell} < 140$ GeV. The expected Higgs signal contributions, assuming m_H=125 GeV, from the ggF (blue histogram), VBF (green histogram) and VH (dark-blue histogram) production modes are included. The expected background contributions, ZZ^* (red histogram) and Z+jets plus $t\bar{t}$ (violet histogram), are also shown. The systematic uncertainty associated to the total background contribution is represented by the hatched areas. The combined 7 TeV and 8 TeV results are shown [4].

from the decay modes $H\to\gamma\gamma$, ZZ^*, WW^*, $Z\gamma$, $b\bar{b}$, $\tau\tau$, $\mu\mu$. The result of the combination, visible in Figure 8.14, is $1.18 \pm 0.10 \pm 0.07^{+0.08}_{-0.07}$, where the first error reflects the statistical uncertainty and the second and third errors reflect the experimental and theoretical systematic uncertainties, respectively [155].

The ambiguity between production and decay is removed in Figure 8.13(b), where the ratio $\mu_{\mathrm{VBF+VH}}/\mu_{\mathrm{ggF}+b\bar{b}H+t\bar{t}H}$ is presented. The measured value of this ratio is $0.2^{+1.2}_{-0.5}$.

Following the recommendation of the LHC Higgs Cross Section Working Group [6], the

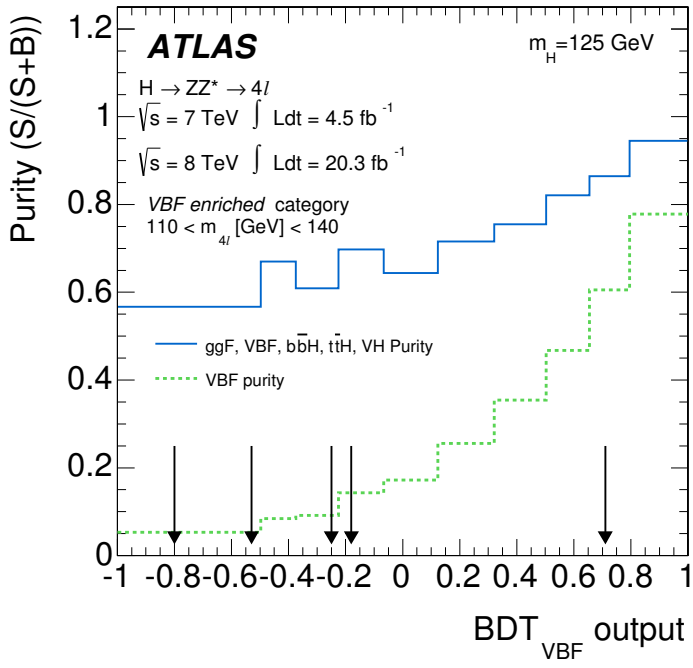

Figure 8.12 Signal purity, defined as $S/(S+B)$, as a function of the $\mathrm{BDT_{VBF}}$ output for the mass fit region $110 < m_{4\ell} < 140$ GeV. The solid blue line shows the purity for all Higgs signal production mechanisms relative to the ZZ^* and reducible backgrounds. The dashed green line shows the purity for VBF events relative to the other Higgs boson production modes. The binning is chosen so that each bin contains 10% of the total expected signal events. Five VBF candidates are observed in data in this region, and are indicated with the black arrows [4].

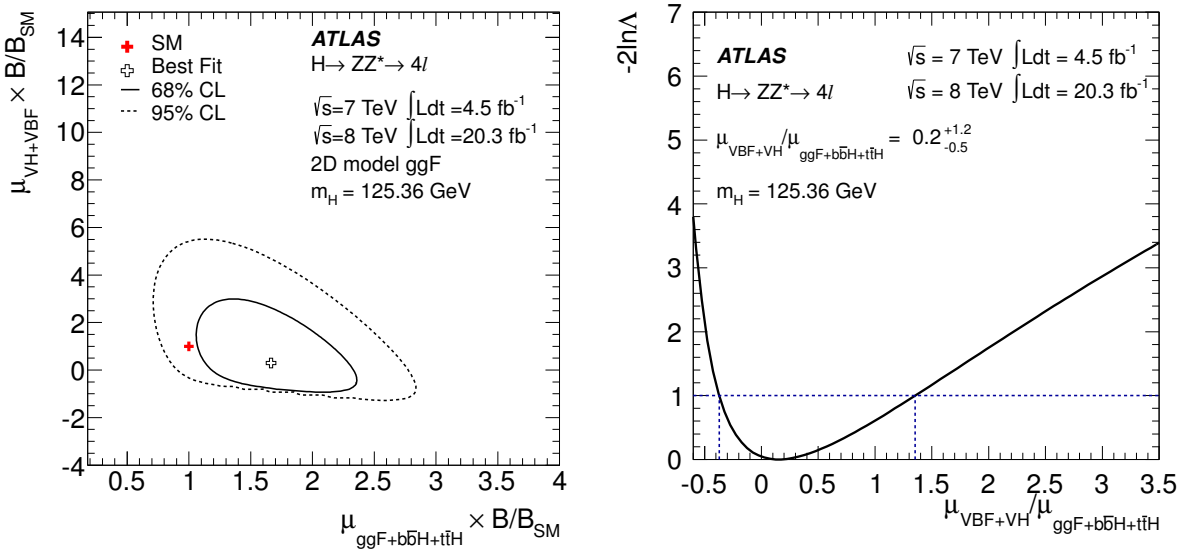

(a) (b)

Figure 8.13 (a) Likelihood contours in the $(\mu_{\mathrm{ggF}+b\bar{b}H+t\bar{t}H} \times B/B_{\mathrm{SM}} - \mu_{\mathrm{VBF+VH}} \times B/B_{\mathrm{SM}})$ plane. Only the part of the plane where the expected number of signal events in each category is positive is considered. The best fit to the data (open cross) and the 68% CL (solid line) and 95% CL (dashed line) contours are also indicated, as well as the SM expectation (red +). (b) Results of the likelihood scan for $\mu_{\mathrm{VBF+VH}}/\mu_{\mathrm{ggF}+b\bar{b}H+t\bar{t}H}$ [4].

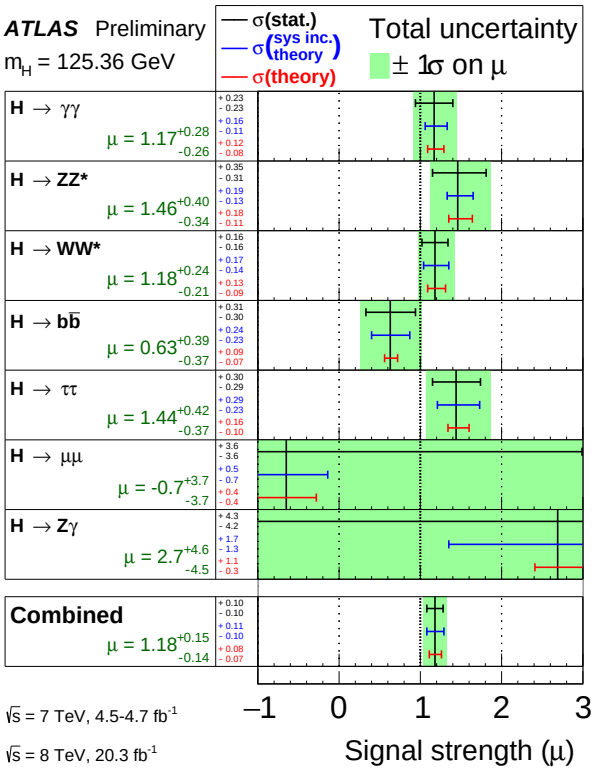

Figure 8.14 The observed signal strengths and uncertainties for different Higgs boson decay channels and their combination for $m_H = 125.36$ GeV. The best-fit values are shown by the solid vertical lines. The total $\pm 1\sigma$ uncertainties are indicated by green shaded bands, with the individual contributions from the statistical uncertainty (top), the total (experimental and theoretical) systematic uncertainty (middle), and the theory systematic uncertainty (bottom) on the signal strength shown as horizontal error bars [155].

measurement of the couplings is implemented using a leading-order tree-level-motivated framework based on the following assumptions: *a*) the Higgs mass value is taken from the combined ATLAS measurement; *b*) the width of the Higgs boson is narrow, justifying the use of the zero-width approximation; and *c*) only modifications of coupling strengths are considered, while the SM tensor structure is assumed, implying that the observed state is a CP-even scalar. Thanks to the zero-width approximation we can factorise the signal cross section in the following way: $\sigma \cdot B\,(i \to H \to f) = \sigma_i \cdot \Gamma_f / \Gamma_H$, where σ_i is the production cross section through the initial state i, B and Γ_f are the branching ratio and partial decay width into the final state f, respectively, and Γ_H the total width of the Higgs boson. Possible deviations from the SM Higgs couplings are introduced via scale factors κ_j, defined in such a way that the cross sections σ_{jj} or the partial decay widths Γ_{jj} associated with the SM particle j scale with the factor κ_j^2 when compared to the corresponding SM prediction. Using the signal cross section factorisation we can thus write, for example: $\sigma \cdot B\,(gg \to H \to ZZ^*) = \sigma_{\mathrm{SM}}(gg \to H) \cdot B_{\mathrm{SM}}(H \to ZZ^*) \cdot (\kappa_g^2 \cdot \kappa_Z^2)/\kappa_H^2$. In this case κ_g, κ_Z, and κ_H are the scale factors for the Higgs couplings to g and Z, and a scale factor for the total Higgs width, respectively. The values of the κ_j are extracted from fits to the data using the profile likelihood ratio $\Lambda(\vec{\kappa})$, in which they are treated either as parameters of interest or as nuisance parameters, depending on the measurement.

In checking whether an observed state is compatible with the SM Higgs boson, one obvious question is whether it fulfils its expected role in the EWSB, which is intimately related to the coupling to the vector bosons (W, Z). An interesting and yet simplified benchmark model can therefore be built assuming only two parameters, one scaling the coupling to the electroweak vector bosons, $\kappa_{\mathrm{V}}(= \kappa_{\mathrm{W}} = \kappa_{\mathrm{Z}})$, and one scaling the coupling common to all fermions, $\kappa_{\mathrm{F}}(= \kappa_{\mathrm{t}} = \kappa_{\mathrm{b}} = \kappa_{\tau})$. Loop-induced processes are assumed to scale as expected from the SM structure. These scale factors are related to the measured signal strengths through $\kappa_{\mathrm{F}}/\kappa_{\mathrm{V}} = \mu_{\mathrm{ggF}+b\bar{b}H+t\bar{t}H}/\mu_{\mathrm{VBF+VH}}$. As seen from Figure 8.13(b), the present measurement of the signal strengths ratio cannot exclude a vanishing value, which leaves κ_{F} unbounded. This can be seen from Figure 8.15(a), where the likelihood contours in the κ_{V}–κ_{F} plane are shown. The compatibility with the SM expectation is 30%. The likelihood scan as a function of the ratio of fermion to vector-boson coupling scale factors, $\lambda_{\mathrm{FV}} = \kappa_{\mathrm{F}}/\kappa_{\mathrm{V}}$, is shown in Figure 8.15(b). The branching ratio of the Higgs boson decaying to ZZ^* cancels out in the λ_{FV} ratio. The result is presented in the same benchmark model but with no assumption on the total decay width made. This result shows how the value $\lambda_{\mathrm{FV}} = 0$, which would correspond to a fermiofobic Higgs boson, is disfavoured at the 4σ level.

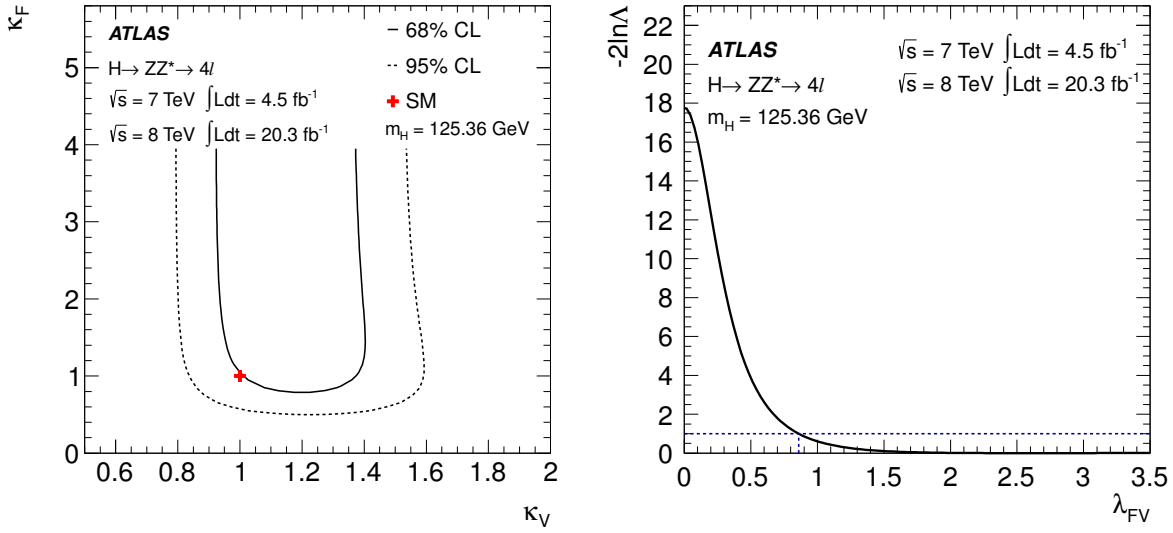

(a) **(b)**

Figure 8.15 (a) Likelihood contours at 68% CL (solid line) and 95% CL (dashed line) in the $\kappa_{\mathrm{V}} - \kappa_{\mathrm{F}}$ plane; the SM expectation (solid red cross) is also indicated. (b) Likelihood scan as a function of the ratio $\lambda_{\mathrm{FV}} = \kappa_{\mathrm{F}}/\kappa_{\mathrm{V}}$. The Higgs boson mass is assumed to be the ATLAS combined value of $m_H = 125.36$ GeV [4].

Chapter 9

Measurement of the Higgs Boson Fiducial and Differential Cross Sections

This chapter presents the recent measurements of the fiducial and differential production cross sections for the $H \to ZZ^* \to 4\ell$ decay channel [5], and compares them to selected theoretical calculations.

The decision to determine the cross sections within a fiducial phase space is related to the intrinsic model dependence of the total cross section definition. The latter is indeed calculated as

$$\sigma_{\text{tot}} \cdot BR = \frac{N_{\text{sig}}}{\varepsilon_{\text{tot}} \cdot \mathcal{L}_{\text{int}}} \ , \tag{9.1}$$

where BR is the branching ratio of the decay mode, N_{sig} is the number of observed signal events, $\mathcal{L}_{\text{int}}$ the integrated luminosity, and ε_{tot} is the efficiency for detecting the signal process (including trigger, reconstruction and identification efficiencies). To estimate the total efficiency, which accounts also for events outside of the detector acceptance, the observed measurements need to be extrapolated to phase-space regions not covered by the detector, and this introduces a dependency on the model. This effect can however be minimised by dividing the total efficiency into two terms and defining a fiducial cross section as follows:

$$\varepsilon_{\text{tot}} = A_{\text{fid}} \ \cdot \ \varepsilon_{\text{fid}} \qquad \sigma_{\text{fid}} \cdot BR = \frac{N_{\text{sig}}}{\varepsilon_{\text{fid}} \cdot \mathcal{L}_{\text{int}}} \ , \tag{9.2}$$

where A_{fid} represents the fraction of events that fall within a defined fiducial volume of the detector, and ε_{fid} is the fiducial efficiency, i.e the signal efficiency within the fiducial volume of the detector. The correction for the fiducial acceptance is not included in the fiducial cross section definition, and thus the model dependence is mostly removed.

The differential measurements are performed in six observables related to the Higgs boson production and decay. These include the transverse momentum $p_{\text{T},H}$ and rapidity $|y_H|$ of the Higgs boson, the invariant mass of the subleading lepton pair m_{34}, the magnitude of the cosine of the decay angle of the leading lepton pair in the four-lepton rest frame with respect to the

beam axis $|\cos\theta^*|$, the number of jets n_{jets}, and the transverse momentum of the leading jet $p_{\text{T,jet}}$.

The distribution of the $p_{\text{T},H}$ observable is sensitive to the Higgs boson production mechanisms as well as the spin/CP quantum numbers, and can be used to test perturbative QCD predictions. The parton distribution functions (PDFs) of the proton can be tested through the distribution of the $|y_H|$ observable. The distributions of the decay variables m_{34} and $|\cos\theta^*|$ are sensitive to the Lagrangian structure of Higgs boson interactions, e.g. spin/CP quantum numbers and higher-dimensional operators. The jet-related variables are sensitive to both QCD radiation effects and to the relative rates of Higgs boson production mechanism, and the distribution of the transverse momentum of the leading jet can be used to probe quark and gluon radiation.

The remainder of this chapter is organised as follows: the simulated samples and theoretical predictions used in the analysis are discussed in Section 9.1. The event selection is only briefly covered in Section 9.2, as it almost completely overlaps with the one described in Chapter 6. The definition of the fiducial region and the unfolding procedure are discussed in Sections 9.3 and 9.4, respectively. The systematic uncertainties affecting the measurements are discussed in Section 9.5, and the results are finally presented in Section 9.6.

The author of this thesis has contributed to the presented results with the measurement of the fiducial cross section and the estimation of the background related systematic uncertainties for both the fiducial and differential measurements.

9.1 Theoretical Predictions and Simulated Samples

The same simulated samples and cross sections described in Section 9.1 are used to model both signal and background events. Additional samples are only used in the final stage of the analysis, in which the derived cross sections are compared to a number of different theoretical predictions. Three ggF calculations are considered: Powheg without the Higgs p_{T} reweighing described in Section 9.1, Powheg interfaced to Minlo (Multi-scale improved NLO) [156] and HRes2 (v.2.2) [157, 158]. Powheg interfaced to Minlo provides predictions for jet-related variables at NLO, for a Higgs boson production in association with one jet. The HRes2 program computes fixed-order cross sections for ggF Higgs production up to NNLO. All-order resummation of soft-gluon effects at small transverse momenta is consistently included up to NNLL, using dynamic factorisation and resummation scales. The program also implements bottom-quark mass dependence up to NLL+NLO, and top-quark mass dependence up to the NNLL+NNLO level. Showering and QED final-state radiation are however not included in HRes2.

The small contributions from the other production modes are added to the ggF predictions. At a centre-of-mass energy of 8 TeV and for a Higgs boson mass of 125.4 GeV, their relative contributions to the total cross section are 87.3% (ggF), 7.1% (VBF), 3.1% (WH), 1.9% (ZH) and 0.6% (ttH), respectively. All theoretical predictions are computed for a SM Higgs boson with mass 125.4 GeV, and normalised to the most precise SM inclusive cross section predictions currently available [6]. In order to be compared to the measured cross sections, the samples are further corrected for the fiducial acceptance derived from the simulation.

9.2 Event Selection

The definition of the reconstructed objects is identical to that seen in Section 6.3 for both electrons and muons, while it is slightly different for jets. The kinematic requirements, which are changed to $p_{\mathrm{T}} > 30$ GeV and $|y| < 4.4$, are chosen to be consistent with the $H \to \gamma\gamma$ cross section measurements [33] in order to facilitate a later combination.

The event selection follows exactly the requirements seen in Section 6.4 for the inclusive analysis. The categorisation into different production modes is not applied, as the limited available statistics does not allow for this.

For the differential cross section measurements, the selected events are divided into bins of the variables of interest, which are computed starting from the reconstructed quantities of the selected quadruplets and jets. These variables of interest, labelled with "reco" to distinguish them from the corresponding unfolded variables, are: the transverse momentum $p_{\mathrm{T},H}^{\mathrm{reco}}$ and the rapidity $|y_H^{\mathrm{reco}}|$ of the four-lepton system, the invariant mass of the subleading lepton pair m_{34}^{reco}, the magnitude of the cosine of the decay angle of the leading lepton pair in the four-lepton rest frame with respect to the beam axis $|\cos\theta^{*\mathrm{reco}}|$, the number of jets $n_{\mathrm{jets}}^{\mathrm{reco}}$, and the transverse momentum of the leading jet $p_{\mathrm{T,jet}}^{\mathrm{reco}}$. The observed distributions for the six reconstructed observables are shown in Figure 9.1, and compared to the signal and background expectations. The background contributions, shown separately for the ZZ^* and the reducible Z+jets and $t\bar{t}$ backgrounds, are estimated as described is Chapter 7.

9.3 Definition of the Fiducial Region

The fiducial selection, summarised in Table 9.1, is chosen to be easily reproducible and to replicate as closely as possible the analysis selection at simulation level, before applying detector effects. This is needed in order to minimise any model-dependent acceptance effect on the measured cross sections.

The selection is applied on born-level muons and electrons arising from a vector-boson decay, i.e. before they emit any photon radiation. The possibility of using dressed leptons was also studied, and the difference in the analysis acceptance between the two definitions was found to be less than 0.5%. Particle-level jets are reconstructed from all stable particles except muons and neutrinos, with the same anti-kt algorithm and distance parameter used for reconstructed jets. As for the kinematic requirements, electrons and muons are required to have $p_{\mathrm{T}} > 7$ GeV and $|\eta| < 2.47$, and $p_{\mathrm{T}} > 6$ GeV and $|\eta| < 2.7$, respectively. Jets are selected if they satisfy $p_{\mathrm{T}} > 30$ GeV and $|y| < 4.4$, and if no electron is found in a $\Delta R = 0.2$ cone around them.

The same pairing procedure described in Section 6.4 is applied, thus allowing the possibility of mispairing leptons, which happens in about 5% of the events. Events with Z bosons decaying into τ leptons are excluded. Within one quadruplet, the three most energetic leptons are required to have $p_{\mathrm{T}} > 20$ GeV, $p_{\mathrm{T}} > 15$ GeV and $p_{\mathrm{T}} > 10$ GeV, respectively. The invariant masses of the leading and subleading lepton pairs are required to be within 50 and 106 GeV for m_{12}, and within 12 and 115 GeV for m_{34}. The same requirements on the separation between leptons and on the J/ψ veto described for the inclusive analysis selection are applied.

Finally, the mass of the four-lepton system $m_{4\ell}$ must be close to m_H, in the range $118 < m_{4\ell} < 129$ GeV.

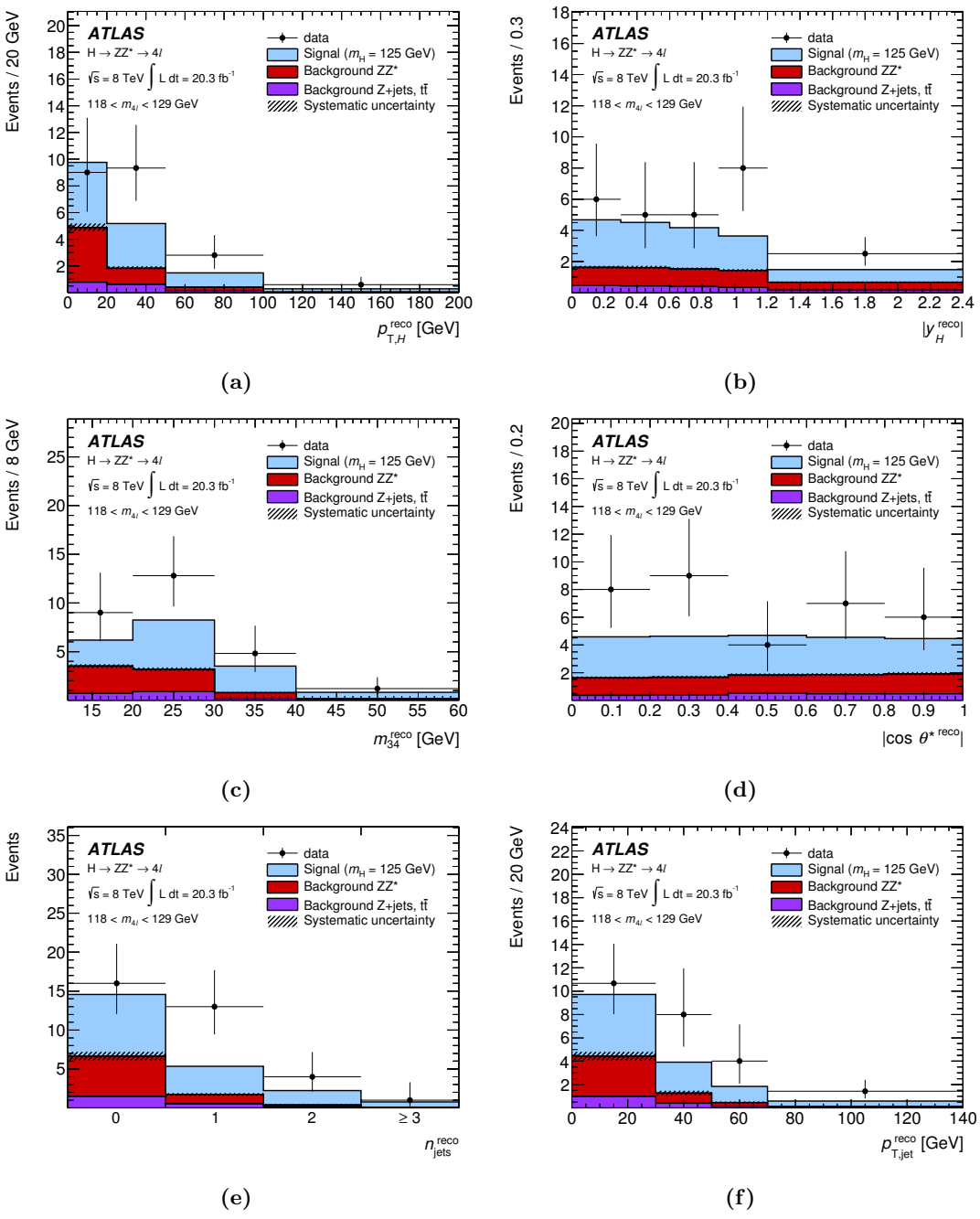

Figure 9.1 Data yield distributions for the six reconstructed variables of interest used in the cross section measurement: (a) $p_{\mathrm{T},H}^{\mathrm{reco}}$, (b) $|y_H^{\mathrm{reco}}|$, (c) m_{34}^{reco}, (d) $|\cos\theta^{*\mathrm{reco}}|$, (e) $n_{\mathrm{jets}}^{\mathrm{reco}}$, and (f) $p_{\mathrm{T,jet}}^{\mathrm{reco}}$, compared to signal and background expectations. The signal prediction includes VBF, ZH, WH, $t\bar{t}H$, and the POWHEG ggF calculation for a Higgs boson with $m_H = 125$ GeV and is normalised to the most precise SM inclusive cross-section calculation currently available [6]. The data is represented as filled circles and the different backgrounds as filled histograms with the total background systematic uncertainty represented by the hatched areas [5].

Table 9.1 List of selection cuts which define the fiducial region of the cross section measurement [5].

Lepton Selection	
Muons: $p_{\mathrm{T}} > 6$ GeV, $\lvert\eta\rvert < 2.7$	Electrons: $p_{\mathrm{T}} > 7$ GeV, $\lvert\eta\rvert < 2.47$
Pairing	
Leading pair:	SFOS lepton pair with smallest $\lvert m_Z - m_{\ell\ell}\rvert$
Subleading pair:	Remaining SFOS lepton pair with smallest $\lvert m_Z - m_{\ell\ell}\rvert$
Event Selection	
Lepton Kinematics:	Leading lepton $p_{\mathrm{T}} > 20, 15, 10$ GeV
Mass Requirements:	$50 < m_{12} < 106$ GeV; $12 < m_{34} < 115$ GeV
Lepton Separation:	$\Delta R(\ell_i, \ell_j) > 0.1(0.2)$ for same (opposite) flavor leptons
J/ψ veto:	$m(\ell_i, \ell_j) > 5$ GeV for all SFOS lepton pairs
Mass window:	$118 < m_{4\ell} < 129$ GeV

This mass window was chosen in order to maximise the statistical significance $S/\sqrt{S+B}$, which implies minimising the uncertainty on the cross section.

For a SM Higgs boson mass of 125.4 GeV, the acceptance of the fiducial selection with respect to the full $H \to ZZ^* \to 4\ell$ phase space is 45.7%. The fiducial efficiency, defined as the ratio between the number of reconstructed and fiducial events, is 55%. Ideally the fiducial efficiency will be independent of the underlying model, thus making the fiducial cross section measurement model-independent. Due to event migrations at the edges of the fiducial region caused by detector and reconstruction effects, a small fraction of events passing the analysis selection is expected not to pass the fiducial selection. This fiducial leakage is equal to approximately 1%, indicating a correct definition of the fiducial region.

9.4 Observed Differential Yields and Unfolding

9.4.1 Fiducial cross section

The signal yield for the measurement of the fiducial cross section is extracted from a fit to the $m_{4\ell}$ distribution using the 1D method described in Section 8.2.1. The Higgs mass is fixed to the combined $H \to ZZ^* \to 4\ell$ and $H \to \gamma\gamma$ value ($m_H = 125.4$ GeV), and the extracted signal strength value is multiplied by the number of expected signal events at m_H to obtain the total number of signal events. The extracted number of observed signal events in the mass window 118–129 GeV is $23.7^{+5.9}_{-5.3}(\mathrm{stat})\pm 0.6(\mathrm{syst})$, where the first error represents the statistical uncertainty and the second the systematic uncertainty. The statistical component is determined by repeating the likelihood scan with all nuisance parameters related to systematic uncertainties fixed to their best fit value (see Figure 9.2). The systematic component is then derived by subtracting in quadrature the statistical one from the total error. It should be noted that all nuisance parameters related to the theoretical systematic uncertainties used in the signal strength measurement are here switched off, as they do not affect the number of observed events.

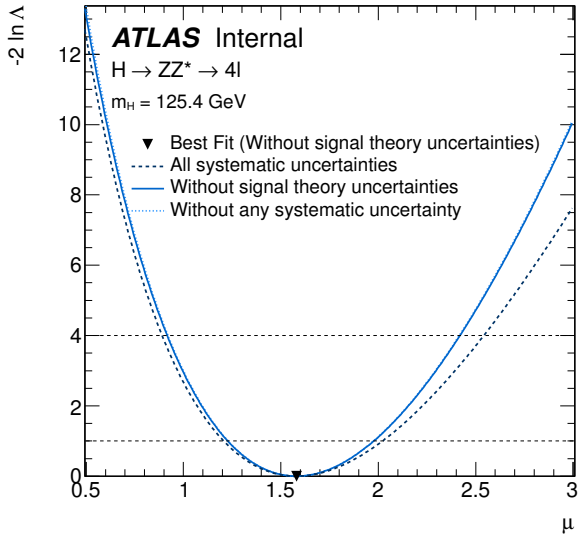

Figure 9.2 The profile likelihood scan as a function of the signal strength μ. The μ value used in the measurement is taken from the solid blue curve, obtained switching off all the theoretical systematic uncertainties, as they do not affect the number of observed events. The dotted light blue curve only includes statistical uncertainties, and it is used to estimate the statistical and systematic component of the uncertainty separately (see text). The dashed dark blue curve is only shown as a reference, and includes, among the systematic uncertainties, also the ones related to theoretical predictions. The dotted and the solid curve overlap almost completely, indicating that the measurement is statistically dominated.

The measured signal yield is then corrected for detector efficiency and resolution effects, using the fiducial efficiency derived from simulated samples for all SM Higgs production modes, weighted with the relative rates predicted by the SM. The inclusive fiducial efficiency is calculated as

$$\varepsilon_{\text{fid}} = \frac{N^{\text{reco}}}{N^{\text{fid}}}, \tag{9.3}$$

where N^{reco} is the number of reconstructed events and N^{fid} is the number of events within the fiducial region, and it is equal to $\varepsilon_{\text{fid}} = 0.553 \pm 0.002(\text{stat}) \pm 0.015(\text{syst})$. The fiducial efficiencies for the different production modes are 0.553 (ggF), 0.572 (VBF), 0.535 (WH), 0.551 (ZH) and 0.417 ($t\bar{t}H$). As expected, these values are close for all production mechanism, the only exception being the $t\bar{t}H$ mode, which is usually accompanied by light- and heavy-flavour jets as well as possible additional leptons from the top-quark decays, and is thus more affected by the absence of the isolation requirements in the fiducial selection.

9.4.2 Differential cross sections

Following the same approach in the differential analysis as that for the inclusive cross section measurement would require the derivation of signal and background templates in each bin of the variables of interest. Given the low number of signal events expected in each measured bin i, the signal yields n_i^{sig} are instead determined by simply subtracting the expected number of background events from the observed number of events in the selected $m_{4\ell}$ window. The total signal yield extracted in this way is $25.1^{+6.3}_{-5.4}(\text{stat})^{+0.6}_{-0.4}(\text{syst})$. The difference with respect to the result seen in the previous section is mainly related to the Higgs mass value, which is fixed to the combined value 125.4 GeV in the $m_{4\ell}$ fit, while the best fit value in the $H \to ZZ^* \to 4\ell$ channel alone is 124.5 GeV.

After subtracting the background events, the measured signal yields are corrected for detector effects using fiducial efficiencies computed separately for each bin i. The unfolded signal yield in each bin is then converted into a differential fiducial cross section via

$$\frac{\mathrm{d}\sigma_{\text{fid},i}}{\mathrm{d}x_i} = \frac{n_i^{\text{sig}}}{\varepsilon_{\text{fid},i} \cdot \mathcal{L}_{\text{int}} \cdot \Delta x_i}, \tag{9.4}$$

where Δx_i is the bin width and $\mathcal{L}_{\text{int}}$ is the integrated luminosity.

For each variable, a profile likelihood ratio is built from the luminosity, the number of observed and expected background events, and the correction factors in each bin. The shape and normalisation uncertainties of backgrounds and correction factors are treated in the likelihood as nuisance parameters, while the parameters of interest are the cross section values in each bin. The correlations of uncertainties between the different bins, as well as between the background estimations and the correction factors, are taken into account.

The cross sections are derived in each bin by minimising the negative logarithm of the profile likelihood ratio -2 ln Λ, and its variations are used to estimate the associated uncertainties. This procedure relies on the assumption that the statistical observable -2 ln Λ behaves as a χ^2 distribution with one degree of freedom, referred to as the asymptotic assumption. This is

indeed the case in most bins, with a few exceptions in which the low number of events causes the profile likelihood ratio to behave differently. For these bins the uncertainties are derived using pseudo-experiments.

The compatibility between the measured and predicted cross sections is estimated from the variation of -2 ln Λ between its best-fit value and the value obtained by fixing the cross sections in all bins to the theoretical predictions. This statistical observable is used as a test statistic to compute the p-values quantifying the compatibility, again under the asymptotic assumption that it behaves as a χ^2 distribution, this time with number of degrees of freedom equal to the number of bins. This assumption was verified with pseudo-experiments for all measured observables.

9.5 Systematic Uncertainties

The systematic uncertainties considered in this analysis can be divided into three different classes: the uncertainties related to the extraction of the signal yields, the ones affecting the unfolding procedure, and finally the theoretical uncertainties which need to be accounted for in the comparison of the measurements with different predictions.

The first category includes uncertainties on the estimated backgrounds. Systematic uncertainties on the data-driven estimate of the reducible background are assigned both to the normalisation and the shapes of the distributions by varying the estimation methods, as described in detail in Chapter 7. These uncertainties are found to be large in some bins, due to the very limited statistics.

Several sources of uncertainties are related to the ZZ^* background, which is evaluated from MC simulation. These include uncertainties on the lepton trigger, reconstruction and identification efficiencies [69, 73], as well as on the luminosity, estimated as described in Section 8.3.2. The uncertainties due to the PDF choice as well as QCD scale variations are also included, and evaluated for most variables as discussed in Section 6.1.2. For the jet-related observables an uncertainty is instead derived by comparing the predicted ZZ^* distributions to the data in the region $m_{4\ell} > 190$ GeV, where the ZZ^* background process is dominant (see also Section 7.3). The systematic uncertainty is taken as the larger of: (1) the data-MC difference and (2) the statistical uncertainty on the data in the control region, after normalising the MC estimate to the observed data yield. This systematic uncertainty accounts for both theoretical and experimental uncertainties in the modelling of the ZZ^* jet distributions; as the event selection does not depend on the jet selection, it will only affect the background shape prediction of the n_{jets} and $p_{\text{T,jet}}$ distributions.

The second category includes uncertainties on the fiducial efficiencies and on the luminosity, both considered when converting the signal yields into cross sections. The experimental uncertainties related to the use of muons and electrons, and the uncertainty on the luminosity measurement, already mentioned for the first category, are propagated in a correlated way also to the fiducial efficiencies.

Furthermore, systematic uncertainties are assigned on the jet resolution and energy scales, exclusively for the jet related variables. The largest systematic uncertainty is due to the uncertainty in the jet flavour composition [77, 78].

Table 9.2 Summary of the relative systematic uncertainties on the total background contribution (top rows) and on the parameters that enter the signal extraction (bottom rows). The ranges indicate the variation across observables and bins [5].

Systematic Uncertainties (%)	
Background	
Luminosity	1.4–2.3
Reducible background	1.6–34
Experimental, leptons	1.3–2.3
PDF/scale	3.0–24
Correction factors/conversion to σ	
Luminosity	2.8
Experimental, leptons	2.1–2.6
Experimental, jets	2.7–13
Production process	0.1–15
Higgs boson mass	0.4–2.7

The theoretical uncertainties on the fiducial efficiencies due to the PDF choice and the QCD scale variations are evaluated as discussed in Section 6.1.2, and found to be negligible. The uncertainties on the predicted relative rates of the Higgs production modes, used in the correction factor calculation, are instead estimated by varying these cross section predictions within the current experimental bounds [1]. The VBF and VH contributions are varied by factors of 0.5 and 2 with respect to the SM prediction, and the $t\bar{t}H$ fraction is varied by factors of 0 and 5. Finally, the experimental uncertainty on the combined Higgs mass value, seen in Eq. 8.7, is propagated to the correction factors by studying their dependence on m_H.

An overview of the systematic uncertainties on the total background prediction and the correction factors is shown in Table 9.2. The ranges indicate the dependence on the different variables and bins, with the upper edges typically corresponding to the highest bins in the n_{jets} and $p_{\text{T,jet}}$ distributions.

As for the third category, the systematic uncertainties on the theoretical predictions include uncertainties on the PDF and QCD scale choices as well as the uncertainty on the $H \to ZZ^*$ branching ratio [6]. The procedure described in Ref. [153] is used to evaluate the scale uncertainties of the predicted n_{jets} distribution.

9.6 Results

The measured value of the inclusive fiducial cross section is

$$\sigma_{\text{tot}}^{\text{fid}} = 2.11^{+0.53}_{-0.47}\ (\text{stat.}) \pm 0.08\ (\text{syst.})\ \text{fb},$$

to be compared with the theoretical prediction from Ref. [6] for a Higgs boson mass of 125.4 GeV, which is 1.30 ± 0.13 fb.

The differential cross sections as a function of $p_{\text{T},H}$, $|y_H|$, m_{34}, $|\cos\theta^*|$, n_{jets}, and $p_{\text{T,jet}}$ are shown in Figure 9.3. The uncertainties on the measurements are dominated by the statistical contribution for all considered variables and bins. The measured cross sections are compared

Table 9.3 Compatibility tests between data and and theoretical predictions from POWHEG, MINLO and HRES2 ggF calculations added to VBF, ZH/WH and $t\bar{t}H$. The compatibility p-values are obtained, as explained in the text, from the difference between $-2\ln\Lambda$ at the best-fit value and $-2\ln\Lambda$ with the cross sections fixed to the theoretical computations [5].

	p-values		
Variable	POWHEG	MINLO	HRES2
$p_{\mathrm{T},H}$	0.30	0.23	0.16
$\lvert y_H \rvert$	0.37	0.45	0.36
m_{34}	0.48	0.60	-
$\lvert \cos\theta^* \rvert$	0.35	0.45	-
n_{jets}	0.37	0.28	-
$p_{\mathrm{T,jet}}$	0.33	0.26	-

to different theoretical calculations of the ggF process, POWHEG, MINLO and HRES2, added to the smaller contributions from VBF, ZH/WH and $t\bar{t}H$. The HRES2 calculation is only used for $p_{\mathrm{T},H}$ and $|y_H|$, as it was developed for modelling the Higgs kinematic variables. As mentioned in Section 9.1, all theoretical calculations are normalised to the most precise SM inclusive cross-section predictions currently available [6].

The p-values quantifying the compatibility between the observed data and the predictions, computed with the method described in Section 9.4, are summarised in Table 9.3, and vary between 0.16 and 0.6. No significant discrepancy is observed, and all predictions provide a similar level of agreement.

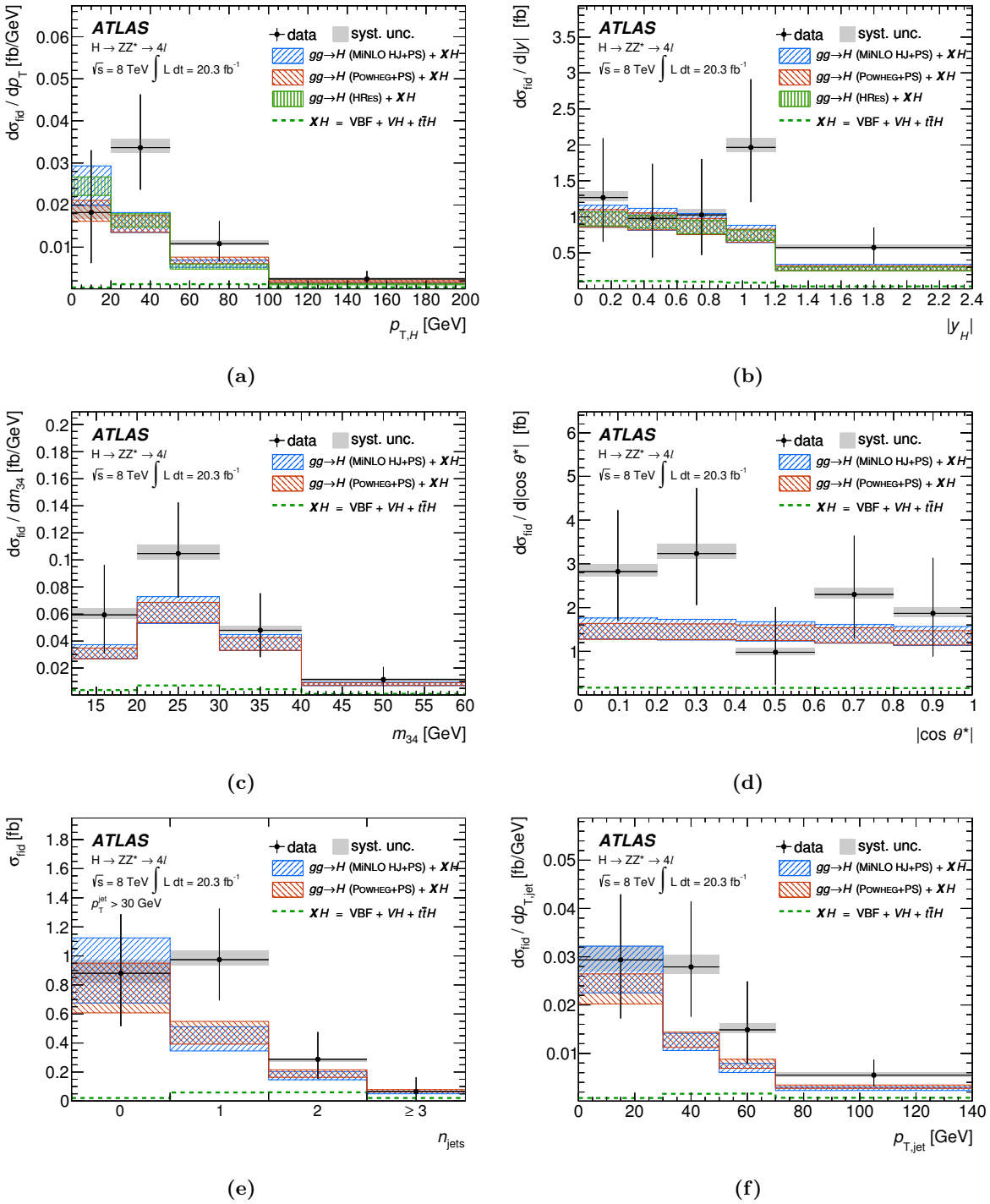

Figure 9.3 Unfolded differential cross sections as a function of (a) $p_{\mathrm{T},H}^{\mathrm{reco}}$, (b) $|y_H^{\mathrm{reco}}|$, (c) m_{34}^{reco}, (d) $|\cos\theta^{*\mathrm{reco}}|$, (e) $n_{\mathrm{jets}}^{\mathrm{reco}}$, and (f) $p_{\mathrm{T,jet}}^{\mathrm{reco}}$ in the $H \to ZZ^* \to 4\ell$ decay channel compared to different theoretical calculations of the ggF process: POWHEG, MINLO and HRES2. The contributions from VBF, ZH/WH and $t\bar{t}H$ are determined as described in Section 9.1 and added to the ggF distributions. All theoretical calculations are normalized to the most precise SM inclusive cross-section predictions currently available [6]. The error bars on the data points show the total (stat $\oplus$ syst) uncertainty, while the grey bands represent the systematic uncertainties. The bands of the theoretical prediction indicate the total uncertainty.

Conclusions

The research described in this thesis has contributed to the exciting discovery and then to the precise measurement of the properties of the Higgs boson, the long-sought particle that eluded physicists for almost 50 years from its first prediction. The work was done in the context of the $H \to ZZ^* \to 4\ell$ analysis, which has provided a unique opportunity to search for the Higgs boson and to confirm its SM-like nature.

The analysis sensitivity relies critically on the ability to efficiently reconstruct and identify leptons, and more generally on the knowledge of the electron and muon response of the detector. Therefore an important part of this thesis work was devoted to the understanding and improvement of several aspects of the electron reconstruction.

A significant improvement to the electron reconstruction came from the introduction of a new electron track reconstruction algorithm. The algorithm was designed to achieve a high and uniform efficiency by accounting for radiative energy losses of electrons, and exploits an optimised electron track fitter, the Gaussian Sum Filter (GSF), to precisely estimate the electron track parameters. It was used for the first time in ATLAS in the $H \to ZZ^* \to 4\ell$ analysis, where the implications were expected to be important, and this required validation and understanding of the new objects. The study indeed demonstrated how the improvement in the fitting procedure yields a better estimate of all the bending-plane track parameters, especially in the low-E_{T} region. A substantial improvement over the entire energy spectrum is achieved in the resolution of the estimated d_0 significance, used in the $H \to ZZ^* \to 4\ell$ event selection to reduce the contamination from heavy-quark decays. Particularly important is also the dependence of the transverse track parameter resolution on the electron pseudorapidity and transverse momentum, which is considerably reduced. Finally, the results proved how the improvements on the electron kinematic quantities also led to an increased accuracy on the invariant mass of the parent resonance, and on its associated uncertainty.

Since the beginning of 2012 data-taking, the GSF algorithm has become part of the standard reconstruction scheme used in ATLAS, and a public note was prepared to summarise the work done [71]. The average increase in the 2012 reconstruction efficiency compared to the previous results is $\sim 2\%$ for high-E_{T} electrons and up-to $\sim 7\%$ for low-E_{T} (< 20 GeV) electrons.

Reconstructed electrons are calibrated to correct for the energy lost in the material before entering the calorimeter, deposited in neighbouring cells, or leaked beyond the calorimeter. A new MVA-based calibration scheme was developed in 2012, and used for the final Run 1

$H \to ZZ^* \to 4\ell$ measurements. The use of the improved procedure in our analysis was thus investigated carefully, and shown to bring marginal improvements upon the energy and invariant mass resolution, predominantly for low-E_{T} electrons. On the other hand, it resulted in a significant reduction in the overall energy scale uncertainty – for $|\eta| < 1.37$ the uncertainty is reduced, for example, from 0.4% to 0.04% for 40 GeV electrons – and has an important impact on the systematic uncertainty of the Higgs boson mass measurement.

Further selections are applied on reconstructed electrons in order to discriminate isolated signal electrons against background objects, including misidentified hadrons as well as electrons from photon conversions and heavy flavour hadron decays. To achieve reliable physics results, the MC-based detector simulation needs to be corrected to reproduce the efficiencies of these identification selections as measured in data. Providing precise efficiency measurements in data and MC is therefore a crucial aspect for all analyses involving electrons in the final state, and particularly challenging in the low E_{T} region. As part of the present work, a completely new method was developed to measure the identification efficiencies, addressing the particular complications of low E_{T} electrons.

$J/\psi \to ee$ events were used to measure efficiencies between 7 and 20 GeV, exploiting a technique called "tag-and-probe". At such low energies, the probe sample suffers from a significant background fraction, which needs to be precisely estimated and subtracted. Moreover, the J/ψ sample is composed of two contributions: in the first one the J/ψ particles are produced in the pp hard scattering (prompt production), while in the second they come from B-hadron decays (non-prompt production). Electrons from prompt $J/\psi \to ee$ decays are isolated and therefore expected to have efficiencies close to those of isolated electrons in the same transverse energy range. In contrast, electrons produced in the busy environment of B-hadron decays are expected to have significantly lower efficiency. In order to extract a clean sample of isolated signal electrons arising from promptly produced J/ψ, a sequential fit on the invariant mass of the electron pair as well as on its pseudo-proper time was thus performed. This method allows for a completely data-driven measurement, and results in a precision of $\sim 3\%$ in the challenging lowest E_{T} region (7-10 GeV) for the identification selections used in the $H \to ZZ^* \to 4\ell$ analysis.

This work on the performance of the ATLAS detector has been documented in a paper [81] (results based on the 2011 dataset) and a public note [69] (results based on the 2012 dataset).

A careful evaluation of the background sources is a key ingredient of the $H \to ZZ^* \to 4\ell$ analysis, and was the objective of the second part of the work done for this thesis.

In order to improve our understanding of the dominant ZZ^* background simulation and to reduce the related uncertainties, the performance of different MC generators have been compared. Based on the results of this study, Powheg-Box was chosen to replace Pythia, which only included LO calculations for the doubly-resonant ZZ^* diagram. Powheg-Box indeed provides an NLO calculation of the di-boson production with the Z/γ interference and the singly-resonant contributions properly taken into account.

Unlike the case of ZZ^* background, MC simulation can't be relied on for the estimation of the reducible backgrounds coming from Z+jets (including both light and heavy flavour jets) and top quark pair production. As part of the present work, the author has thus developed a

new, fully data-driven method for the estimation of these background sources in the final states with sub-leading electrons ($\ell\ell + ee$).
The method exploits two background-enriched control regions with relaxed electron requirements: the $Z + XX$, used to estimate the background yields, and the much larger $Z + X$, needed to extract the extrapolation efficiency, or transfer factor, from the $Z + XX$ control region to the signal region.

The complexity of the measurement was primarily related to the different fractions of true isolated electrons, fakes, photon conversions and heavy-flavour semileptonic decays present in the two control regions. The experimental properties of these various components are indeed completely different, and having the composition of the control regions match as closely as possible is thus essential. Thanks to the definition of a new $Z + X$ control region enriched with $b \to e$ decays, defined by requiring the presence of a b-jet in the event, it was possible to overcome this problem without relying on simulation. The fraction of electrons from heavy-flavour decays in the original $Z + X$ sample was indeed seen to be suppressed compared to the one in the $Z + XX$, but by scanning the possible values of the b-tagger output we were able to properly adjust the composition. Thanks to this new method we have provided a solid and fully data-driven estimation of the reducible background. The use of the new control region also allowed us to compute corrections on MC normalisation and efficiencies which are used in all other MC-based background estimation methods in the analysis. This allowed to improve the baseline method's uncertainties by ∼10%. These results are documented in the paper presenting the most recent $H \to ZZ^* \to 4\ell$ measurements of the Higgs boson production and couplings [4].

Thanks to the aforementioned achievements in the electron reconstruction, identification and energy calibration, as well as in other aspects of the analysis including the background estimation, an improved measurement of the Higgs boson mass in the $H \to ZZ^* \to 4\ell$ decay channel was recently published. The new measurement, based on the full Run 1 integrated luminosity recorded by the ATLAS detector (~ 25 fb^{-1}), features both statistical and systematic uncertainties reduced, compared to the previous publication [1] based on the same dataset. The measured mass, $m_H = 124.51 \pm 0.52$ (stat) ± 0.04 (syst) GeV, was combined with the result obtained in the $H \to \gamma\gamma$ decay channel to provide the best ATLAS measurement of the Higgs boson mass [2].

Furthermore, with an achieved precision of better than 0.2%, the combination of these results with those from the CMS collaboration represent the most precise measurement of the Higgs boson mass yet and among the most precise measurements performed at the LHC to date [3].

An improved measurement of the Higgs boson production and couplings was also recently finalised, again exploiting the entire Run 1 data statistics [4]. This analysis, which performs an event categorisation according to the ggF, VBF and VH production modes, measured the signal strengths for gluon fusion and for vector-boson fusion to be $1.66^{+0.45}_{-0.41}$ (stat.)$^{+0.25}_{-0.15}$ (syst.) and $0.26^{+1.60}_{-0.91}$ (stat.)$^{+0.36}_{-0.23}$ (syst.), respectively. A fit to the different categories assuming a single overall signal strength was also performed, resulting in $\mu = 1.44^{+0.34}_{-0.31}$ (stat.)$^{+0.21}_{-0.11}$ (syst.).

The categorised analysis was also used to quantify the compatibility with the SM predictions

in the framework of the coupling scale factors for weak vector bosons (κ_V) and fermions (κ_F), and no significant deviation was observed.

Finally, the last part of the work done for this thesis has focused on the first measurement of the fiducial and differential cross sections of the Higgs boson production in the $H \to ZZ^* \to 4\ell$ analysis, which is based on 20.3 fb^{-1}of pp collision data produced at $\sqrt{s} = 8$ TeV. Fiducial cross sections are quoted in order to minimise the model dependence of the acceptance corrections related to the extrapolation to phase-space regions not covered by the detector. A fit to the $m_{4\ell}$ distribution is performed in order to extract the fiducial cross section, while a simpler cut-and-count method is used to determine the signal yields for the differential cross section measurements, performed in several observables related to the Higgs boson production and decay. The fiducial cross sections are corrected for detector effects to be directly compared to theoretical calculations. No significant deviations from the SM have been observed. The measured value of the inclusive fiducial cross section is $\sigma_{\text{tot}}^{\text{fid}} = 2.11^{+0.53}_{-0.47}$ (stat.) ± 0.08 (syst.) fb^{-1}, to be compared with the theoretical prediction from Ref. [6] for a Higgs boson mass of 125.4 GeV, which is 1.30 ± 0.13 fb^{-1}. The results of this analysis have been published in [5].

In February 2012 the first three-year LHC running period has reached its conclusion. The LHC's first run has seen major advances in physics, including the discovery of a new particle consistent with the Higgs boson, which has set a milestone in our understanding of nature. Up to now, increasingly precise measurements have established that all observed properties of the Higgs boson, including its cross section, couplings, spin, and parity are consistent with the SM predictions. With the upcoming LHC Run 2, the increased centre-of-mass energy and the larger statistics will open the way to even more detailed studies of the Higgs properties, as well as to searches for additional Higgs states, which could shed light on other mysteries of our universe, hinting at new physics beyond the Standard Model.

Bibliography

[1] ATLAS Collaboration, *Measurements of Higgs boson production and couplings in diboson final states with the ATLAS detector at the LHC*, Phys.Lett. **B726** (2013) 88–119, arXiv:1307.1427 [hep-ex].

[2] ATLAS Collaboration, *Measurement of the Higgs boson mass from the $H \to \gamma\gamma$ and $H \to ZZ^* \to 4\ell$ channels with the ATLAS detector using 25 fb^{-1} of pp collision data*, Phys.Rev. **D90** (2014) 052004, arXiv:1406.3827 [hep-ex].

[3] ATLAS and CMS Collaborations, *Combined Measurement of the Higgs Boson Mass in pp Collisions at $\sqrt{s} = 7$ and 8 TeV with the ATLAS and CMS Experiments*, Phys.Rev.Lett. **114** (2015) 191803, arXiv:1503.07589 [hep-ex].

[4] ATLAS Collaboration, *Measurements of Higgs boson production and couplings in the four-lepton channel in pp collisions at center-of-mass energies of 7 and 8 TeV with the ATLAS detector*, Phys.Rev. **D91** no. 1, (2015) 012006, arXiv:1408.5191 [hep-ex].

[5] ATLAS Collaboration, *Fiducial and differential cross sections of Higgs boson production measured in the four-lepton decay channel in pp collisions at $\sqrt{s}$=8 TeV with the ATLAS detector*, Phys.Lett. **B738** (2014) 234–253, arXiv:1408.3226 [hep-ex].

[6] LHC Higgs Cross Section Working Group, S. Heinemeyer, C. Mariotti, G. Passarino, and R. Tanaka (Eds.), *Handbook of LHC Higgs Cross Sections: 3. Higgs Properties*, CERN-2013-004 (CERN, Geneva, 2013), arXiv:1307.1347 [hep-ph].

[7] S. Glashow, *Partial Symmetries of Weak Interactions*, Nucl.Phys. **22** (1961) 579–588.

[8] S. Weinberg, *A Model of Leptons*, Phys.Rev.Lett. **19** (1967) 1264–1266.

[9] A. Salam, *Weak and Electromagnetic Interactions*, Proceedings of the 8th Nobel Symposium on 'Elementary Particle Theory, Relativistic Groups and Analyticity', edited by Svartholm, Almqvist and Wiksells, Stockholm (1968) 367–377.

[10] S. Glashow, J. Iliopoulos, and L. Maiani, *Weak Interactions with Lepton-Hadron Symmetry*, Phys.Rev. **D2** (1970) 1285–1292.

[11] G. 't Hooft and M. Veltman, *Regularization and Renormalization of Gauge Fields*, Nucl.Phys. **B44** (1972) 189–213.

[12] H. D. Politzer, *Asymptotic Freedom: An Approach to Strong Interactions*, Phys.Rept. **14** (1974) 129–180.

[13] D. Gross and F. Wilczek, *Asymptotically Free Gauge Theories I*, Phys.Rev. **D8** (1973) 3633–3652.

[14] D. Gross and F. Wilczek, *Asymptotically Free Gauge Theories II*, Phys.Rev. **D9** (1974) 980–993.

[15] H. D. Politzer, *Reliable Perturbative Results for Strong Interactions?*, Phys.Rev.Lett. **30** (1973) 1346–1349.

[16] E. Fermi, *Tentativo di una Teoria Dei Raggi β*, Il Nuovo Cimento (1924-1942) **11** (1934) 1–19.

[17] F. Englert and R. Brout, *Broken Symmetry and the Mass of Gauge Vector Mesons*, Phys.Rev.Lett. **13** (1964) 321–323.

[18] P. W. Higgs, *Broken symmetries, massless particles and gauge fields*, Phys.Lett. **12** (1964) 132–133.

[19] P. W. Higgs, *Broken Symmetries and the Masses of Gauge Bosons*, Phys.Rev.Lett. **13** (1964) 508–509.

[20] J. M. Cornwall, D. N. Levin, and G. Tiktopoulos, *Uniqueness of spontaneously broken gauge theories*, Phys.Rev.Lett. **30** (1973) 1268–1270.

[21] J. M. Cornwall, D. N. Levin, and G. Tiktopoulos, *Derivation of Gauge Invariance from High-Energy Unitarity Bounds on the s-Matrix*, Phys.Rev. **D10** (1974) 1145.

[22] C. Llewellyn Smith, *High-Energy Behavior and Gauge Symmetry*, Phys.Lett. **B46** (1973) 233–236.

[23] B. W. Lee, C. Quigg, and H. Thacker, *Weak Interactions at Very High-Energies: The Role of the Higgs Boson Mass*, Phys.Rev. **D16** (1977) 1519.

[24] A. Wingerter, *Implications of the Stability and Triviality Bounds on the Standard Model with Three and Four Chiral Generations*, Phys.Rev. **D84** (2011) 095012, arXiv:1109.5140 [hep-ph].

[25] LEP Working Group for Higgs boson searches, ALEPH, DELPHI, L3, OPAL Collaboration, R. Barate et al., *Search for the standard model Higgs boson at LEP*, Phys.Lett. **B565** (2003) 61–75, arXiv:hep-ex/0306033 [hep-ex].

[26] M. Baak, M. Goebel, J. Haller, A. Hoecker, D. Ludwig, et al., *Updated Status of the Global Electroweak Fit and Constraints on New Physics*, Eur.Phys.J. **C72** (2012) 2003, arXiv:1107.0975 [hep-ph].

[27] CDF, D0 Collaboration, T. Aaltonen et al., *Higgs Boson Studies at the Tevatron*, Phys.Rev. **D88** no. 5, (2013) 052014, arXiv:1303.6346 [hep-ex].

[28] ATLAS Collaboration, *Observation of a new particle in the search for the Standard Model Higgs boson with the ATLAS detector at the LHC*, Phys.Lett. **B716** (2012) 1–29, arXiv:1207.7214 [hep-ex].

[29] CMS Collaboration, *Observation of a new boson at a mass of 125 GeV with the CMS experiment at the LHC*, Phys.Lett. **B716** (2012) 30–61, arXiv:1207.7235 [hep-ex].

[30] CMS Collaboration, *Precise determination of the mass of the Higgs boson and tests of compatibility of its couplings with the standard model predictions using proton collisions at 7 and 8 TeV*, Eur.Phys.J. **C75** no. 5, (2015) 212, arXiv:1412.8662 [hep-ex].

[31] ATLAS Collaboration, *Evidence for the spin-0 nature of the Higgs boson using ATLAS data*, Phys.Lett. **B726** (2013) 120–144, arXiv:1307.1432 [hep-ex].

[32] CMS Collaboration, *Constraints on the spin-parity and anomalous HVV couplings of the Higgs boson in proton collisions at 7 and 8 TeV*, arXiv:1411.3441 [hep-ex].

[33] ATLAS Collaboration, *Measurements of fiducial and differential cross sections for Higgs boson production in the diphoton decay channel at $\sqrt{s} = 8$ TeV with ATLAS*, JHEP **1409** (2014) 112, arXiv:1407.4222 [hep-ex].

[34] ATLAS Collaboration, *The ATLAS Experiment at the CERN Large Hadron Collider*, JINST **3** (2008) S08003.

[35] CMS Collaboration, *The CMS experiment at the CERN LHC*, JINST **3** (2008) S08004.

[36] ALICE Collaboration, *The ALICE experiment at the CERN LHC*, JINST **3** (2008) S08002.

[37] LHCb Collaboration, *The LHCb Detector at the LHC*, JINST **3** (2008) S08005.

[38] S. Myers and E. Picasso, *The Design, construction and commissioning of the CERN Large Electron Positron collider*, Contemp.Phys. **31** (1990) 387–403.

[39] A. Jeff, A. Boccardi, E. Bravin, A. Fisher, T. Lefevre, et al., *First results of the LHC longitudinal density monitor*, Nucl.Instrum.Meth. **A659** (2011) 549–556.

[40] L. Evans and P. Bryant, *LHC Machine*, JINST **3** (2008) S08001.

[41] O. S. Brüning, P. Collier, P. Lebrun, S. Myers, R. Ostojic, J. Poole, and P. Proudlock, *LHC Design Report*. CERN, Geneva, 2004.

[42] ATLAS Collaboration, "Luminosity Public Results." https://twiki.cern.ch/twiki/bin/view/AtlasPublic/LuminosityPublicResults.

[43] ATLAS Collaboration, *ATLAS inner detector: Technical Design Report, 1*. CERN, Geneva, 1997.

[44] ATLAS Collaboration, *ATLAS inner detector: Technical Design Report, 2*. CERN, Geneva, 1997.

[45] ATLAS Collaboration, *The ATLAS SemiConductor Tracker operation and performance*, JINST **7** (2012) C04001.

[46] ATLAS Collaboration, *Particle Identification Performance of the ATLAS Transition Radiation Tracker*, Tech. Rep. ATLAS-CONF-2011-128, CERN, Geneva, Sep, 2011. http://cds.cern.ch/record/1383793.

[47] ATLAS Collaboration Collaboration, ATLAS Collaboration, *Calibration of the ATLAS Transition Radiation Tracker*, Tech. Rep. ATLAS-CONF-2011-006, CERN, Geneva, Feb, 2011. http://cds.cern.ch/record/1330712.

[48] ATLAS Collaboration, *ATLAS liquid-argon calorimeter: Technical Design Report*. Technical Design Report ATLAS. CERN, Geneva, 1996.

[49] ATLAS Collaboration, *ATLAS calorimeter performance Technical Design Report*. Technical Design Report ATLAS. Geneva, 1996.

[50] ATLAS Liquid Argon HEC Collaboration, B. Dowler et al., *Performance of the ATLAS hadronic end-cap calorimeter in beam tests*, Nucl.Instrum.Meth. **A482** (2002) 94–124.

[51] J. Archambault, A. Artamonov, M. Cadabeschi, V. Epshteyn, C. Galt, et al., *Performance of the ATLAS liquid argon forward calorimeter in beam tests*, JINST **8** (2013) P05006.

[52] ATLAS Collaboration, *ATLAS muon spectrometer: Technical Design Report*. Technical Design Report ATLAS. CERN, Geneva, 1997.

[53] ATLAS Collaboration, *Performance of the ATLAS Trigger System in 2010*, Eur.Phys.J. **C72** (2012) 1849, arXiv:1110.1530 [hep-ex].

[54] ATLAS Collaboration, *ATLAS detector and physics performance: Technical Design Report, 1*. Technical Design Report ATLAS. CERN, Geneva, 1999. https://cds.cern.ch/record/391176.

[55] ATLAS Collaboration, *ATLAS level-1 trigger: Technical Design Report*. Technical Design Report ATLAS. CERN, Geneva, 1998.

[56] ATLAS Collaboration, *ATLAS high-level trigger, data-acquisition and controls: Technical Design Report*. Technical Design Report ATLAS. CERN, Geneva, 2003.

[57] A. Hocker, V. Perez-Reale, J. Steltzer, J. Haller, T. Eifert, et al., *Overview of the High Level Trigger Steering and Selection for the ATLAS experiment at the LHC*, IEEE Trans.Nucl.Sci. **55** (2008) 165–171.

[58] Y. Nakahama, *Designing the ATLAS trigger menu for high luminosities*, Tech. Rep. ATL-DAQ-PROC-2012-037, CERN, Geneva, Jun, 2012.

[59] ATLAS Collaboration, *Performance of the ATLAS Electron and Photon Trigger in p-p Collisions at sqrts = 7 TeV in 2011*, Tech. Rep. ATLAS-CONF-2012-048, CERN, Geneva, May, 2012. http://cds.cern.ch/record/1450089.

[60] ATLAS Collaboration, *Performance of the ATLAS muon trigger in 2011*, Tech. Rep. ATLAS-CONF-2012-099, CERN, Geneva, Jul, 2012. http://cds.cern.ch/record/1462601.

[61] ATLAS Collaboration, *Operation and performance of the ATLAS semiconductor tracker*, JINST **9** (2014) P08009, arXiv:1404.7473 [hep-ex].

[62] ATLAS Collaboration, "SCT Public Results." https://twiki.cern.ch/twiki/bin/view/AtlasPublic/SCTPublicResults.

[63] H. Bethe and W. Heitler, *On the Stopping of fast particles and on the creation of positive electrons*, Proc.Roy.Soc.Lond. **A146** (1934) 83–112.

[64] L. D. Landau and I. J. Pomeranchuk, Dokl. Akad. Nauk. SSSR **92** (1953) 535.

[65] M. L. Ter-Mikaelian, Dokl. Akad. Nauk. SSSR **94** (1954) 1033.

[66] A. B. Migdal, *Bremsstrahlung and pair production in condensed media at high-energies*, Phys.Rev. **103** (1956) 1811–1820.

[67] ATLAS Collaboration, *Electron and photon energy calibration with the ATLAS detector using LHC Run 1 data*, Eur.Phys.J. **C74** no. 10, (2014) 3071, arXiv:1407.5063 [hep-ex].

[68] R. Fruhwirth, *Application of Kalman filtering to track and vertex fitting*, Nucl.Instrum.Meth. **A262** (1987) 444–450.

[69] ATLAS Collaboration, *Electron efficiency measurements with the ATLAS detector using the 2012 LHC proton-proton collision data*, Tech. Rep. ATLAS-CONF-2014-032, CERN, Geneva, Jun, 2014. http://cds.cern.ch/record/1706245.

[70] Particle Data Group, *Review of particle physics*, J. Phys. **G37** (2010) 075021.

[71] ATLAS Collaboration, *Improved electron reconstruction in ATLAS using the Gaussian Sum Filter-based model for bremsstrahlung*, Tech. Rep. ATLAS-CONF-2012-047, CERN, Geneva, May, 2012. http://cds.cern.ch/record/1449796.

[72] A. Hocker et al., *TMVA - Toolkit for Multivariate Data Analysis*, PoS **ACAT** (2007) 040, arXiv:physics/0703039 [PHYSICS].

[73] ATLAS Collaboration, *Measurement of the muon reconstruction performance of the ATLAS detector using 2011 and 2012 LHC proton-proton collision data*, Eur.Phys.J. **C74** no. 11, (2014) 3130, arXiv:1407.3935 [hep-ex].

[74] S. Hassani, L. Chevalier, E. Lançon, J.-F. Laporte, R. Nicolaidou, and A. Ouraou, *A muon identification and combined reconstruction procedure for the ATLAS detector at the LHC using the (MUONBOY, STACO, MuTag) reconstruction packages*, Nucl.Instrum.Meth. **A572** (2007) 77–79.

[75] ATLAS Collaboration, *Jet energy measurement with the ATLAS detector in proton-proton collisions at* $\sqrt{s} = 7$ *TeV*, Eur.Phys.J. **C73** no. 3, (2013) 2304, arXiv:1112.6426 [hep-ex].

[76] M. Cacciari, G. P. Salam, and G. Soyez, *The Anti-k_t jet clustering algorithm*, JHEP **0804** (2008) 063, arXiv:0802.1189 [hep-ph].

[77] ATLAS Collaboration, *Jet energy measurement and its systematic uncertainty in proton-proton collisions at* $\sqrt{s} = 7$ *TeV with the ATLAS detector*, Eur.Phys.J. **C75** no. 1, (2015) 17, arXiv:1406.0076 [hep-ex].

[78] ATLAS Collaboration, *Jet energy resolution in proton-proton collisions at* $\sqrt{s} = 7$ *TeV recorded in 2010 with the ATLAS detector*, Eur.Phys.J. **C73** no. 3, (2013) 2306, arXiv:1210.6210 [hep-ex].

[79] ATLAS Collaboration, *Calibration of the performance of b-tagging for c and light-flavour jets in the 2012 ATLAS data*, Tech. Rep. ATLAS-CONF-2014-046, CERN, Geneva, Jul, 2014. http://cds.cern.ch/record/1741020.

[80] ATLAS Collaboration, *Electron performance measurements with the ATLAS detector using the 2010 LHC proton-proton collision data*, Eur.Phys.J. **C72** (2012) 1909, arXiv:1110.3174 [hep-ex].

[81] ATLAS Collaboration, *Electron reconstruction and identification efficiency measurements with the ATLAS detector using the 2011 LHC proton-proton collision data*, Eur.Phys.J. **C74** no. 7, (2014) 2941, arXiv:1404.2240 [hep-ex].

[82] G. Artoni, "*Search for a Standard Model Higgs boson in the* $H \to ZZ^* \to 4\ell$ *decay channel with the ATLAS Experiment at CERN.*" https://cds.cern.ch/record/1613869/files/CERN-THESIS-2012-359.pdf, 2013.

[83] C. Blocker, "*Uncertainties on Efficiencies.*" CDF/MEMO/STATISTICS/PUBLIC/7168 (http://www-cdf.fnal.gov/physics/statistics/notes/cdf7168_eff_uncertainties.ps), 2004.

[84] CDF Collaboration, D. Acosta et al., *Measurement of the J/ψ meson and b−hadron production cross sections in $p\bar{p}$ collisions at* $\sqrt{s} = 1960$ *GeV*, Phys. Rev. **D71** (2005) 032001, arXiv:hep-ex/0412071 [hep-ex].

[85] ATLAS Collaboration, *Measurement of the differential cross-sections of inclusive, prompt and non-prompt J/ψ production in pp collisions at* $\sqrt{s} = 7$ *TeV*, Nuclear Physics B **850** (2011) 387, arXiv:1104.3038 [hep-ex].

[86] CMS Collaboration, *J/ψ and ψ_{2S} production in pp collisions at* $\sqrt{s} = 7$ *TeV*, JHEP **1202** (2012) 011, arXiv:1111.1557 [hep-ex].

[87] P. Nason, *A New method for combining NLO QCD with shower Monte Carlo algorithms*, JHEP **0411** (2004) 040, arXiv:hep-ph/0409146 [hep-ph].

[88] P. Nason and C. Oleari, *NLO Higgs boson production via vector-boson fusion matched with shower in POWHEG*, JHEP **1002** (2010) 037, arXiv:0911.5299 [hep-ph].

[89] D. de Florian, G. Ferrera, M. Grazzini, and D. Tommasini, *Higgs boson production at the LHC: transverse momentum resummation effects in the $H \to \gamma\gamma$, $H \to WW^* \to \ell\nu\ell\nu$ and $H \to ZZ^* \to 4\ell$ decay modes*, JHEP **1206** (2012) 132, arXiv:1203.6321 [hep-ph].

[90] M. Grazzini and H. Sargsyan, *Heavy-quark mass effects in Higgs boson production at the LHC*, JHEP **1309** (2013) 129, arXiv:1306.4581 [hep-ph].

[91] E. Bagnaschi, G. Degrassi, P. Slavich, and A. Vicini, *Higgs production via gluon fusion in the POWHEG approach in the SM and in the MSSM*, JHEP **1202** (2012) 088, arXiv:1111.2854 [hep-ph].

[92] T. Sjostrand, S. Mrenna, and P. Z. Skands, *PYTHIA 6.4 Physics and Manual*, JHEP **0605** (2006) 026, arXiv:hep-ph/0603175 [hep-ph].

[93] T. Sjostrand, S. Mrenna, and P. Z. Skands, *A Brief Introduction to PYTHIA 8.1*, Comput.Phys.Commun. **178** (2008) 852–867, arXiv:0710.3820 [hep-ph].

[94] P. Golonka and Z. Was, *PHOTOS Monte Carlo: A Precision tool for QED corrections in Z and W decays*, Eur.Phys.J. **C45** (2006) 97–107, arXiv:hep-ph/0506026 [hep-ph].

[95] N. Davidson, T. Przedzinski, and Z. Was, *PHOTOS Interface in C++: Technical and Physics Documentation*, arXiv:1011.0937 [hep-ph].

[96] LHC Higgs Cross Section Working Group, S. Dittmaier, C. Mariotti, G. Passarino, and R. Tanaka (Eds.), *Handbook of LHC Higgs Cross Sections: 1. Inclusive Observables*, CERN-2011-002 (CERN, Geneva, 2011), arXiv:1101.0593 [hep-ph].

[97] LHC Higgs Cross Section Working Group, S. Dittmaier, C. Mariotti, G. Passarino, and R. Tanaka (Eds.), *Handbook of LHC Higgs Cross Sections: 2. Differential Distributions*, CERN-2012-002 (CERN, Geneva, 2012), arXiv:1201.3084 [hep-ph].

[98] A. Djouadi, M. Spira, and P. Zerwas, *Production of Higgs bosons in proton colliders: QCD corrections*, Phys.Lett. **B264** (1991) 440–446.

[99] S. Dawson, *Radiative corrections to Higgs boson production*, Nucl.Phys. **B359** (1991) 283–300.

[100] M. Spira, A. Djouadi, D. Graudenz, and P. Zerwas, *Higgs boson production at the LHC*, Nucl.Phys. **B453** (1995) 17–82, arXiv:hep-ph/9504378 [hep-ph].

[101] R. V. Harlander and W. B. Kilgore, *Next-to-next-to-leading order Higgs production at hadron colliders*, Phys.Rev.Lett. **88** (2002) 201801, arXiv:hep-ph/0201206 [hep-ph].

[102] C. Anastasiou and K. Melnikov, *Higgs boson production at hadron colliders in NNLO QCD*, Nucl.Phys. **B646** (2002) 220–256, arXiv:hep-ph/0207004 [hep-ph].

[103] V. Ravindran, J. Smith, and W. L. van Neerven, *NNLO corrections to the total cross-section for Higgs boson production in hadron hadron collisions*, Nucl.Phys. **B665** (2003) 325–366, arXiv:hep-ph/0302135 [hep-ph].

[104] S. Catani, D. de Florian, M. Grazzini, and P. Nason, *Soft gluon resummation for Higgs boson production at hadron colliders*, JHEP **0307** (2003) 028, arXiv:hep-ph/0306211 [hep-ph].

[105] U. Aglietti, R. Bonciani, G. Degrassi, and A. Vicini, *Two loop light fermion contribution to Higgs production and decays*, Phys.Lett. **B595** (2004) 432–441, arXiv:hep-ph/0404071 [hep-ph].

[106] S. Actis, G. Passarino, C. Sturm, and S. Uccirati, *NLO Electroweak Corrections to Higgs Boson Production at Hadron Colliders*, Phys.Lett. **B670** (2008) 12–17, arXiv:0809.1301 [hep-ph].

[107] D. de Florian and M. Grazzini, *Higgs production at the LHC: updated cross sections at* $\sqrt{s} = 8$ *TeV*, Phys.Lett. **B718** (2012) 117–120, arXiv:1206.4133 [hep-ph].

[108] C. Anastasiou, S. Buehler, F. Herzog, and A. Lazopoulos, *Inclusive Higgs boson cross-section for the LHC at 8 TeV*, JHEP **1204** (2012) 004, arXiv:1202.3638 [hep-ph].

[109] J. Baglio and A. Djouadi, *Higgs production at the LHC*, JHEP **1103** (2011) 055, arXiv:1012.0530 [hep-ph].

[110] M. Ciccolini, A. Denner, and S. Dittmaier, *Strong and electroweak corrections to the production of Higgs + 2jets via weak interactions at the LHC*, Phys.Rev.Lett. **99** (2007) 161803, arXiv:0707.0381 [hep-ph].

[111] M. Ciccolini, A. Denner, and S. Dittmaier, *Electroweak and QCD corrections to Higgs production via vector-boson fusion at the LHC*, Phys.Rev. **D77** (2008) 013002, arXiv:0710.4749 [hep-ph].

[112] K. Arnold, M. Bahr, G. Bozzi, F. Campanario, C. Englert, et al., *VBFNLO: A Parton level Monte Carlo for processes with electroweak bosons*, Comput.Phys.Commun. **180** (2009) 1661–1670, arXiv:0811.4559 [hep-ph].

[113] P. Bolzoni, F. Maltoni, S.-O. Moch, and M. Zaro, *Higgs production via vector-boson fusion at NNLO in QCD*, Phys.Rev.Lett. **105** (2010) 011801, arXiv:1003.4451 [hep-ph].

[114] T. Han and S. Willenbrock, *QCD correction to the* $pp \to WH$ *and* ZH *total cross-sections*, Phys.Lett. **B273** (1991) 167–172.

[115] O. Brein, A. Djouadi, and R. Harlander, *NNLO QCD corrections to the Higgs-strahlung processes at hadron colliders*, Phys.Lett. **B579** (2004) 149–156, arXiv:hep-ph/0307206 [hep-ph].

[116] M. Ciccolini, S. Dittmaier, and M. Kramer, *Electroweak radiative corrections to associated WH and ZH production at hadron colliders*, Phys.Rev. **D68** (2003) 073003, arXiv:hep-ph/0306234 [hep-ph].

[117] W. Beenakker, S. Dittmaier, M. Kramer, B. Plumper, M. Spira, et al., *Higgs radiation off top quarks at the Tevatron and the LHC*, Phys.Rev.Lett. **87** (2001) 201805, arXiv:hep-ph/0107081 [hep-ph].

[118] W. Beenakker, S. Dittmaier, M. Kramer, B. Plumper, M. Spira, et al., *NLO QCD corrections to $t\bar{t}H$ production in hadron collisions*, Nucl.Phys. **B653** (2003) 151–203, arXiv:hep-ph/0211352 [hep-ph].

[119] S. Dawson, L. Orr, L. Reina, and D. Wackeroth, *Associated top quark Higgs boson production at the LHC*, Phys.Rev. **D67** (2003) 071503, arXiv:hep-ph/0211438 [hep-ph].

[120] S. Dawson, C. Jackson, L. Orr, L. Reina, and D. Wackeroth, *Associated Higgs production with top quarks at the large hadron collider: NLO QCD corrections*, Phys.Rev. **D68** (2003) 034022, arXiv:hep-ph/0305087 [hep-ph].

[121] A. Bredenstein, A. Denner, S. Dittmaier, and M. Weber, *Precise predictions for the Higgs-boson decay $H \to WW/ZZ \to 4leptons$*, Phys.Rev. **D74** (2006) 013004, arXiv:hep-ph/0604011 [hep-ph].

[122] A. Bredenstein, A. Denner, S. Dittmaier, and M. Weber, *Radiative corrections to the semileptonic and hadronic Higgs-boson decays$H \to WW/ZZ \to 4fermions$*, JHEP **0702** (2007) 080, arXiv:hep-ph/0611234 [hep-ph].

[123] A. Djouadi, J. Kalinowski, and M. Spira, *HDECAY: A Program for Higgs boson decays in the standard model and its supersymmetric extension*, Comput.Phys.Commun. **108** (1998) 56–74, arXiv:hep-ph/9704448 [hep-ph].

[124] M. Botje, J. Butterworth, A. Cooper-Sarkar, A. de Roeck, J. Feltesse, et al., *The PDF4LHC Working Group Interim Recommendations*, arXiv:1101.0538 [hep-ph].

[125] H.-L. Lai, M. Guzzi, J. Huston, Z. Li, P. M. Nadolsky, et al., *New parton distributions for collider physics*, Phys.Rev. **D82** (2010) 074024, arXiv:1007.2241 [hep-ph].

[126] A. Martin, W. Stirling, R. Thorne, and G. Watt, *Parton distributions for the LHC*, Eur.Phys.J. **C63** (2009) 189–285, arXiv:0901.0002 [hep-ph].

[127] R. D. Ball, V. Bertone, F. Cerutti, L. Del Debbio, S. Forte, et al., *Impact of Heavy Quark Masses on Parton Distributions and LHC Phenomenology*, Nucl.Phys. **B849** (2011) 296–363, arXiv:1101.1300 [hep-ph].

[128] ATLAS and CMS Collaborations, *Procedure for the LHC Higgs boson search combination in Summer 2011*, Tech. Rep. CMS-NOTE-2011-005. ATL-PHYS-PUB-2011-11, CERN, Geneva, Aug, 2011.

[129] T. Melia, P. Nason, R. Rontsch, and G. Zanderighi, *W^+W^-, WZ and ZZ production in the POWHEG BOX*, J. High Energy Phys. **11** (2011) 078, arXiv:1107.5051 [hep-ph].

[130] T. Binoth, N. Kauer, and P. Mertsch, *Gluon-induced QCD corrections to $pp \to ZZ \to \ell\bar{\ell}\ell'\bar{\ell}'$*, arXiv:0807.0024 [hep-ph].

[131] M. L. Mangano, M. Moretti, F. Piccinini, R. Pittau, and A. D. Polosa, *ALPGEN, a generator for hard multiparton processes in hadronic collisions*, JHEP **0307** (2003) 001, arXiv:hep-ph/0206293 [hep-ph].

[132] M. L. Mangano, M. Moretti, F. Piccinini, and M. Treccani, *Matching matrix elements and shower evolution for top-quark production in hadronic collisions*, JHEP **0701** (2007) 013, arXiv:hep-ph/0611129 [hep-ph].

[133] K. Melnikov and F. Petriello, *Electroweak gauge boson production at hadron colliders through O(alpha(s)**2)*, Phys.Rev. **D74** (2006) 114017, arXiv:hep-ph/0609070 [hep-ph].

[134] C. Anastasiou, L. J. Dixon, K. Melnikov, and F. Petriello, *High precision QCD at hadron colliders: Electroweak gauge boson rapidity distributions at NNLO*, Phys.Rev. **D69** (2004) 094008, arXiv:hep-ph/0312266 [hep-ph].

[135] J. M. Campbell and R. Ellis, *MCFM for the Tevatron and the LHC*, Nucl.Phys.Proc.Suppl. **205-206** (2010) 10–15, arXiv:1007.3492 [hep-ph].

[136] J. M. Campbell and R. K. Ellis, *Radiative corrections to Z b anti-b production*, Phys.Rev. **D62** (2000) 114012, arXiv:hep-ph/0006304 [hep-ph].

[137] S. Jadach, Z. Was, R. Decker, and J. H. Kuhn, *The tau decay library TAUOLA: Version 2.4*, Comput.Phys.Commun. **76** (1993) 361–380.

[138] P. Golonka, B. Kersevan, T. Pierzchala, E. Richter-Was, Z. Was, et al., *The Tauola photos F environment for the TAUOLA and PHOTOS packages: Release. 2.*, Comput.Phys.Commun. **174** (2006) 818–835, arXiv:hep-ph/0312240 [hep-ph].

[139] T. Gleisberg, S. Hoeche, F. Krauss, M. Schonherr, S. Schumann, et al., *Event generation with SHERPA 1.1*, JHEP **0902** (2009) 007, arXiv:0811.4622 [hep-ph].

[140] ATLAS Collaboration, *The ATLAS simulation infrastructure*, Eur. Phys. J. **C 70** (2010) 823, arXiv:1005.4568 [physics.ins-det].

[141] S. Agostinelli et al., *GEANT4: a simulation toolkit*, Nucl. Instr. and Meth. **A 506** (2003) 250.

[142] ATLAS Collaboration, *Search for the Standard Model Higgs boson in the decay channel $H \to ZZ^{(*)} \to 4\ell$ with the ATLAS detector*, Phys.Lett. **B705** (2011) 435–451, arXiv:1109.5945 [hep-ex].

[143] ATLAS Collaboration, *Measurements of the photon identification efficiency with the ATLAS detector using 4.9 fb^{-1} of pp collision data collected in 2011*, Tech. Rep. ATLAS-CONF-2012-123, CERN, Geneva, Aug, 2012. https://cds.cern.ch/record/1473426.

[144] M. Pivk and F. R. Le Diberder, *SPlot: A Statistical tool to unfold data distributions*, Nucl.Instrum.Meth. **A555** (2005) 356–369, arXiv:physics/0402083 [physics.data-an].

[145] P. Speckmayer, A. Hocker, J. Stelzer, and H. Voss, *The toolkit for multivariate data analysis, TMVA 4*, J.Phys.Conf.Ser. **219** (2010) 032057.

[146] J. Alwall, M. Herquet, F. Maltoni, O. Mattelaer, and T. Stelzer, *MadGraph 5 : Going Beyond*, JHEP **1106** (2011) 128, arXiv:1106.0522 [hep-ph].

[147] ATLAS Collaboration, *Determination of the off-shell Higgs boson signal strength in the high-mass ZZ final state with the ATLAS detector*, Tech. Rep. ATLAS-CONF-2014-042, CERN, Geneva, Jul, 2014. http://cds.cern.ch/record/1740973.

[148] K. S. Cranmer, *Kernel estimation in high-energy physics*, Comput.Phys.Commun. **136** (2001) 198–207, arXiv:hep-ex/0011057 [hep-ex].

[149] L. A. Piegl and W. Tiller, *The NURBS book: Monographs in visual communication*, ch. 2. Springer, 2nd ed., 1997.

[150] ATLAS Collaboration, *Combined search for the Standard Model Higgs boson in pp collisions at $\sqrt{s} = 7$ TeV with the ATLAS detector*, Phys.Rev. **D86** (2012) 032003, arXiv:1207.0319 [hep-ex].

[151] G. Cowan, K. Cranmer, E. Gross, and O. Vitells, *Asymptotic formulae for likelihood-based tests of new physics*, Eur.Phys.J. **C71** (2011) 1554, arXiv:1007.1727 [physics.data-an].

[152] ATLAS Collaboration, *Improved luminosity determination in pp collisions at sqrt(s) = 7 TeV using the ATLAS detector at the LHC*, Eur.Phys.J. **C73** no. 8, (2013) 2518, arXiv:1302.4393 [hep-ex].

[153] I. W. Stewart and F. J. Tackmann, *Theory uncertainties for Higgs and other searches using jet bins*, Phys. Rev. **D 85** (2012) 034011, arXiv:1107.2117 [hep-ph].

[154] G. Cowan, K. Cranmer, E. Gross, and O. Vitells, *Asymptotic formulae for likelihood-based tests of new physics*, Eur. Phys. J. **C 71** (2011) 1554, arXiv:1007.1727.

[155] *Measurements of the Higgs boson production and decay rates and coupling strengths using pp collision data at $\sqrt{s} = 7$ and 8 TeV in the ATLAS experiment*, Tech. Rep. ATLAS-CONF-2015-007, CERN, Geneva, Mar, 2015. https://cds.cern.ch/record/2002212.

[156] K. Hamilton, P. Nason, and G. Zanderighi, *MINLO: Multi-Scale Improved NLO*, JHEP **1210** (2012) 155, arXiv:1206.3572 [hep-ph].

[157] D. de Florian, G. Ferrera, M. Grazzini, and D. Tommasini, *Higgs boson production at the LHC: transverse momentum resummation effects in the $H \to 2\gamma$, $H \to WW \to l\nu l\nu$ and $H \to ZZ \to 4l$ decay modes*, JHEP **1206** (2012) 132, arXiv:1203.6321 [hep-ph].

[158] M. Grazzini and H. Sargsyan, *Heavy-quark mass effects in Higgs boson production at the LHC*, JHEP **1309** (2013) 129, arXiv:1306.4581 [hep-ph].